Hadron Ratio Fluctuations in Heavy-Ion Collisions

Dissertation zur Erlangung des Doktorgrades der Naturwissenschaften

vorgelegt beim Fachbereich Physik
der Johann Wolfgang Goethe-Universität in Frankfurt am Main

von Tim Schuster aus Bad Soden am Taunus

Frankfurt am Main 2011
(D 30)

Vom Fachbereich Physik der Johann Wolfgang Goethe-Universität als Dissertation angenommen.

Dekan:	Prof. Dr. Michael Huth
Gutachter:	Prof. Dr. Dr. h.c. Reinhard Stock
	Prof. Dr. Joachim Stroth
Datum der Disputation:	Dezember 2011

Zusammenfassung der vorliegenden Arbeit

Kollisionen schwerer Ionen bei relativistischen Energien stellen die Möglichkeit dar, im Labor Kernmaterie unter extremen Bedingungen zu untersuchen. Diskretisierte numerische Berechnungen in der Eichtheorie der starken Wechselwirkung (lattice QCD) sagen voraus, dass die erreichte Energiedichte den Übergang zu einem exotischen Zustand stark wechselwirkender Materie ermöglicht: das Quark-Gluon-Plasma. Durch die hohe Energiedichte ist eine grundlegende Eigenschaft der starken Wechselwirkung zeitweise aufgehoben: das *confinement* der Partonen genannten Quarks und Gluonen zu Hadronen; statt dessen können sich die Partonen über einen Kern-großen Bereich frei bewegen. Dieser Materiezustand herrschte im frühen Universum, bis etwa eine μs nach dem Urknall vor. Auch im Innern schwerer kompakter Sterne geht man davon aus, dass hochdichte Materie im Zustand des de-confinement vorliegt.

Die Kompression und das Aufheizen von Kernmaterie in Schwerionenkollisionen bei unterschiedlicher Energie ermöglicht eine Erforschung des Phasendiagramms stark wechselwirkender Materie, das in Abbildung 1.3 dargestellt ist. Im Ablauf einer Schwerionenkollision folgt auf den Aufprall der Lorentz-kontrahierten Kerne die dichteste und heisseste Phase. Von hier aus expandiert das System binnen weniger fm/c. Bei ausreichender Kollisionsenergie liegt im frühen Stadium ein Quark-Gluon-Plasma vor, das am Phasenübergang hadronisiert. Die entstandenen Hadronen können wegen der hohen Temperaturen als ein relativistisches Gas beschrieben werden. Der Punkt, an dem es sich so weit verdünnt (und damit abgekühlt) hat, dass keine inelastischen Wechselwirkungen mehr stattfinden kann als *chemisches Ausfrieren* aus der gemessenen Zusammensetzung der Hadronarten bestimmt werden. Ausfrierpunkte für verschiedene Strahlenergien sind im Phasendiagramm zusammen mit den dazugehörigen angenommenen Expansionskurven dargestellt. Mit zunehmender Strahlenergie steigt das Verhältnis neu produzierter zu bestehenden Valenzquarks, wobei das baryonische chemische Potential μ_B abnimmt (siehe Abbildung 1.5).

Lattice QCD-Rechnungen sehen die kritische Temperatur für den Übergang zum Quark-Gluon-Plasma bei ca. $T_c \approx 170 \pm 10$ MeV, und die Ausfrierpunkte nähern sich mit zunehmender Kollisionsenergie dieser Phasengrenze an. Es gibt Anzeichen, wonach der Phasenübergang im Energiebereich des CERN-SPS zum ersten Mal erreicht wird, der auch Gegenstand der vorliegenden Studie ist. Eine Vielzahl von Anzeichen für diesen Phasenübergang wurden beobachtet, dazu gehören die relative Produktion seltsamer Teilchen oder kollektive Effekte, die sich während der Expansion in Impulskorrelatio-

nen der Teilchen niederschlagen. Auch seltene Prozesse wie die Produktion schwerer Quarkonium-Zustände oder die harte Streuung von Partonen im frühen Stadium der Kollision lassen Rückschlüsse zu. Die letzten beiden Beispiele haben den Vorteil, dass sie durch nicht-relativistische oder Störungstheoretische Ansätze vorhergesagt werden können, während viele Prozesse in Schwerionenkollisionen im nicht störungstheoretisch beschreibbaren Bereich der QCD stattfinden. Hier helfen die oben genannten Gittereichrechnungen oder effektive Modelle.

Theoretische Vorhersagen über die Natur des Phasenüberganges erwarten einen kontinuierlichen (cross-over) Übergang bei kleinen μ_B-Werten, der an einem kritischen Punkt in einen Phasenübergang ersten Ordnung mündet. Besonders an letzteren erwartet man verstärkte Fluktuationen in der Impulsraum- und Häufigkeitsverteilung. Bei Fluktuationsmessungen müssen potentielle Hintergrundeffekte bedacht werden, sowie die Gefahr, dass eindeutige Signale des Phasenüberganges in späteren hadronischen Phasen der Expansion ausgelöscht werden. Im Allgemeinen hängen die beobachtbaren Fluktuationen auch von der Akzeptanz des Experiments ab. Diese muss gut bekannt sein und in Modellvergleichen berücksichtigt werden. Wird beispielsweise ein Fluktuation durch den Zerfall einer Resonanz ausgelöst, deren charakteristischer Zerfallswinkel nicht von der Akzeptanz des Experiments abgedeckt wird, ist diese Korrelation im Experiment nicht sichtbar. Ein Rundblick über bereits untersuchte Fluktuationsmessgrößen in Abschnitt 1.4 zeigt Vor- und Nachteile unterschiedlicher Ansätze auf. So erwies sich, dass Ladungsfluktuationen die auf den Phasenübergang hinweisen nicht bis in den beobachtbaren Endzustand erhalten bleiben. Fluktuationen der Gesamtteilchenzahl oder des mittleren Transversalimpulses in Hinblick auf den kritischen Punkt lassen nur ein Signal erwarten, das von der Größe und Lebensdauer des beobachteten Systems erheblich eingeschränkt ist.

Die vorliegende Analyse zielt auf die Fluktuationen identifizierter Teilchen ab. Für diese erwartet man ein aussagekräftiges Signal sowie eine geringe Abschwächung. Von den hier untersuchten Fluktuationen des Kaon zu Proton-Verhältnisses erwartet man einen Rückschluss auf die zugrundeliegenden Korrelationen zwischen den Erhaltungsgrößen Baryonzahl und Strangeness. Kaonen und Protonen sind die häufigsten Vertreter dieser Quantenzahlen. Die Baryon-Strangeness-Korrelation wird mittels der Größe C_{BS} gemessen, und ein merklicher Wechsel am Phasenübergang wird vorausgesagt. C_{BS} wird deshalb als “Diagnosewerkzeug für den Zustand stark wechselwirkender Materie” gesehen. Darüber hinaus sieht man in lattice QCD-Berechnungen der Quark-Anzahl-Suszeptibilitäten starke Effekte am kritischen Punkt, die sich in Häufigkeitsfluktuationen niederschlagen sollen.

In zentralen Pb+Pb Kollisionen im Bereich von Schwerpunktsenergien ($\sqrt{s_{NN}}$) zwischen 6.3 und 17.3 GeV können Häufigkeitsverhältnisse zwischen Kaonen und Protonen in jedem Kollisionsereignis ermittelt werden, um daraus die Fluktuationen von Ereignis zu Ereignis zu berechnen. Die vorliegende Arbeit entstand am NA49 Experiment, einem Hadronen-Spektrometer mit großer Akzeptanz, das in Kapitel 3 beschrieben wird. Es wird vom umfassenden Beschleunigersystem des europäischen Teilchenphysik-Forschungszentrums CERN bedient. Dabei durchlaufen die untersuchten Bleikerne zwischen Ionenquelle und Experiment eine Kette von Beschleunigern, zuletzt das Super Proton Synchrotron SPS. Die große Akzeptanz von NA49 ermöglicht die Identifikation von 60 bis 600 Hadronen pro Kollision, so dass die Momente der Häufigkeitsverteilung der Verhältnisse $(\mathrm{K}^+ + \mathrm{K}^-)/(\mathrm{p} + \overline{\mathrm{p}})$ und K^+/p aussagekräftig bestimmt werden konnten. Die Auswahl zentraler Kollisionsereignisse wird durch eine Messung der Energie der Projektilspektatoren erreicht, also derjenigen Nukleonen aus dem Projektilkern, die nicht an der Kollision beteiligt waren. Eine zentrale Kollision weist kaum Spektatoren auf, während bei einer peripheren Kollision eine hohe Spektatorenergie im entsprechenden Kalorimeter gemessen wird.

Die Teilchenidentifikation beruht auf dem spezifischen Energieverlust ($\mathrm{d}E/\mathrm{d}x$) geladener Teilchen im Detektorgas der Spurendriftkammern (TPCs) von NA49. Kalibrierungen und Korrekturen sind dabei die unerlässliche Grundlage für die vorliegende Messung. Die Auflösung der $\mathrm{d}E/\mathrm{d}x$-Methode hängt von der Anzahl gemessener Spurpunkte in den TPCs ab, und Qualitätskriterien zur Auswahl von Spuren müssen definiert werden. Eine gute Kenntnis der inklusiven $\mathrm{d}E/\mathrm{d}x$-Verteilung ist die Basis der Identifikation in einzelnen Ereignissen. Dabei erfordert die Unterscheidung von Kaonen und Protonen wegen ihrer großen Nähe im $\mathrm{d}E/\mathrm{d}x$-Signal eine besonders sorgfältige Betrachtung. Die Energieverlustmessung in den NA49-TPCs erfolgt im Bereich des *logarithmischen Anstiegs* der Bethe-Bloch-Kurve. Die in der vorliegenden Arbeit angewendete Teilchenidentifikationsmethode ist ein zweistufiger Prozess, der bereits in der Analyse der Fluktuationen des $(\mathrm{K}^+ + \mathrm{K}^-)/(\pi^+ + \pi^-)$ und des $(\mathrm{p} + \overline{\mathrm{p}})/(\pi^+ + \pi^-)$ Verhältnisses Anwendung gefunden hat. Zunächst erfolgt eine inklusive $\mathrm{d}E/\mathrm{d}x$-Analyse, bei der mittels einer χ^2-Anpassung in diskret getrennten Phasenraumbereichen die Wahrscheinlichkeitsverteilungen in Phasenraum und $\mathrm{d}E/\mathrm{d}x$ bestimmt wird (siehe Abschnitt 5.3). Diese Wahrscheinlichkeitsverteilung ist die Basis des zweiten Schritts. In einzelnen Kollisionsereignissen wird jetzt ein ungebintes Likelihood-Verfahren angewendet. Die inklusiven Verteilungen werden dabei zugrunde gelegt, und nur die relativen Teilchenhäufigkeiten werden variiert. Auf diese Weise werden wie in Abschnitt 5.4 beschrieben die Verteilungen der Teilchenverhältnisse ermittelt.

Um die Stabilität der beobachteten Fluktuationswerte sicherzustellen, wurden im Rahmen dieser Arbeit eine Vielzahl experimenteller Parameter variiert. Beispielsweise wurden die Ereignisselektion und Zetralitätsbestimmung untersucht. Qualitätskriterien in der Spurauswahl garantieren eine verlässliche Teilchenidentifikation, und der Einfluss einer Veränderung dieser Kriterien wurde ebenfalls betrachtet. Hier konnte etwa gezeigt werden, dass das Verfahren unter unterschiedlichen $\mathrm{d}E/\mathrm{d}x$-Auflösungen zuverlässig arbeitet. Auch ein Beitrag von schwachen Zerfällen zum Fluktuationsergebnis konnte mit Hilfe dieser Studien ausgeschlossen werden. Die beobachteten Fluktuationen sind ebenfalls vom kinematischen Bereich der Messungen abhängig. Studien auf diesem Gebiet stellen sicher, dass die Ergebnisse mit Modellen verglichen werden können. Auf Basis all dieser Untersuchungen wurde der systematische Fehler der Fluktuationsmessung bestimmt.

Zur Bestimmung der physikalisch relevanten *dynamischen* Fluktuationen müssen Hintergrundeinflüsse abgezogen werden. Diese setzen sich aus statistischen sowie durch das Identifikationsverfahren entstandenen Fluktuationen zusammen. Diese Referenz wird in zwei Stufen ermittelt. Zuerst werden durch Event-Mixing Ereignisse erzeugt, die frei von physikalischen Korrelationen sind, aber die statistischen Eigenschaften der ursprünglichen Ereignisse aufweisen. Um den Einfluss der Teilchenidentifikation nachzuvollziehen, wird dann in den Mixed Events die identische Likelihood-Methode wie in den normalen Daten angewendet. Schließlich erfolgt durch die hier benutzte Variable σ_{dyn} die Subtraktion der so ermittelten Hintergrundbeiträge. σ_{dyn} beruht auf den skalierten Breiten der Daten- und Mixed Event-Verteilungen.

Die Mixed Event-Methode und die Teilchenidentifikation wurden durch Modellrechnungen und Simulationen sorgfältig geprüft um sicherzustellen, dass der Hintergrund korrekt bestimmt und abgezogen wird. So wurden etwa im hadronischen Transportmodell UrQMD erzeugte Ereignisse zunächst analysiert, indem auf die eindeutige Teilchenidentifikation zurückgegriffen wurde. Danach wurde jedem UrQMD-Teilchen ein $\mathrm{d}E/\mathrm{d}x$-Wert zugeordnet und das experimentelle Verfahren vollständig angewendet. Die Ergebnisse der beiden Methoden stimmen überein.

In den Gemessenen Wert von σ_{dyn} gehen Fluktuationen der betrachteten Teilchen ein, er enthält aber auch Informationen über Korrelationen zwischen den verschiedenen Teilchensorten. Die Messgröße gibt also eine Summe mehrerer Effekte an, die miteinander verknüpft sind. Eine direkte Messung, etwa von Korrelationskoeffizienten, ist nicht sinnvoll, weil diese von Volumenfluktuationen und experimentellen Effekten überlagert werden. σ_{dyn} ist unabhängig von diesen Hintergrundbeiträgen, für eine Interpretation sind aber Modellvergleiche notwendig. Auch die Messung verschiedener Kombinationen, wie

hier $(K^+ + K^-)/(p + \overline{p})$ und K^+/p ermöglicht die Unterscheidung einzelner Beiträge. Neue Messgrößen werden derzeit innerhalb der NA49 Kollaboration erprobt und ermöglichen vielleicht in Zukunft direktere Interpretationen.

Im beobachteten SPS-Energiebereich weisen die σ_{dyn} Ergebnisse für $(K^+ + K^-)/(p + \overline{p})$ und K^+/p beide einen Übergang von Werten um die -5% bei den höheren Energien hin zu positiven Werten von 5–8% bei der niedrigsten Energie auf. Die Ergebnisse sind in Abbildung 6.1 dargestellt. Die Übereinstimmung für die beiden Verhältnisse bei der kleinsten Energie ist dadurch plausibel, dass K^- und $\overline{p}$ dort keine Rolle spielen. Die hadronischen Transportmodelle UrQMD und HSD dienen zum Vergleich, um den Effekt hadronischer Fluktuationen und Korrelationen auf die Messgröße zu bestimmen. Beide Modelle basieren auf dem Boltzmann-Transportansatz. In keinem der beiden Modelle wird die abrupte Energieabhängigkeit reproduziert, die in den Daten beobachtet wird. Die Wendung zu positiven Werten bei kleinen Energien impliziert eine dort auftretende Anti-Korrelation unbekannter Herkunft, die nicht intuitiv erklärbar ist.

Die Messergebnisse wurden auch im Rahmen bestehender anderer Messungen eingeordnet. Im Vergleich mit dem STAR Experiment (in Abschnitt 6.3) kann gezeigt werden, dass die dort verwendete Messgröße ν_{dyn} mit den σ_{dyn}-Messungen von NA49 vergleichbar ist. Im überlappenden Bereich der beiden Experimente besteht Übereinstimmung, nur die STAR-Messung mit der niedrigsten Energie bei $\sqrt{s_{NN}} = 7.7$ GeV weicht von den NA49 Ergebnissen ab. In Zusammenarbeit zwischen den beiden Kollaborationen wurden mögliche Ursachen ausgedeutet. Ein Hauptunterschied ist die Akzeptanz der beiden Experimente. Während STAR als Collider-Experiment eine im Schwerpunktsystem feststehende Akzeptanz besitzt, muss in der fixed target-Geometrie von NA49 das Spektrometer-Magnetfeld an die Strahlenergie angepasst werden um eine gleichbleibende Akzeptanz zu gewährleisten. Weitere mögliche Unterschiede zwischen NA49 und STAR liegen in der Teilchenidentifikationsmethode, der Zentralitätsbestimmung oder doch der verwendeten Messgröße. Neue Messgrößen, die auf beide Experimente anwendbar sind versprechen für zukünftige Untersuchungen eine bessere Vergleichbarkeit und ein Verständnis verbliebener Unterschiede.

Eine intrinsische Multiplizitätsabhängigkeit der Messgröße σ_{dyn} ermöglicht die Beschreibung der früher schon gemessenen $(K^+ + K^-)/(\pi^+ + \pi^-)$ und $(p + \overline{p})/(\pi^+ + \pi^-)$ Fluktuationen. Deren Energie- und Zentralitätsabhängigkeit kann in einer einheitlichen Beschreibung auf die triviale Änderung der durchschnittlichen Multiplizitäten zurückgeführt werden. Dies ist in Abschnitt 6.2 dargestellt. Nur die in der vorliegenden Analyse gemessenen $(K^+ + K^-)/(p + \overline{p})$ und K^+/p Fluktuationen widersetzen sich wegen des

Vorzeichenwechsels in σ_{dyn} einer solchen Beschreibung und erfordern eine zusätzliche Änderung der zugrundeliegenden Korrelationsprozesse.

Die vorliegenden Fluktuationsergebnisse können nicht per se interpretiert werden, statt dessen beruht eine Auflösung der überlagerten Effekte und damit ein Verständnis der Daten immer auf Modellvergleichen. Daher wäre es wünschenswert, zusätzlich zu der nicht-Übereinstimmung mit hadronischen Modellen einen Vergleich mit solchen Modellen zu suchen, die Phasenübergangseffekte beinhalten. Derartige Ansätze existieren und Fortschritte auf diesem Gebiet lassen hoffen, dass die vorliegenden Daten in neuen Modellen besser verstanden werden.

Contents

1 Overview **5**

1.1 Phases of Nuclear Matter . . . 6
1.2 Relativistic Heavy-Ion Collisions . . . 10
1.3 NA49 Evidence for the Onset of Deconfinement . . . 19
1.4 Fluctuations in Heavy-Ion Collisions . . . 21
1.5 NA49 Fluctuation Results . . . 28

2 Hadron Ratio Fluctuations **33**

2.1 Measuring Hadron Ratio Fluctuations . . . 36
2.2 Ratio Fluctuations and the underlying correlations . . . 38
2.3 Baryon-Strangeness Correlations . . . 41

3 The NA49 Experiment **47**

3.1 Particle Accelerators at CERN . . . 48
3.2 The SPS Energy Scan . . . 50
3.3 Experiment Overview . . . 52
3.4 Centrality Determination . . . 56
3.5 The Time Projection Chambers . . . 58
3.6 NA49 Acceptance Overview . . . 60
3.7 Data Flow . . . 62

4 Data Processing in NA49 **65**

4.1 Computing Resources at CERN . . . 65
4.2 Reconstruction Chain . . . 67
4.3 The Analysis Framework ROOT . . . 74

5 Data Analysis **77**

5.1 Selection of Central Pb+Pb Collisions . . . 77
5.2 Track Selection Quality Criteria . . . 79

5.3 Inclusive $\mathrm{d}E/\mathrm{d}x$ Particle Identification . . . 83
5.4 Event-by-Event Particle Identification . . . 92
5.5 Mixed Event Generation . . . 96
5.6 Signal Extraction: Determination of σ_{dyn} . . . 97
5.7 Systematic Studies on the Result . . . 100
5.8 The Variable σ_{dyn} . . . 108

6 Kaon-to-proton ratio fluctuations in central Pb+Pb collisions 113
6.1 Hadron Transport Model Comparison . . . 114
6.2 Multiplicity Scaling of Ratio Fluctuations . . . 118
6.3 Comparison to STAR Data . . . 121
6.4 Contribution to C_{BS} from Kaon-Proton Correlations . . . 124
6.5 Conclusion . . . 128

A Relativistic Kinematics 131

B Statistical Error on σ_{dyn} 135

Bibliography 147

Curriculum Vitae 163

Chapter 1

Overview

The idea that basic constituents make up our world by far preceded the experimental opportunities to explore this elementary part of nature. The antique concept of an indivisible entity, the atom, was based upon philosophical considerations. Experiments conducted from the 19th century on substantiated this concept, and contributed to its improvement. In the course of these experiments, not only the atom itself was revealed, but found to be composed of subatomic particles again.

Today, physicists are celebrating the hundredth anniversary of Rutherford's publication describing the discovery of the atomic nucleus [1], that is generally seen as the starting point of understanding sub-atomic physics. This field has evolved toward a standard model [2, 3] that describes hundreds of subatomic particles [4] with just a dozen of elementary particles held together by three fundamental interactions. Among these basic forces, the *strong interaction* governs the world within nucleons and is indirectly responsible for the attractive forces between nucleons, and with it for the structure of the nucleus. The strong interaction, its many facets and possible forms of strongly interacting matter still hold exciting puzzles. They center around the "confinement" phase transition from quarks and gluons to hadrons, which occurs at a high energy density. This transition governs the microsecond era of the big bang evolution, but likewise the interior structure of neutron stars, and the dynamics of supernovae. In the laboratory, some aspects of high energy density matter are tackled in heavy-ion physics. This rather technical term translates into "collisions of heavy nuclei at relativistic energy"—the field that is entered in the present thesis.

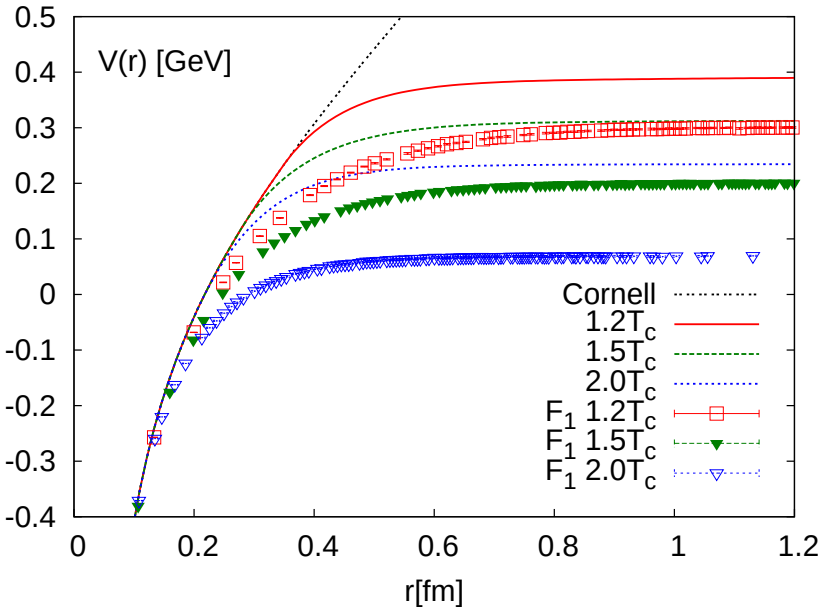

Figure 1.1: The heavy quark-antiquark potential. At low temperatures, the Cornell potential (equation (1.1)) is realized, while above T_c, lattice QCD predicts a screening of the confinement potential. Figure from [8].

1.1 Phases of Nuclear Matter

The understanding of the inner structure of the nucleon began with the discovery of the "hadron zoo" since the 1950s and the subsequent categorization of hadrons in the static quark model. Today, the dynamics of quarks and gluons as the constituents of hadrons can be described in quantum chromodynamics (QCD), the relativistic quantum field theory of strong interaction, with two peculiar features. At high energy densities, corresponding to large momentum transfers and small distances, the strong interaction is dominated by the exchange of single gluons between interacting quarks, and can be described in perturbation theory, similar to quantum electrodynamics. This behavior was observed in deep inelastic lepton-proton scattering [5] and in QCD is attributed to the diminished coupling constant and the *asymptotic freedom* [6, 7] in this regime. While quarks in the dense interior of hadrons can thus behave like quasi-free particles, at larger distance (or going to softer interactions) the gluon self-interaction leads to a much stronger coupling. The strong force stays constant, eventually resulting in the *confinement* of quarks in the hadrons.

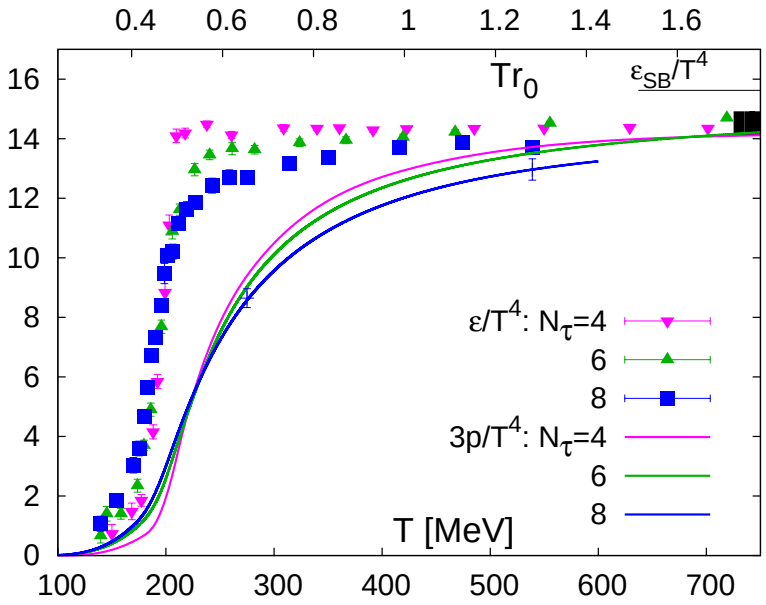

Figure 1.2: Lattice QCD calculations for the energy density and pressure as a function of temperature T, both normalized by T^4. The figure was taken from [13].

Both features are illustrated in the simple *Cornell* formulation of the heavy quark-antiquark potential [9]

$$V(r) = -\frac{\alpha_s}{r}\left[1 - (r/a)^2\right], \tag{1.1}$$

where asymptotic freedom is manifest in the Coulomb-like $1/r$ term, while confinement is reached via the $\propto r$ part, dominating at larger distance r. The grey dotted line in Figure 1.1 [8] sketches this Cornell potential. A direct derivation of these features from QCD is however complicated by the non-abelian nature of the field theory. While the high momentum transfer part is still tangible via perturbation theory (perturbative QCD, pQCD), in the limit of strong coupling, perturbation expansions of QCD do not converge. This non-perturbative regime can however be simulated on a discrete space-time lattice [10]. Lattice QCD at low temperatures (e.g. [11, 12]) confirms the Cornell potential.

The study of extended many-particle systems or *matter* governed by the strong interaction promises to shed additional light on this enigmatic natural force. The theoretical description of such a system, QCD thermodynamics, is however theoretically accessible only by effective models or by lattice calculations. One important feature of QCD matter emerges from these calculations: At sufficiently high energy density and

temperature, the confinement of quarks and gluons to hadrons is overcome. In Figure 1.2, a sudden rise of the energy density and pressure at a critical temperature T_c is seen in lQCD calculations [13], indicating the new, partonic degrees of freedom. The deconfinement is a consequence of larger momentum transfer at higher temperature (but not to be confused with asymptotic freedom at TeV momentum transfer) and, more importantly, the higher color charge density leading to a screening of the QCD potentials. Lattice QCD calculations for the modified quark-antiquark potential above the critical temperature $T_c \approx 170 \pm 10$ MeV are also shown in Figure 1.1. Under these extreme conditions, the confinement part of the potential disappears, allowing quarks and gluons to move freely. QCD matter thus has distinct phases: hadronic matter and, above the *deconfinement phase transition*, the *quark-gluon plasma*.

Another singular feature of low temperature QCD, chiral symmetry breaking, is expected to be overcome in the quark gluon plasma. Lattice QCD calculations [13] show characteristic signatures of both transitions at the same temperature T_c: The Polyakov loop, order parameter of the deconfinement phase transition rises, and a sudden drop in the chiral condensate indicates chiral restoration, making the deconfinement phase transition the line of chiral symmetry restoration at the same time.

This leads to the current picture of the phase diagram of strongly interacting matter, sketched in Figure 1.3. Ordinary nuclear matter is found at low temperature T and a baryonic chemical potential μ_B with a value of $\mu_B \approx m_N$, the nucleon mass. Another phase transition line in Figure 1.3, not discussed here, separates the bound state of nuclear "liquid" from a hadron gas. Going to higher T and/or μ_B, the transition to the quark-gluon plasma, indicated by the grey line in Figure 1.3 is expected. The most extensive lQCD calculations cover the region of vanishing μ_B, but recent technical advancements allow extrapolations to finite μ_B [14, 15, 16, 17]. The characteristics of the phase transition seen in lQCD indicate a smooth cross-over from one phase to the other at low μ_B, while in the high μ_B part, a first order phase transition is expected in effective models [18]. The changeover from first order to cross-over transition is marked by a critical point [19, 10, 14, 15]. Indications of this point have been seen in diverging lQCD quark number susceptibilities [16, 17, 20] at finite μ_B (see Figure 2.1).

First perception of the universe is dominated by normal nuclear matter, and thus the low temperature part of the phase diagram. Even the highest temperatures reached in the sun ($1.6 \cdot 10^7$ K) are still five orders of magnitude below T_c. Nevertheless, the phase transition studied here plays a role on the cosmological scale. Extreme conditions in the interior of neutron stars are expected to lie beyond the hadron-parton phase transition at

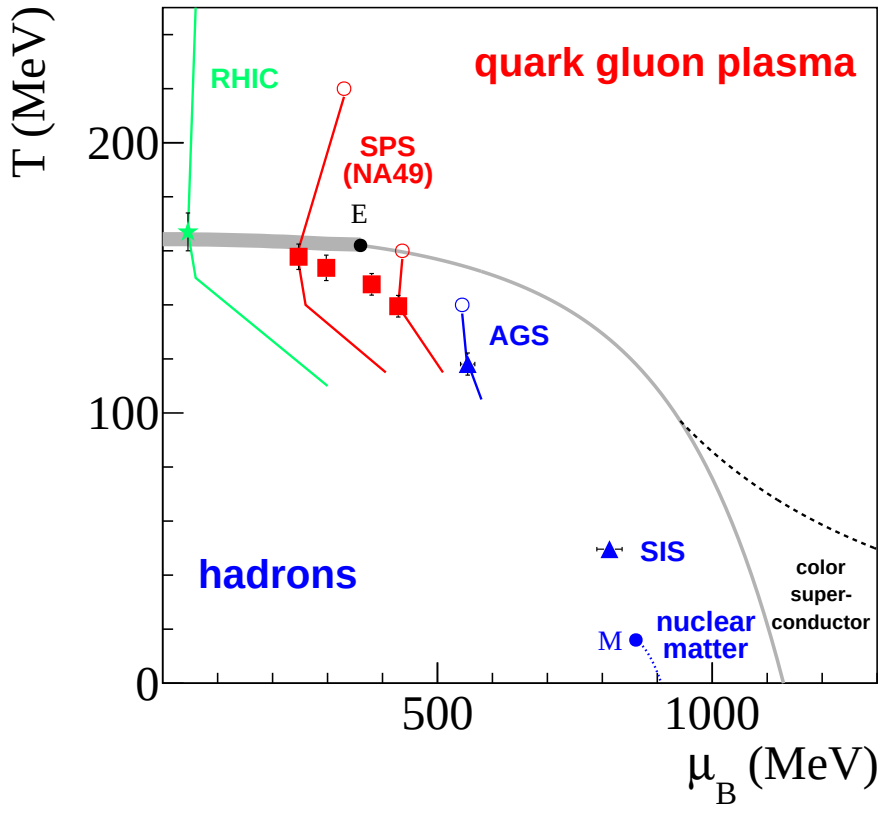

Figure 1.3: Phases of nuclear matter. M indicates the endpoint of the hadronic liquid-gas transition line, while the critical point E separates the cross-over (low μ_B) from the first order transition between hadron gas and quark-gluon plasma. Markers indicate the freeze-out conditions from heavy-ion collisions at various energies.

low temperatures but high baryon densities. The early universe on the other hand went through a phase of quark-gluon plasma at extreme temperatures and $\mu_B \approx 0$, before eventually condensing into hadrons approximately 10^{-5} s after the big bang.

Collisions of heavy ions at relativistic energies provide the possibility to study the phase diagram of strongly interacting matter in the laboratory. The results of experimental programs at various energies lead to the trajectories sketched in Figure 1.3. They represent the dynamical evolution of the interior sections of the collisional "fireball" volume in the (T, μ_B) plane, indicating that heavy-ion collisions probe strongly interacting matter at high temperatures and the phase transition region. This experimental access to the phase diagram will be the subject of the following section.

1.2 Relativistic Heavy-Ion Collisions

The technical term "Heavy Ion Collisions" refers to the physics of nucleus-nucleus collisions which, with increasing energy, required acceleration of highly, or completely ionized nuclear species. A heavy nucleus represents a saturated volume of nuclear matter in its ground state. The idea that shock compression of nuclear matter can be achieved via high energy nuclear collisions [21] was tested in exploratory experiments at Berkeley Lab's Bevalac [22] and the Synchrophasotron [23] at the Joint Institute of Nuclear Research (JINR) in the 1970s. Nuclei up to the size of Argon were brought to kinetic energies between 0.2 and 3.5 GeV per nucleon and collided with heavy nuclei. The analysis of particle and transverse energy spectra in such collisions led to the conclusion that a thermal "fireball" of high temperature and density was created here, with shock compression leading to densities even beyond the density $\rho = 2\gamma\rho_0$, expected from overlap of two nuclei with ground state density $\rho_0 = 0.15$ GeV/fm^3 and contracted by a Lorentz-factor γ [24].

The field of relativistic heavy-ion collisions moved on to higher energies at Brookhaven National Lab's Alternating Gradient Synchrotron (BNL-AGS) and the Super Proton Synchrotron SPS at CERN [25]. A highlight was reached in 1999, when the SPS experiments announced the discovery of a new state of matter [26, 27] based on the combined evidence from several experiments. The energy density reached in the initial state of collisions at the highest SPS energy of $\sqrt{s_{NN}} = 17.3$ GeV amounts to about 3 GeV/fm^3. This by far exceeds the critical energy density $\epsilon_c = 1$ GeV/fm^3 determined in lattice QCD, corresponding to T_c described in Section 1.1. ϵ_c coincides with the

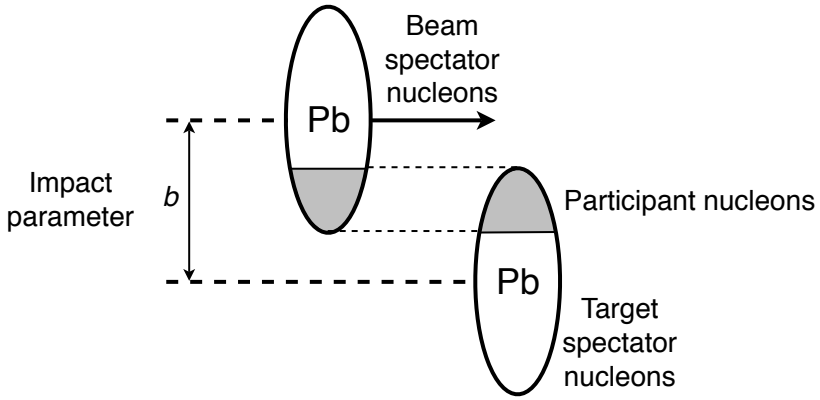

Figure 1.4: Side view of a non-central heavy-ion collision. The Lorentz-contracted nuclei are displaced by the impact parameter b, and as a result only a part of the nucleons participates in the collision.

energy density within hadrons, and the attainment of this density over an extended volume is equivalent with the creation of a quark-gluon plasma. In an energy scan at the SPS, first indications for the onset of the deconfinement phase transition in the range $6.3 < \sqrt{s_{NN}} < 17.3$ GeV have been reported [28] (see Section 1.3).

While the previous fixed-target experiments at AGS and SPS re-used accelerators from high energy physics, the Relativistic Heavy-Ion Collider (RHIC) at BNL was the first dedicated heavy-ion machine, and the currently highest energy collider LHC was designed and built with both communities in mind. The early discoveries at RHIC [29, 30, 31, 32] established the canonical picture of deconfined matter that was confirmed by the LHC experiments.

Phases of a heavy-ion collision

The initial state of a heavy-ion collision is governed by the relativistic length contraction of the nuclei accelerated to relativistic energies. The Lorentz factor γ reaches ≈ 10 at top SPS energy and ≈ 100 at RHIC. Following this contraction, and due to the parton kinematic range probed at increasing energy, parton saturation effects [33] may play a role here.

Independent of the exact nature of the initial conditions, the subsequent collision stage will compress and heat the incident nuclear matter. Primary scattering between

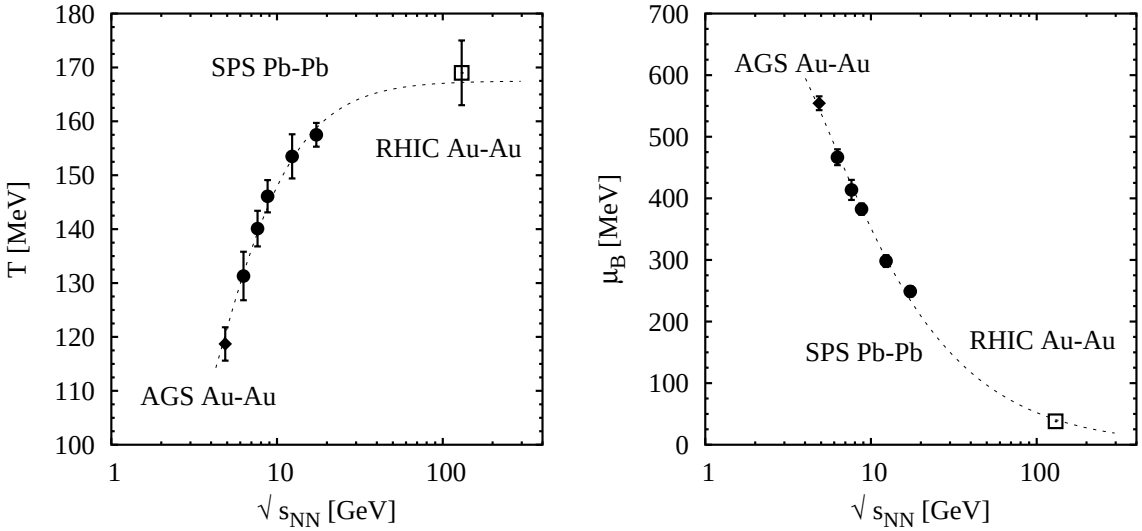

Figure 1.5: Energy dependence of chemical freeze-out conditions in heavy-ion collisions, from [34]. The temperature T_{ch} (left) saturates approaching T_{c}, while the baryonic chemical potential μ_B(right) goes to zero with rising energy $\sqrt{s_{NN}}$.

partons, characterized by high momentum transfer, may create *hard probes*, such as heavy particles or high transverse momentum (p_{T}) particles. The subsequent multiple interactions between nucleons further increase the energy density in the center-of-mass. Given the nuclear radii $r \approx 7$ fm of heavy ions, the collision geometry has a stochastic nature. The collision centrality is characterized by the closest approach of the nucleus centers, the impact parameter b, as sketched in Figure 1.4. Head-on collisions of the nuclei, corresponding to $b = 0$, produce the highest energy density at a given collision energy, and the selection of centralities allows for the study of system size and shape effects.

Given a sufficient incident energy, the created fireball surpasses ϵ_{c}, and the quark-gluon plasma is created. In the course of the temporal evolution, the highest density is reached at the reversal point between initial compression and the expansion that will follow. Open symbols in Figure 1.3 indicate this point of highest energy density for different collision energies. In analogy to the classical harmonic oscillator, the system remains at the reversal point for a while before the expansion with associated cooling sets in. This adiabatic expansion path is sketched by a line in Figure 1.3. Reaching ϵ_{c}, a phase transition back to confined matter is passed.

Hadrons in the resulting relativistic gas still contain sufficient thermal kinetic energy to create new particles and resonances. These inelastic collisions cease at a point in

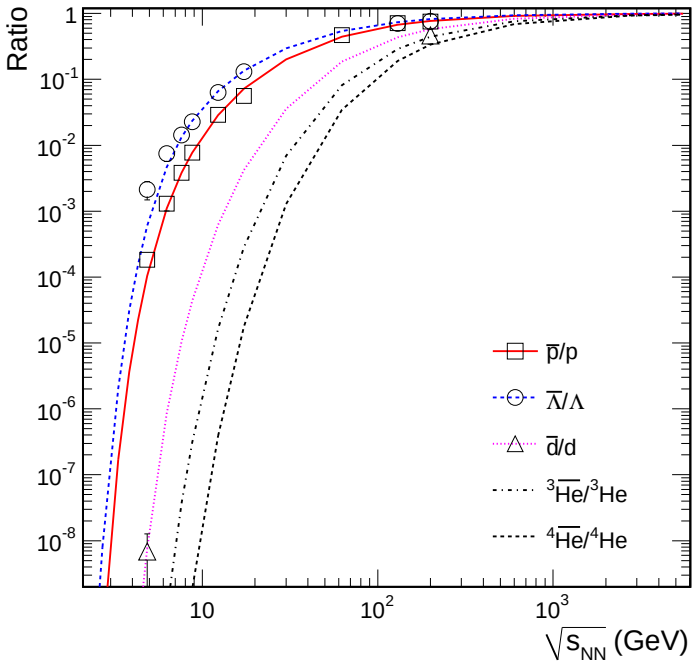

Figure 1.6: Anti-baryon to baryon ratios as a function of $\sqrt{s_{NN}}$. Experimental data (symbols) is compared to statistical model fits (lines). With rising energy, the anti-matter matter asymmetry goes away, corresponding to $\mu_B \to 0$. The figure is taken from [35].

further expansion marking the *chemical freeze-out* at temperature T_{ch}. Except for resonance decays, no process can change the hadronic abundances, or the hadro-chemical composition in the further evolution, the conditions at T_{ch} are "frozen in" and can be derived from the measurable final state through statistical models [36, 37, 38, 39]. The resulting thermodynamic parameters are marked using solid symbols in Figure 1.3 and represent a curve of quasi-stable hadron-resonance matter in the phase diagram. With rising energy, T_{ch} approaches the transition temperature T_{c}. At the same time μ_B gets smaller, as the produced particles (symmetric in matter and anti-matter) start to dominate over the initial baryon number excess of the incident nuclei. Both features can be seen in the energy dependence of T_{ch} and μ_B [34] depicted in Figure 1.5. At SPS energies, the ratio between valence quarks and newly produced quark-antiquark pairs is ≈ 1, dropping to $\approx 5\%$ at the LHC [40]. The cosmic evolution even features a matter-antimatter asymmetry of $\approx 10^{-9}$ only [41]. This trend to more symmetric matter is also visible in the anti-baryon to baryon ratios depicted in Figure 1.6. Consequently, heavy-ion collisions at the SPS probe the region $200 < \mu_B < 500$ MeV, while phase trajectories for LHC or the cosmic evolution would feature at $\mu_B \to 0$ in Figure 1.3, with initial temperatures beyond the GeV range. Despite this large span of conditions probed

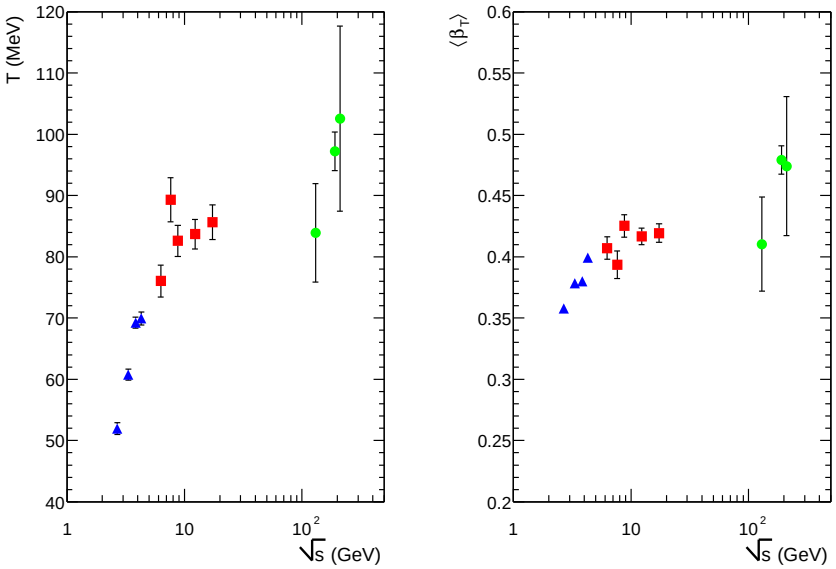

Figure 1.7: The blast wave model parameters extracted from hadron momentum spectra describe the thermal decoupling stage of a heavy ion collision. The temperature T_f (left) rises with energy, the average transverse flow velocity $\langle\beta_\mathrm{T}\rangle$ (right) seems to reach a plateau at SPS energies [43].

in heavy-ion experiments, the chemical freeze-out was found to occur independent of the collision energy at an average energy per hadron of ≈ 1 GeV [42], a quantity apparently governing QCD hadronization.

Upon further expansion from chemical freeze-out onward, the system reaches *thermal decoupling*, where also the elastic collisions among hadrons cease. With no further momentum transfer possible, this stage characterized by the temperature T_f is imprinted on the momentum spectra of the hadrons that now stream freely toward the particle detectors. The conditions of this thermal decoupling can be determined by a fit to the spectra. In contrast to exponential spectra as expected from a static source with temperature T_f, a collective motion is observed. A simple description of this fact is the *blast-wave model* [44, 45, 46] that assumes thermal hadron emission from an expanding source. While the flow velocity profile is boost invariant in longitudinal direction, the transverse flow velocity β_T increases radially. The model has been applied to heavy-ion collisions from AGS to RHIC energies [43] and the resulting parameters temperature T_f and average transverse radial flow velocity $\langle\beta_\mathrm{T}\rangle$ are shown in Figure 1.7. T_f has a similar energy dependence as T_ch (cf. Figure 1.5), but at considerably lower values. $\langle\beta_\mathrm{T}\rangle$ exhibits a saturation at SPS energies, but the large error bars at higher energies make a strong conclusion difficult.

Figure 1.3 traces the phase evolution of heavy-ion collisions at different energies. At AGS and the even lower GSI-SIS energies, the initial density does not exceed ϵ_c. In this case, the stopped nucleons and the newly produced hadrons form a hadron gas which cools and expands in a similar manner as described above. In the following section, we will describe several observables that will help to distinguish between the evolution of such a hadronic fireball and one at higher energies, reaching the quark-gluon plasma.

Signatures from the fireball

All along the time evolution of a heavy-ion collision sketched above, characteristic signatures are formed, as a result of previous or ongoing dynamics. They can serve as valuable observables if they become stationary right after their phase of generation, i.e. if they "freeze out" at a distinct stage of the evolution, staying unobliterated throughout the subsequent system expansion. In the interpretation of the final state, it is thus important to keep in mind that the early deconfined state has a lifetime of only a few fm/c and that certain signals from the early stage may be affected by the consecutive expansion dynamics. The final state of a relativistic heavy-ion collision consists of thousands (at SPS, five-thousands at RHIC and ten-thousands at the LHC) of hadrons, leptons and photons. Depending on the specialization and acceptance of the experiment, fractions of those are detected and identified. The following list, with no claim of being complete, introduces the most important observables evolving from late to early stages of the collision.

- In analogy to the Hanbury Brown and Twiss effect in astronomy, the source size of correlated hadron emission can be determined using two-particle correlations [47]. Bose-Einstein statistics can be probed by using identical boson correlations while non-identical two-particle correlations reveal other quantum effects or correlations owing to Coulomb and strong interaction.
- A collective particle motion, or "flow" is expected from a thermalized system in hydrodynamic expansion. The evolution of radial flow as a function of incident beam energy as described in the previous section (cf. Figure 1.7) and the translation of initial spacial anisotropy in peripheral collisions into "directed" and "elliptic" flow are sensitive to the build-up of pressure throughout the fireball evolution [49]. Figure 1.8 shows the elliptic flow v_2 as an example, the second Fourier component of the azimuthal momentum distribution. v_2 is shown to scale with the initial geometrical eccentricity (that is governed by the collision centrality) and the flow

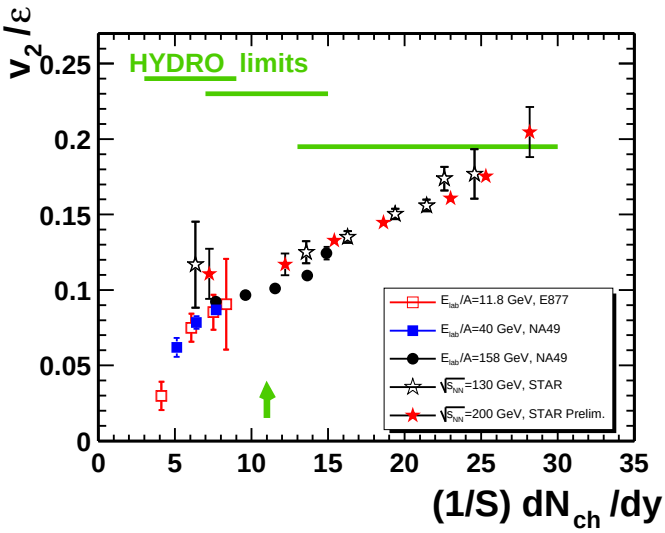

Figure 1.8: The elliptic flow v_2, scaled by initial-state eccentricity ϵ shows a universal rise with density [48]. A detailed modeling of this behavior can provide access to the equation of state of nuclear matter under the extreme conditions in heavy-ion collisions.

increases with particle density. Hydrodynamic models are used to describe the measured flow patterns and thus give access to the equation of state (EOS), relating the energy density to the pressure that drives the expansion. At the transition from partonic to hadronic fluids, the associated change in the EOS induces signatures for the phase transition.

- Average hadron multiplicities are fixed at chemical freeze-out, and its parameters are extracted using statistical model fits. The applicability of these models suggests that the hadrons freeze out from a thermalized system, an important precondition in the further discussion. The strangeness enhancement seen in comparison to p+p collisions indicates the formation of an extended coherent system that can be described in the grand-canonical ensemble, while p+p collisions in contrast show canonical effects. Finally with T_{ch} approaching and saturating close to T_{c}, this analysis helps us map the phase diagram with evolution trajectories.

- Enhanced fluctuations are a general feature of phase transitions. In heavy-ion collisions close to the threshold to deconfinement, small initial density fluctuations lead to single events crossing the phase boundaries. The radical change of conditions leads to large event-by-event fluctuations of hadronic observables. The critical point is expected to induce particular fluctuations, that have been observed in lattice QCD calculations at finite μ_B. Distinct fluctuation patterns are established in all

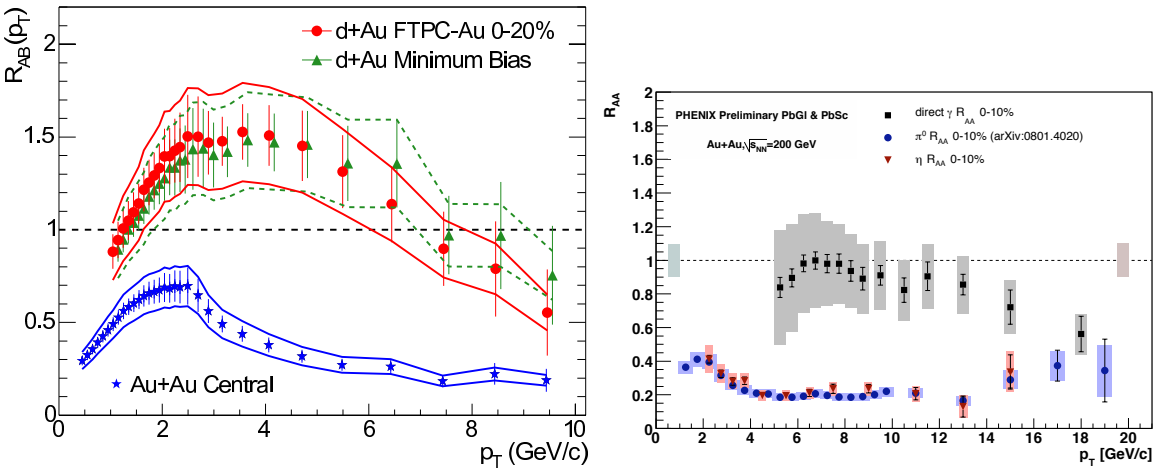

Figure 1.9: The nuclear modification factor R_{AB} measured at $\sqrt{s_{NN}} = 200$ GeV. Charged hadrons show a strong suppression in central Au+Au collisions, while this effect is absent in d+Au (left) [50]. Photons do not interact strongly and are thus unaffected by the fireball created in Au+Au collisions. This is reflected in an $R_{\mathrm{AA}} \approx 1$ (right) [51, 52, 53].

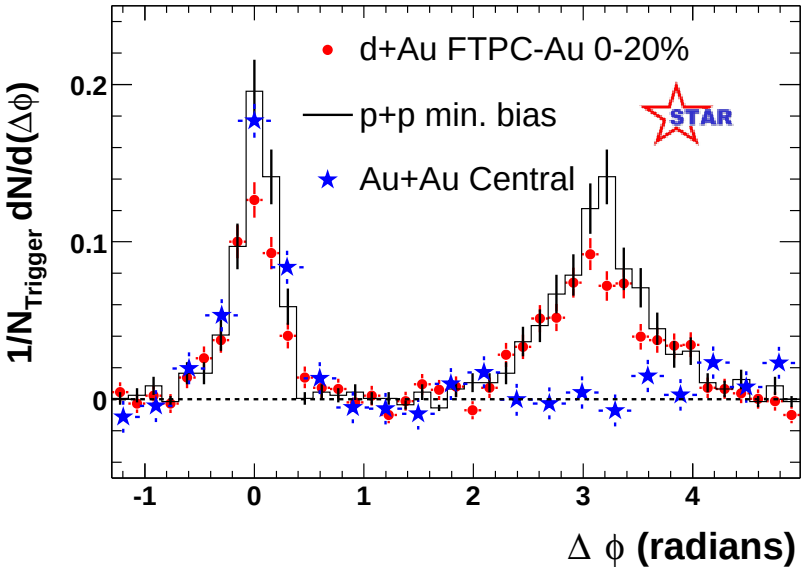

Figure 1.10: Angular correlation of charged hadrons. While in p+p collisions, a two-jet structure is visible, the away-side jet is attenuated in central Au+Au collisions [50].

phases of the heavy-ion collision, and the aim of a fluctuation analysis is to find an observable that conveys information about the early stage. The next section (Section 1.4) is devoted to the topic of event-by-event fluctuations, the subject of the present thesis.

- Very hard parton scattering with momentum transfer in the GeV range can only occur in the early stage, in initial collisions. The forming partonic medium affects the deflected, energetic particles on their way, manifest as an energy loss. The observable hadrons in the high p_{T} range are less abundant compared to scaled p+p collisions. This can be quantified in a nuclear modification factor $R_{\mathrm{AA}} < 1$, as depicted in Figure 1.9. Cold nuclear matter effects, recreated in the p+A or d+A control experiments do not lead to a suppression [50] due to the lacking open color charges. Another important confirmation also shown in Figure 1.9 are direct photons that do not interact with the color charged medium and, as a consequence are not suppressed in A+A collisions [51]. Angular correlations between high p_{T} hadrons support the picture by revealing an attenuation of back-to-back jets [54]. The angular correlation shown in Figure 1.10 reveals a two jet structure in p+p, a slight attenuation in d+Au due to cold matter effects, and a complete obliteration of the away side in central Au+Au collisions studied at RHIC [50].
- Heavy quark-antiquark pairs play a similar role. At SPS and RHIC energies, their large mass makes their production possible only in the initial high momentum transfer regime. The presence of a medium with open color charges would prevent their binding to quarkonium states [55], an idea that is confirmed in lattice QCD calculations (see Figure 1.1). At the point of hadronization in the further evolution of the collision, the $q\bar{q}$ pair is too far separated, favoring the formation of open heavy flavor hadrons. Indeed, a J/ψ suppression is observed [56]. At LHC, due to higher temperatures, charm can also be produced in later stages, leading to a complicated suppression/enhancement pattern.
- Electromagnetic probes (photons and leptons) can reach the detectors from every stage of the collision without being affected by the strongly interacting medium, thus representing an average of differential luminosity over collision time. They suffer from small production rates and large backgrounds, as photons and leptons are produced over the whole evolution. Nevertheless, direct photons do not only provide an important baseline for high p_{T} jet suppression (see above), but also promise a direct access to the initial temperature. Likewise, di-electron spectra reveal details of chiral symmetry restoration [57].

As an alternative to heavy-ion collisions, compact stars can be used to study nuclear matter under extreme conditions. Their large distance and low characteristic radiation however limits the observable signatures to parameters like the mass/radius relation. Nevertheless, hydrodynamic models indicate that in their interior, the phase transition

to deconfined quarks and gluons is crossed. Complementary to heavy-ion collisions, this represents the low temperature/large μ_B part of the phase diagram.

1.3 NA49 Evidence for the Onset of Deconfinement

As discussed in Section 1.2, the energy density created in heavy-ion collisions surpasses the critical value ϵ_c starting at collision energies provided by the CERN SPS. Several signatures of deconfined matter have been reported at the top SPS energy of $\sqrt{s_{NN}} = 17.3$ GeV [26, 27]. In a subsequent energy scan, Pb+Pb collisions at $\sqrt{s_{NN}} = 6.3, 7.6, 8.7$ and 12.3 GeV were probed in search of signatures indicating the onset of deconfinement [58]. Measurements in the NA49 experiment (for experimental details see Chapter 3) [59, 28] found anomalies in the energy dependence of hadron production around $\sqrt{s_{NN}} = 8$ GeV, that are consistent with theoretical expectations for the onset of deconfinement. Among the reported anomalies are:

- The energy dependence of the pion yield per participating nucleon becomes steeper at SPS energies. $\langle\pi\rangle/\langle N_w\rangle$ is interpreted in a statistical model as a measure of the entropy density. The change of slope can be seen as an increase of degrees of freedom [58] as expected at the deconfinement phase transition.
- The relative strangeness production [60] can be experimentally approximated via the K^+/π^+ ratio. Figure 1.11 [28, 61] shows the excitation function in nucleus-nucleus collisions from AGS to LHC energies. The sharp rise to a peak at $\sqrt{s_{NN}} \approx 8$ GeV followed by a drop to a constant value up to LHC energies has been predicted for the deconfinement phase transition [58] and is neither present in p+p collisions [28] nor in hadronic models. A similar structure has been observed for the spectra of other hadrons [28].
- The transverse momentum distributions also show an anomaly in the SPS energy range. Figure 1.12 shows the inverse slope parameter T of positive kaons. Consistent with the expectations from increasing transverse flow and temperature, T rises quickly at low energies. At SPS energies, a plateau is seen, followed by a rise from top SPS onward to LHC energies, a feature that is again absent in hadronic models or p+p collisions [28]. The step structure suggests a first order phase transition with a mixed phase and is indeed reproduced in a hydrodynamic simulation incorporating such a transition [62].

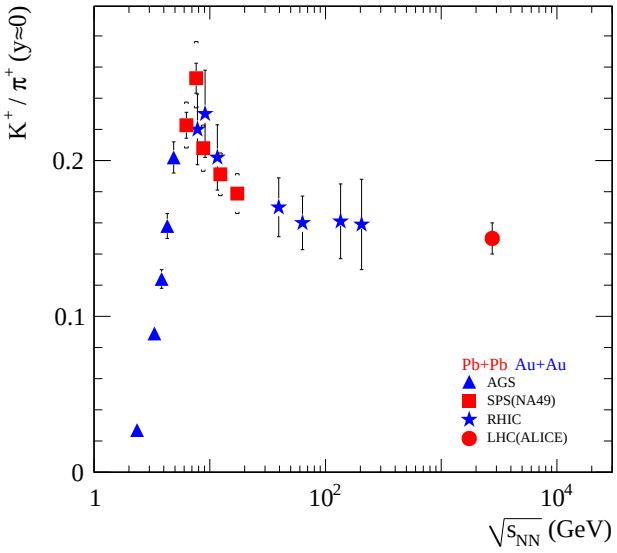

Figure 1.11: Excitation functions of the ratio K^+/π^+ measured at midrapidity in nucleus-nucleus collisions as compiled in [61]. The steep maximum and subsequent leveling out can be attributed to the onset of deconfinement [58].

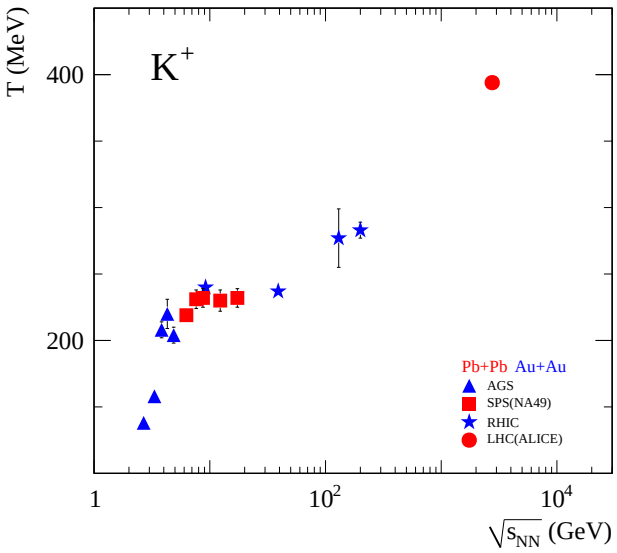

Figure 1.12: The inverse slope parameter T of K^+ spectra is constant in the SPS energy range and suggests a first-order phase transition here [62]. The figure is taken from [61].

$\sqrt{s_{NN}}$	$\langle\pi^+\rangle$	$\langle\pi^-\rangle$	$\langle\mathrm{K}^+\rangle$	$\langle\mathrm{K}^-\rangle$	$\langle\mathrm{p}\rangle$	$\langle\overline{\mathrm{p}}\rangle$
6.3 GeV	16	16	5	1	28	0
7.6 GeV	32	35	8	2	35	0
8.7 GeV	50	55	12	4	41	0
12.3 GeV	109	119	22	9	53	1
17.3 GeV	201	217	34	20	72	3

Table 1.1: Average uncorrected multiplicities of charged hadrons within the acceptance of the present study, cf. [64]. The actual observed number of tracks is larger, but reduced due to the track quality criteria defined in Section 5.2. For the details of the acceptance, see Section 5.3.

These examples represent only a small part of the NA49 results. In addition to the energy scan, NA49 has also collected data on smaller systems (lighter ion collisions and minimum bias Pb+Pb), as well as reference data in proton-nucleus and proton-proton collisions. This program is expanded and continued by the NA61 collaboration. For a recent review of NA49 results and the NA61 status and plans see e.g. [63].

1.4 Fluctuations in Heavy-Ion Collisions

The evidence for the observation of a deconfined state created in heavy-ion collisions at the highest SPS energy ($\sqrt{s_{NN}} = 17.3$ GeV) [26, 27] was mainly based on inclusive (event-averaged) observables. The later ascertainment of the properties of the deconfined matter at SPS and RHIC [29, 30, 31, 32] added information also from correlation analyses, notably flow and angular correlation measurements.

Due to the very high multiplicity of created hadrons, each individual event created in a central Pb+Pb collision becomes, in a certain sense, "self-analyzing": a completely novel property of nuclear collisions. As shown in Table 1.1, the multiplicities per event of the "bulk hadrons" π, K and p range up to hundreds, from top SPS energies onward. Thus, beyond ensemble averages, we may inspect event-wise properties of bulk hadron production. For example, directed flow observables depend on an event-wise determination of the azimuthal impact plane. Alternatively, one inspects the event-by-event fluctuation e.g. of total p_{T}, midrapidity charged particle density, etc.. Moreover, such event-by-event fluctuations of individual hadron yields, and of certain hadron yield ratios may reveal

properties of the expanding fireball system as it crosses the hadronization line indicated in Figure 1.3. Does it hadronize in a first order phase transition? Does it hadronize in the close vicinity of the QCD critical point?

The measurement of event-by-event fluctuations allows to probe the underlying correlations [65]. This can be used to determine the effective degrees of freedom in the quark-gluon plasma as a function of energy, e.g. to ascertain whether partially bound objects still exist [66]. In the vicinity of the phase transition between hadrons and partons, fluctuations play an even stronger role. The initial expectation [67] was that at collision energies that are just on the verge of deconfinement, small initial geometry fluctuations result in some events surpassing the critical density criteria, others not. Enhanced fluctuations are a general feature of phase transitions, where the degrees of freedom change, not only in the case of QCD thermodynamics. The energy range covered at the SPS, where indications for the phase transition are first observed [28] and the freeze-out points approach phase transition and critical point is thus the ideal place for fluctuation studies. Two main expectations arise from the conjectured structure of the phase diagram (cf. Section 1.1): Fluctuations as a general consequence of the phase transformation from hadrons to quarks and those in the vicinity of the critical point, where the first order phase transition turns into the crossover observed at low μ_B.

The NA49 experiment has been designed for fluctuation measurements [67, 69, 70]. Its large acceptance makes it possible to track and identify a large fraction of produced particles in single events, a prerequisite to study event-by-event fluctuations of the momentum space distribution [68] or the hadronic composition [71]. Figure 1.13 shows one example from these pilot studies, the distribution of the event-wise average transverse momentum $M\left(p_{\mathrm{T}}\right) = \langle p_{\mathrm{T}} \rangle$ [68]. Over several orders of magnitude, it does, remarkably, not deviate from a statistically generated, "no new physics" background histogram.

A large number of fluctuation observables has been investigated, and a comprehensive review of concepts and results can be found in [65]. One indispensable ingredient of all fluctuation measurements is to control background fluctuations, or to subtract them from the observed signal. An example of such a background is the fluctuation in the reaction volume with collision centrality that can be circumvented by looking at volume-independent quantities. Another thing to keep in mind is the influence of later stages on the fluctuation signal during the evolution of the fireball. Distinct fluctuation patterns expected from the deconfined phase might be obliterated by the hadron-resonance expansion that follows the confinement phase transition. It will be pointed out in the

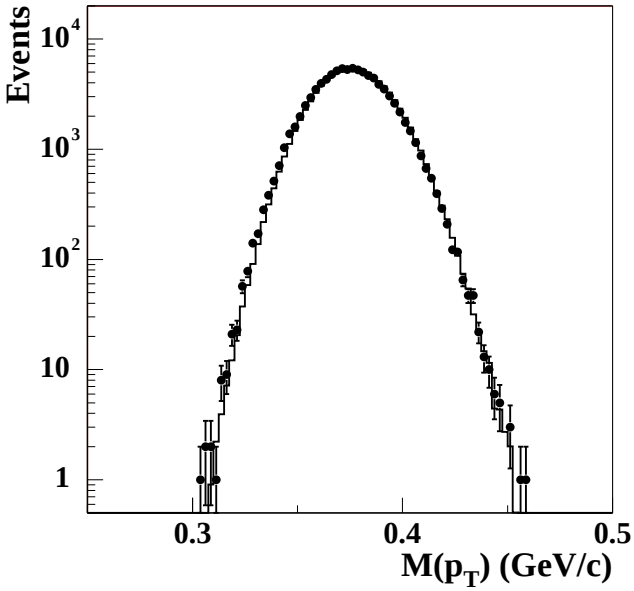

Figure 1.13: An exemplary event-by-event distribution. Here: the mean transverse momentum $M\,(p_{\mathrm{T}}) = \langle p_{\mathrm{T}} \rangle$ of accepted particles (points) compared to a mixed event distribution (histogram) in central Pb+Pb collisions at 158A GeV [68].

end of this section and in Chapter 2 that this effect can be avoided by a careful selection of the studied quantity.

The analysis of electric charge correlations is an important example in this context. The measurements in NA49 were performed so that background such as volume fluctuations were minimized [72] (details on this analysis are presented in Section 1.5), but the initial expectation of reduced fluctuations in the quark-gluon plasma due to the fractional quark charges [73, 74] was not observed. It turned out that the initial electric charge fluctuation pattern is washed out after hadronization by hadronic effects such as resonance decays [75]. For example, the decay of a ρ resonance into pions with a Q-value of $\approx$ 470 MeV re-distributes the initial electric charge over the final state phase space, annihilating correlation information from earlier stages. In order to make inferences about the early stage of a heavy-ion collision, a fluctuation observable where the initial fluctuations are still present in the final state, i.e. their relaxation time is longer than the hadronic expansion stage [76] is required. Although charge fluctuations do not fulfill this, they can be used to study the freeze-out conditions, and infer e.g. about thermalization [77].

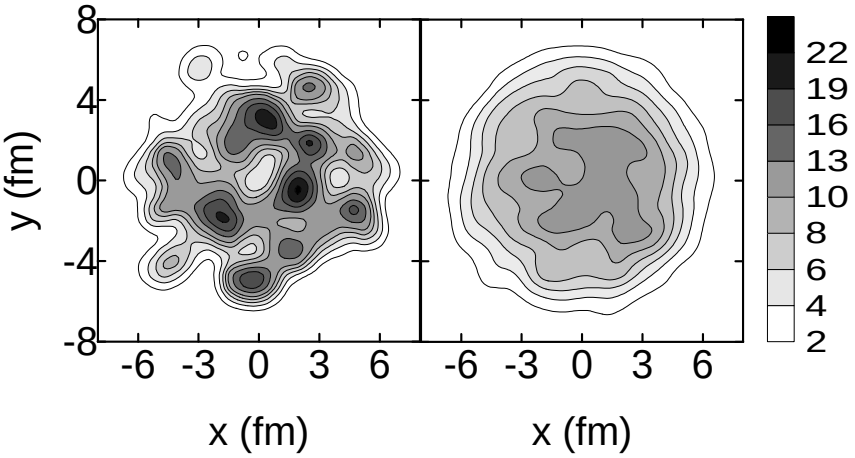

Figure 1.14: Initial state energy density distribution in the transverse plane from the NeXus event generator [78]. The result for one random heavy-ion collision (left) is compared to the average over 30 initializations (right), to demonstrate the accompanying smoothing of initial state inhomogeneities.

The causes of fluctuations in the observed particle numbers or kinematic distributions are not limited to the thermodynamic sources described above. During a heavy-ion collision, there are random processes that are also reflected in the final state. Density inhomogeneities in the initial state of the colliding nuclei are amplified by fluctuations in the stopping power, caused by the stochastic nature of the nucleon-nucleon scattering. This effect is illustrated in Figure 1.14, where the initial state energy density distribution in the plane transverse to the beam axis as obtained from the NeXus event generator [78] is plotted. While for a single random heavy-ion collision (Figure 1.14, left) an inhomogeneous distribution is visible, the averaging over 30 random events (Figure 1.14, right) leads to a smoothing. In a hydrodynamic model, smooth and isotropic initial conditions can be used to predict inclusive, bulk features of heavy-ion collisions. However to compare to data on flow fluctuations, or for the recent explanation of triangular flow [79, 80], the event-by-event fluctuations have to be considered. These *non-thermal fluctuations* are sensitive to the state of matter and its equation of state. The connection of the initial state density distribution via pressure gradients to final state flow fields depends on the EOS, making them a suitable probe in heavy-ion collisions.

Event-by-event Hadron Yield Fluctuations

The present study is focussed on thermal fluctuations. Here, an important class of fluctuation observables is based on consequences of chiral symmetry restoration [19, 81]. A massless σ field at the critical point is manifested in strong fluctuations of the number of low momentum pions, coupled via the $\sigma \rightarrow \pi\pi$ decay. As pions constitute the largest fraction of produced particles, this effect can be approached by a measurement of total multiplicity fluctuations [82, 83]. The reciprocal quantity, the mean transverse momentum $\langle p_{\mathrm{T}} \rangle$ per particle is also expected to show enhanced event-by-event fluctuations. The latter measurement is illustrated in Figure 1.13, where the $\langle p_{\mathrm{T}} \rangle$ distribution in central Pb+Pb collisions at 158A GeV is compared to a mixed event reference. The two distributions agree, indicating that no fluctuations in excess of the statistical, uncorrelated background are visible here. Such an excess would be expected e.g. at the critical point. Multiplicity and $\langle p_{\mathrm{T}} \rangle$ fluctuations have been studied as a function of beam energy [83, 84], with the expectation of a fluctuation maximum when approaching the critical point. The finding that both measurements (a detailed presentation of the results is found in Section 1.5) showed no irregular energy dependence was explained by the fact that the expected enhancement at the critical point is limited by the finite size and lifetime of the system close to the critical point [85]. This limitation can be overcome by studying higher moments of event-by event distributions, which are expected to be more sensitive and enhance the observable consequences of even small critical effects [86]. First results at STAR showed the feasibility of this ambitious measurement [87].

Fluctuations in conserved quantities [88], if they are not connected to a strong dispersion mechanism as seen for electric charge above, have the best prospects to convey information about early stage correlations to the observable final state. They are expected to show signatures of the critical point or the phase transition, irrespective of its order. In thermodynamical models, which give a good description of the inclusive properties of heavy-ion collisions, they are described via the susceptibilities of the respective conserved charge [65]: Like in classical thermodynamics, the susceptibility

$$\chi_{i,j} = \frac{1}{V} \frac{\mathrm{d}F}{\mathrm{d}\mu_i \mu_j} \tag{1.2}$$

specifies how the free energy F changes upon external modification of the chemical potentials μ_i, μ_j related to the charges Q_i and Q_j, and is proportional to their (co-)

variance

$$\langle \delta Q_i \delta Q_j \rangle = TV\chi_{i,j}. \tag{1.3}$$

Thus, e.g. the electric charge fluctuations $\langle (\delta Q)^2 \rangle$ [74, 73] and the correlation between baryon number and strangeness $\langle \delta B \delta S \rangle$ [66] can be related to thermodynamic quantities via

$$\langle (\delta Q)^2 \rangle = TV\chi_{Q,Q} = T\frac{\mathrm{d}F}{\mathrm{d}\mu_Q \mu_Q} \tag{1.4}$$

$$\langle \delta B \delta S \rangle = TV\chi_{B,S} = T\frac{\mathrm{d}F}{\mathrm{d}\mu_B \mu_S}. \tag{1.5}$$

This definition of fluctuation is only meaningful in the presence of chemical potentials for the conserved charges under consideration, i.e. in the grand-canonical ensemble [88]. In a system that is hermetic for the considered charge, as realized in the canonical or micro-canonical ensemble, the total charge is conserved and can thus not show any fluctuation. The latter case is comparable to a heavy-ion experiment with full 4π acceptance, where the observed total electric charge will always remain that of the incoming nuclei, $Q = 2Z$ and thus $\delta Q = 0$ for all events. Less extreme effects of global charge conservation are already visible in smaller acceptances and become more pronounced when approaching full acceptance [89, 90].

The grand-canonical case is approximated by realistic experiments (finite acceptance) where the observed fraction of the phase space distribution can exchange charge with the surrounding, unobserved medium. Ideally, in order to avoid density or temperature gradients between the observed medium and the heat bath, the partition should be done in the boost invariant regime of the rapidity distribution, as sketched in Figure 1.15. The grand-canonical approach is affirmed for inclusive observables [36], even though the ratio between "heat bath" and the observed system does not reach the thermodynamic requirement to be $\gg 1$. For fluctuation measurements, a minimal acceptance limit applies: In the limit of a "keyhole" experiment, where the studied charge is either observed or not, the event-by-event distribution degrades to a binomial distribution with possible values zero and one. This distribution is described by a single moment, making fluctuation studies futile.

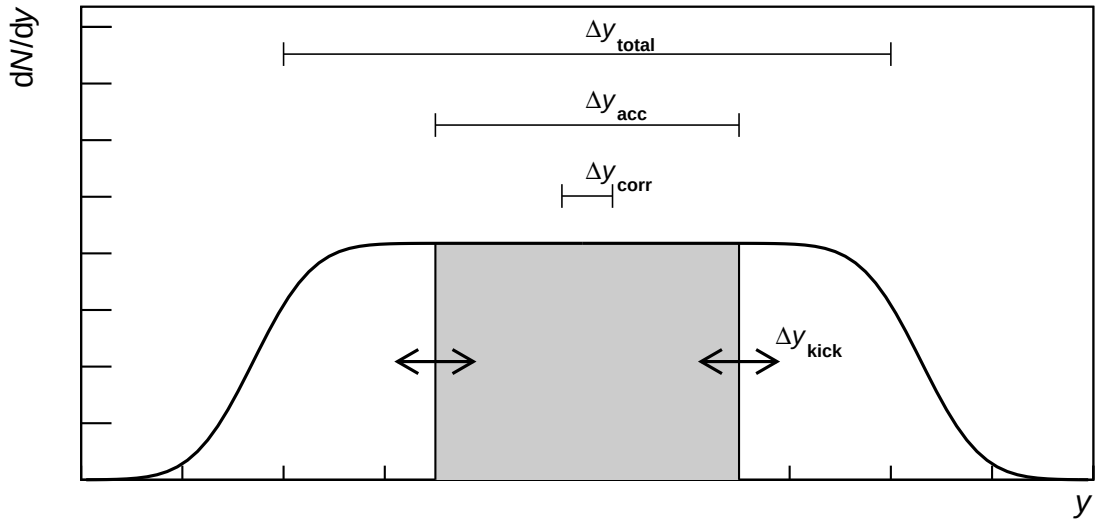

Figure 1.15: Illustration of the acceptance requirements [88] on the analysis of fluctuations of a conserved quantity, according to [65].

To summarize, the following requirements on the acceptance for studies of the fluctuation of conserved charges have been postulated in [88, 65]. Figure 1.15 illustrates the relevant quantities:

- To cover the physics of interest, their typical correlation length Δy_{corr} should be covered by the acceptance interval Δy_{acc}:

$$\Delta y_{\mathrm{corr}} \ll \Delta y_{\mathrm{acc}} \tag{1.6}$$

- In order to escape global charge conservation effects, the observed system (rapidity range $\Delta y_{\mathrm{accept}}$) has to be small compared to the total system (rapidity gap $\Delta y_{\mathrm{total}}$):

$$\Delta y_{\mathrm{accept}} \ll \Delta y_{\mathrm{total}} \tag{1.7}$$

- At the same time, all processes that disperse the studied charge (by a rapidity kick Δy_{kick}) in later stages should be insignificant compared to the observed region:

$$\Delta y_{\mathrm{kick}} \ll \Delta y_{\mathrm{accept}} \tag{1.8}$$

In addition to these general considerations, the details of the experimental acceptance are relevant to interpret fluctuation measurements, as they determine the possibility to study correlations. As an example, back-to-back azimuthal correlations can not be studied

in an experiment that does not cover $\delta\phi = \pi$ in its acceptance. Even correlations due to momentum and energy conservation result in fluctuation signals dependent on the phase space under consideration [91]. To account for this, detailed model comparisons are called for. In the present work, simulations in the hadronic transport model UrQMD [92, 93, 94] were performed and used to study acceptance effects. Experimental results were also compared to existing HSD [95] calculations [96] where experimental acceptance filters were applied.

In review of the strengths and limitations of fluctuation measures sketched in this section, the study of hadron ratio fluctuations presents a promising way to infer about the properties of the matter produced in heavy-ion collisions in the CERN-SPS energy range. The relevant observables and their connection to the underlying correlations are discussed in Chapter 2.

1.5 NA49 Fluctuation Results

Before turning to the main topic of the present thesis, this section gives a brief overview on important fluctuation studies performed within the NA49 collaboration. A common variable, used in different event-by-event analyses was introduced in [97]:

$$\Phi := \sqrt{\frac{\langle Z^2 \rangle}{\langle N \rangle}} - \sqrt{\overline{z^2}}, \tag{1.9}$$

where $z = x - \overline{x}$ is the difference of the single-particle variable x from its ensemble average $\overline{x}$ and

$$Z = \sum_{i=1}^{N} (x_i - \overline{x}) \tag{1.10}$$

is the deviation of a whole event with multiplicity N from the ensemble average. The $\langle \ldots \rangle$ braces denote an average over events.

For the charge fluctuation measurements [72], the observable Φ_q has been defined according to equations 1.9 and 1.10, using the particles' electric charge q for x in the above definition. Another modification from Φ_q to $\Delta\Phi_q$ was in place to account for trivial charge conservation effects. Following the suggested drop in charge fluctuations as a

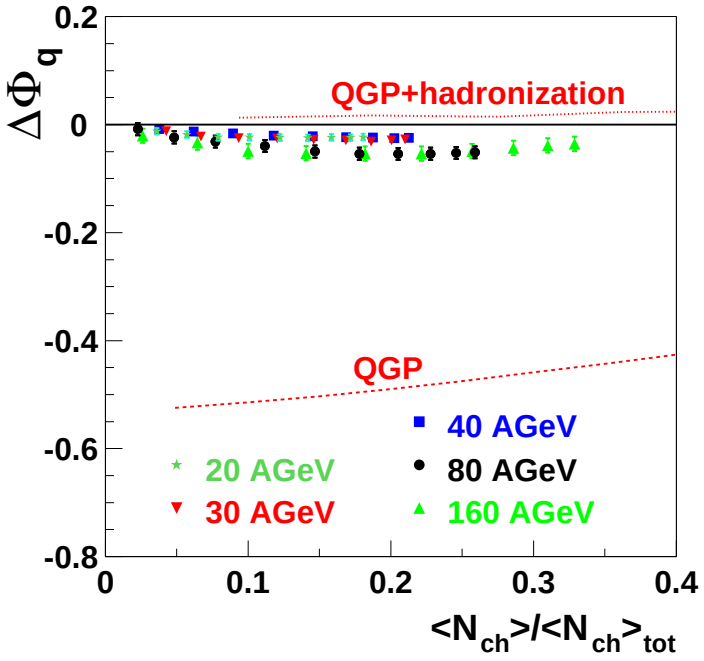

Figure 1.16: Electric charge fluctuations for the different SPS energies, as a function of acceptance size. The NA49 measurements agree with the expected effects from hadronization and resonance decay [72].

consequence of deconfinement [73, 74], more observables have been suggested [89], but $\Delta\Phi_q$ turned out to be the most robust one [75].

Figure 1.16 shows the results of the charge fluctuation analysis as a function of $\sqrt{s_{NN}}$. The expected reduced fluctuation level in a quark-gluon plasma [73, 74] is significantly different from the value expected for a hadron gas and is indicated as a line in the figure. In contrast to this prediction, $\Delta\Phi_q$ stays on the level of zero, at the same time expected from a hadron gas and from a quark-gluon plasma after hadronization, rescattering and resonance decay effects. Unfortunately, as reported in Section 1.4, this observable proved to be insensitive to the ascertainment of early stage degrees of freedom [76, 75]. A sensitivity of charge fluctuations on critical point effects has not been predicted.

The Φ fluctuation measure had originally been conceived for continuous kinematic variables [97], such as p_{T}. In the form of $\Phi_{p_{\mathrm{T}}}$ it can thus be used to study average transverse momentum fluctuations. The average p_{T} of particles in one event, $\langle p_{\mathrm{T}} \rangle$, is, at given total energy, reciprocal to the number of produced particles N. The enhanced fluctuations in pion number expected from a diverging σ field at the critical point [19] (see Section 1.4) are therefore expected to be reflected in both $\langle p_{\mathrm{T}} \rangle$ and N fluctuations. Background effects from finite number statistics and collision geometry fluctuations are

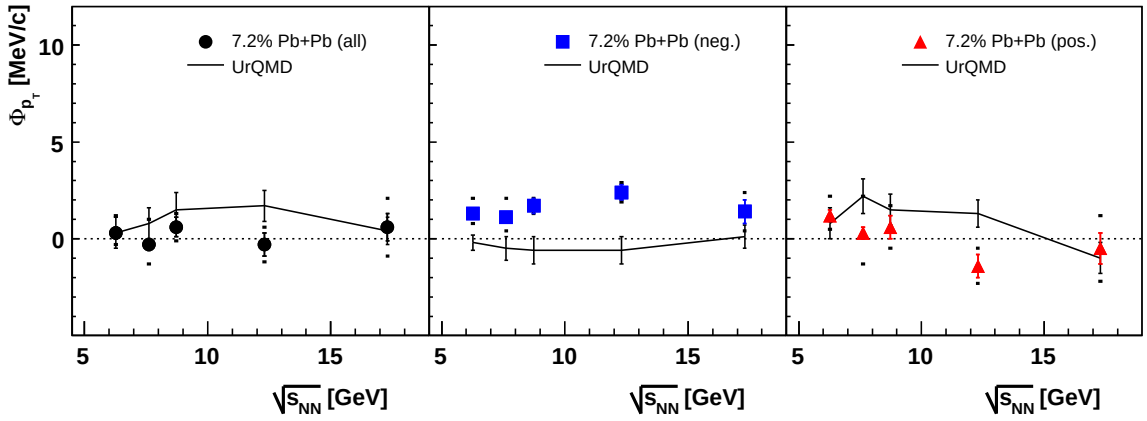

Figure 1.17: Excitation function of Φ_{p_T} measurements from NA49, for all charged (left), negatively charged (center) and positively charged particles (right) compared to UrQMD model calculations (black lines) performed within the experimental acceptance [84].

eliminated by construction in Φ_{p_T}. Multiplicity fluctuations are quantified using the scaled variance $\omega = \mathrm{Var}(N)/\langle N \rangle$ [83], and impact parameter variations are suppressed by a very strict centrality selection. The use of the NA49 zero degree VETO calorimeter for centrality determination is discussed in Section 3.3. By a variation of T and μ_B via $\sqrt{s_{NN}}$, a peak in the excitation function of Φ_{p_T} and ω would indicate the position of the critical point.

The energy dependence of mean p_T fluctuations [84] are shown in Figure 1.17. The measured values of Φ_{p_T} are close to zero at all energies, and for the considered subsets of all charged (Figure 1.17 left), negatively (center) or positively charged particles (right). Calculations in the hadronic transport model UrQMD [92, 98] yield a similar energy dependence. For the multiplicity fluctuations [83] depicted in Figure 1.18, the agreement with UrQMD [99] is even better, and no discontinuous energy dependence is observed.

Lattice QCD calculations see the location of the critical point in the (T, μ_B) domain covered by the freeze-out points at SPS energies [15]. Further numerical QCD calculations evaluated the width of critical effects [100] and found it to be sufficiently large to be reflected in the NA49 measurements. However, first attempted comparison [101] overestimated the amplitude of critical effects reflected in Φ_{p_T} and ω. When properly taking into account finite size and lifetime of a heavy-ion collision fireball close to the critical point [85], the anticipated effect is rather moderate, rendering the situation inconclusive.

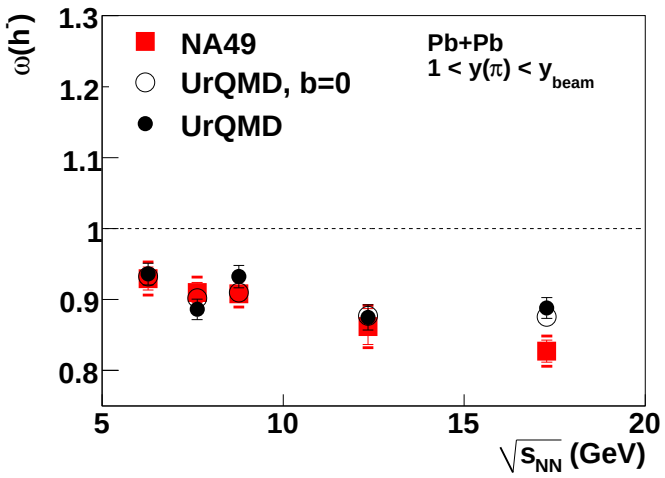

Figure 1.18: Energy dependence of fluctuations in the multiplicity of negatively charged hadrons [83] compared to UrQMD calculations [99].

A connection to deconfinement effects is not given in the case of $\langle p_{\mathrm{T}} \rangle$ fluctuations. The expected discontinuity in multiplicity fluctuations due to the onset of deconfinement [82] is on the order of $\Delta\omega = 0.02$ and thus smaller than the systematic error on the measurement.

Studying smaller collision systems, enhanced fluctuations have been observed at $\sqrt{s_{NN}} = 17.3$ GeV [102, 103]. In peripheral Pb+Pb collisions, this enhancement could be explained by target spectator fluctuations [104]. For central collisions of lighter nuclei, a connection to the critical point is discussed [105, 34]. This finding is promising and will be evaluated in a systematic energy and system size scan by the NA61 collaboration [63].

Chapter 2

Hadron Ratio Fluctuations

Following the general remarks about fluctuation studies in the previous chapter, event-by-event studies of hadron ratios represent a promising observable to examine the properties of matter produced in heavy-ion collisions. Just as the average hadron multiplicities can be used to extract thermodynamical properties from an event ensemble (cf. Section 1.2), hadronic abundances characterize the hadro-chemical composition of the "fireball" created in an individual heavy-ion collision. At a phase transition, where the basic degrees of freedom are converted, this composition is expected to show distinct fluctuation patterns [65]. The study of these "chemical fluctuations" is the topic of the present work.

The quark number susceptibilities that are related to number fluctuations via equation (1.3) have been evaluated in lattice QCD [10], and show a steep rise at the critical temperature. In addition, calculations at finite baryo-chemical potential μ_B [16, 17]

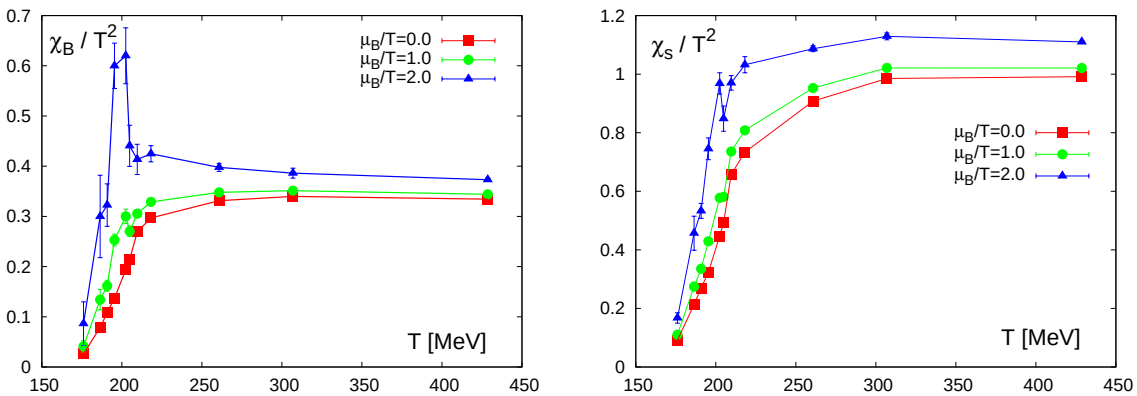

Figure 2.1: The light (left) and strange (right) quark number susceptibilities from lattice QCD calculations at different values of baryo-chemical potential μ_B [16].

report diverging susceptibilities when approaching μ_B values where the QCD critical point is expected. Both features can be seen in Figure 2.1.

Hadron ratio fluctuations are well suited to study these phase transition effects. In contrast to multiplicity fluctuations, they are less sensitive to volume fluctuations: A ratio of two (extensive) hadron multiplicities is an intensive quantity, in addition, the average hadron ratios only change modestly with centrality. The effect of centrality selection (Section 5.1) and centrality bin size [106] has been verified experimentally, and found to be insignificant for the present analysis. Also the dispersion of the conserved quantities under consideration here is expected to be smaller compared to the charge fluctuation case [75] discussed in Section 1.4.

The initial expectation from the study of hadron ratio fluctuations [67] was that density fluctuations close to the phase boundary have as a consequence some (exceptionally dense) events surpassing the transition to the quark-gluon plasma, while others remain in the confined domain. The suggested overall enhancement of strangeness production in the quark-gluon plasma [107] in combination with the two event classes would then lead to enhanced fluctuations in the ratio of strange to non-strange particles. This ratio can be expressed in terms of the "Wroblewski Factor" $\lambda = 2\left(s + \bar{s}\right) / \left(u + \bar{u} + d + \bar{d}\right)$ [60] or can be measured via the kaon-to-pion ratio $\left(K^+ + K^-\right) / \left(\pi^+ + \pi^-\right)$. The pion number in the denominator is also an approximation for the entropy, a quantity that is conserved during the hydrodynamic expansion of the system.

Following the interpretation of the observed inclusive strangeness enhancement rather as a consequence of the transition from canonical suppression in p+p to grand-canonical physics in heavy-ion collisions, the interpretation of relative strangeness fluctuations was also expanded. Several scenarios are discussed in this context, with a common general expectation of a nonmonotonic energy dependence:

- A mixed phase in the transition region allows for the coexistence of confined and deconfined domains. Their variation in relative size [109] is reflected in the hadron production, and conserved charges such as strangeness preserve the fluctuation patterns until the final state.

- Fluctuations arising from a mixed phase as described above are enhanced in the presence of the rapid hadronization of a supercooled quark-gluon plasma expected at a first order phase transition with large latent heat [110].

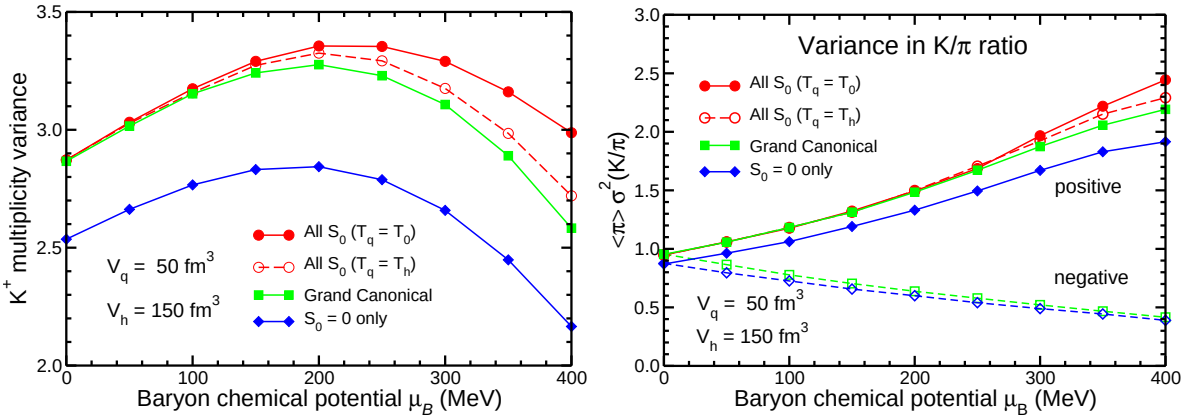

Figure 2.2: Enhanced fluctuations in the kaon multiplicity (left) and in the K/π ratio (right), as expected from a spinodal phase separation at hadronization [108].

- The approach of spinodal decomposition at the phase transition [108] has a similar effect. Strangeness is "trapped" in particular domains where it remains conserved. One consequence on strangeness production are enhanced fluctuations. The predictions for kaon multiplicity and K/π ratio fluctuations are shown in Figure 2.2.

- The assumption of early thermalization and thus the consideration of the equation of state in the early stage of heavy-ion collisions [58] also leads to a distinct fluctuation signature. When going through the mixed phase, enhanced multiplicity to energy fluctuations are expected [82]. For strangeness fluctuations, a characteristic dip is predicted [111].

- Modifications of hydrodynamic expansion trajectories are expected in the presence of a critical point and the phase transition [112]. Depending on the structure of the phase diagram, varying thermodynamic freeze-out parameters will result from this characteristic re-focussing, and will be reflected in the event-by-event hadron ratios.

Although the details of the discussed model scenarios differ, a common feature emerges: The phase transition leaves its characteristic fluctuation pattern in the relative strangeness production. Even without a quantitative prediction, and given the lacking conclusion about the sign of the expected effect, the results suggest looking at the excitation function of ratio fluctuations. The variation of collision energy entails a scanning of the (T, μ_B) phase diagram [113], and phase transition effects are expected to appear and disappear as a function of $\sqrt{s_{NN}}$. The sensitivity of ratio fluctuations is however not limited to mixed phase and first order phase transition effects. Fluctuations arising at the critical point as discussed in Section 1.4 are likewise expected to be reflected in hadron ratios [19, 114].

2.1 Measuring Hadron Ratio Fluctuations

To establish the relevant quantities, a sketch of the method used in the present analysis is given in this section, and is compared to other possible ways to analyze hadron ratio fluctuations. For a detailed description, the reader is however referred to Chapter 5. The method has been developed within the NA49 collaboration [115, 116] and has successfully been applied in the analysis of the energy dependence of $(\mathrm{K}^+ + \mathrm{K}^-)/(\pi^+ + \pi^-)$ and $(\mathrm{p}+\overline{\mathrm{p}})/(\pi^+ + \pi^-)$ fluctuations [116, 117, 118], as well as for the centrality dependence [106]. The present work is focussed on the energy dependence of kaon-to-proton ratio fluctuations in central Pb+Pb collisions.

The particle identification (PID) relies on the specific energy loss ($\mathrm{d}E/\mathrm{d}x$) charged particles suffer in the NA49 Time Projection Chambers (TPCs, see Section 3.5). In a whole event ensemble, inclusive PID is done by unfolding $\mathrm{d}E/\mathrm{d}x$ spectra in momentum space bins using a χ^2 fit, and thus extracting the average yields of different hadron species. Event-by-event particle identification poses the challenge that only a small number of particles (between 60 and 600, depending on $\sqrt{s_{NN}}$ in the present case) is available, rendering the conventional statistical method useless. It is impossible to just count particles based on cuts in $\mathrm{d}E/\mathrm{d}x$ space, as the distributions for different hadron species overlap in most regions of phase space. Instead, an unbinned maximum likelihood method is applied in two steps: The inclusive analysis is used to extract probability density functions (PDFs) as a function of $\mathrm{d}E/\mathrm{d}x$ and phase space. The PDFs are then used as an input for the likelihood fit, to determine hadron ratios in single events. The inclusive and the event-by-event PID methods are presented in detail in Sections 5.3 and 5.4.

The event-by-event fluctuation of a hadron ratio can be extracted as the width of the corresponding event-by-event distribution. An example of a ratio distribution is shown in Figure 2.3. The width of an A/B ratio distribution can be quantified as the dispersion scaled by the mean

$$\sigma := \frac{\sqrt{\mathrm{Var}\,(A/B)}}{\langle A/B \rangle} \tag{2.1}$$

and is governed by different effects. In general, finite number statistics contribute. An additional contribution may arise from the PID method. These two background effects can be modeled in a reference by applying the same PID scheme to mixed events. In a mixed event, described in more detail in Section 5.5, tracks are combined from different

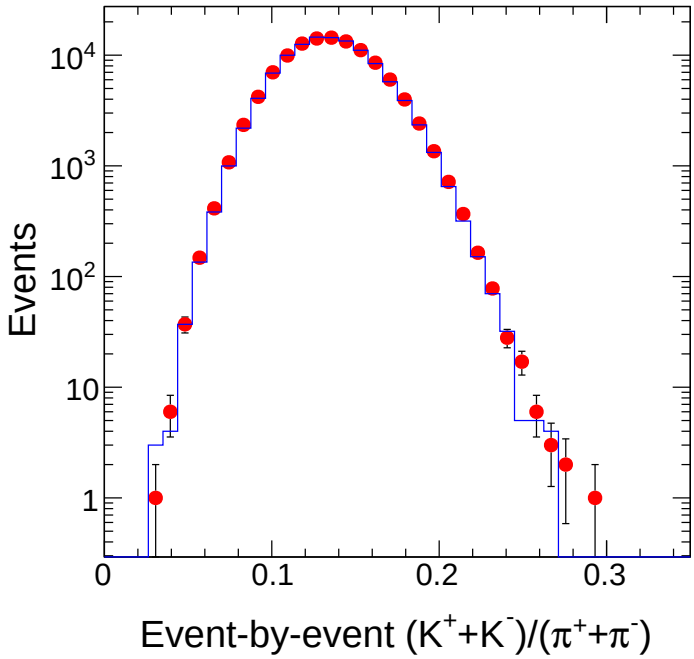

Figure 2.3: Event-by-event distribution of the $(K^+ + K^-)/(\pi^+ + \pi^-)$ ratio in central Pb+Pb collisions at $\sqrt{s_{NN}} = 17.3$ GeV [116]. The distribution in real data events (red markers) is compared to a reference extracted from mixed events (blue histogram).

events, removing all physics correlation. At the same time, finite number statistics and PID effects remain present in the reference. The resulting event-by-event distribution is also shown in Figure 2.3.

These contributions have been studied in detail in the analysis of $(K^+ + K^-)/(\pi^+ + \pi^-)$ fluctuations at $\sqrt{s_{NN}} = 17.3$ GeV [116, 117], and a scaled dispersion in mixed events of $\sigma_{\text{mix}} = 23.1\%$ has been found. The two background effects introduced above were evaluated separately and amount to

- $\sigma_{\text{stat}} = 15.9\%$ for finite number statistics and
- $\sigma_{\text{PID}} = 16.7\%$ for the experimental PID resolution.

As the variances add linearly, the σ components have to be added in quadrature. It turns out that $\sigma^2_{\text{mix}} = \sigma^2_{\text{stat}} + \sigma^2_{\text{PID}}$. The width of the mixed event distribution can thus be explained purely by the two background effects, whereas excess fluctuations are observed in real data events: A scaled dispersion of $\sigma_{\text{data}} = 23.27\%$ was reported in [117]. Remaining fluctuations after the subtraction of "trivial" background fluctuations are attributed to the dynamics in the studied matter [65], hence "dynamical" fluctuations

are the sought-for signal and have been defined [115] as

$$\sigma_{\mathrm{dyn}} := \mathrm{sign}\left(\sigma^2_{\mathrm{data}} - \sigma^2_{\mathrm{mix}}\right)\sqrt{|\sigma^2_{\mathrm{data}} - \sigma^2_{\mathrm{mix}}|}. \tag{2.2}$$

In the above example, the quadratic difference amounts to $\sigma_{\mathrm{dyn}} = 2.8\%$ for $(\mathrm{K}^+ + \mathrm{K}^-)/(\pi^+ + \pi^-)$ at $\sqrt{s_{NN}} = 17.3$ GeV [117, 118]. A positive value $\sigma_{\mathrm{dyn}} > 0$ corresponds to a broader ratio distribution and larger fluctuations compared to the reference events.

2.2 Ratio Fluctuations and the underlying correlations

For the interpretation of σ_{dyn}, the following leading order expansion [65, 77] of equation (2.1) is helpful:

$$\sigma^2\left(\frac{A}{B}\right) = \frac{\langle\left(\delta\frac{A}{B}\right)^2\rangle}{\langle\frac{A}{B}\rangle^2} \approx \frac{\langle(\delta A)^2\rangle}{\langle A\rangle^2} + \frac{\langle(\delta B)^2\rangle}{\langle B\rangle^2} - 2\frac{\langle\delta A\delta B\rangle}{\langle A\rangle\langle B\rangle}. \tag{2.3}$$

Using the expressions for the variance and for the covariance

$$\begin{aligned}\mathrm{Var}\,(A) &:= \langle(\delta A)^2\rangle = \langle(A - \langle A\rangle)^2\rangle = \langle A^2\rangle - \langle A\rangle^2 \\ \mathrm{Cov}\,(A,B) &:= \langle\delta A\delta B\rangle = \langle(A - \langle A\rangle)\,(B - \langle B\rangle)\rangle = \langle AB\rangle - \langle A\rangle\langle B\rangle,\end{aligned}$$

equation (2.3) can alternatively be written as

$$\sigma^2\left(\frac{A}{B}\right) \approx \frac{\langle A^2\rangle}{\langle A\rangle^2} + \frac{\langle B^2\rangle}{\langle B\rangle^2} - 2\frac{\langle AB\rangle}{\langle A\rangle\langle B\rangle}. \tag{2.4}$$

It can be seen from this approximation, that each term σ^2_{data} and σ^2_{mix} in equation (2.2) contains variances ($\langle(\delta A)^2\rangle$ and $\langle(\delta B)^2\rangle$) as well as a covariance ($\langle\delta A\delta B\rangle$) term. It would be desirable to directly analytically extract each of these correlation and fluctuation measures separately [119] to enable a direct theory comparison. Experimentally, this is however not possible as e.g. the direct measurement of $\langle\delta A\delta B\rangle$ would be by far dominated by the multiplicity distribution in a studied event ensemble. While the single terms in equation (2.3) is affected by centrality variations, their sum is not. The three terms are correlated, allowing this cancelation. σ_{dyn} has been defined to be independent of small variations in centrality that can not be fully avoided in heavy ion collisions.

A quantitative interpretation requires the evaluation of $\sigma_{\rm dyn}$ from model calculations. Overall, competing effects contribute to $\sigma_{\rm dyn}$ and its sign:

- A correlation among particles that are either in the enumerator A or in the denominator B leads to a larger variance term compared to the reference. Consequently, a positive $\sigma_{\rm dyn}$ as observed for the $(\mathrm{K}^+ + \mathrm{K}^-)/(\pi^+ + \pi^-)$ case above could be caused by enhanced fluctuations of a particle number as expected at the critical point. A possible correlated production mechanism of kaons without a phase transition scenario is e.g. the decay $\phi \rightarrow \mathrm{K}^+ + \mathrm{K}^-$ [77, 120]. Hadronic transport models are a helpful tool to distinguish different correlation mechanisms.
- The covariance term enters equation (2.3) with a negative sign. Negative values of $\sigma_{\rm dyn}$ thus indicate correlated production of A and B. This has been observed in the analysis of $(\mathrm{p} + \overline{\mathrm{p}})/(\pi^+ + \pi^-)$ ratio fluctuations at SPS energies [118], as shown in the left panel of Figure 2.4. Nucleon resonance decays (e.g. $\Delta \rightarrow N + \pi$) are the dominant source of such a correlation. Simulations in hadronic transport models [121, 96] contain this process and the calculations give a good description of the NA49 data, as indicated by the blue lines in Figure 2.4 (left).
- Anti-correlation between enumerator A and denominator B leads to $\langle \delta A \delta B \rangle < 0$, and is again reflected in a positive contribution to $\sigma_{\rm dyn}$. One possible mechanism leading to such an anti-correlation is energy-momentum conservation [122]: The production of one particle A (in the observed part of phase space) suppresses the production of particle B (in the same direction). This is of course more important when heavy particles are considered.

It is clear from equation (2.3) and from the above listing, that the direct connection between a measured value of $\sigma_{\rm dyn}$ and the correlation causing it can not be made unambiguously. Model simulations as suggested above are needed. In the case of $(\mathrm{K}^+ + \mathrm{K}^-)/(\pi^+ + \pi^-)$ fluctuations, possible hadronic correlation processes as $\mathrm{K}^* \rightarrow \mathrm{K}^+ + \pi^-$ and the aforementioned ϕ decay are implemented in hadronic transport models. The energy dependence of $\sigma_{\rm dyn}$ for $(\mathrm{K}^+ + \mathrm{K}^-)/(\pi^+ + \pi^-)$ measured by NA49 [118] (see Figure 2.4, right) is however not reproduced in these models. Chapter 6 contains a more extensive discussion of these results. For this detailed interpretation the measurements are put into the context of other existing data, and the systematics are worked out to understand the results of the present work.

Depending on the PID techniques and other technical requirements, fluctuation measures other than $\sigma_{\rm dyn}$ are used. For comparisons to measurements in the STAR

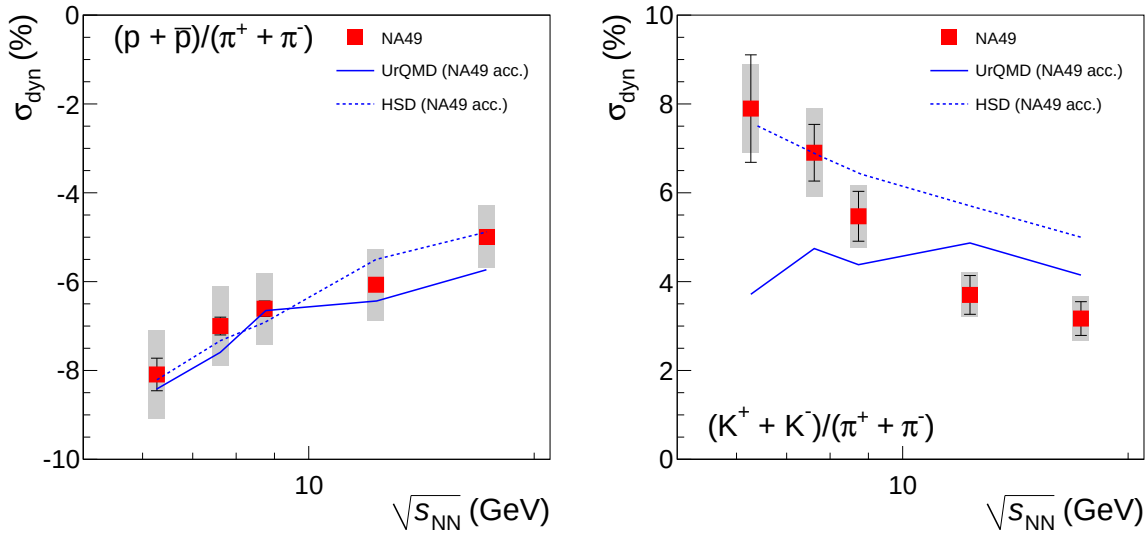

Figure 2.4: Energy dependence of σ_{dyn} for the $(\mathrm{p}+\overline{\mathrm{p}})/(\pi^+ + \pi^-)$ and $(\mathrm{K}^+ + \mathrm{K}^-)/(\pi^+ + \pi^-)$ ratios in central Pb+Pb collisions [118]. The NA49 results are compared to calculations in the transport models UrQMD [94, 121] and HSD [96, 123].

experiment [124, 125] the introduction of the variable ν_{dyn} [126] is necessary. In contrast to σ_{dyn}, ν_{dyn} can only be applied when no corrections due to the PID method are required. It is derived from the variable

$$\nu_{AB} := \left\langle \left(\frac{A}{\langle A \rangle} - \frac{B}{\langle B \rangle} \right)^2 \right\rangle = \frac{\langle A^2 \rangle}{\langle A \rangle^2} + \frac{\langle B^2 \rangle}{\langle B \rangle^2} - 2\frac{\langle AB \rangle}{\langle A \rangle \langle B \rangle}. \tag{2.5}$$

As above, $\langle \ldots \rangle$ denotes an event average. This ν_{AB} is identical with the approximation for σ^2 from equation (2.4). The remaining difference between σ^2 and ν are higher orders that are neglected in the approximation. Their role is examined in Chapter 5. In order to consider the influence of finite number statistics, a statistical reference background

$$\nu_{\mathrm{stat}} = \frac{1}{\langle A \rangle} + \frac{1}{\langle B \rangle} \tag{2.6}$$

is assumed, where the correlation-free Poisson case $\langle AB \rangle = 0$, $\langle A^2 \rangle = \langle A \rangle$ and $\langle B^2 \rangle = \langle B \rangle$ is only one possibility to obtain ν_{stat} from ν_{AB}. As in equation (2.3), the individual terms are correlated. The constraint to reproduce the multiplicity distribution of the original sample in the reference may lead to a non-zero correlation term, compensated by the other correlated terms to result in ν_{stat}. The quantity ν_{dyn}, independent of statistical fluctuations, and only containing the "dynamical" fluctuations is then defined as the

difference

$$\nu_{\rm dyn} := \nu - \nu_{\rm stat} = \frac{\langle A\,(A-1)\rangle}{\langle A\rangle^2} + \frac{\langle B\,(B-1)\rangle}{\langle B\rangle^2} - 2\frac{\langle AB\rangle}{\langle A\rangle\langle B\rangle}. \tag{2.7}$$

Experimental results and the role of the different variables will be compared in Chapter 6. Another combination of PID and quantification of fluctuations is currently under development. This "identity" method will be of particular use for fluctuation studies in small systems, with a small number of observed particles, as planned by the NA61 collaboration [63]. As this is not the major concern in the present study of central Pb+Pb collisions, the reader is referred to [127, 128, 129].

2.3 Baryon-Strangeness Correlations

The general sensitivity of hadron ratio fluctuations towards correlations governing the studied matter has been laid out in the previous section. Among these correlations are basic effects like energy-momentum conservation, signatures from after the hadronization like resonance decays and more sophisticated mechanisms. A careful separation of these effects is necessary to conclude about the early stage and potentially be sensitive to phase transition effects. Correlation signatures that convey this information to the final, detectable stage can use conserved charges with a low effect of hadronization and later hadronic interactions on their momentum distribution. The correlation between baryon number B and strangeness S has been suggested as a "Diagnostic of strongly interacting matter" [66] and promises to meet the above expectations.

A fundamental change in the baryon number-strangeness correlation is expected between the quark-gluon plasma and the hadronic domain. To quantify this effect the correlation coefficient

$$C_{BS} := -3\frac{\sigma_{BS}}{\sigma_S^2} = -3\frac{\langle BS\rangle - \langle B\rangle\langle S\rangle}{\langle S^2\rangle - \langle S\rangle^2} \tag{2.8}$$

has been defined in [66]. As $\langle S\rangle = 0$ due to strangeness conservation, C_{BS} can be rewritten as

$$C_{BS} = -3\frac{\langle BS\rangle}{\langle S^2\rangle}. \tag{2.9}$$

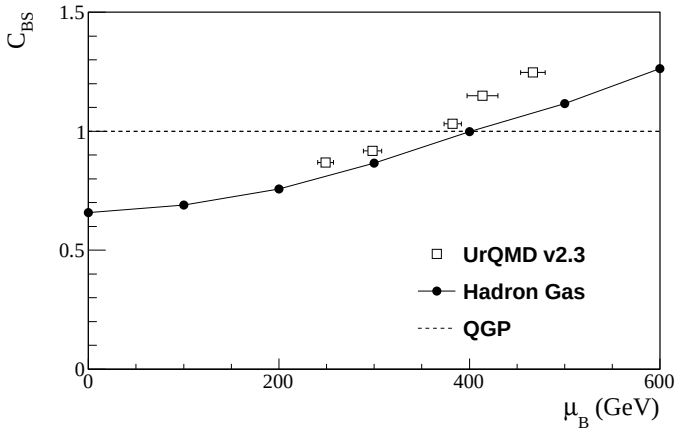

Figure 2.5: The baryon-strangeness correlation coefficient C_{BS} as a function of μ_B, as expected in a quark-gluon plasma, a hadron gas model [66] and in hadronic transport model (UrQMD) calculations [130].

In this definition, only strange particles contribute. Above the deconfinement phase transition strange quarks are the only strangeness carriers, with a fixed connection of $S = -1$ and $B = 1/3$. $C_{BS} = 1$ is therefore expected in a quark-gluon plasma. This expectation is indicated in Figure 2.5, showing C_{BS} as a function of μ_B. A hadron gas holds more possibilities for baryon-strangeness correlation. While kaons ($S = -1$, $B = 0$) carry strangeness unrelated to baryon number, a system where only Λ ($S = -1$, $B = 1$) carry strangeness would be characterized by $C_{BS} = 3$. In a hadron gas, the relative contributions of strange mesons and hyperons change as a function of μ_B, and with it, a changed overall baryon-strangeness correlation is expected. Even the remaining presence of quasi-bound objects above the deconfinement temperature would be reflected in a distinct baryon-strangeness correlation signature [66].

In thermodynamic models, C_{BS} can be evaluated from susceptibilities, and according to equations 1.4 and 1.5

$$C_{BS} = -3\frac{\chi_{B,S}}{\chi_{S,S}}. \tag{2.10}$$

The hadron gas model calculation [66] shown in Figure 2.5 exhibits the expected transition from meson- to baryon-dominated matter in form of a μ_B-dependence of C_{BS}.

Compared to the hadron gas that only features correlations due to energy-momentum conservation (and resonance decay if applicable), additional processes generate a baryon-strangeness correlation in a dense hadronic medium. One example is the associated strangeness production $N + N \rightarrow N + \Lambda + K^{\pm}$. These hadronic correlation processes

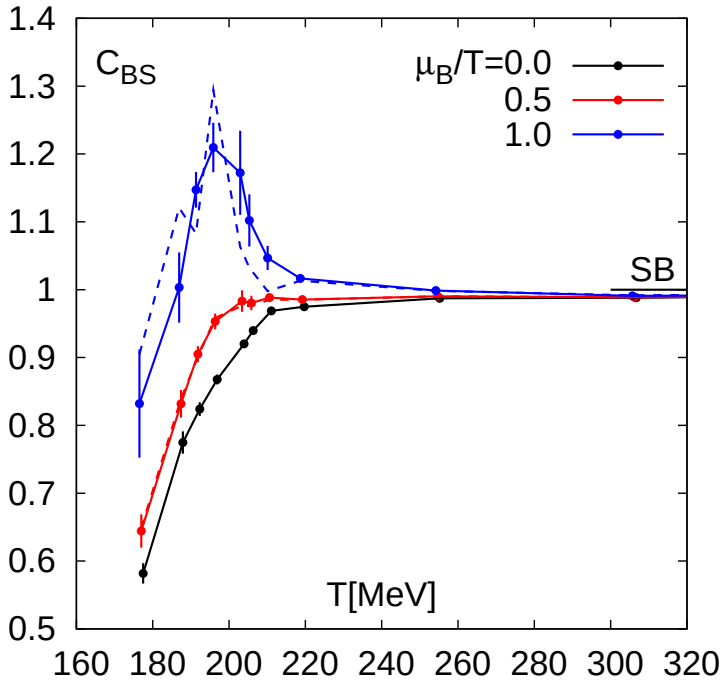

Figure 2.6: Temperature dependence of C_{BS} calculated in lattice QCD, for different values of μ_B [131, 132].

are modeled in the transport model UrQMD [92, 93, 94]. Their impact on C_{BS} has been studied (see Section 6.4 for details) and was found to be small. The result of an evaluation of C_{BS} in UrQMD [130] is also illustrated in Figure 2.5.

At $\mu_B = 0$, the susceptibilities $\chi_{B,S}$ and $\chi_{S,S}$ have also been evaluated in lattice QCD [131]. The resulting C_{BS} confirms the expected change at the phase transition and is shown in Figure 2.6 as a function of the temperature T. The part below T_c agrees with the hadron gas result at $\mu_B = 0$ of $C_{BS} \approx 0.6$, while the high temperature limit meets the quark-gluon plasma expectation, $C_{BS} = 1$, and thus excludes the hypothesis of quasi-bound states. Simulations extending the lattice results to finite μ_B [132] are also shown in Figure 2.6. They confirm the rising C_{BS} in the hadronic phase and, in addition hint at a maximum related to diverging light quark number susceptibilities at the critical point.

The UrQMD simulations in Figure 2.5 mark the μ_B values corresponding to the five SPS energies [34]. If deconfinement is reached in this energy domain, a change in C_{BS} is expected, from following the hadron gas curve to a constant correlation. Unfortunately, the full baryon number and strangeness are experimentally inaccessible as this would require the measurement of neutrons and the event-by-event reconstruction of V^0 particles

and cascading hyperons. Given reconstruction efficiencies between 1% and 10% [133, 134], this is not practicable.

On the other side studying baryon-strangeness correlation via charged kaons and protons brings the large advantage that they can readily be identified event-by-event and carry a substantial part of the total baryon number and strangeness. The kaon-proton correlation $\langle Kp \rangle$ therefore constitutes an important part of the baryon-strangeness correlation. Using the knowledge from Section 2.2, a connection can be made between $\langle Kp \rangle$ and $\sigma_{\mathrm{dyn}}\,(K/p)$. A relation between C_{BS} and the kaon-proton ratio fluctuations is attempted in Section 6.4.

Using kaons and protons as the carriers of the conserved charges strangeness and baryon number has the advantage that their dispersion in momentum space during the expansion phase of the heavy-ion collision is only moderate (cf. Section 1.4) in comparison to the analysis of electric charge correlations. In the latter case, Q is mainly carried by the light pions [75] and is thus easily reshuffled in phase space by multiple scattering or resonance decays. These transport processes are weaker in case of kaons and protons making the measured, final state hadron distributions a better reflection of the initial B, S distributions. When considering only positive hadrons, the influence of resonance decays can even be completely excluded as no resonance decays into $\mathrm{K}^+ + \mathrm{p}$. A similarly small impact on the correlation signal is expected from hadronization. When applying a quark coalescence approach to hadronization, on the contrary an obliteration of the quark-gluon plasma signature has been observed [135, 136, 137]. While the true nature of hadronization remains under debate, and coalescence is generally not seen as the prevalent hadronization mechanism in all kinematic domains, experimental investigation is necessary.

This experimental study is undertaken in the present thesis. The analysis results presented here are the first attempt to use kaon-to-proton ratio fluctuations as an experimental probe for the baryon-strangeness correlation. Given the expected robustness and sensitivity of the probe, and keeping in mind that the SPS energies are the relevant range for this study, we expect distinct fluctuation patterns in the energy dependence resulting from the critical point or the onset of deconfinement. Before immersing into the experimental details of the analysis, Figure 2.7 gives a preview on the final results. They have been presented and discussed at conferences [130, 121] and were published in [64].

Figure 2.7 shows the excitation function of σ_{dyn} for the $(\mathrm{K}^+ + \mathrm{K}^-)/(\mathrm{p} + \overline{\mathrm{p}})$ ratio. The fluctuation measure changes from $\sigma_{\mathrm{dyn}} = 5\%$ at $\sqrt{s_{NN}} = 6.3$ GeV to -5% at the

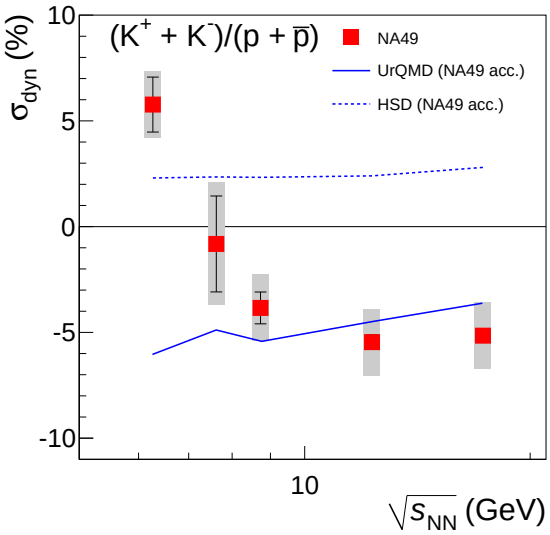

Figure 2.7: Fluctuations of the $(K^+ + K^-)/(p + \bar{p})$ ratio in central Pb+Pb collisions at SPS energies [64]. The NA49 results are compared to calculations in the transport models UrQMD [94, 121] and HSD [96].

high SPS energies. This change of sign can be seen as a fundamental change in the underlying correlations. The hadronic transport models UrQMD and HSD that are shown for comparison in Figure 2.7 show a contrastingly weak energy dependence. The consequences of this observation are still under discussion, but an explanation within a continuously hadronic scenario is not found as of yet. While this is just a preview on the results, their full presentation and discussion is reserved for Chapter 6.

Chapter 3

The NA49 Experiment

The NA49 experiment has been designed with a large acceptance with particle identification (PID) capabilities for charged hadrons. The coverage of a large fraction of each event is the important prerequisite for event-by-event studies [69, 70]. This chapter introduces the experimental details relevant to the present analysis and is in large parts adopted from [138]. For further details, the most comprehensive description of the experiment is found in [139]. Since the idea for NA49 came up [69, 70], many hundreds of physicists have participated in the design, development and construction of the detector, the electronics and the software that all are necessary to make the physics processes under investigation accessible to analysis. The collaboration has taken data from 1994 to 2002. All this is the indispensable basis for the analysis presented in this thesis.

The name NA49 derives from the experiment's location in the North Area, one of CERN's experimental sites. It is a fixed target experiment served by the H2 beam line of the *Super Proton Synchrotron* (SPS). Section 3.1 briefly describes the accelerators involved in the chain, delivering lead ion beams to NA49. Other experiments in the SPS heavy ion program are introduced in Section 3.2. A global overview of the NA49 setup is then given in Section 3.3, followed by a more detailed presentation of main detector components. The veto calorimeter used for centrality determination is described in Section 3.4). The emphasis of Section 3.5 is placed on the main tracking detectors of NA49, the TPCs, that also provide the $\mathrm{d}E/\mathrm{d}x$ measurement for particle identification. Finally, the electronics involved in the data taking and recording are presented in Section 3.7.

3.1 Particle Accelerators at CERN

The CERN accelerator complex consists of a wide variety of accelerators to provide lepton, hadron and ion beams for the various experiments in the fields of particle and heavy ion physics. Figure 3.1 shows a schematic plan of the accelerators. The combination of the different accelerators makes it possible to produce hadron, lepton, ion and antimatter beams at a large energy range. In order to reach the experiments of the heavy ion program, Pb ions coming from the ion source pass a chain of accelerators with increasing output energy: the linear accelerator LINAC3, the PS Booster (PSB), the Proton Synchrotron (PS) and finally the SPS. The accelerators are linked together and can provide different beams to various experiments at the same time. Their operation is therefore organized in so called *super-cycles*, the combination of acceleration *cycles* for different purposes. For the PS, a typical super-cycle at the time of data taking of the heavy ion experiments took 19.2 s and contained four ion fillings for the SPS of 1.2 s each (this example describes the 1994 Pb run at a beam energy of $E_{\mathrm{Beam}} = 158A$ GeV). In the remaining time, needed by the SPS for the acceleration, the PS can serve other purposes, e.g. providing p beams to experiments or conducting accelerator tests in "machine development" cycles. The SPS cycle also took 19.2 s, the beam was extracted over a time period of 4.2 s and split up into six beam lines [140].

Since its foundation in 1954, CERN played an important role in accelerator development [141]. When the PS came into operation in 1959 [142], its 24 GeV proton beam took over the world record for the highest energy available from the Synchrophasotron at the Joint Institute for Nuclear Research (JINR) in Dubna, Russia. The beam intensity rose since then by a factor of about 10^3, also through the addition of the PS Booster synchrotron in 1972. Completed in 1976, the SPS was CERN's first accelerator exceeding its main site near Meyrin, Switzerland. The underground accelerator ring has a diameter of 6.9 km. The experimental halls for fixed-target experiments are situated in the West Area (WA) on the main site and the North Area (NA) near Prevessin, France. In addition, the SPS features two underground experimental areas, where $\mathrm{p} + \overline{\mathrm{p}}$ collisions were studied in collider mode from 1981 until 1990. Protons can be accelerated in the SPS to a maximum energy of 450 GeV, for ions it is limited to 400 GeV per charge unit.

The chain of accelerators used by the heavy ion program was originally built to provide proton or electron beams for high-energy physics experiments. The production of ion beams started in 1986 with the acceleration of ^{16}O, followed by ^{32}S shortly after that. These isotopes were eventually brought to a beam energy of $200A$ GeV in the SPS.

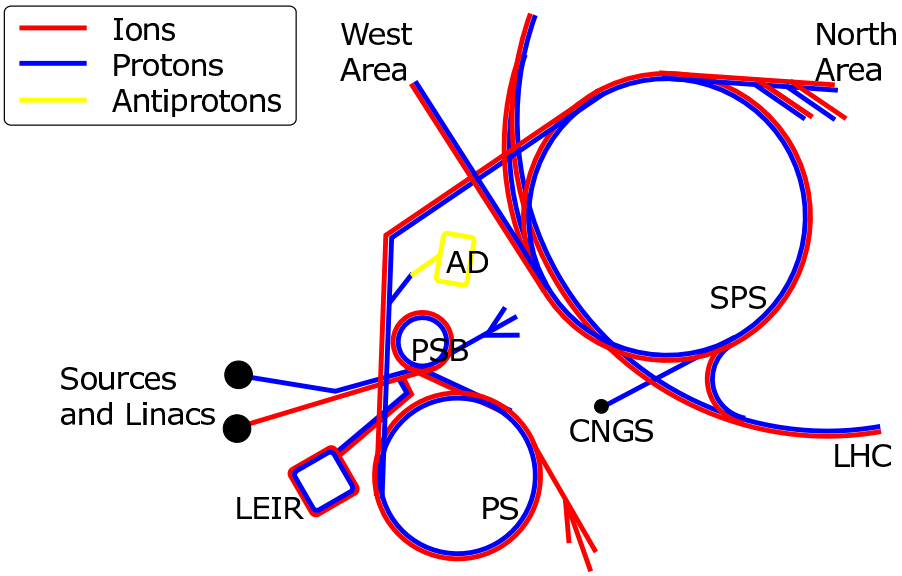

Figure 3.1: Parts of the CERN accelerator complex. Shown are the Antiproton Decelerator (AD), PS Booster (PSB), Proton Synchrotron (PS), Low Energy Ion Ring (LEIR), Super Proton Synchrotron (SPS) and only parts of the Large Hadron Collider (LHC). The experimental facilities shown are the SPS North and West areas as well as the CERN Neutrinos to Gran Sasso (CNGS) production facility.

This beam was used by the first generation of SPS heavy ion experiments. Following the installation of the new Electron Cyclotron Resonance (ECR) ion source and a new linear accelerator (LINAC3) [140], ^{208}Pb ions at 158A GeV were available from 1994 on. This is equivalent to a total energy of $\approx$ 33 TeV per Pb ion. The second generation of SPS heavy ion experiments that was constructed for the Pb beams recorded data until 2004, and is introduced in Section 3.2. Besides the top energy Pb ions, the H2 beam line can provide smaller nuclei (e.g. Si, C) from a fragmentation target or protons, all at various energies. This made the SPS size and energy scan program (see Section 3.2) possible.

Following CERN's principle to reuse existing infrastructure, PS and SPS were used to pre-accelerate electrons and positrons for the Large Electron Positron Collider (LEP). And also today, with the Large Hadron Collider (LHC) in operation, PS and SPS continue to provide the proton (since 2008) and Pb ion (2010) beams for further acceleration in the LHC. Fixed target experimental activity at CERN [143] continues with an extended system size and energy scan program of the NA61 collaboration using an upgraded version of the NA49 detector to search for the critical point of the QCD phase diagram [144, 145, 146, 147].

3.2 The SPS Energy Scan

The indication of a new state of matter created in Pb+Pb collisions at $\sqrt{s_{NN}} = 17.3$ GeV reported by the second generation of heavy-ion experiments at the CERN-SPS [26, 27] (see Section 1.2) was based on the combination of results from different experiments, each with its particular specialization in one or more of the relevant observables identified in Section 1.2. Besides the NA49 experiment, that is presented in detail in this chapter, other experiments of this group comprise

- the WA80/WA98 experiment [148], with a focus on electromagnetic probes like direct photons,
- NA45/CERES [149], specialized in electron pair measurements to study low mass resonances via their dileptonic decay,
- the dimuon experiment NA50/NA60 [150], searching for signatures of heavy quarkonium suppression and
- WA97/NA57 [151], reconstructing multi-strange hadrons via their weak decay.

The initial program expanded from the highest SPS energy of $\sqrt{s_{NN}} = 17.3$ GeV (corresponding to $E_{\text{Beam}} = 158A$ GeV, cf. Section A) to lower energies in order to establish the systematics of several observables. In 1999 and 2000, Pb+Pb collisions at approximately half ($E_{\text{Beam}} = 80A$ GeV and $\sqrt{s_{NN}} = 12.3$ GeV) and a quarter ($E_{\text{Beam}} = 80A$ GeV and $\sqrt{s_{NN}} = 8.7$ GeV) of the beam energy were studied. The results [59] supported the predicted signatures of the onset of deconfinement [58], and motivated a further study. Until 2002, the energy scan has been expanded to $20A$ GeV ($\sqrt{s_{NN}} = 6.3$ GeV) and $30A$ GeV (7.6 GeV), with the positive result [28] reported in Section 1.3.

Table 3.1 gives an overview on the nucleus-nucleus collisions studied in the NA49 experiment. In addition to the central Pb+Pb collisions that will be the topic of this thesis, this A+A program also comprised minimum bias Pb+Pb as well as collisions of smaller systems such as C+C and Si+Si. They can be used to study system size effects. Reference data on p+p and p+A collisions (not shown in Table 3.1) complete the picture.

This large range of different systems studied with the NA49 experiment leads to a variation in experimental conditions. The number of reconstructed particles for example changes from just a handful in p+p to more than 1,000 in full energy Pb+Pb collisions.

Beam Energy	$\sqrt{s_{NN}}$	System	Centrality	Statistics
20A GeV	6.3 GeV	Pb+Pb	7%	360k
			35%	330k
30A GeV	7.6 GeV	Pb+Pb	7%	440k
			35%	230k
40A GeV	8.7 GeV	Pb+Pb	7%	700k
			minimum bias	430k
		C+C	66%	240k
		Si+Si	29%	130k
80A GeV	12.3 GeV	Pb+Pb	7%	300k
158A GeV	17.3 GeV	Pb+Pb	10%	800k
			23%	3000k
			minimum bias	410k
		C+C	15%	220k
		Si+Si	12%	300k

Table 3.1: Overview of NA49 data sets collected during the SPS energy and system size scan. In addition, reference data on p+p and p+A collisions was taken.

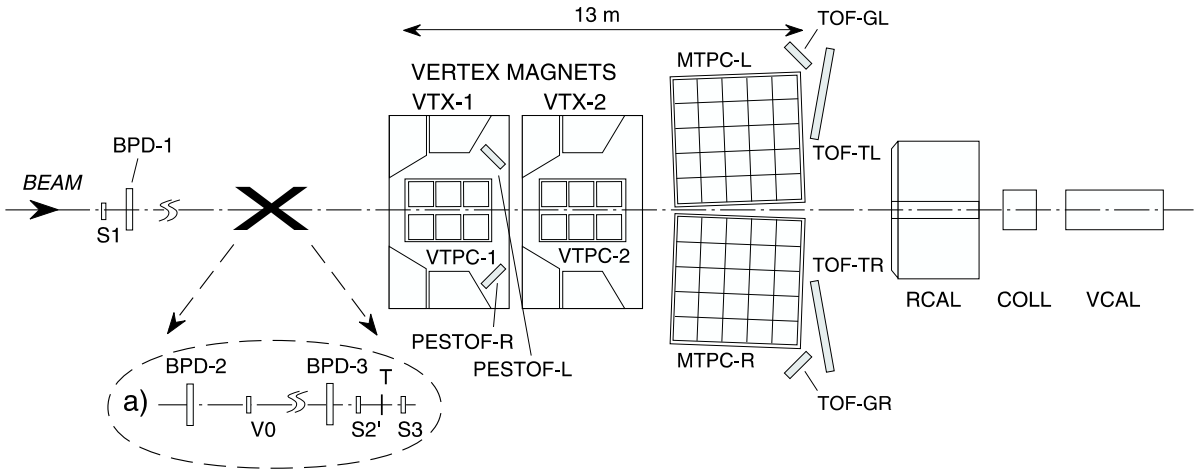

Figure 3.2: Schematic setup of the NA49 experiment. The figure is taken from [139].

Varying the collision energy in a fixed target setup may lead to a different part of the momentum space being probed at each energy. In NA49, the spectrometer magnetic field was set proportional to the beam momentum so that the acceptance could be kept approximately constant with respect to midrapidity. Further details on the acceptance in the present analysis can be found in Chapter 5.

3.3 Experiment Overview

The NA49 experiment [139] is a large acceptance spectrometer, designed to track and identify the charged hadrons produced in nucleus-nucleus (A+A), proton-nucleus (p+A) and proton-proton (p+p) collisions. Considering the high charge of the ion beam as well as the high number of particles produced in A+A interactions, the detector design had to be geared to the requirements for these collisions. The high beam charge requires a low material budget in the passage of the beam. The high multiplicity calls for good resolution tracking detectors combined with strong magnetic fields. For this purpose, Time Projection Chambers (TPCs) as main tracking detectors were the natural choice. The resulting schematic layout is shown in Figure 3.2. This section describes the setup as it was used for recording central Pb+Pb collisions at 158A GeV in 1996. Only minor changes were necessary for the lower energies [28, 59] and are described where it applies.

In the most central Pb+Pb interactions at the top SPS energy of 158A GeV, approximately 1,700 charged hadrons are produced (in contrast to about 10 in p+p reactions). To separate this large number of particle tracks, downstream of the target two super-

conducting dipole magnets expand the cone of produced particles. Together, they can provide a maximum bending power of 9 Tm. The aperture inside the yoke has a constant height of 1 m and a horizontal width increasing in downstream direction, giving room for tracking detectors.

Four large volume TPCs serve as tracking detectors, the two Vertex TPCs (VTPC1 and VTPC2) lie within the magnetic field while the Main TPCs MTPC-L and MTPC-R are situated downstream of the magnets. The basic principles on TPCs are described in Section 3.5. Charged particles' momenta are determined by tracking their paths through the magnetic field. Figure 3.3 shows an event recorded by the TPCs. The reconstruction chain described in Section 4.2 was used to convert the raw TPC data to space points (red), and connect them to local (purple lines) and global (yellow lines) tracks. The TPC system can track particles over up to 14 m length with an resolution below 200 μm. Depending on the phase space region, a momentum resolution between $\mathrm{d}p/p^2 = 3 \cdot 10^{-5}(\mathrm{GeV}/c)^{-1}$ and $\mathrm{d}p/p^2 = 7 \cdot 10^{-4}(\mathrm{GeV}/c)^{-1}$ is reached. In addition to tracking, the TPCs provide a measurement of energy loss per unit of length ($\mathrm{d}E/\mathrm{d}x$) in the detector gas. As the energy loss is a function of the particle velocity, particle identification can be obtained through simultaneous measurement of momentum and $\mathrm{d}E/\mathrm{d}x$. So, $\mathrm{e}^{\pm}$, $\pi^{\pm}$, $\mathrm{K}^{\pm}$, p, $\overline{\mathrm{p}}$, d and $\bar{\mathrm{d}}$ can be distinguished in the momentum region where the Bethe-Bloch curve is in the *relativistic rise*. The geometrical acceptance of the TPCs is limited by the fact that the region around the beam axis is excluded from its sensitive volume. The Pb beam particles would deposit too much charge in the detector. Nonetheless, 70% of all charged particles are accepted.

The particle identification capability of the TPCs is complemented by the Time Of Flight (TOF) detectors. They provide a velocity measurement of low momentum particles and thus add PID information in the phase space region where the specific energy loss functions of different particles overlap. The TOF detector consists of finely granulated scintillator walls with photomultiplier readout with a time resolution of approximately 60 ps. Its acceptance is limited to a small midrapidity window. This makes it unsuitable for event-by-event measurements, while it provides an important, independent confirmation of inclusive $\mathrm{d}E/\mathrm{d}x$ measurements.

Also for the beam counters the aim was to minimize the amount of material in the beam. For this reason, the beam counters for the A+A setting of NA49 were chosen to be a thin (200μm) Quartz Cherenkov detector (S1) and two thin He gas Cherenkov detectors (S2' and S3). The beam counters measure the beam charge, so S1 and S2' are used to select incoming Pb ions. In the case of an inelastic interaction in the target, the

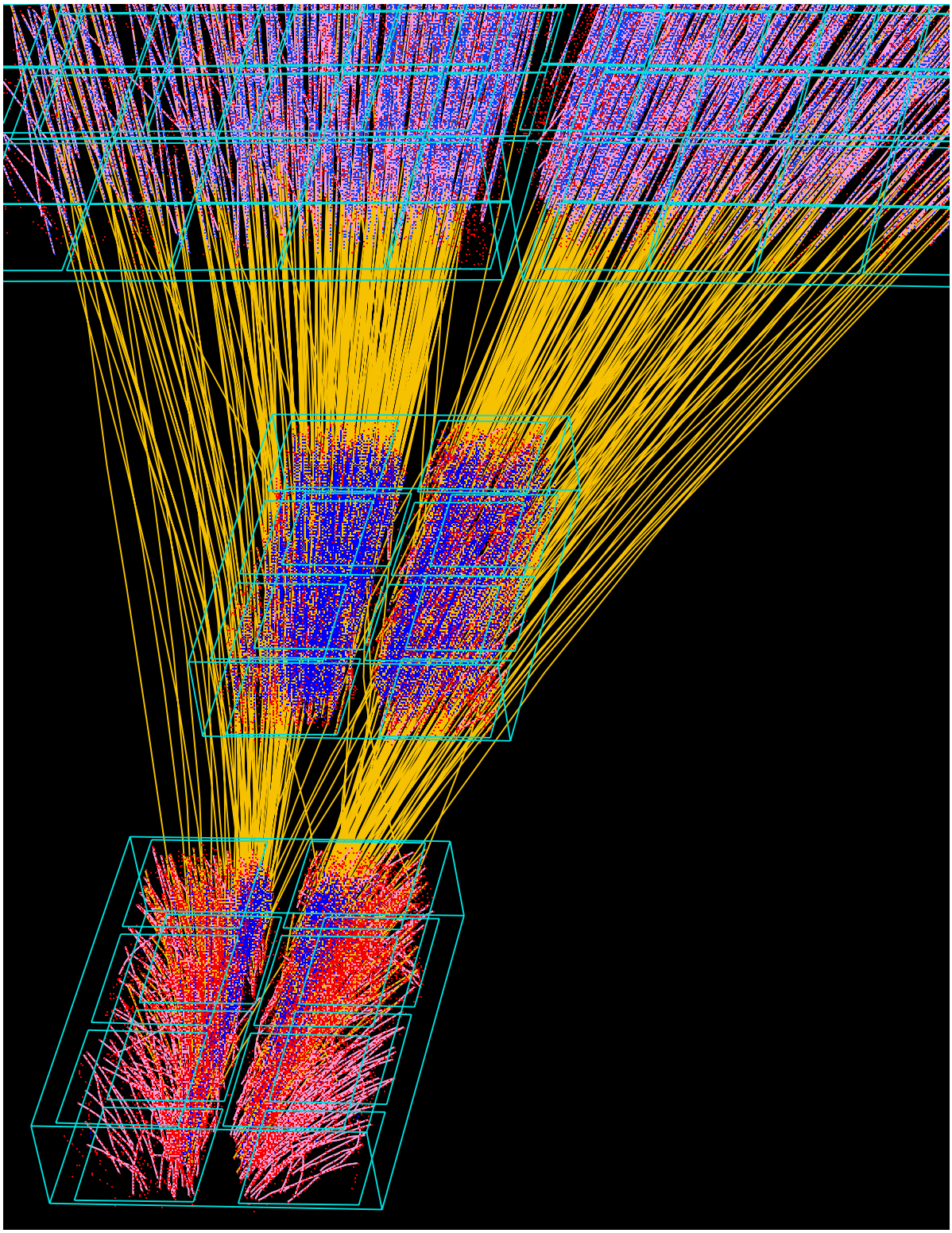

Figure 3.3: Charged particle tracks detected in the NA49 TPCs. The tracks are bent by the magnetic field in the Vertex TPCs (bottom and center), and leave straight tracks in the Main TPCs (only partially visible on the upper edge of the image).

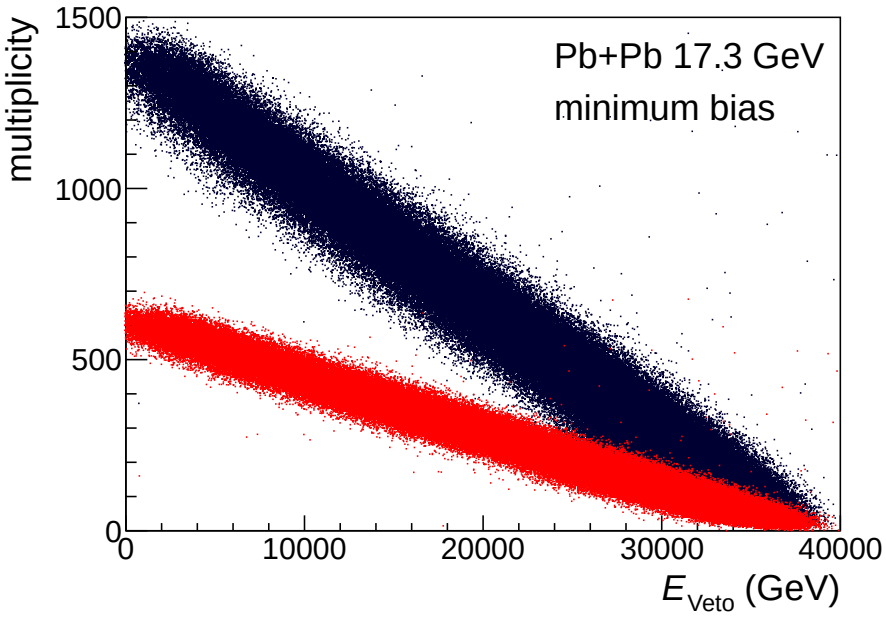

Figure 3.4: The energy detected in the veto calorimeter E_{Veto} exhibits an anti-correlation to the multiplicity: a central collision produces high multiplicity and shows few spectators. The data is extracted from a minimum bias Pb+Pb dataset at $\sqrt{s_{NN}} = 17.3$ GeV. Blue points indicate the number of charged tracks within the TPC acceptance, while the red points result after applying the track quality cuts as defined in Section 5.2. These track cuts ensure the PID resolution necessary for the present analysis and require points in the MTPCs.

signal in S3 is lower hence an anti-coincidence of the beam counters upstream of the target with it is used as a trigger signal. S1 furthermore serves as a start counter for the TOF measurement. The three Beam Position Detectors (BPD) consist of proportional chambers. By extrapolating from the hits in the BPDs to the target position, the main interaction vertex can be determined with an accuracy of 40 μm.

The centrality of an A+A collision (cf. Section 1.2) is determined by a measurement of projectile spectators in the Veto Calorimeter (VCAL). The collimator COLL has an aperture allowing neutrons, protons and fragment nuclei with beam momentum to reach the calorimeter. The total energy deposited is denoted E_{Veto}. A low E_{Veto} value then refers to a central collision and vice versa (see Figure 3.4). A more detailed review of the centrality determination procedure is given in Section 3.4.

To start a measurement, *trigger detectors* send a signal to the detector control when several conditions are fulfilled. The beam counters and the VCAL serve as trigger detectors. To select a central Pb+Pb collision, a Pb ion has to be recognized in the beam counters before the target S1 and S2'. At the same time, S3 behind the target has

to measure a lower value than the two, indicating a target interaction. To add online centrality selection, the above trigger conditions are combined with the requirement of an energy measurement below a threshold in the Veto calorimeter.

All coordinates given in this thesis refer to the NA49 coordinate system: The z-axis follows the beam direction, y represents the drift direction of electrons in the TPCs (upwards) and x (pointing towards the jura mountains) completes them to a right-handed system. The origin lies in the centre of VTPC2, the target (depending on the run period) at $z \approx -580$ cm.

3.4 Centrality Determination

The NA49 veto calorimeter [152] is a hadronic calorimeter composed of stacks of lead-scintillator and iron-scintillator layers, read out by photomultipliers. Its total material budget amounts to 10 interaction lengths. The relative energy resolution has been evaluated to be $\sigma(E)/E = 2/\sqrt{E\,(\mathrm{GeV})}$. Beam spectator nucleons (cf. the sketch in Figure 1.4) are present either in form of light nuclei (fragments), protons or neutrons. The collimator placed in front of the veto calorimeter is set to let all of these nucleons and fragments (taking into account their deflection in the magnetic field with Z/A ratios ranging between zero and one) pass if they carry beam momentum $\pm$ a smearing caused by the Fermi motion inside the nucleus. On the other hand, the collimator prevents most newly produced particles from reaching the calorimeter. Therefore the aperture is adjusted according to each studied beam energy.

A nearly linear dependence between E_{Veto} and the multiplicity of produced particles has been observed, as seen in Figure 3.4. In order to map veto energy measurements to microscopic collision parameters like the impact parameter b, number of participating nucleons $\langle N_{\mathrm{w}} \rangle$ etc., model calculations are required. The VENUS model [153] has been used as an input for such simulations [139, 154], and the resulting correlation plot is shown in Figure 3.5. In the model, the centralities are randomly sampled and as expected from geometrical considerations, the cross section rises in proportion to $\sqrt{b}$ up to the maximal impact parameter $b_{\mathrm{max}} \approx 2r_{\mathrm{nucleus}}$. At higher impact parameters, no inelastic collisions take place. The scale on the right hand side indicates, which fraction of all inelastic events (and the total inelastic cross-section, respectively) is found in the interval between $b = 0$ and the value on the opposite b-axis. For each event, the veto calorimeter response is simulated and tabulated on the bottom scale. The top scale indicates the

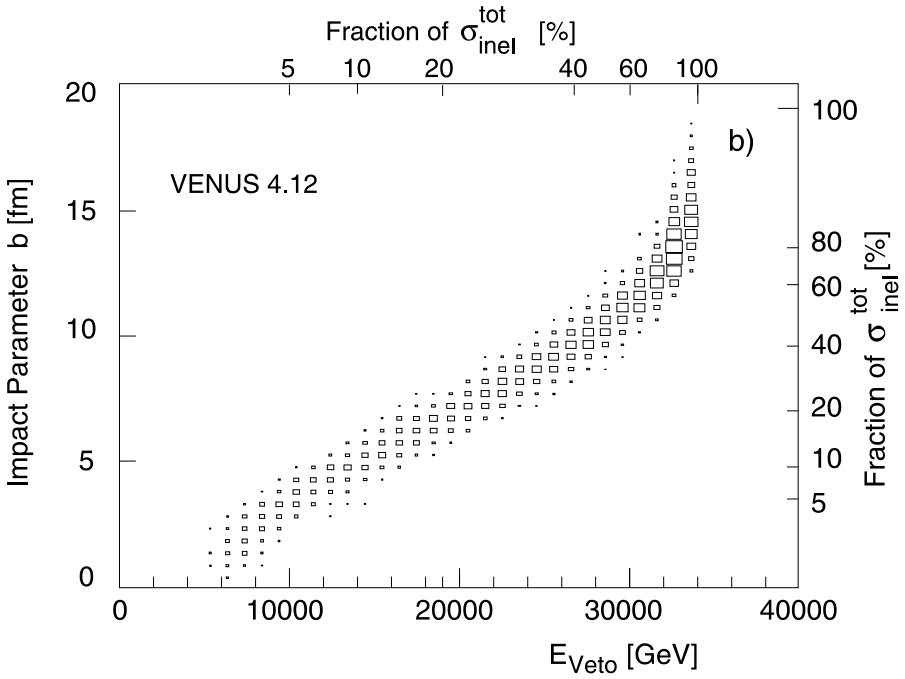

Figure 3.5: Mapping of E_{Veto} to collision parameters calculated with the VENUS model [153]. The figure is taken from [139] and refers to Pb+Pb collisions at $\sqrt{s_{NN}} = 17.3$ GeV.

fraction of events in the E_{Veto} interval below, compared to all events. Thus the term "the 3.5% most central events" can either refer to the 3.5% of the events with the lowest E_{Veto} values or those with the smallest impact parameter. The usage depends on the knowledge about the centrality: in the model, all parameters are known, while in the experiment one has to rely on the measured quantities. Figure 3.5 is thus also an important illustration to keep in mind that the control parameter E_{Veto} is not identical with the centrality and that especially a too tight centrality selection may cause a bias on fluctuation measurements [155].

A common experimental issue in calorimetric measurements is a time dependence of the signal. Often, this is caused by scintillator and photomultiplier aging, especially when, like here, the calorimeter operates in high radiation areas. The NA49 veto calorimeter signals show a slight time dependence. It has been evaluated, and a correction procedure was developed [156]. The influence of this effect on the present fluctuation measurement has also been studied and found to be nonexistent, see Chapter 5.

3.5 The Time Projection Chambers

TPCs are detectors capable of recording the tracks of charged particles in three dimensions. They consist of proportional chambers for the two-dimensional readout, extended by a large gas volume. This gas volume is surrounded by a field cage providing a homogeneous electric field, the *drift field*, which allows the determination of the third coordinate.

The NA49 TPCs have a cuboidal shape, the drift field is applied between the base plate and the readout chamber on the top end, so it is antiparallel to the y-axis in all four TPCs. Strips of Mylar foil coated with aluminum define the field on the sides with a minimum amount of material to be traversed by the particles. By this a homogeneous field of 200 V/cm (VTPC) and 170 V/cm (MTPC), respectively, can be provided over the large volume of the TPC. On its way through the detector gas, a charged particle ionizes gas molecules. The drift field accelerates the freed electrons towards the readout chamber. A constant drift velocity results from an equilibrium between the acceleration and the energy loss through elastic interaction with the gas molecules. This proportionality between drift time and space in drift direction permits the determination of the y-coordinate.

During the drift time of 50 μs, the charge distribution broadens due to diffusion. A final width of the electron cloud around 5 mm could be achieved through an addition of CO_2 to the usual noble gas-methane gas mixture [139, 157]. While in the VTPCs, Ne/CO_2 with a ratio 90/10 was used, $Ar/CH_4/CO_2$ in the ratio 90/5/5 was selected. For a stable TPC operation, contaminations with water and oxygen have to be avoided. The NA49 gas control system makes sure the purities remain at the level of 2–4 ppm for oxygen and around 20 ppm for water.

In the readout chambers, the drifting electron clouds are converted into electronic signals from which their three dimensional position as well as their total charge (which is proportional to the energy initially deposited by the ionizing particle) can be reconstructed. The readout chamber consists of three wire planes and a readout plane segmented into pads (see Figure 3.6). Electrons produced by an ionizing track will first encounter the *gating grid*. In case of a trigger signal, the voltage corresponding to an undisturbed drift field is applied, making the gating grid permeable for electrons. Without a trigger, alternating wires are brought to ± 100 V relative to the drift field, preventing electrons from entering the readout chamber. The gating grid also hinders ions produced in the gas amplification from moving into the drift volume where their space charge would cause problems. The *cathode plane* is at 0 V potential and separates the drift field from

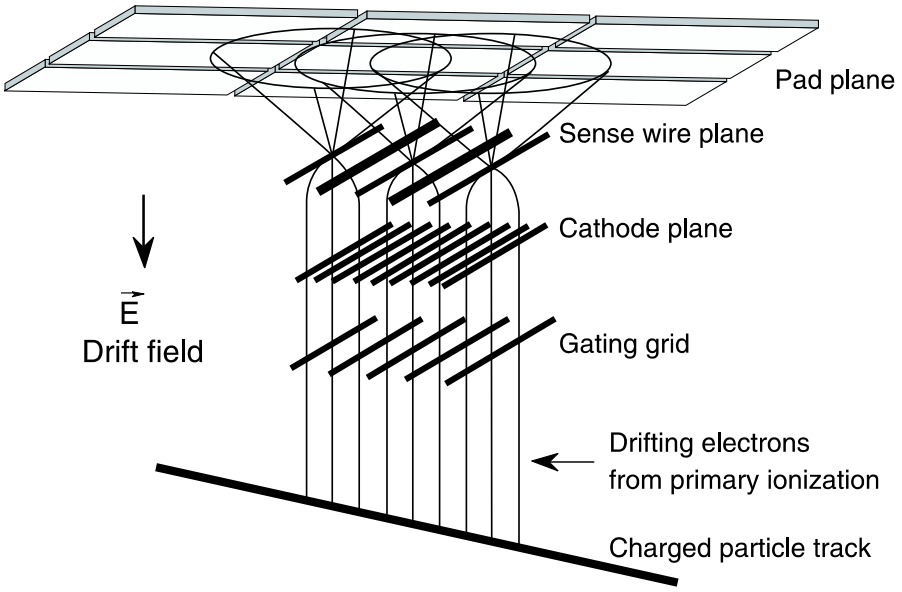

Figure 3.6: Layout of the TPC readout chamber. The figure is taken from [139].

the amplification field of the proportional chamber. The *sense wire plane* alternately consists of sense wires, which possess a potential of ≈ 1 kV, and of field wires at 0 V. Gas amplification takes place in the vicinity of the high potential sense wires, where the electric field is not homogeneous but proportional to r^{-2} with respect to the wire centre. An avalanche of electrons is produced, multiplying one electron to $2 \cdot 10^4$ in the VTPCs and to $0.5 \cdot 10^4$ in the MTPCs. The electrons are quickly absorbed by the wires, leaving the heavier thus slowly drifting ions behind. Their space charge induces a mirror charge on the readout pads. The current building up this mirror charge is amplified on the Front-End Cards (FEC), sitting directly on the back of the readout plane. One FEC processes the signals from 32 pads by amplifying, shaping and digitizing them. The total drift length of the chambers (VTPC: 0.66m, MTPC: 1.1m) is equivalent to a drift time of 50 μs. 512 time samples are extracted at 10 MHz by the Analog-to-Digital Converters (ADCs) on the FECs. Control and Transfer (CT) boards collect the signal from 24 FECs and send them to the counting house via optical fibers. The further way of the signals is described in Section 3.7.

The segmentation of the readout plane into pads follows the track geometry. Having a rectangular shape, the pads have lengths of $16 - 40$ mm but widths of only $3.5 - 5.5$ mm, as a higher resolution is required perpendicular to the tracks to be able to separate two tracks lying close to each other. For the same reason, the alignment angle of the pads is adapted to the most common track direction. A sequence of pads perpendicular to the

	VTPC-1	VTPC-2	MTPC-L/R		
Gas mixture	Ne/CO_2 (90/10)		$Ar/CH_4/CO_2$ (90/5/5)		
Width	200 cm		390 cm		
Length	250 cm		390 cm		
Height	98 cm		180 cm		
Drift length	66.6 cm		111.7 cm		
Sectors	6		25		
Pad rows / sector	24		25		
Pads	27648		63360		
Sector subtype			HR	SR	SR'
Pads / pad row	192		192	128	128
Pad length	1.6/2.8 cm	2.8 cm		4 cm	
Pad width	0.35 cm		0.36 cm	0.55 cm	0.55 cm
Pad Angle	12-55°	3-20°	0°	0°	15°

Table 3.2: Dimensions and characteristics of the NA49 TPCs [139].

tracks is referred to as a *pad row*. The MTPCs have different subsets of sectors: high resolution (HR) in the high track density region close to the beam, standard resolution (SR) as well as tilted (SR') pads at the outside, where the tracks have larger angles to the beam axis. All the dimensions and characteristic numbers of the TPCs are summarized in Table 3.2. The space resolution of the TPC is better than the pad dimensions, as the simultaneous measurement of one charge cluster on neighboring pads is used to calculate the charge distribution's centre of gravity during the reconstruction (see Section 4.2). The same is done in y direction over several time bins.

3.6 NA49 Acceptance Overview

The NA49 TPCs cover a large part ($\approx$ 70%) of the particles produced in heavy-ion collisions. Very low momentum particles are deflected by the magnets before reaching even the first VTPC, causing acceptance losses at backward rapidities. The gap left around the beam induces further losses at very forward rapidities and in the azimuthal up and down regions. The event display in Figure 3.3 suggests that the acceptance of

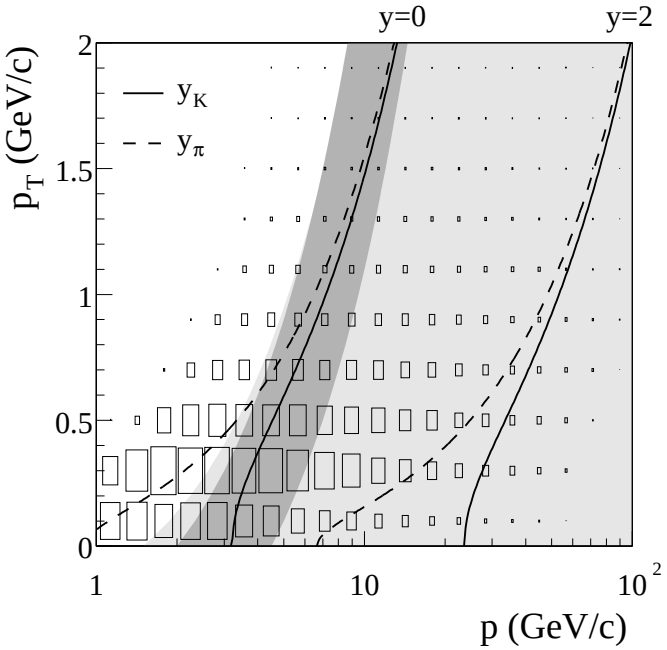

Figure 3.7: The total momentum p vs. transverse momentum p_{T} distribution of charged particles observed in Pb+Pb collisions at 80A GeV ($\sqrt{s_{NN}} = 12.3$ GeV, from [59]). The acceptance of the TPCs is indicated by the box histogram and spans from backward to forward rapidity. The TOF acceptance is focussed at midrapidity (dark grey area), while the MTPC acceptance covers central to forward rapidities (light grey area). Lines indicate constant rapidity y for pions and kaons.

the MTPCs is focussed to the more forward region, as low momentum particles are deflected after traversing the VTPCs. Indeed, the MTPCs were designed to cover the forward hemisphere of the produced particles, i.e. those particles with momenta larger than the center of mass of the collision. These fast particles have the advantage that they can be identified in the relativistic rise. Figure 3.7 represents an overview of the NA49 acceptance via the total vs. transverse momentum distribution of accepted particles. The largest coverage is provided by the whole TPC system, as indicated by the box histogram. The MTPCs constitute a subset at central to forward rapidity, and are indicated by the lightly shaded area. The complementing PID capabilities of the TOF (darker shades) are available at midrapidity.

To determine inclusive spectra in symmetric collisions, like p+p or A+A, it is sufficient to cover one hemisphere. Complete rapidity spectra can then be inferred from symmetry considerations. The same applies for the azimuthal acceptance gaps, where a flat distribution on average can be assumed for extrapolations to the unmeasured phase space. In event-by-event fluctuation measurements, such extrapolations can not be made. The acceptance affects the observable correlation signal and needs to be taken into account in the interpretation by e.g. applying the acceptance restrictions in model comparisons.

3.7 Data Flow

Receiver boards located in the counting house pick up the signals from four CT boards each. Their function is to reduce the raw data size and to buffer the information until it is required by the *event builder*, a CPU arranging the raw data of all detectors. The event building is necessary because the transfer from the detector is done unsorted to increase speed. From the event builder, the raw events are transferred to a tape recorder.

The event builder accumulates the data from all detectors, but the TPC with its total number of $182,016$ individual channels contributes the largest data volume. Each of the "three-dimensional pixels" made up by one pad $\times$ one time bin is sampled in the ADCs with a precision of 8 bit. At 512 time bins, this leads to an event size of $182,016 \cdot 512 \cdot 8\text{bit} \approx 90\text{Mbyte}$ of raw data flow to the receiver boards per event. However, only a fraction of these pixels contains charge from a track. A considerable amount of memory can be economized when the empty bins are not saved. The residual signal for all pads is therefore recorded with no beam present and then subtracted from the measured signal. Points with a signal below a threshold of 5 ADC counts are not stored.

In this way, the raw event volume is reduced on the receiver boards by 90%, to only 8 Mbyte per event.

During the $\approx$ 5 s of one SPS spill, in average 30 central Pb+Pb events are selected by the triggers. A maximum of 32 events can be buffered on the receiver boards. While data transfer from the detector to the receiver boards is in progress, the buffered information is not accessible for the event builder. During the spill, only few events can be transferred to the event builder to free the buffer position occupied by them. This means that the buffer limits the maximum event rate and that the largest part of event building is done in the $\approx$ 15 s between two spills. This spill structure leads to a varying time pattern of events, with some events in close temporal context, others further apart. In principle, this might lead to systematic gain variations from event to event. A detailed investigation [158] however found no signs of such an effect.

The events are then recorded by a Sony DIR-100M tape recorder at a writing speed of 16 Mbyte/s. The operation of the tape recorder is not influenced by the pulsed data output resulting from the spill structure as the tape controller unit can buffer data and temporarily acquire it at a higher rate than the actual writing speed. An equivalent of 12,000 central Pb+Pb events fits on one of the Sony D1 cassettes with a capacity of 100 Gbyte each.

Chapter 4

Data Processing in NA49

The large amount of raw experimental data collected from the different detectors has to undergo processing toward a form that is accessible to further analysis and interpretation of the recorded observations. The computing framework for this purpose is as vital to the results as the detector setup itself. The NA49 reconstruction chain has been improved over the years of NA49 analyses and has reached a stage where more complex subjects can be covered. The involved computer hardware and software has not changed since it was extensively described so that the following chapter could be adopted from [138] in large parts, with appended sections where details for the present analysis were required.

On the hardware side, NA49 relies on clusters of computers and large data storage facilities situated at CERN. They are presented in Section 4.1. The software consists of two major parts: The reconstruction chain (Section 4.2) finds tracks in the raw ADC counts and stores momentum, energy loss and other information about the particles observed in so-called Data Summary Tape (DST) files. To further investigate this information, the object-oriented analysis-framework ROOT (Section 4.3) provides the necessary tools.

4.1 Computing Resources at CERN

Data Mass Storage

The raw data collected over NA49's nine years of running adds to a total of 100 Tbyte. To access this raw data for processing, a second Sony DIR-100M tape drive was installed in a tape robot holding up to 24 tapes, or 2.4 Tbyte at the same time. As data on

tape is not randomly accessible, every tape system needs to be complemented by disk pools where the data is temporarily staged when in use. For the Sony robot, a stage pool with a capacity of 900 Gbyte was used. The raw data has been reconstructed and is now accessible in the DST files. The Sony system is thus no longer needed and was phased out in the end of 2005. But parts of the raw data are still required: Samples from every run period have to be retained for efficiency studies using embedding, and some datasets will be reprocessed to include more information into the DSTs. For this purpose, 7.5 Tbyte have been copied from the Sony tapes to the *CERN Advanced STORage Manager* (CASTOR) prior to the phase-out.

While the Sony system has been installed by the NA49 collaboration and was only used within the experiment, CASTOR is a CERN-wide installation, maintained and operated by the CERN IT division [159, 160] currently holding a data volume of almost 50 Pbyte. The project is recording the large data streams that are produced by the LHC experiments. CASTOR, being in operation since 2001, is a storage manager enabling access to the data kept on tape from a large number of different operating systems. It is a hierarchical storage manager, because the files contained are accessed via path names with organization in directories like in a standard unix file system, so that the user does not need to know on which tape a particular file is stored. So one internal part of CASTOR is the name server mapping these path names to the actual file location on tape, other components are handling and controlling the transfer from tape to stage pools. The most important module visible to the user is the `rfio` package providing command line facilities to create, access or remove files on CASTOR and an API enabling the communication between applications and CASTOR.

Computing Clusters

To avoid long distance transfers of data, processing and analysis of the data stored in CASTOR are done on computing farms that are also located at CERN. PLUS (Public Login User Service) provides a cluster of computers for interactive logon, *lxplus*. It is operating under a CERN-specific version of Scientific Linux (SLC). All CERN users can use it to develop and test software, access the Mail and News Servers, their AFS (Andrew File System, [161]) home directory and many other services provided by the CERN IT Division. The data stored on CASTOR can also be accessed via lxplus.

In addition to the interactive nodes, a batch farm consisting of $\approx$ 30,000 CPU cores (*lxbatch*) is provided for more time-consuming and CPU-intensive processes. They are

likewise running under SLC. The software LSF (Load Sharing Facility) takes care of the distribution of batch jobs to the computers in the farm and for allocation of computing power to the different experiments. NA49 has a share of on average 100 jobs running in parallel on lxbatch.

4.2 Reconstruction Chain

The reconstruction chain's role is to convert the raw data into DST files for making the physics information gathered in the experiment accessible to analysis. While this was traditionally done in a single-threaded process, a different approach was used in NA49: DSPACK [162], a client/server architecture developed for this purpose. The reconstruction procedure is split into many client processes. This structure was supposed to make distributed development and debugging easier. The small size clients are better than single-thread solutions in terms of performance and resource usage. Other advantages are that client software can be written in different programming languages, that the clients can be reused in different steps of the reconstruction, and that clients can easily be exchanged or modified. DSPACK files like the DSTs used in NA49 can be directly accessed; for other files like the raw data format plug-ins are required. A DSPACK server connects all the pieces by providing the communication between input and output files and the clients.

The reconstruction of each event starts with the merging of pixels from the raw data into space points. Corrections have to be applied on the points to determine the real positions where a track has traversed the detector. The next step is to assemble the corrected points for forming tracks from primary charged particles or those that may originate from secondary vertices, e.g. of V^0 decays. Many other clients complete the reconstruction by gaining information from hits in the TOF detectors, determining the $\mathrm{d}E/\mathrm{d}x$ signal from the measured cluster charge etc.. The latter is the most essential part of the reconstruction for the analysis presented in this thesis. $\mathrm{d}E/\mathrm{d}x$ determination and calibration is described in more detail below. An overview of the whole reconstruction process is provided in Figure 4.2 on page 69, where the sequence of the reconstruction steps is schematically depicted.

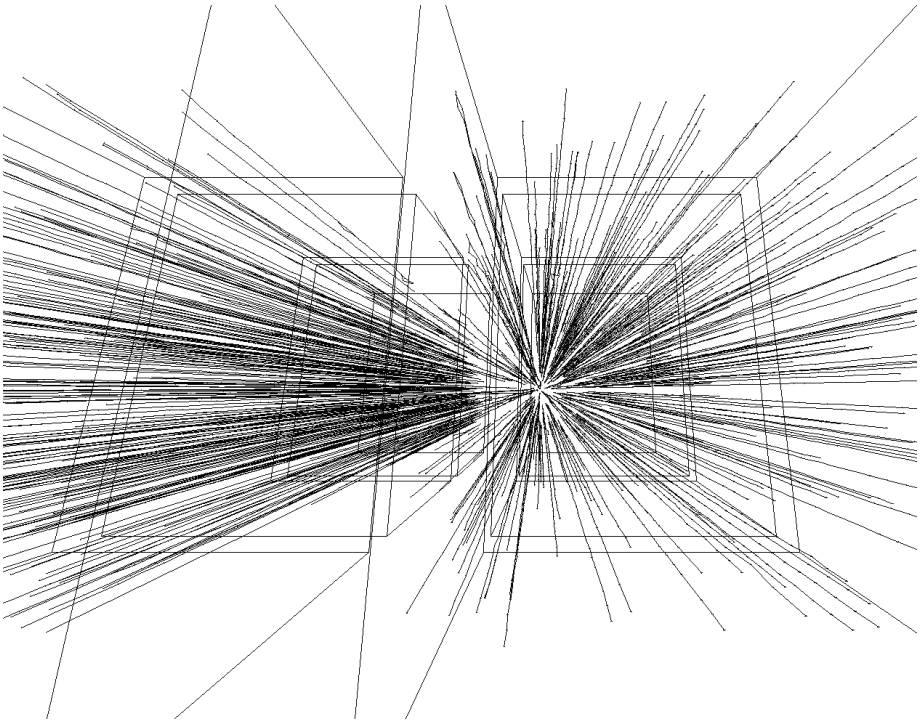

Figure 4.1: Reconstructed tracks in VTPC2.

Cluster Finding and Corrections

The `dipt` client does the cluster finding in all TPCs. On the plane spanned by a pad row and the drift time in raw data coordinates, neighboring pixels containing charge are combined to form a charge cluster. The position of its centre of gravity is converted to the NA49 coordinate system. The true position of the charge underlies several distortions. The drift in the VTPCs does not exactly follow the electric field due to $\boldsymbol{E} \times \boldsymbol{B}$ effects in the regions where the magnetic field is not parallel to the electric field. This is taken care of by the `vt_ncalc` client. Distortions due to inhomogeneities in the electric field are settled in the `edisto` client. Variations in the signal propagation delay between the different channels are corrected by `tpc_calib`.

With the resulting points, a first attempt is made to assemble tracks. A phenomenological correction table is calculated from the remaining systematic position deviations between corrected points and reconstructed tracks [163]. These residuals are small: on the order of 100 μm or up to 500 μm at the edges of TPC sectors. Before the actual tracking, these corrections are applied in the client `tpc_res_corb`.

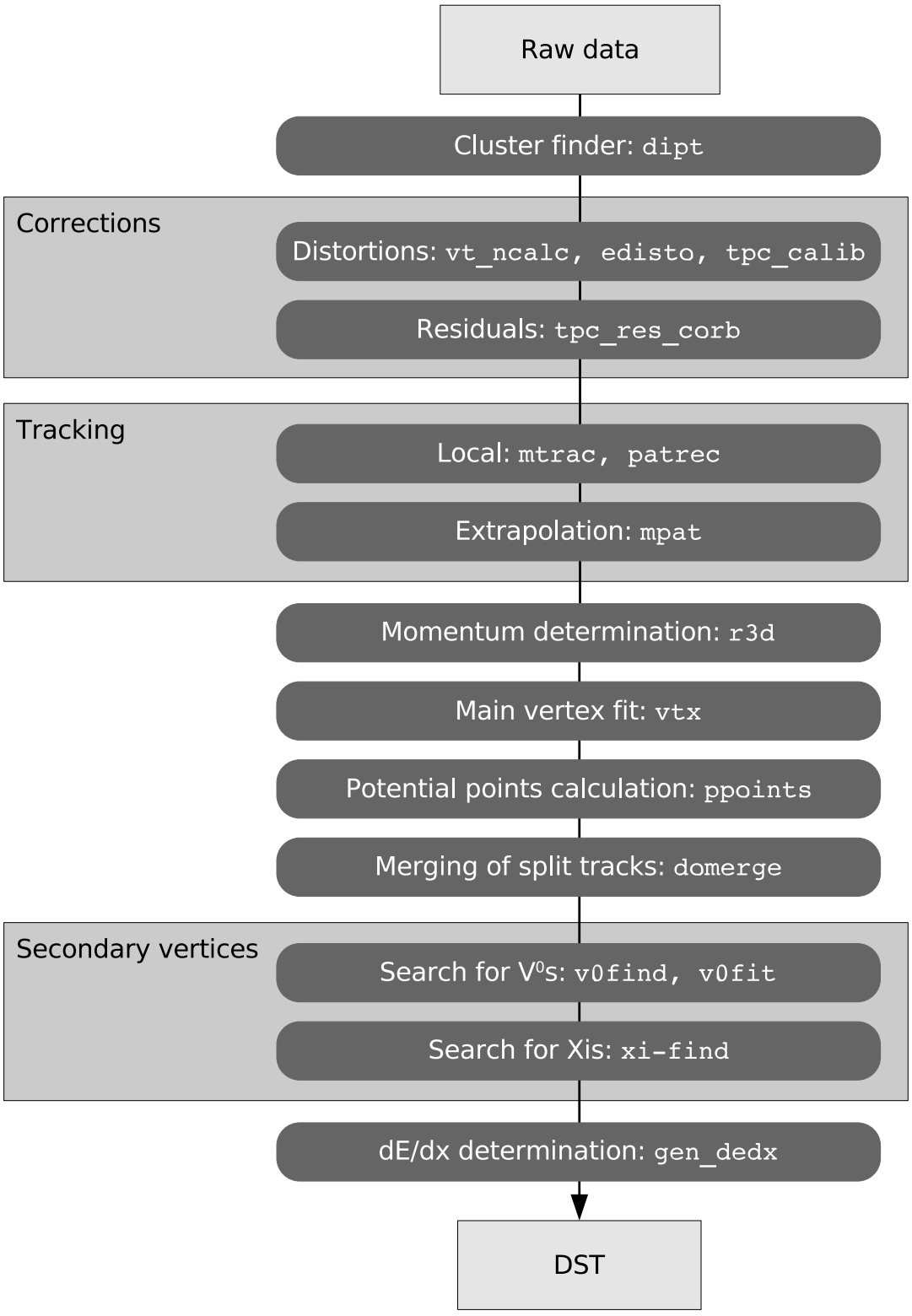

Figure 4.2: Flow chart for the reconstruction chain. The steps of the reconstruction process are depicted together with the involved clients.

Tracking

The environment to form tracks from the space points is different for each TPC. The VTPCs exhibit very high track densities, making it hard to discriminate tracks. But the magnetic field that is present here allows for momentum determination independent of the track's origin. In the MTPCs, tracks are easier to separate. But a particle's momentum can only be calculated with the assumption that the track originates from the main interaction vertex. To make use of the advantages complementing each other, a global tracking scheme has been developed [164]. It subsequently runs local tracking clients to find track parts in a single detector and then connects it to points measured in other TPCs. In the beginning, those tracks that can be easily identified are looked for. The points associated to tracks that have already been found are removed, so the point density decreases. This makes the recognition of more complicated track geometries feasible in the later stages. `mtrac`, the client for the MTPCs, uses straight lines as a track model, while `patrec` for the VTPCs has to describe the particle tracks in the magnetic field by a helical trajectory. The third client involved in the global tracking scheme is `mpat`, doing the extrapolation to other TPCs. Thereby "extrapolation" means calculating the trajectory according to the known magnetic field and attaching measured points to the track that are found close enough to the prediction.

A good knowledge of the magnetic field is essential for the extrapolation and later momentum resolution. Before the installation of the TPCs, the magnetic field was therefore measured with Hall probes, and found to agree with field simulations within 0.5% [139]. The time stability of the field strength was ensured by Hall probe monitors. The lower field used at smaller beam energies could not be measured due to the installed detectors. Here, a calibration could be achieved through a reconstruction of the weak V^0 decays of Λ and K^0_S. Their invariant mass, calculated as introduced in Section A, is extremely sensitive to systematic errors in the momentum determination. The improved calibration of the magnetic field is fed back to the reconstruction chain for a more precise tracking and momentum determination.

The tracking process starts with `mtrac` at the downstream end of the MTPCs, where the track density is the lowest. The tracks found there are extrapolated to VTPC2. The points belonging to those MTPC tracks that do not find matching points in VTPC2 are released to be reused later. On the remaining points in VTPC2, `patrec` performs local tracking and the tracks found thereby are extrapolated to the MTPCs. All tracks are now extrapolated to VTPC1. MTPC tracks, for which points in VTPC1 suggested by

the extrapolation are not found, are discarded and their points released. Local tracking on the remaining VTPC1 points is done, and the tracks found are extrapolated to the MTPCs.

To save the information obtained in the tracking, the DSTs provide two different data structures: `rtrack` and `track`. The first stands for raw track and holds all information about a particle that is independent of assumptions. The position of the particle's first and last point or the number of points (`NPoint`) left in the detectors is stored here along with the momentum at the first measured point that has been calculated by the momentum reconstruction client `r3d` based on the track curvature in the magnetic field. After this first momentum fit, the client `vtx` determines the main vertex position by a fit on the closest approach of all tracks.

This fitted main vertex position is included as the origin of the track, when the momentum is calculated for a second time to be stored in the `track` structure. So, a `track` contains the information about a particle valid under the assumption about its origin. From the `track`, there is always a link to the `rtrack` it is based on. When searching for secondary vertices later on, it is possible to find more `track`s to the same `rtrack`. It is then left to the later analysis to clarify whether a particle comes from the main vertex or a secondary vertex.

For each track, the *impact parameters* `Bx` and `By` are determined. They denote the difference in x and y between the fitted main vertex position and the track's extrapolation back to the target z position. Furthermore, the *number of potential points* (`NMaxPoint`) is calculated by counting how many pad rows were traversed by the reconstructed track. This is the number of points on the track that would have been recorded under ideal circumstances. These values are also stored in the `rtrack` structure.

The tracking is completed by clients that add particle identification information to the tracks like the energy loss measured in the TPCs [165] or the time of flight measured in the TOF detectors [166]. Other clients make sure that the track of one particle has not been identified as two separate tracks [117].

$\mathrm{d}E/\mathrm{d}x$ Calculation

The indispensable basis of the reliable particle identification that is required in this analysis is the calculation and calibration of the $\mathrm{d}E/\mathrm{d}x$ measurement. With each cluster on a track, its total charge content is recorded as a measure for the specific energy loss

$\mathrm{d}E/\mathrm{d}x$. Certain calibrations are needed to correct the measured charge for e.g. baseline shifts, detector effects and drift length dependent charge losses, in order to render the measured cluster charge proportional to the energy loss. The most important effects are briefly discussed in the following, for a more comprehensive list the reader is referred to [117, 167].

- The individual electronic channels are calibrated from a reference energy deposit by injection of radioactive *Krypton* gas (^{83}Kr) into the TPC volume, a method developed in the ALEPH collaboration [168]. Thereby, the amplification factor and the signal propagation of the channels can be determined, the correction is then applied on the raw data.
- A *baseline shift* may arise in a high track density environment resulting from long time tail structures in the pulse shape. The charge restoration on the pads leads to these negative tails that would affect the cluster charge measurement when adding up after multiple tracks. During the reconstruction, the known electronics response is folded into the observed signal to remove the baseline shift and allow a precise determination of the cluster charge [117]. This correction proved to be especially important in course of event-by-event particle identification studies [116, 118].
- Lateral *cross talk effects* are introduced when the gas amplification voltage drops as a consequence of massive gas amplification, an effect with a strong dependence on the track density. It leads to a small gain variation, and a signal induced on neighboring pad rows by recharging currents. A parameterization of the effect is used to correct for it during the determination of the cluster charge [117].
- Parts of the electrons from the drifting charge clouds are absorbed from remaining oxygen impurities in the gas. This leads to a *drift length dependence* of the observed signal.
- The environmental parameters *pressure and temperature* are constantly monitored, as they affect the gas parameters. The temperature is kept constant by an air conditioning envelope around the TPCs, while the measured pressure enters corrections on the cluster charge.

Each resulting corrected and calibrated cluster charge now represents a measurement that is proportional to the energy loss in the gas cell below the traversed pad row, a gas layer of a defined thickness. For gases, the probability distribution of energy loss is not Gaussian, as different energy loss mechanisms contribute. Besides ionization energy loss,

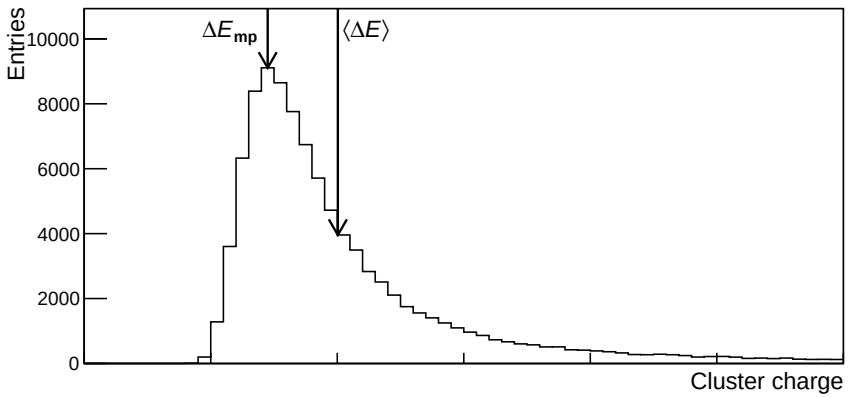

Figure 4.3: Sketch of the Landau distribution governing the energy loss in thin media. The tail to high energy loss values moves the mean of the sample $\langle \Delta E \rangle$ away from the most probable value ΔE_{mp}.

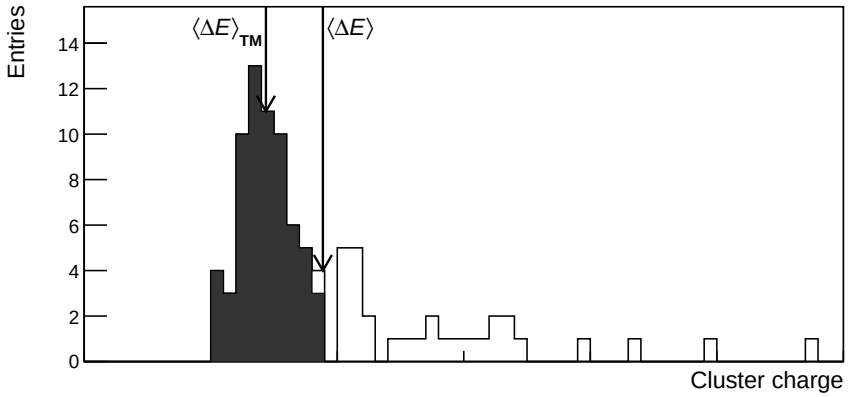

Figure 4.4: The same distribution as in Figure 4.3, sampled only 100 times. The truncated mean $\langle \Delta E \rangle_{\mathrm{TM}}$ is calculated from the grey histogram that is obtained after truncating the top 35% measurements.

where the relativistic particle interacts electromagnetically with the whole gas atom or molecule, direct collisions with electrons lead to the release of a δ-electron connected with a large energy loss. The sampled energy loss ΔE is thus not distributed normally, but follows the Landau distribution [169] depicted in Figure 4.3. The collisional energy loss is represented by the distinct tail to higher ΔE. In the present analysis, the energy loss is sampled between 30 and 90 times along one track, governed by the number of pad rows crossed by the particle trajectory and the resulting number of measured points or charge clusters, respectively. Number of point distributions for the analyzed tracks are shown in Section 5.2. An example for a low statistics sample along the Landau distribution is given in Figure 4.4. The most reliable determination of the parameters of a Landau distribution under the present conditions is the *truncated mean* method. By discarding those 35% of the charge clusters with the highest signal, a more Gaussian distribution shape is obtained. The mean of the resulting distribution, $\langle \Delta E \rangle_{\mathrm{TM}}$, is a good approximation of the most probable energy loss.

The momentum dependence of the truncated mean energy loss proves to be well described by the Bethe-Bloch description of relativistic charged particles propagating through a dilute medium. The parameters specific to detector material and conditions (gas composition, temperature, etc.) are summarized in a phenomenological approach. The width of the distribution around the value expected from the Bethe-Bloch curve is governed by the number of $\mathrm{d}E/\mathrm{d}x$ samples along the track. The $\mathrm{d}E/\mathrm{d}x$ distribution for the tracks selected under the track quality criteria in the present analysis (as defined in Section 5.2) is shown in Figure 5.6. This $\mathrm{d}E/\mathrm{d}x$ information is used in the two PID steps of the present ratio fluctuation analysis, the inclusive fit in distinct phase space bins (see Section 5.3) and the unbinned event-by-event likelihood fit (Section 5.4).

4.3 The Analysis Framework ROOT

ROOT [170, 171] is an object-oriented analysis framework developed in the context of NA49 for the needs of analyses in the fields of heavy ion and high energy physics. On the advent of the LHC experiments and the challenges expected from the analysis of their huge amounts of data, procedure-oriented data analysis software like PAW (Physics Analysis Workstation) were at their limits. Their successor ROOT, implemented in C++, not only proved to be mature enough to deal with the LHC data, but is even used in other fields today. ROOT is available on many platforms.

As a framework, ROOT provides the basic resources a user often needs. These are classes for histograms with their filling, analysis and display methods, mathematical functions with the ability to e.g. do fits to measured distributions and input/output facilities for accessing and storing the data analyzed. Among the collection classes in ROOT the data container *tree* is an important tool to organize the data. Along with ROOT comes the C++ interpreter CINT. C++ basically is a compiled language, but CINT manages to execute scripts at a speed of up to 60% of the compiled version. It can be used both as a command line and as a script interpreter for development, testing or just to generally run shorter programs.

ROOT Mini-DSTs

The evolution of the size of an event in NA49 starts with ≈ 90 Mbyte raw data coming from the detector, and is reduced to 8 Mbyte at the time of recording (see Section 3.7). After reconstruction, in the DSPACK DSTs each event still needs 2–3 Mbyte which is not so easily manageable when analyzing many events. Therefore the DSTs are converted to *ROOT mini-DSTs*, which only contain the most relevant information, but on the other hand only need 150-200 kbyte per event. In each mini-DST, the information is arranged as a ROOT tree, making it easily accessible during analysis.

All produced mini-DSTs together make up a data volume of 1.35 Tbyte. They are stored in CASTOR like the DSTs, but are kept permanently staged in a special pool, making sure that they are always accessible for analysis without the delay caused by recalling from tape.

ROOT49

ROOT was extended to *ROOT49* [172] through the addition of the *T49* classes specific to NA49. The T49 classes are subdivided into

- Mini-DST Classes (T49DST) for the storage of the information extracted from the DSTs in the mini-DST tree. Examples are `T49ParticleRoot` for holding the most important data from the DSPACK `track` structure (see Section 4.2), or `T49VertexRoot` for storing the information about vertices e.g. V^0s.
- Analysis Classes (T49ANA) providing tools for the mini-DST analysis like applying cuts or analyzing $\mathrm{d}E/\mathrm{d}x$ information.

- DSPACK Interface Classes (TRootDS) allow the access to DSPACK DSTs and can be used when copying the information from them to mini-DSTs.

The abilities of ROOT49 in connection with the small size of the mini-DSTs are the prerequisite to analyze a large number of events in a reasonable time. The datasets used in this analysis (consisting of 100k-200k events) require $\approx$ 80 Gbyte space and can be analyzed within a day on the lxbatch cluster (see Section 4.1).

Chapter 5

Data Analysis

Focus of this thesis is to measure the event-by-event fluctuations of the $(K^+ + K^-)/(p + \overline{p})$ and K^+/p ratios in central Pb+Pb collisions at the five energies of the SPS energy scan (cf. Section 3.2). The event-by-event hadron ratio analysis has been sketched in Section 2.1, and its details will be presented in this chapter. It is based on a method developed in [115, 116] and relies on the dE/dx measurement in the NA49 TPCs (cf. Section 3.5). In a first step, it requires an inclusive particle identification that is described in Section 5.3. The information extracted in this inclusive analysis is then used in the event-by-event analysis as explained in Section 5.4. The first analysis step however is the choice of datasets and the selection of events to be analyzed. For the event selection, the relevant criterion is the collision centrality. While the experimental foundations for this have been laid out in Section 3.4, the procedure for the present analysis is described in Section 5.1. After all analysis ingredients have been introduced, Section 5.7 can go into the detailed systematic checks that were applied to evaluate the significance of the analysis results. A systematic error is obtained for $\sigma_{\mathrm{dyn}}\left((K^+ + K^-)/(p + \overline{p})\right)$ and $\sigma_{\mathrm{dyn}}\left(K^+/p\right)$.

5.1 Selection of Central Pb+Pb Collisions

At all five energies, the 3.5% most central collisions were selected. This is the same choice as for the analysis of $(K^+ + K^-)/(\pi^+ + \pi^-)$ and $(p + \overline{p})/(\pi^+ + \pi^-)$ fluctuations [118]. It is justified by the considerations to minimize volume fluctuation effects given in Chapter 2, and at the same time retaining sufficient statistics for a significant measurement. In a Glauber Monte Carlo model [173, 174], the selected centrality interval corresponds to an average of 367 participating nucleons and an impact parameter range $b < 2.75$ fm.

$\sqrt{s_{NN}}$	beam energy	dataset	E_{Veto} cut	statistics
6.3 GeV	20A GeV	03A	777.344	196k
7.6 GeV	30A GeV	02J	1227.34	179k
8.7 GeV	40A GeV	00W	1218.75	195k
12.3 GeV	80A GeV	01E	9593.75	142k
17.3 GeV	158A GeV	00B	8093.75	115k

Table 5.1: Overview of analyzed datasets from the NA49 energy scan.

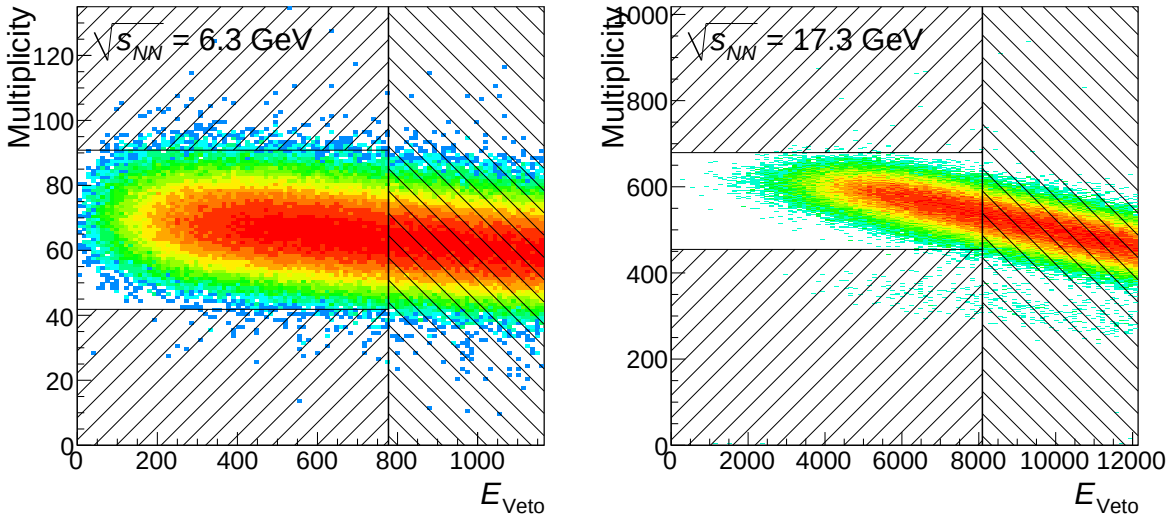

Figure 5.1: The correlation between calibrated E_{Veto} and multiplicity of tracks meeting the quality criteria defined in Section 5.2. Hashed areas indicate events rejected by centrality and multiplicity cuts.

The veto calorimeter (see Section 3.4) is used for this selection. The used datasets have been recorded with an online veto calorimeter cut, and this trigger setting accepted the 7% (10% for $\sqrt{s_{NN}} = 17.3$ GeV) most central events (cf. Table 3.1). An offline cut on E_{Veto} further constrained the event sample to the common centrality of 3.5%. The standard method is to apply the time dependent correction method introduced in [156]. Data sets used in this analysis are summarized in Table 5.1, where also the cut value on the calibrated veto energy is given. The time dependence does not play a strong role in the central region. The analysis has been repeated using centrality selection without time dependent veto calorimeter calibration. No effect on the fluctuation signal was observed.

The correlation between multiplicity used in the present analysis and the calibrated veto energy is shown in Figure 5.1 for $\sqrt{s_{NN}} = 6.3$ and 17.3 GeV. The calibrated E_{Veto} cut as defined in Table 5.1 is indicated by a vertical line. In addition, a multiplicity event cut was applied. The horizontal lines show the events that deviate more than three σ from the mean of the multiplicity distribution. The effect of this multiplicity cut is small, but it was taken into account in the systematic error determination as described in Section 5.7.

5.2 Track Selection Quality Criteria

The charged hadron tracks used in the present analysis have to persist under a set of quality criteria. They are chosen such that the $\mathrm{d}E/\mathrm{d}x$ quality required in the event-by-event analysis is given. This is made sure by requiring measured points in one of the main TPCs with their large sampling length and good $\mathrm{d}E/\mathrm{d}x$ resolution. The ROOT mini-DSTs store the number of measured points in the variable `NPoint(i)`, where the index `i` denotes the TPC chamber: `i = 0` for VTPC1, `1` for VTPC2 and `2` for the MTPCs. If `i` is omitted, `NPoint()` stands for global points in all TPCs. The same TPC number conventions hold for the variable `NMaxPoint(i)`, which denotes the number of potential points the track could achieve under ideal conditions (e.g. low track density). It is calculated in the course of the reconstruction as the number of pad planes crossed by the extrapolated track. Potential point information can be used to avoid split tracks, where one physical particle trace is interpreted as two separate tracks in two sub-detectors.

For the interpretation of the results, it is also important to make sure primary tracks are studied, not decay products stemming from secondary decay vertices. This can be ascertained by a cut on the pointing accuracy of a track toward the main vertex. The x

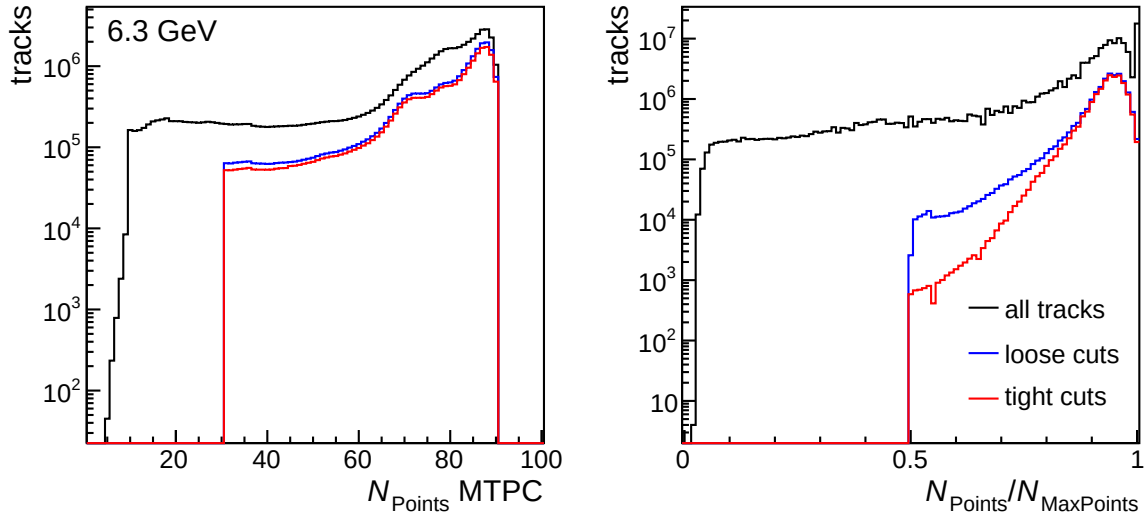

Figure 5.2: Distribution of the number of measured points in the MTPCs (left) and the ratio of measured to potential points in all TPCs. This figure is for Pb+Pb collisions at $\sqrt{s_{NN}} = 6.3$ GeV.

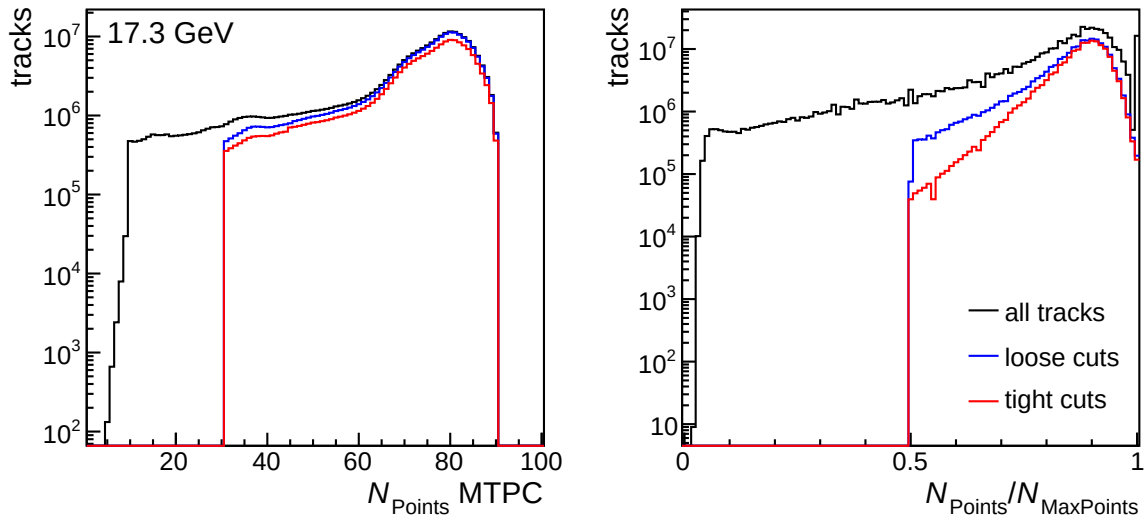

Figure 5.3: Distribution of the number of measured points in the MTPCs (left) and the ratio of measured to potential points in all TPCs. This figure is for Pb+Pb collisions at $\sqrt{s_{NN}} = 17.3$ GeV.

and y coordinate of the track extrapolation to the target plane are stored in the `Bx` and `By` variables.

Throughout the analysis, two different sets of cuts are used to study the effect of track quality variations. They have also been used in other analyses [118, 106]. The

less restrictive of the two sets is denoted *loose* track cuts and comprises the following requirements:

- `(NPoint(2) > 30)`
  More than 30 measured points in the MTPCs. A track that traverses the whole length of a MTPC can leave a maximum of 125 points (one per pad row). This cut assures the $\mathrm{d}E/\mathrm{d}x$ quality.
- `(NMaxPoint() > 0)`
  At least one potential point in any detector, as a consistency check in the tracking.
- `(NPoint()/NMaxPoint() > 0.5)`
  A ratio of measured to potential points larger than 50% avoids split tracks.

The *tight* set of cuts applies the loose cuts and additionally

- `(NMaxPoint(0) >= 10 || NMaxPoint(1) >= 10 || NMaxPoint(2) >= 30)`
  At least 10 potential points in a VTPC or 30 in a MTPC.
- `(NPoint(i)/NMaxPoint(i) > 0.5)`
  Measured to potential point ratio larger than 50% *in that TPC*.
- `(Bx < 4.0 cm, By < 0.5 cm)`
  Requiring a close approach to the primary vertex suppresses secondary decay particles.
- `!(particle->GetIflag() & 0xF000000)`
  Accept only tracks that receive a flag during the reconstruction as fitted to the main vertex.

The impact of the different cut sets is illustrated in Figures 5.2–5.5. The number of point (and ratio) distributions are shown in Figures 5.2 and 5.3 for $\sqrt{s_{NN}} = 6.3$ and 17.3 GeV. Here, the left panel shows `NPoint(2)`, the number of MTPC points that is important for the PID quality. The right panels show the ratio `NPoint()/NMaxPoint()` that is an important indicator to avoid split tracks. The track impact parameters before and after cuts are shown in Figures 5.4 and 5.5. Likewise the highest and lowest energy are shown as an example. The loose set of track cuts already narrows down the `Bx` and `By` distributions without explicitly regarding them. Nevertheless the required track quality leads to a better pointing accuracy. The tight track cuts directly exclude the larger impact parameter tracks, an implicit check of the potential influence from secondary

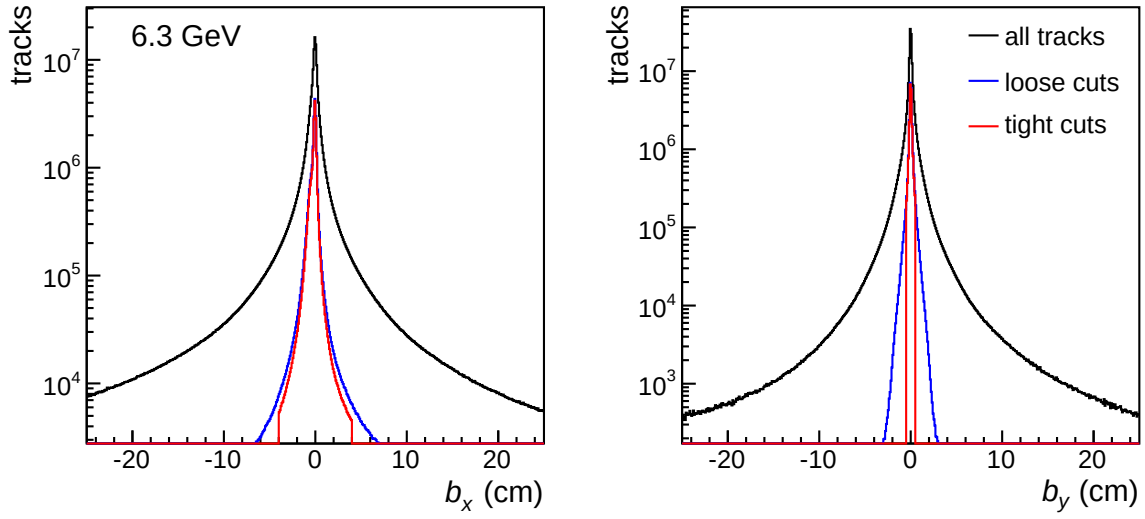

Figure 5.4: Distribution of the track impact parameters `Bx` (left) and `By` (right) in Pb+Pb collisions at $\sqrt{s_{NN}} = 6.3$ GeV.

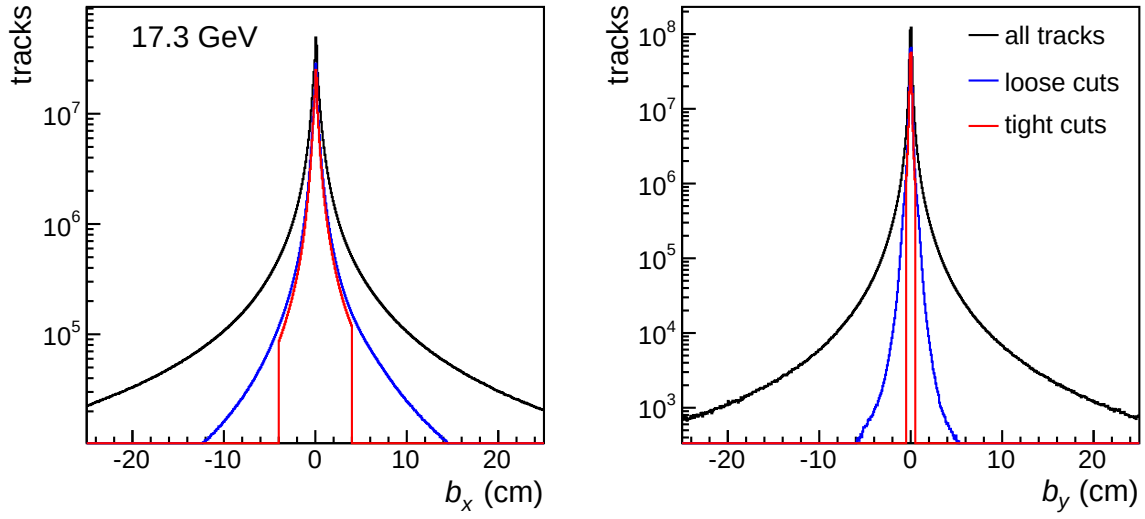

Figure 5.5: Distribution of the track impact parameters `Bx` (left) and `By` (right) in Pb+Pb collisions at $\sqrt{s_{NN}} = 17.3$ GeV.

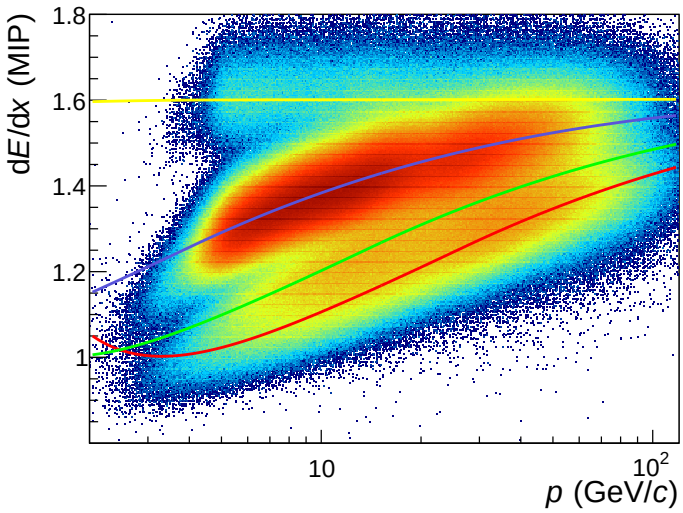

Figure 5.6: Differential energy loss ($\mathrm{d}E/\mathrm{d}x$) in the relativistic rise region for hadrons produced in Pb+Pb collisions at $\sqrt{s_{NN}} = 17.3$ GeV measured in the NA49 TPCs as a function of total momentum. The track selection criteria presented in Section 5.2 have been applied, and the restriction to tracks with MTPC information affects low momentum particles, as described in Section 3.6. The colored lines indicate the predicted $\mathrm{d}E/\mathrm{d}x$ values for electrons (yellow), pions (blue), kaons (green) and protons (red).

tracks. As shown in Section 5.7, the fluctuation results only vary modestly under this track cut variation, indicating that secondary particles do not contribute to the signal.

5.3 Inclusive $\mathrm{d}E/\mathrm{d}x$ Particle Identification

NA49 $\mathrm{d}E/\mathrm{d}x$ analysis is carried out in the relativistic rise region of the Bethe-Bloch description of differential energy loss, as illustrated in Figure 5.6. The $\mathrm{d}E/\mathrm{d}x$ information extracted from the TPC measurements described in Section 4.2 follows the Bethe-Bloch formula with suitable parameters for the NA49 environment [175, 117]. $\mathrm{d}E/\mathrm{d}x$ thus depends on the velocity β. The conversion $\beta \rightarrow p$ according to equation (A.2) leads to a separation by mass when $\mathrm{d}E/\mathrm{d}x$ is plotted as a function of total momentum p as can be seen in Figure 5.6.

Despite the good $\mathrm{d}E/\mathrm{d}x$ resolution of the NA49 TPCs, the distributions for different particle species overlap. An unfolding is however possible using statistical methods. This is even more pronounced when going to a finer partition of phase space. For this reason,

Variable	Minimum	Maximum	Bins	Bin size
Charge q	-1	+1	2	-
Total momentum p:				
for $\sqrt{s_{NN}} \leq 8.7$ GeV	1.0 GeV/c	40.0 GeV/c	20	Logarithmic
for $\sqrt{s_{NN}} > 8.7$ GeV	2.0 GeV/c	120.0 GeV/c	20	Logarithmic
Transverse momentum p_{T}	0.0 GeV/c	2.0 GeV/c	10	0.2 GeV/c
Azimuthal angle ϕ	0.0	2π	8	$\pi/4$

Table 5.2: Binning of the dE/dx containers. The first three p bins are not used in the analysis due to too strong overlap of the distributions.

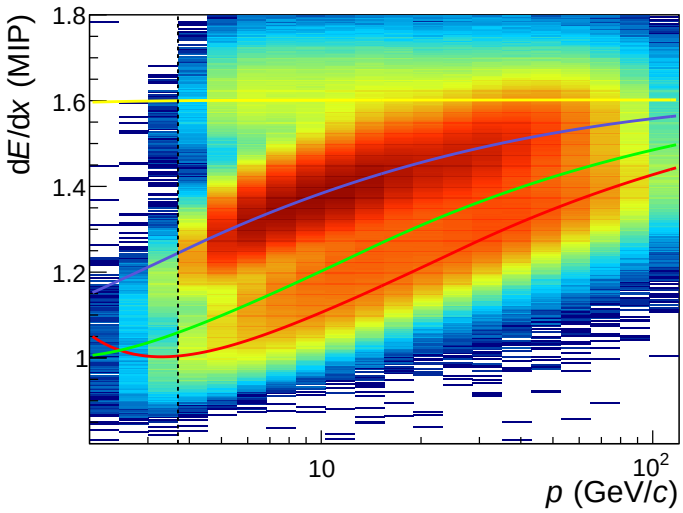

Figure 5.7: The dE/dx) distribution from Figure 5.6 in the logarithmic momentum binning described in the text. The black, dashed line indicates the low momentum cutoff used in the analysis.

the tracks that fulfill the quality criteria defined above are prepared for the inclusive $\mathrm{d}E/\mathrm{d}x$ analysis by filling them into *containers*, with the four-dimensional binning defined in Table 5.2. In addition to the total momentum p, a distinction by charge q, transverse momentum p_T and azimuthal angle ϕ, as defined in Section A applies. The bin size in p increases exponentially. The resulting binning, and the phase space coverage of NA49 is illustrated in Figures 5.7, 5.9, 5.10 and 5.11. Due to the TPC layout, the azimuthal acceptance develops two wedges at higher p_T, what can be seen in Figure 5.9.

For the inclusive particle identification, the measured $\mathrm{d}E/\mathrm{d}x$ distribution in each bin is now described by four single particle functions. A Gaussian shape is assumed for each particle m (where $m \in \{\mathrm{e}, \pi, \mathrm{K}, \mathrm{p}\}$ runs over the considered particles electrons, pions, kaons and protons):

$$f'_m\left(\mathrm{d}E/\mathrm{d}x\right) = A_m \exp\left(-\frac{\left(\left(\mathrm{d}E/\mathrm{d}x\right) - \langle \mathrm{d}E/\mathrm{d}x\rangle_m\right)^2}{2\sigma_m^2}\right), \tag{5.1}$$

with a normalization factor A_m. The width scales with the mean $\mathrm{d}E/\mathrm{d}x$ value, according to:

$$\sigma_m^2 = \langle \mathrm{d}E/\mathrm{d}x\rangle_m^{(2\alpha)} \cdot \sigma_\mathrm{gen}^2. \tag{5.2}$$

The scaling factor has been evaluated to best describe the data with a value of $\alpha = 0.65$. The total $\mathrm{d}E/\mathrm{d}x$ distribution can now be described by the sum of four Gaussian distributions with nine free parameters. They comprise four positions $\langle \mathrm{d}E/\mathrm{d}x\rangle_m$, four normalization factors A_m and the generic width σ_gen^2. A χ^2 minimization is applied to each container bin to extract these nine parameters.

A careful analysis makes sure that the fit gives reliable results in all phase space domains. One example is shown in Figure 5.8, where positive and negative particles in the phase space bin $11.00 < p < 13.23$ GeV/c, $0.4 < p_\mathrm{T} < 0.6$ GeV/c and $\pi < \phi < 5\pi/4$ are compared. Protons dominate the positive particles in this example. Practically no antiprotons are present in the negative track sample, making the kaon peak well visible here. The TPC response is independent of the charge so that the $\langle \mathrm{d}E/\mathrm{d}x\rangle_m$ for a phase space bin can be determined in the q bin where it is better constrained. In this case, the proton peak position is determined from the positive tracks, while the kaon parameter is determined in the negative sample. For pions and electrons, both signs contribute. It is obvious from Figure 5.8 that the separation of kaons represents a very delicate task.

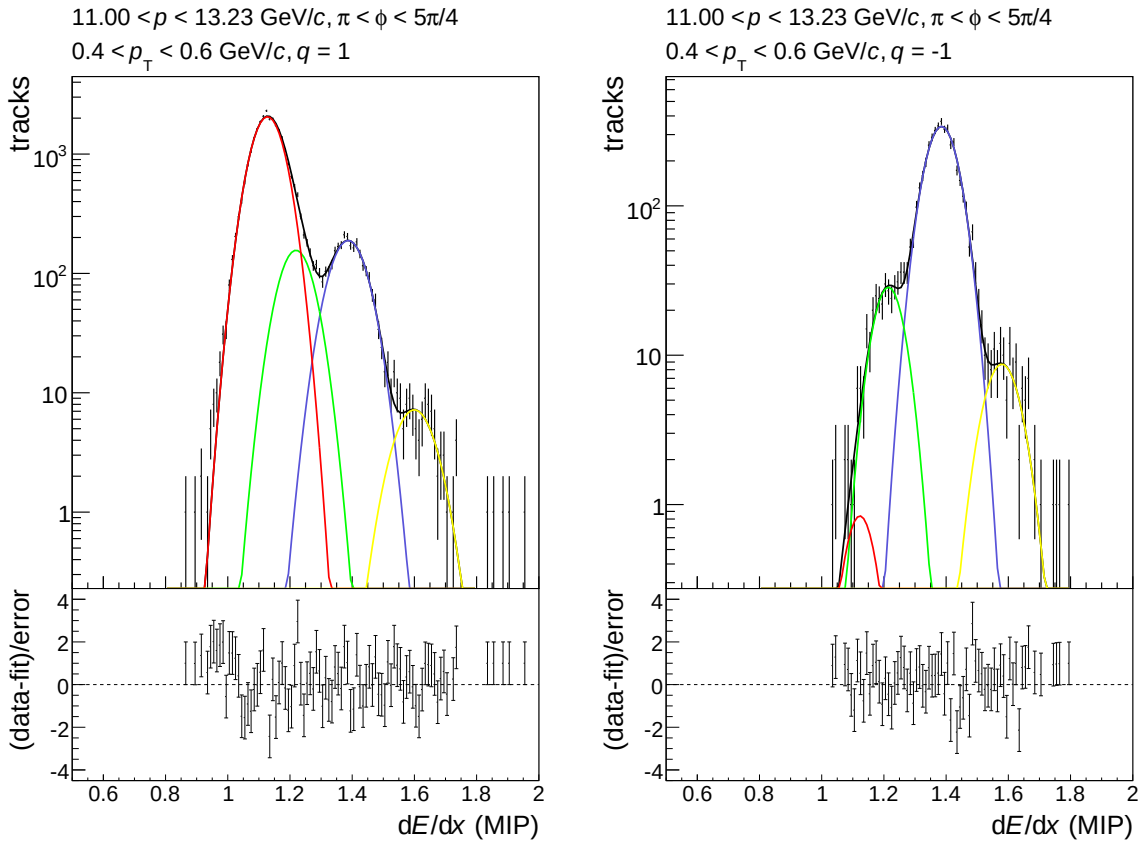

Figure 5.8: Exemplary inclusive $\mathrm{d}E/\mathrm{d}x$ fit in one phase space bin at $\sqrt{s_{NN}} = 6.3$ GeV. The positive particles (left) are dominated by protons, while among the negative particles (right), pions are the most abundant. Antiprotons play no role at this energy.

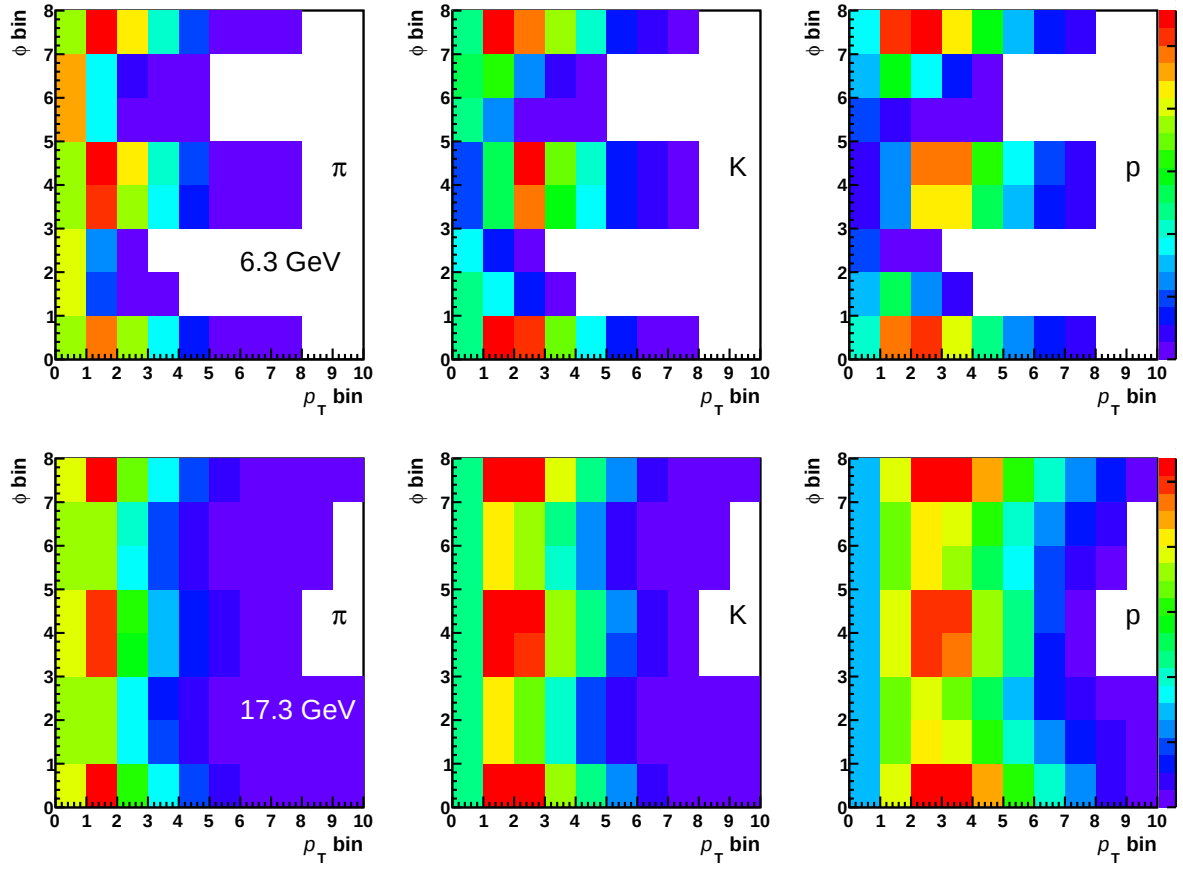

Figure 5.9: The distribution of pions, kaons and protons in p_{T} vs. azimuthal angle ϕ bins from the inclusive $\mathrm{d}E/\mathrm{d}x$ fit at $\sqrt{s_{NN}} = 6.3$ and 17.3 GeV. The wedge structure of the NA49 TPCs is visible here.

To ensure the convergence of the χ^2 fit, a minimum number of 3000 tracks are required. This criterion imposes a statistical limit on the acceptance. This is e.g. the limiting factor at high p_{T}, where the geometrical acceptance is not limited, but the statistics decline exponentially. The exact acceptance thus depends on the analysis method. For this reason, an acceptance table has been prepared for the publication of the results on $(\mathrm{K}^+ + \mathrm{K}^-)/(\pi^+ + \pi^-)$ and $(\mathrm{p} + \overline{\mathrm{p}})/(\pi^+ + \pi^-)$ fluctuations [118], and the present analysis on $(\mathrm{K}^+ + \mathrm{K}^-)/(\mathrm{p} + \overline{\mathrm{p}})$ and K^+/p fluctuations was conducted in the same acceptance. Systematic checks on the results included variations of the acceptance and of the track selection criteria. The resulting variations are included in the systematic errors as presented in Section 5.7. For model comparisons, the acceptance tables are available in electronic format [176].

An overview of the acceptance can be obtained from Figures 5.9, 5.10 and 5.11. They also provide the first result of the inclusive PID method. Figure 5.9 shows the distribution

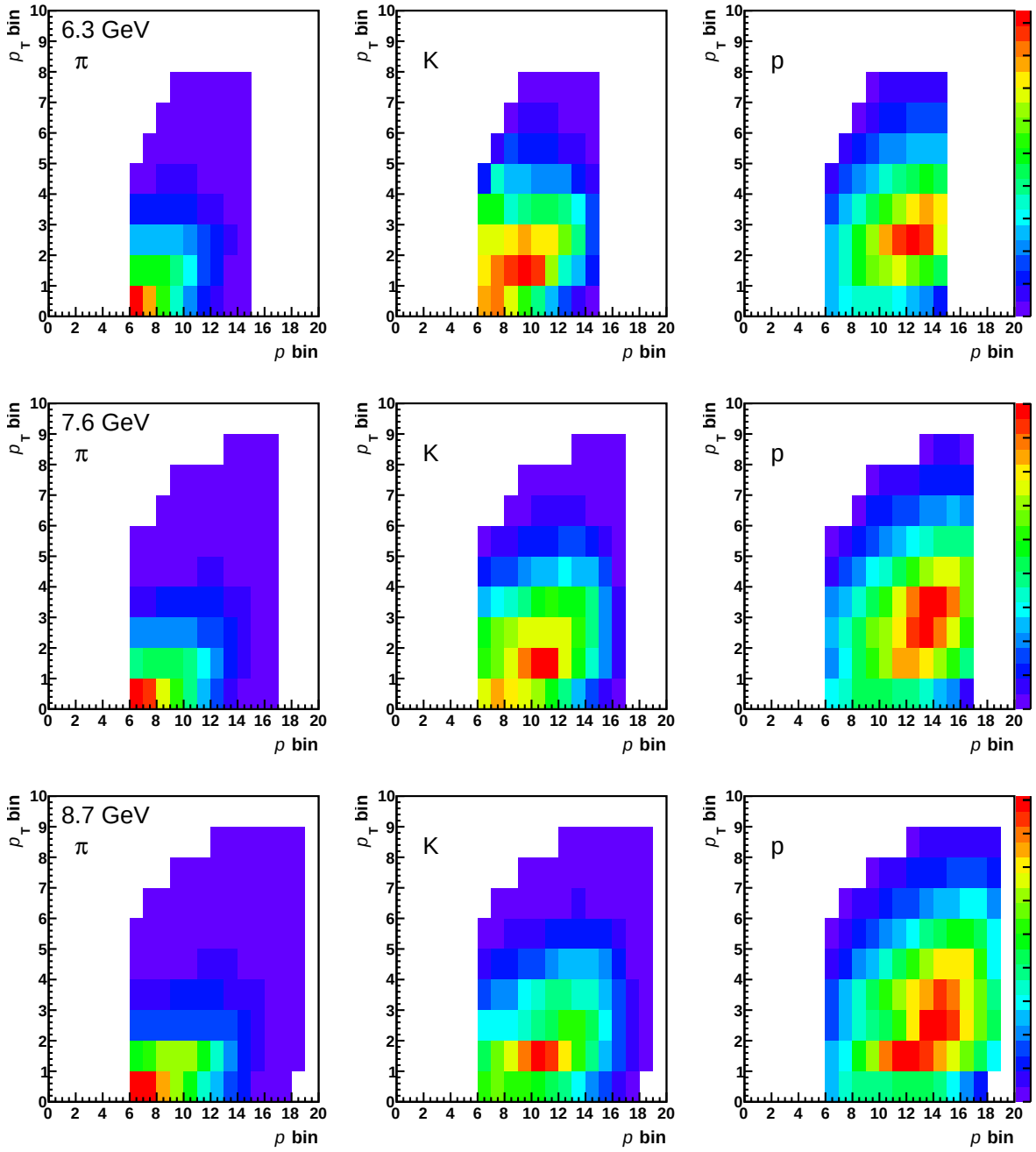

Figure 5.10: Distribution of pions, kaons and protons in p vs. p_{T} bins, as extracted in the inclusive $\mathrm{d}E/\mathrm{d}x$ fit. The shown, lower energies use the range 1 GeV $< p <$ 40 GeV, as described in Table 5.2.

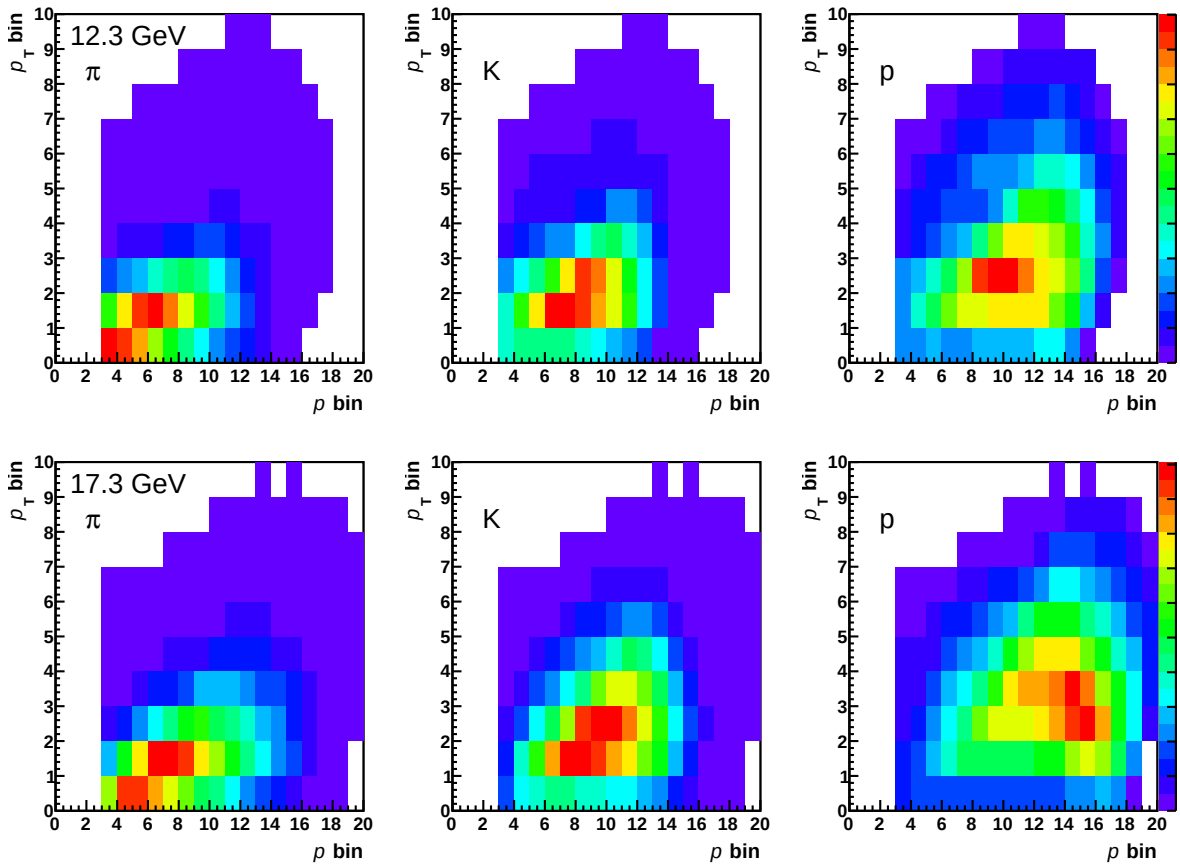

Figure 5.11: Distribution of pions, kaons and protons in p vs. p_{T} bins, as extracted in the inclusive $\mathrm{d}E/\mathrm{d}x$ fit. The shown, higher energies use the range 2 GeV $< p <$ 120 GeV, as described in Table 5.2.

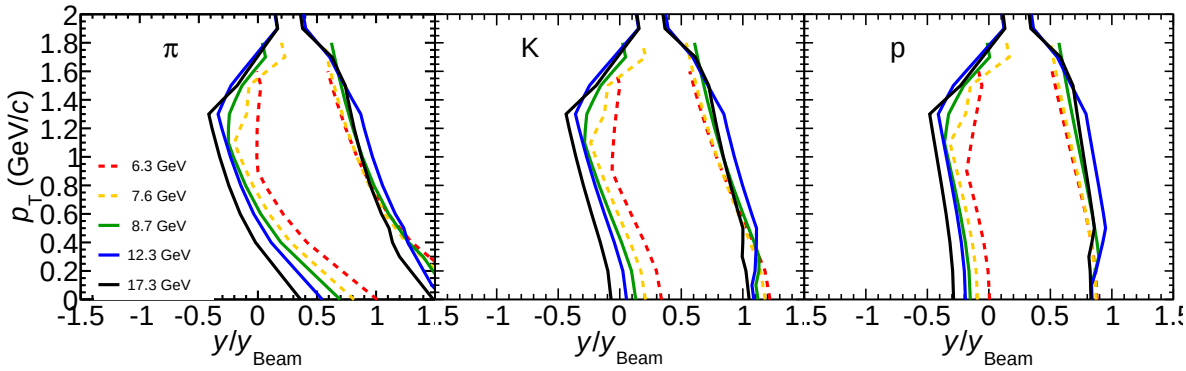

Figure 5.12: The acceptance used in the present analysis as a function of transverse momentum p_T and the center-of-mass rapidity y, normalized by the corresponding beam rapidity y_{Beam}, for all analyzed energies. Phase space regions in which particles can be identified are delimited by lines. Limitations result from geometric acceptance and the available statistics, the latter dominating at large momenta p and transverse momenta p_T [64].

of pion, kaon and proton yields in p_T vs. ϕ bins at $\sqrt{s_{NN}} = 6.3$ and 17.3 GeV. At high p_T, the wedge geometry of the NA49 TPCs becomes visible, with a better acceptance in the bending plane of the magnetic field (close to $\phi = 0$ and $\phi = \pi$) than perpendicular to it. This result is not directly comparable to data on pion, kaon and proton production published by NA49, as in the present event-by-event study, no corrections for acceptance, efficiency or feed-down apply.

Looking at the p vs. p_T distributions in Figures 5.10 and 5.11, the changing beam momentum becomes visible: the peak of produced particles moves through phase space along with the center of mass (note that the lower energies shown in Figure 5.10 have a different p binning compared to the higher energies in Figure 5.11). The acceptance relative to the center of mass however stays relatively constant, as the magnetic field of the NA49 vertex magnets was adjusted proportionally to the beam momentum (see Section 3.2). For Figure 5.12, the acceptance limits from Figures 5.10 and 5.11 were converted to the center-of-mass system according to Section A. The momentum limits were also converted to rapidity under different mass assumptions for pions, kaons and protons. At all energies, a similar portion of the produced particles is accepted, ranging from the center of mass (midrapidity) to forward rapidities. The kinematic range of the beam is not within the acceptance, a fact that can be seen on the proton rapidity panel (right) of Figure 5.12.

The acceptance can also be illustrated using a model. Pb+Pb collisions have been simulated in the hadronic transport model UrQMD [92, 93, 94] for the same energies and

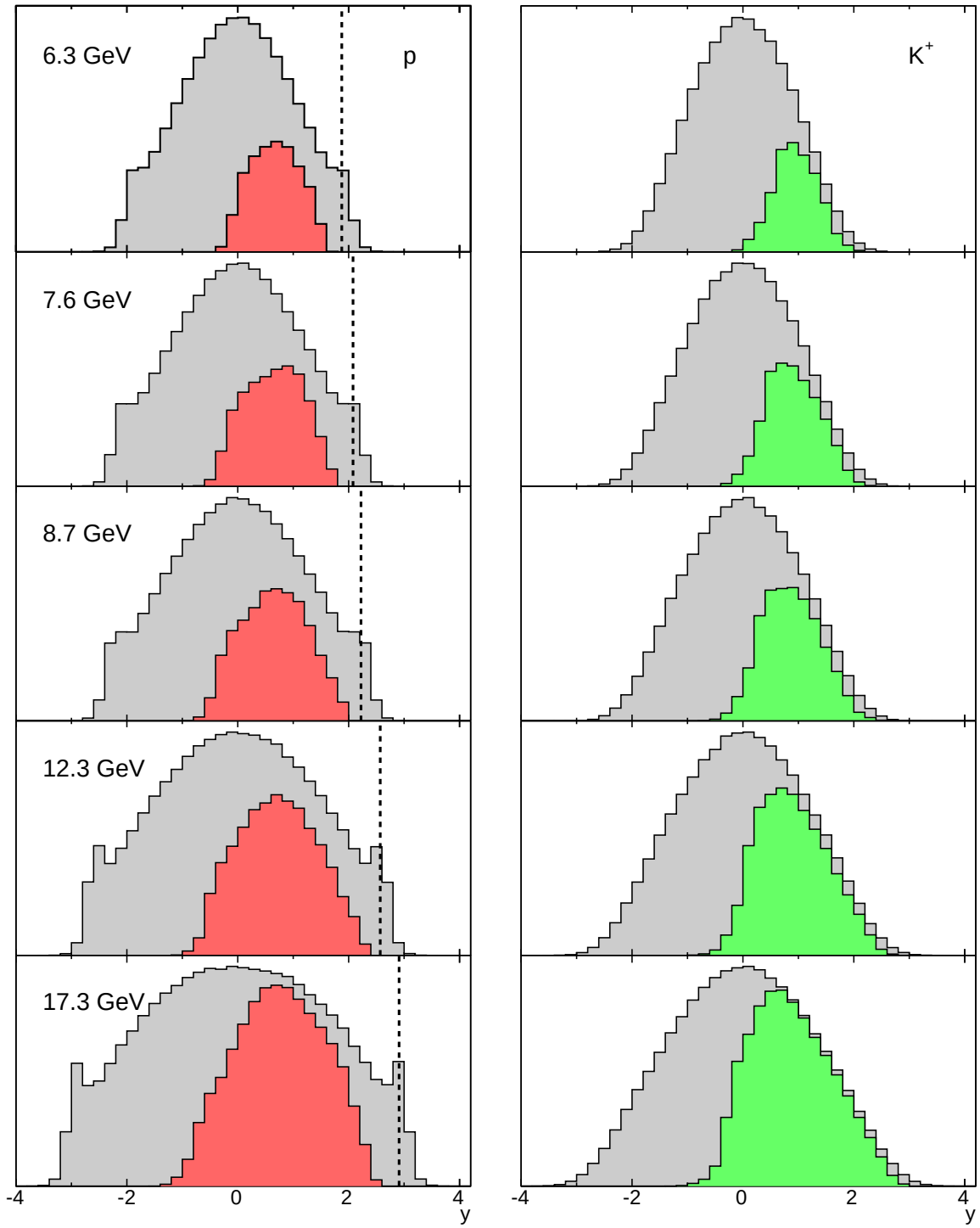

Figure 5.13: The NA49 acceptance as tabulated in [176], evaluated using the hadronic transport model UrQMD. The grey histograms represent the unaffected rapidity distribution from the model, while the colored histograms show the accepted particles. Vertical lines indicate beam rapidity.

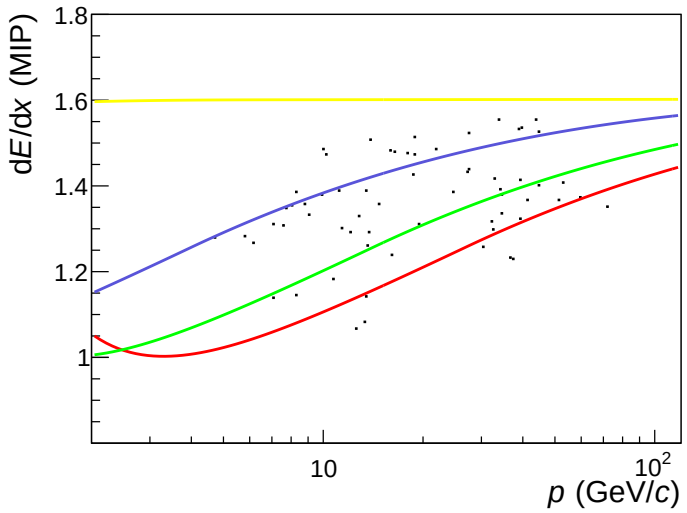

Figure 5.14: The dE/dx distribution from Figure 5.6 for a single Pb+Pb event at $\sqrt{s_{NN}}$ = 17.3 GeV.

centrality as in the data analysis. Here, the full phase space distribution of identified particles can be compared to that of particles within the experimental acceptance. For the model study, the acceptance tables [176] were used. The resulting rapidity distributions for protons and positive kaons is shown in Figure 5.13 for all five energies. The largest part of the forward rapidity hemisphere is covered, missing parts are due to the incomplete ϕ coverage. The beam rapidity is also indicated in the figure and can be seen as a slight peak in the proton distribution, however is not covered by the acceptance.

The aim of this thesis is the event-by-event extraction of proton and kaon yields. Average multiplicities for these particles are listed in Table 1.1 on page 21. It is obvious that in single events, the binned χ^2 fit method introduced in this section will not work. To make full use of the available information, an unbinned likelihood fit is used and will be explained in the next section.

5.4 Event-by-Event Particle Identification

Under the track quality criteria required for reliable particle identification, a single event only provides a multiplicity between 60 (at $\sqrt{s_{NN}}$ = 6.3 GeV) and 600 ($\sqrt{s_{NN}}$ = 17.3 GeV). The distribution of dE/dx measurements in a single event is sketched in Figure 5.14. Out of the potentially 3,200 container bins (cf. Table 5.2), the phase space within the NA49 acceptance covers between 500 and 1,500 bins. A χ^2 fit to less than one particle

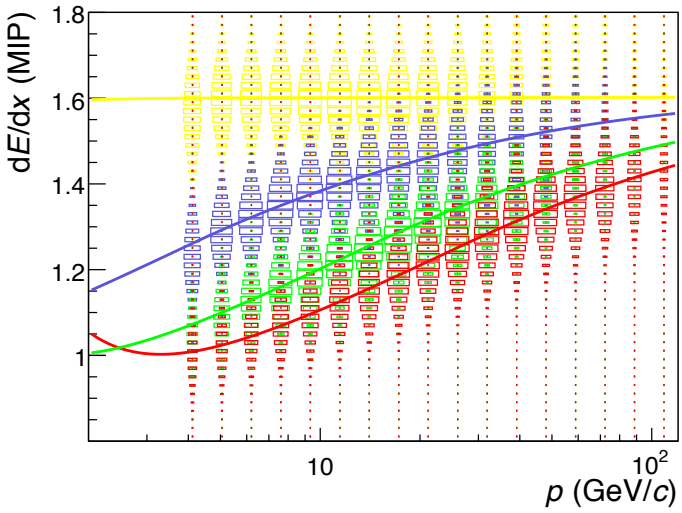

Figure 5.15: Normalized probability distributions as extracted from the inclusive $\mathrm{d}E/\mathrm{d}x$ fit.

per bin is excluded. Therefore, the unbinned likelihood method [116, 115] as introduced in Section 2.1 is used.

It builds on the outcome of the inclusive fit from Section 5.3. The parameters of the fit functions in all of the analyzed bins describe the probability distribution of identified particles in $\mathrm{d}E/\mathrm{d}x$ and phase space. Through a normalization, probability density functions (PDFs) can be constructed. Overall, the PDFs depend on six parameters and variables: The three kinematic variables p, p_T and ϕ are summarized as $\boldsymbol{p} = (p, p_\mathrm{T}, \phi)$ for brevity. Furthermore the electric charge q, the particle identity m and the energy loss $\mathrm{d}E/\mathrm{d}x$. A two-dimensional projection of the PDFs is shown in Figure 5.15. An integral over p_T, ϕ and q was made to produce this representation in p vs. $\mathrm{d}E/\mathrm{d}x$. All four distributions for electrons, pions, kaons and protons have similar amplitudes due to the normalization.

For the analysis, the overall probability density is factorized into two parts, a $\mathrm{d}E/\mathrm{d}x$ distribution and a momentum distribution. The former is produced in each container bin by normalization of equation (5.1) for each particle m. This PDF is denoted $f_{m,\boldsymbol{p},q}\left(\mathrm{d}E/\mathrm{d}x\right)$ and is based on the good knowledge of the $\mathrm{d}E/\mathrm{d}x$ distribution and its reliable description by the parameters $\langle \mathrm{d}E/\mathrm{d}x \rangle_m$ and σ_m^2 in each bin. The momentum distribution of the particles constitutes the second part and is based on the bin-by-bin weights A_m extracted in the inclusive fit. The relative momentum distribution is maintained, but the total multiplicity is normalized to one in order to construct the momentum PDF $F_m\left(\boldsymbol{p_i}, q\right)$.

To summarize, the probability distribution of particle species m is given by

$$P_m\left(\boldsymbol{p}, q, \mathrm{d}E/\mathrm{d}x\right) = F_m\left(\boldsymbol{p}, q\right) f_{m,\boldsymbol{p},q}\left(\mathrm{d}E/\mathrm{d}x\right). \tag{5.3}$$

The normalization makes sure that the integral over $\boldsymbol{p}$, q and $\mathrm{d}E/\mathrm{d}x$, $\int P_m = 1$. For the upcoming event-by-event PID fit, a parameter set $\boldsymbol{\Theta} = \left(\Theta_\mathrm{e}, \Theta_\pi, \Theta_\mathrm{K}, \Theta_\mathrm{p}\right)$ is introduced. It describes the relative abundances Θ_m of the hadron species in the event. It is secured that $\sum_m \Theta_m = 1$. A measured particle is represented by the vector $X_i = (\boldsymbol{p}_i, q_i, \mathrm{d}E/\mathrm{d}x_i)$ of its measured quantities. The probability that a single particle is described with a chosen set of parameters $\boldsymbol{\Theta}$ is

$$Q\left(X_i, \boldsymbol{\Theta}\right) = \sum_m \Theta_m P_m\left(\boldsymbol{p}_i, q_i, \mathrm{d}E/\mathrm{d}x_i\right) = \sum_m \Theta_m F_m\left(\boldsymbol{p_i}, q_i\right) f_{m,\boldsymbol{p}_i,q_i}\left(\mathrm{d}E/\mathrm{d}x_i\right). \tag{5.4}$$

The aim of the event-by-event PID fit is to determine the parameter set $\boldsymbol{\Theta}$ that best describes all particles in the event at the same time. The event is represented by the set of its n particles, $X = \{(\boldsymbol{p}_1, q_1, \mathrm{d}E/\mathrm{d}x_1), \ldots, (\boldsymbol{p}_n, q_n, \mathrm{d}E/\mathrm{d}x_n)\}$. The *likelihood function* L is obtained by multiplying the probabilities $Q\left(X_i, \boldsymbol{\Theta}\right)$ of the n particles in the event (recall that the average multiplicity ranges from $\langle n \rangle \approx 60$ at $\sqrt{s_{NN}} = 6.3$ GeV to $\langle n \rangle \approx 600$ at $\sqrt{s_{NN}} = 17.3$ GeV):

$$L_{\boldsymbol{\Theta}}\left(X\right) = \prod_{i=1}^{n} Q\left(X_i, \boldsymbol{\Theta}\right) = \prod_{i=1}^{n} \left[\sum_m \Theta_m F_m\left(\boldsymbol{p_i}, q\right) f_{m,\boldsymbol{p},q}\left(\mathrm{d}E/\mathrm{d}x\right)\right]. \tag{5.5}$$

The task is now to find the values for the Θ_m that maximize L. Θ_m are the only free parameters in this optimization problem. For technical reasons, instead of maximizing the likelihood function, it is more practical to minimize the *negative log likelihood function*

$$l_{\boldsymbol{\Theta}}\left(X\right) = -\ln L_{\boldsymbol{\Theta}}\left(X\right) = -\sum_{i=1}^{n} \ln Q\left(X_i, \boldsymbol{\Theta}\right). \tag{5.6}$$

as the sum is easier to evaluate than the product. Technically, the `TMinuit` package [177, 178] is used in the likelihood fitting. The initially four parameters Θ_e, Θ_π, Θ_K and Θ_p are reduced to three by the constraint $\sum_m \Theta_m = 1$. The assumption that the relative electron contribution is constant in each event further reduces the number of free fit parameters to two, that are sequentially varied to obtain the optimal value. The choice of variables and the sequence of their fit has been studied in detail [117, 106] and found not to influence the outcome. In [106], an alternative manual optimum search also confirmed the results obtained in the fit.

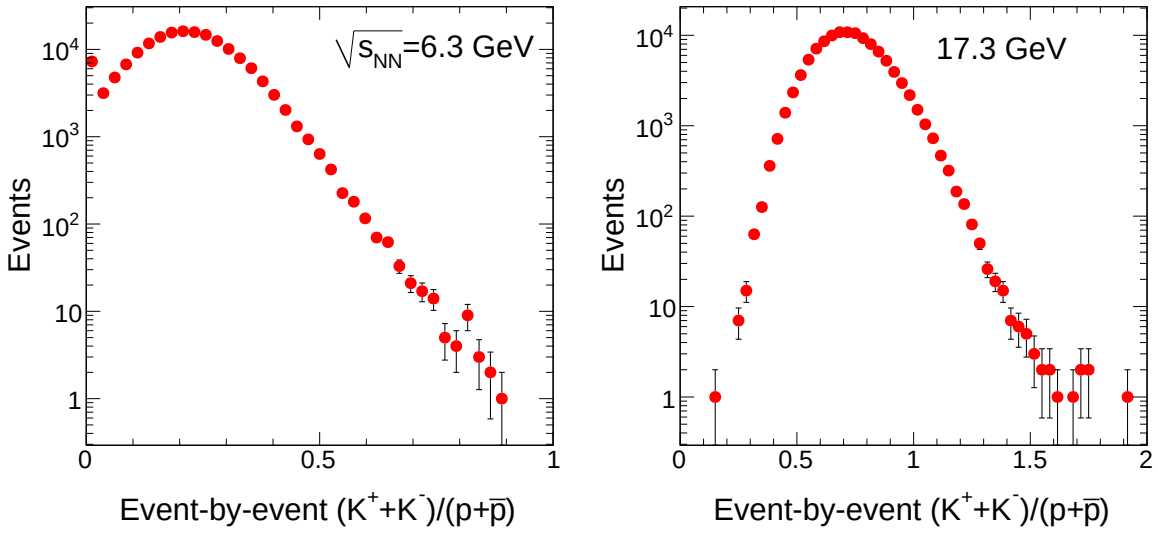

Figure 5.16: Event-by-event distribution of the $(K^+ + K^-)/(p + \bar{p})$ ratio in Pb+Pb collisions at $\sqrt{s_{NN}} = 6.3$ and 17.3 GeV, extracted using the likelihood method described in this section.

The event-wise hadron ratios are then calculated from the fitted values of Θ_m. For example, the kaon-to-proton ratio is $n_K/n_p = \Theta_K/\Theta_p$, the event-wise multiplicity of kaons is $n_K = \Theta_K n$. It is from the distribution of these event-wise quantities, that the fluctuation signals are extracted. As an example, the quantity of interest in the present thesis, the $(K^+ + K^-)/(p + \bar{p})$ ratio is histogrammed and shown for two energies in Figure 5.16.

The representation as a histogram may be misleading as in the course of the binning, information is lost. The fluctuation observable reported as final result is however based on the exact moments of the distribution, irrespective of binning. The relative width of the ratio distribution is determined as introduced in equation (2.1):

$$\sigma = \frac{\sqrt{\mathrm{Var}\,(A/B)}}{\langle A/B \rangle}.$$

For the measured data events treated here (in contrast to the mixed events discussed in the next step) the width is designated σ_{data}. It goes down from $\sigma_{\mathrm{data}} = 50\%$ at $\sqrt{s_{NN}} = 6.3$ GeV to 21% at 17.3 GeV. The excitation function of σ^2_{data} will be presented in Figure 5.19 for further discussions below.

A comparison of the distribution shape for the two energies reveals that more than just the first two moments contribute. Symmetry and form change with energy, not only

the width. An obvious change in the shape that appears at low energies comes from the distribution approaching zero and will be duly discussed in Section 5.7. Beyond that, in the light of the recent interest in higher order fluctuations [87, 90, 179], it would be desirable to also measure skewness, kurtosis etc. of identified hadron distributions. They have been suggested to be more sensitive to critical point effects [86, 180, 181] compared to the conventional second moment fluctuation measures, a finding that was confirmed in lattice QCD calculations [182, 183]. However in the present study, no way to remove experimental background effects for higher moment observables could be found. For the second moment variable σ studied here, an assertion of background contributions is however possible and will be demonstrated in the next section.

5.5 Mixed Event Generation

In order to draw a physics conclusion from the event-by-event ratio distribution determined in the previous section, a careful analysis of background effects is necessary. Those can be assessed in a mixed event method [117]. Measured tracks X_i are gathered from multiple events in a track pool and are then re-distributed into *mixed events*. Care is taken to ensure that no two tracks in a mixed event stem from the same original data event. By this, it is ensured that no physics correlation is conveyed to the mixed events. It is also made sure during event mixing that the original multiplicity distribution $P(n)$ is preserved.

With these precautions, the mixed events represent the statistical properties of the original sample. The inclusive momentum and $\mathrm{d}E/\mathrm{d}x$ distributions are identical to the original event ensemble, as the tracks are only re-distributed. They keep their $\mathrm{d}E/\mathrm{d}x$ information attached so that the PID procedure from Section 5.4 can be applied to the mixed events in the same way as to normal measured events. The extracted distribution is shown in Figure 5.17. The width of this reference distribution is that of uncorrelated kaon and proton production, only governed by finite number statistics and correlations induced by the particle identification scheme. Extensive checks on the mixed event method have been done in respect of the results published in [118]. The present analysis relies on this proven event mixing scheme. The stability and reliability of the mixed event method was further examined in the UrQMD simulations testing the PID scheme described in Section 5.7, as well as for the UrQMD model comparisons of Section 6.1.

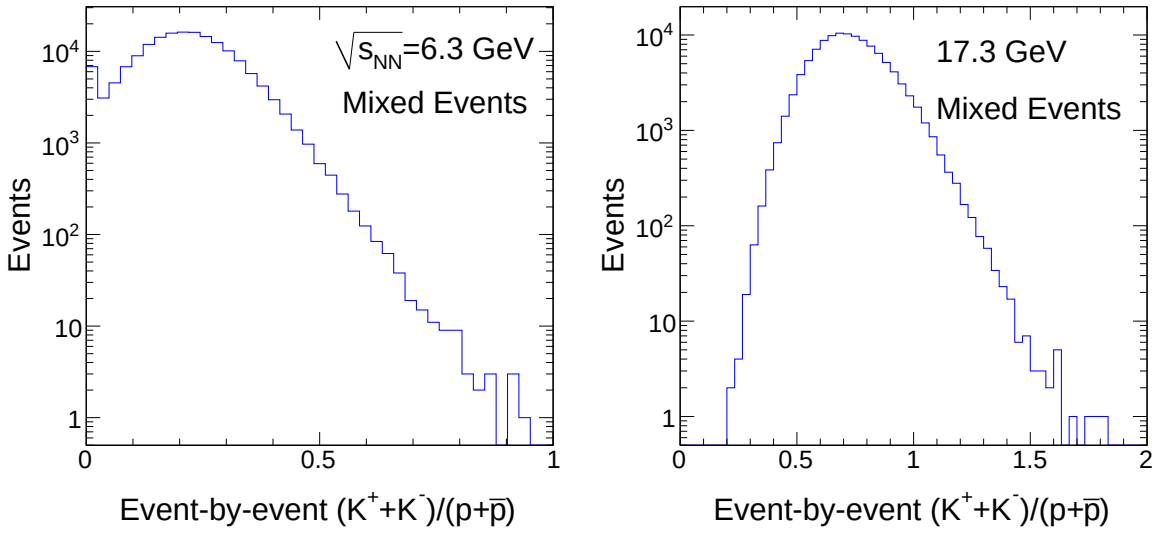

Figure 5.17: Event-by-event distribution of the $(K^+ + K^-)/(p + \bar{p})$ ratio extracted from mixed events using the likelihood method described in Section 5.4. The shown examples are for Pb+Pb collisions at $\sqrt{s_{NN}} = 6.3$ and 17.3 GeV.

The relevant information extracted from the mixed event distribution is the relative width σ_{mix}, calculated according to equation (2.1). Just as the mixed event distributions from Figure 5.17 resemble the data distributions in Figure 5.16, σ_{mix} turns out to be very similar to σ_{data}. In Figure 5.19, the excitation function of σ^2_{mix} is compared to σ^2_{data} for the $(K^+ + K^-)/(p + \bar{p})$ ratio. As a consequence of Equations 2.3 and 2.6, σ^2_{mix} should in a fully uncorrelated case reduce to

$$\sigma^2_{\text{mix}} \approx \nu_{\text{stat}} = \frac{1}{\langle K^+ + K^- \rangle} + \frac{1}{\langle p + \bar{p} \rangle}. \tag{5.7}$$

Figure 5.19 shows that this is not the case. The remaining difference shows that as discussed in Section 2.1, the mixed events contain the correlation induced by the PID fit. The expression in equation (5.7) is thus not valid for the present analysis. Approximation properties of the variable σ_{dyn} are further discussed in Section 5.8.

5.6 Signal Extraction: Determination of σ_{dyn}

The data and mixed event distributions from Figures 5.16 and 5.17 are very similar for the same energy. A direct comparison can be made in Figure 5.18, where the two distributions are plotted on top of each other for $\sqrt{s_{NN}} = 6.3$ (left) and 17.3 GeV (right).

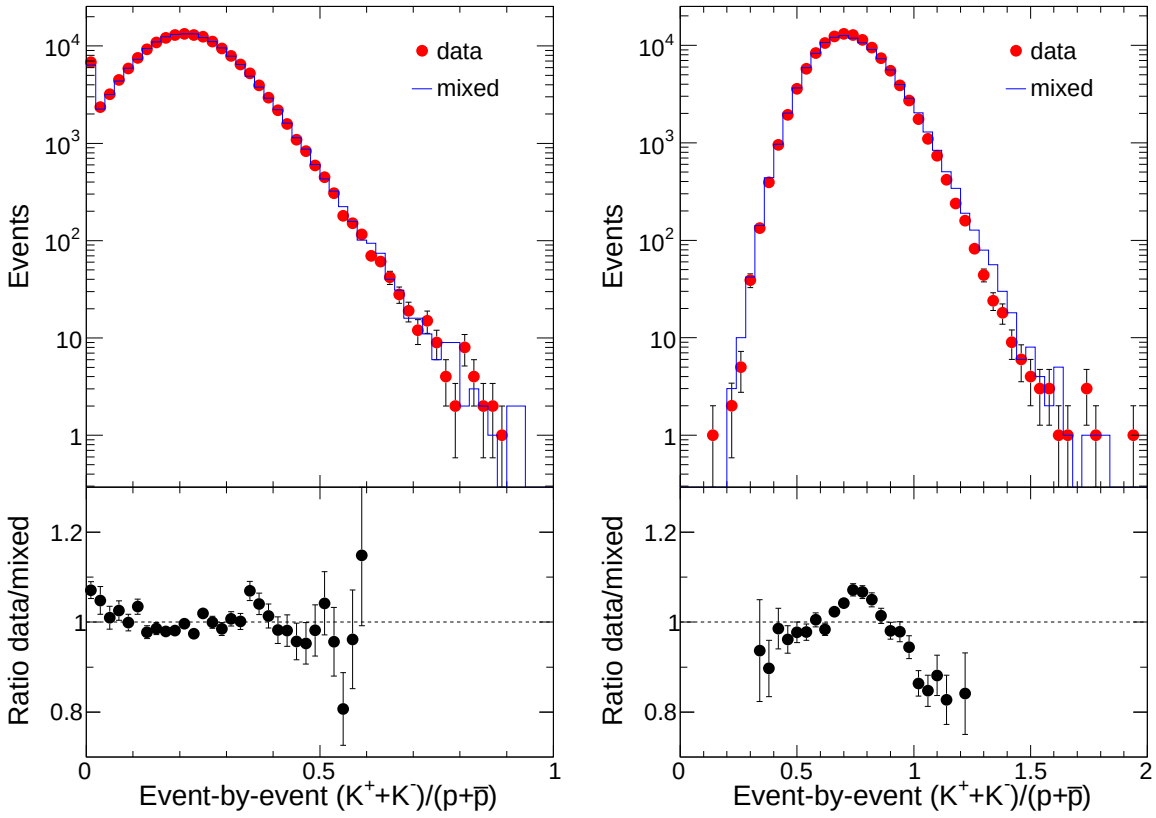

Figure 5.18: Event-by-event distribution of the $(K^+ + K^-)/(p + \bar{p})$ ratio at $\sqrt{s_{NN}} = 6.3$ (left) and 17.3 GeV (right). Real data events (red markers) are compared to the mixed event reference (blue histogram). The lower panel shows the ratio data/mixed, where the concave shape at $\sqrt{s_{NN}} = 6.3$ GeV indicates positive dynamical fluctuations, while the convex shape at 17.3 GeV hints at $\sigma_{\mathrm{dyn}} < 0$. Only in the ratio plot, for better readability, statistically insignificant bins are not shown [64].

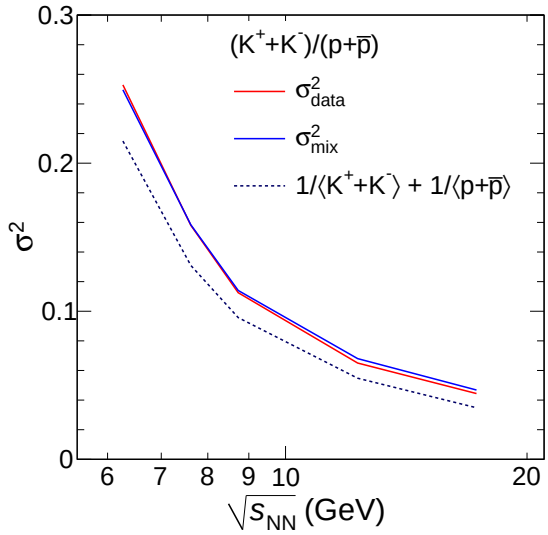

Figure 5.19: Excitation function of the square of the relative widths σ_{data} and σ_{mix} of the $(\mathrm{K}^+ + \mathrm{K}^-)/(\mathrm{p} + \overline{\mathrm{p}})$ ratio. While $\sigma^2_{\mathrm{data}} > \sigma^2_{\mathrm{mix}}$ at $\sqrt{s_{NN}} = 6.3$ GeV, the lines cross going to higher energies. For comparison the expectation from an uncorrelated background, $1/\langle \mathrm{K}^+ + \mathrm{K}^- \rangle + 1/\langle \mathrm{p} + \overline{\mathrm{p}} \rangle$ is shown.

At the top energy, a narrower data distribution compared to mixed events is clearly visible. This is further visualized in the lower panel of Figure 5.18 (right): the ratio between data and mixed event distributions shows a convex shape. The dynamical fluctuation signal σ_{dyn} is extracted as defined in equation (2.2):

$$\sigma_{\mathrm{dyn}} := \mathrm{sign}\left(\sigma^2_{\mathrm{data}} - \sigma^2_{\mathrm{mix}}\right) \sqrt{|\sigma^2_{\mathrm{data}} - \sigma^2_{\mathrm{mix}}|}.$$

Recall that according to this definition, dynamical fluctuations are the excess of the observed signal over the reference. The data distribution at $\sqrt{s_{NN}} = 17.3$ GeV being narrower than the reference thus results in a negative value of σ_{dyn} here. The further implications of this observation will be discussed in Chapter 6. Conversely, at 6.3 GeV (Figure 5.18, left) σ_{data} is larger than σ_{mix} and thus $\sigma_{\mathrm{dyn}} > 0$. Following from the less symmetrical shape of the event-by-event distribution here, this result is not so straight-forwardly inferred from the ratio plot.

Any quantitative interpretation from the ratio panel must be drawn with care. The weight of a specific ratio is not indicated in the ratio plot but ranges from 10,000 to one. Judging the contribution of many events with a small deviation from the mean compared to few events with a large deviation may be misleading. For the representation in Figure 5.18, the continuous ratio distribution also has to be binned, a source of further

ambiguities in the visual interpretation. σ_{dyn} is the exact way to quantify the observation. The widths σ_{data} and σ_{mix} that go into σ_{dyn} are calculated from the exact moments of the ratio distributions, maintaining the full information. Their energy dependence is shown in Figure 5.19, and where the two cross, σ_{dyn} changes sign.

5.7 Systematic Studies on the Result

Before reporting, the final results have been subjected to systematic scrutiny. Although the analysis builds upon a proven method, it was ensured that the same quality and stability requirements from [118] also hold for the present kaon-to-proton ratio fluctuation analysis. In this case, the particle separation is more difficult compared to the kaon-to-pion or the proton-to-pion ratios. The results proved to be stable under variations of the track quality criteria and modest changes in the kinematic acceptance. Further checks concerned the PID method and finite number effects, all of which will be reported in this section.

Kinematic Constraints

In an analysis sensitive to proton correlations, it is important to distinguish between correlations among unaffected spectator protons from the incident nuclei and those with produced protons. The former are found in the forward region close to beam rapidity (spectator region) and are not of interest for the question about baryon-strangeness correlation in a conjectured quark-gluon plasma. An impact of high rapidity particles on the fluctuation signal was found in the study of mean transverse momentum fluctuations [84]. The same phase space regions have been taken into separate consideration here to clarify the situation.

In Figure 5.20, different phase space cuts are illustrated. The standard method is to apply no high momentum cut. To check the potential influence of spectators on the fluctuation signal, the momentum region close to beam rapidity was excluded. The momentum cuts are illustrated in Figure 5.20. As a first test, the region $y_{\mathrm{p}} > y_{\mathrm{Beam}} - 1 \wedge p_{\mathrm{T}} < 0.2$ GeV/c (black line in Figure 5.20) was excluded. y_{p} is the rapidity, calculated under the assumption that the particle is a proton. For a further test, in addition the kinematic range $y_{\mathrm{p}} > y_{\mathrm{Beam}} - 0.5$ (blue line in Figure 5.20) was excluded. Under this variation of acceptance, the observed σ_{dyn} changed on a level far below the

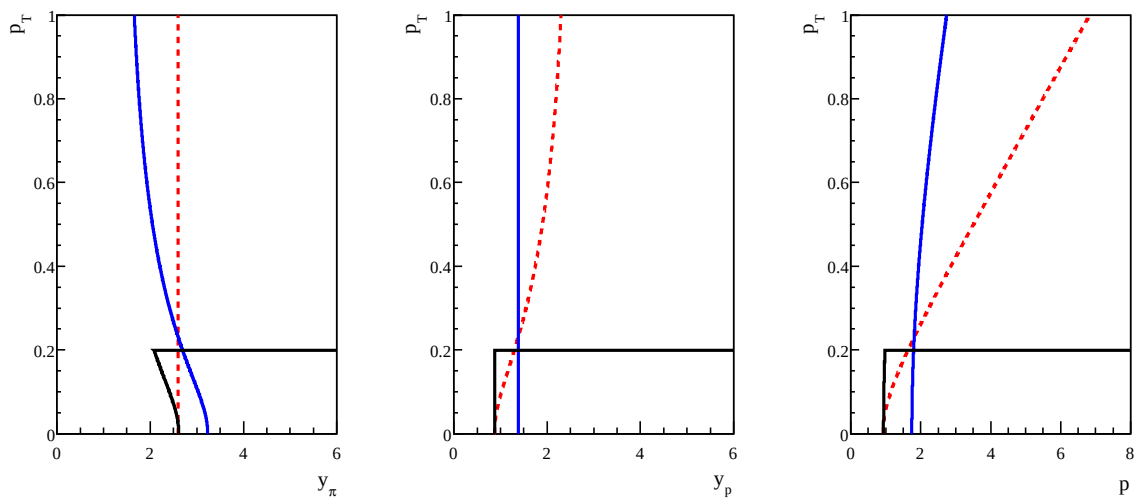

Figure 5.20: Illustration of momentum cuts as described in the text. The calculations are performed in the center-of-mass system, this example is for $\sqrt{s_{NN}} = 6.3$ GeV, where $y_{\mathrm{Beam}} = 1.88$.

systematic error reported on the final result in Figure 6.1. It was therefore not considered for further error estimation.

In Figure 5.20, the cutoff lines are sketched in three different kinematic variables on the abscissa. All use transverse momentum on the ordinate. The left panel uses pion rapidity, the middle panel proton rapidity and the right panel total momentum as the longitudinal measure. All refer to the center of mass frame. Figure 5.20 thus also illustrates the change between the relativistic kinematics as introduced in Chapter A.

The finding that spectator protons play no role in the present analysis is further substantiated by the acceptance plots in Figures 5.10, 5.11 and 5.12, as well as the model studies on the acceptance presented in Figure 5.13. The common finding is that the spectator region does not play a role in the acceptance of the present analysis.

Outlier Studies

An important difference between the ratio distributions at high and low energies comes up when looking at Figures 5.16, 5.17 and 5.18. The smaller mean, combined with the larger relative width at $\sqrt{s_{NN}} = 6.3$ GeV leads to the development of a pile-up of events at $(\mathrm{K}^+ + \mathrm{K}^-)/(\mathrm{p} + \overline{\mathrm{p}}) = 0$. The same was observed for the $(\mathrm{K}^+ + \mathrm{K}^-)/(\pi^+ + \pi^-)$ ratio, and its influence on the reliable determination of σ_{dyn} was studied. The discontinuous

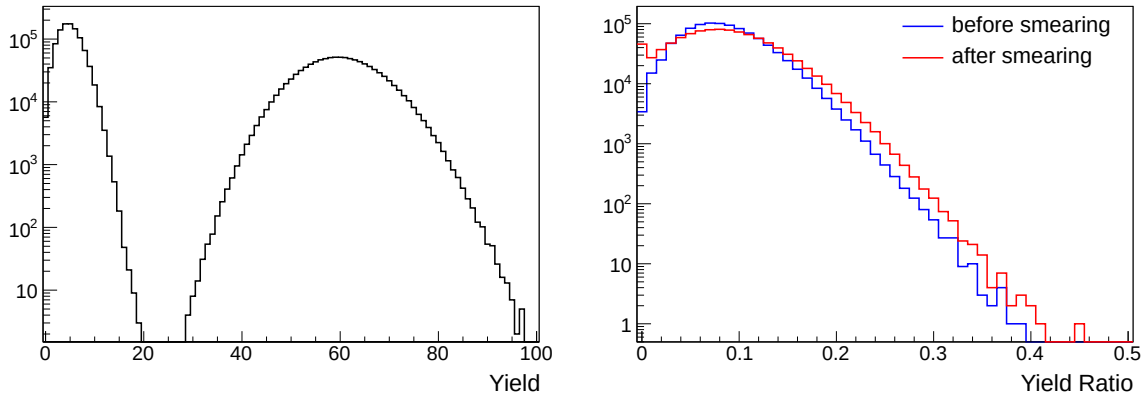

Figure 5.21: Illustration of the pile-up observed for low kaon multiplicities. Poisson distributions (left panel), their ratio (blue line in the right panel) and the result of a folding with a Gaussian (red line, right panel). See the text for details.

behavior can not be explained by physical effects. Detector or reconstruction failures leading to a discontinuous behavior were also considered but could be excluded [118]. Finite number effects also play no role here, as in the likelihood fit, the hadron yields are not constrained to integer values. As introduced in Section 5.4, the parameters Θ_m with the highest probability are extracted by the fit, going to integer values for the multiplicities n_m would lead to a lower significance.

The origin of the pile-up can be traced in a simple Monte Carlo model. The uncertainty in the ratio determination by the event-by-event fit was demonstrated to correspond to a Gaussian smearing around the true value [117]. This width is later subtracted by the mixed event method. For the illustration in Figure 5.21, two Poisson distributions with a mean of 5 and 60 respectively were generated. They are depicted in the left panel, and the lower mean "kaon" distribution evolves smoothly toward a residual value at zero multiplicity as expected from a Poisson distribution with a small mean. The $\langle N \rangle = 60$, "proton" distribution has a large enough mean to resemble a symmetrical normal distribution, the high $\langle N \rangle$ limit of the Poisson distribution. Their ratio distribution, indicated with a blue line in the right panel of Figure 5.21, resembles a Poisson. When each randomly drawn ratio is now smeared according to a Gaussian with a constant width of 0.03, the resulting distribution (red line in Figure 5.21) develops a structure at zero similar to the one observed in the data. Thus those events with a small ratio that are pushed towards even lower values by the folding with the Gaussian distribution meet a constraint that does exist in the experiment and in the Monte Carlo model: Negative hadron ratios are excluded by construction. The smeared distribution would extend into the negative values, what is not physically plausible.

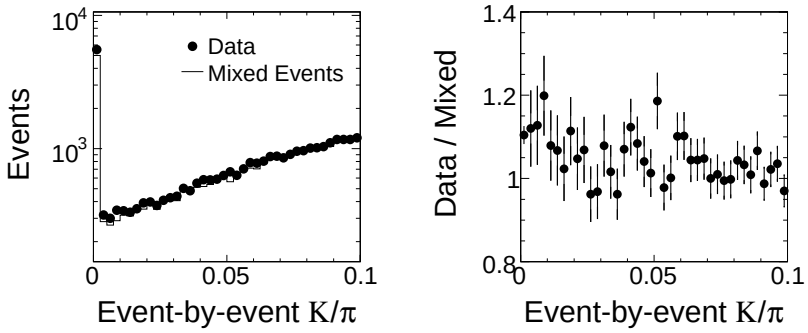

Figure 5.22: The pile-up of events with $(K^+ + K^-)/(\pi^+ + \pi^-) = 0$ seen as a close-up towards low ratios, from [118]. The structure is seen in data and is well reproduced by the mixed events (left). This is underlined by the smooth evolution of the ratio data/mixed toward zero.

The approach to weaken the constraint to non-negative yields proved unsatisfactory. Allowing negative multiplicities induces compensation effects between the species causing the fit to diverge. An unconstrained fit may be desirable but is not possible in practice here. It has been observed in other analyses that fits tend to not converge in unphysical regions [184, 185], and mathematical and statistical considerations do not limit the extraction of moments to unconstrained distributions [184, 185, 177].

The pile-up proved to be an effect that is well reproduced by the mixed event method. The mixed event distribution is so similar to the data distribution that the same structure is present there. Figure 5.22 shows a close-up of small ratios from the $(K^+ + K^-)/(\pi^+ + \pi^-)$ study published in [118]. The same was tested and holds true for the kaon-to-proton ratio. As noted above, the representation of the continuous ratio distribution as a histogram is afflicted by the binning. In the very fine binning chosen in Figure 5.22, the structure at $(K^+ + K^-)/(\pi^+ + \pi^-) = 0$ appears even more pronounced. While the left panel already suggests from the comparison that the peak is well reproduced by the mixed events, the ratio of the two distributions in the right panel showing a smooth behavior toward zero confirms this. It was further checked that the other properties of $(K^+ + K^-)/(p + \overline{p}) = 0$ events are also reproduced in mixed events. They consistently feature smaller multiplicities and a trend to larger proton numbers.

σ_{dyn} was also evaluated under a cut on the extreme outliers in the ratio distribution, e.g. removing the 1% largest or smallest ratios. The outcome reported for $(K^+ + K^-)/(\pi^+ + \pi^-)$ fluctuations in [118] also holds in the present study. Whether an unconstrained end of the distribution is examined, or one affected by the pile-up, the distribution tails proved not to dominate the overall fluctuation signal. The particular shape of the ratio distributions

at small values is well reproduced in the reference distribution obtained by the mixed event procedure. UrQMD studies including the dE/dx PID method are presented in the next paragraph. They also confirm that this feature is an artifact of the particle identification not affecting the extracted fluctuation signal.

Simulation of the dE/dx response

The particle identification method applied in the present analysis introduces an anti-correlation among the particle yields that is reflected in a widening of the event-by-event ratio distributions. This effect is reproduced in the reference ensemble constructed by event mixing and a subsequent PID fit on the mixed events [115, 116]. A model simulation has been employed to provide further confirmation of this method. A similar study was also performed in the analysis of the centrality dependence of hadron ratio fluctuations in Pb+Pb collisions at $\sqrt{s_{NN}} = 17.3$ GeV [106, 186], with agreeing results.

For the present study, 100k central Pb+Pb collision events were generated in the hadronic transport model UrQMD 2.3 at the five collision energies studied here. Model details are described in Section 6.1. The standard way to analyze hadron ratio fluctuations from an event generator such as UrQMD is to rely on the accurate particle identification provided by the model output. By this, PID effects are completely absent. The experimental acceptance is studied by applying phase space cuts that correspond to the experimental limitations. They have been evaluated and are tabulated in [176]. This method is referred to as *MC PID* because the information directly from the "Monte Carlo" event generator is used. The results are compared to an approach where the experimental PID method is used on the model data, denoted the dE/dx fit here. The dE/dx distribution for all individual particle species is known from the inclusive fit (cf. Section 5.3). Based on that knowledge each particle from the UrQMD events is assigned a randomly drawn dE/dx value. The resulting events are stored in NA49 ROOT mini-DSTs like normal experimental data. They can now be subjected to the unmodified analysis chain.

A comparison of the analysis results from the two methods can be seen in Figure 5.23. The results from the MC PID counting method, where experimental biases are excluded, are recovered by the dE/dx fit method. The remaining maximal difference of 1.5% is accounted for in the systematic error of the method (cf. Section 5.7).

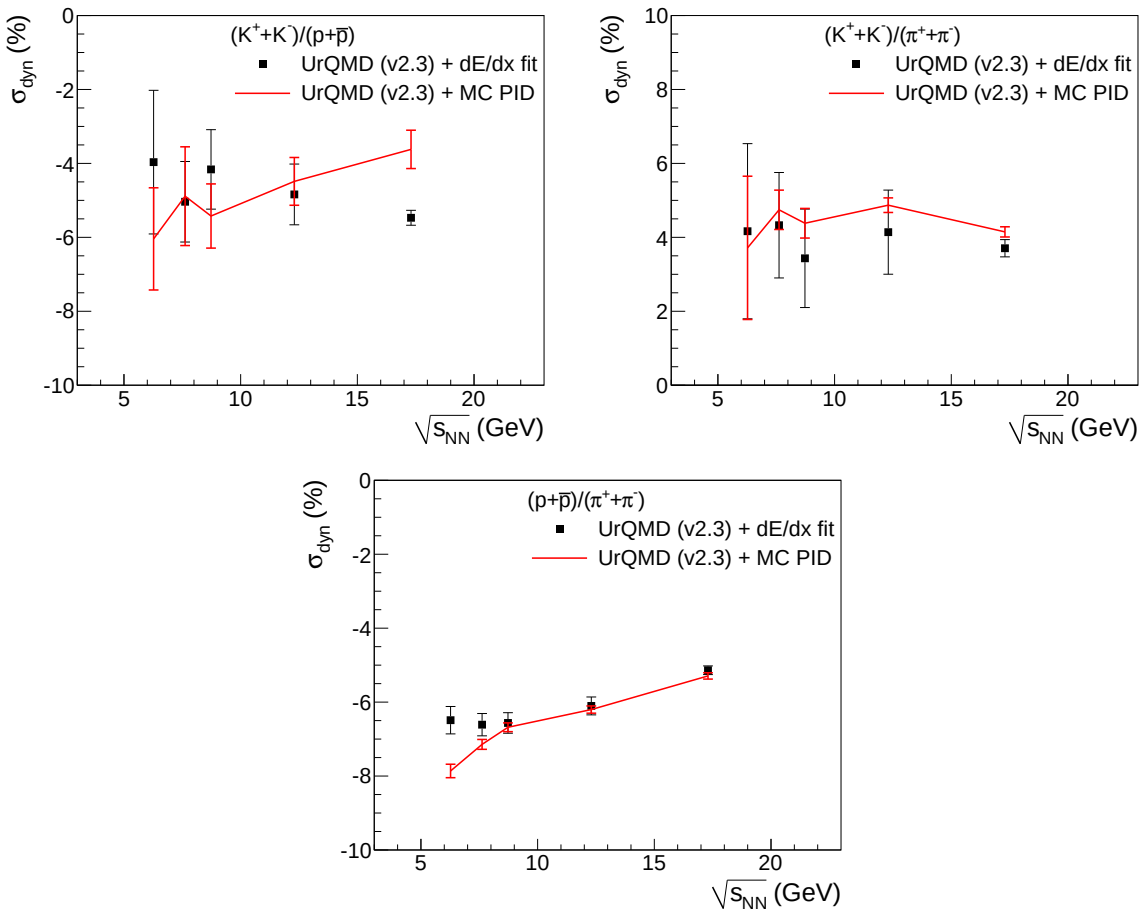

Figure 5.23: Comparison of UrQMD model simulations using different particle identification methods. The result from unambiguous particle counting based on the particle identification codes provided from the model (MC PID) is essentially reproduced when applying the experimental likelihood PID scheme (dE/dx fit) to the model data. Remaining differences go into the systematic error.

Track Quality Cut Studies

By the variation of track cuts as described in Section 5.2, the stability of the results is tested under a variety of changed preconditions. The statistical basis of the σ_{dyn} measurement is modified, and fewer particles result in a less constrained likelihood. The quality criteria on the $\mathrm{d}E/\mathrm{d}x$ measurement are also varied and thus the PID separation power. Of course, the PDFs for Section 5.4 have to be re-generated for each analysis variant. Another consequence of the track quality cut studies is a slightly changed acceptance, resulting from the minimum required statistics in each phase space bin for the inclusive $\mathrm{d}E/\mathrm{d}x$ fit as described in Section 5.4.

The signal proves to be very stable under this multitude of changes, as Figures 5.24 and 5.25 show. The only large deviation is observed for the $(\mathrm{K}^+ + \mathrm{K}^-)/(\mathrm{p} + \overline{\mathrm{p}})$ ratio at $\sqrt{s_{_{NN}}} = 7.6$ GeV, where σ_{dyn} is very close to zero. Such small signals are accompanied by a large statistical error as explained in Section 5.8 and Appendix B. The observed difference between the track cut variations is related to this property of σ_{dyn}.

In Section 5.2, weak decays were introduced as a potential bias to fluctuation measurements. Only when a decay product carries a large fraction of the decaying "mother" particle's momentum, it may be tracked back to the main vertex and be mistaken for a primary particle. In addition, the point requirements on the ratio of measured to potential points avoid tracks with a kink decay. As an example, the decay muon from the kaon decay (that might be mistaken for a pion) is not reconstructed to the main vertex due to the large Q value in the decay [187, 188]. In the present analysis, the daughter proton from the $\Lambda \rightarrow \mathrm{p} + \pi^-$ decay might play a role. The `Bx` and `By` limits defined in Section 5.2 cut into the secondary proton impact parameter distribution [133], strongly suppressing potential decay protons. No sensitivity of the signal to this cut is observed, limiting the influence of weak decays on the results presented here.

Systematic Error Calculation

Besides the systematic studies presented in the previous section, the results proved stable under further modifications to the analysis. As an example, no restrictions of the considered phase space changed the results beyond expectation. Among these studies are restrictions in the azimuthal acceptance to check the symmetry and cuts in the momentum range. The latter have the positive side effect that phase space regions with

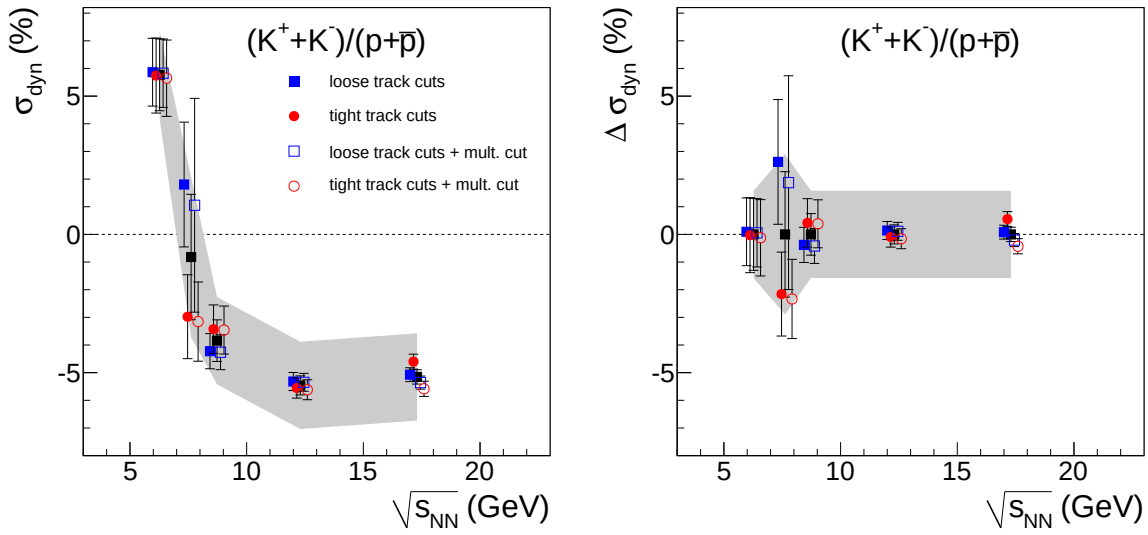

Figure 5.24: Variation in σ_{dyn} for the $(\mathrm{K}^{+}+\mathrm{K}^{-})/(\mathrm{p}+\overline{\mathrm{p}})$ ratio due to variations in event and track cuts. The right panel indicates the difference of the variants to the average value. The grey band indicates the final systematic error on the result as described in the text.

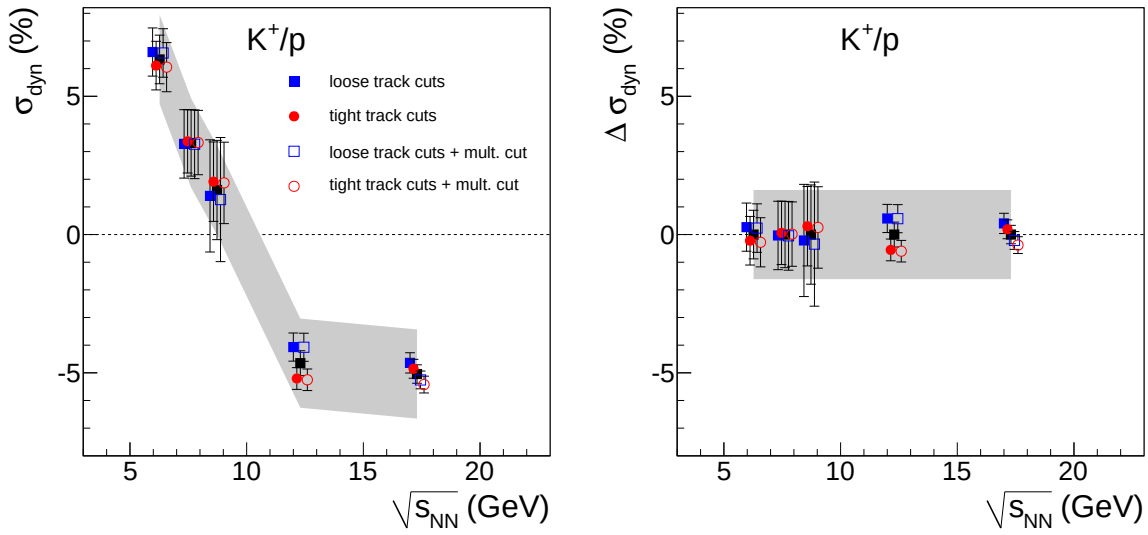

Figure 5.25: Systematic error calculation as in Figure 5.24, but for $\mathrm{K}^{+}/\mathrm{p}$ fluctuations.

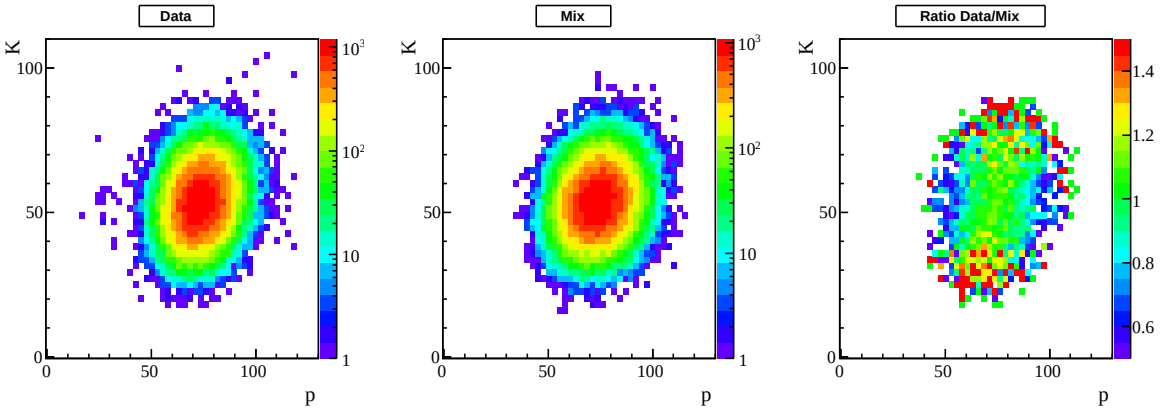

Figure 5.26: Correlation of kaon and proton multiplicities in Pb+Pb collisions at $\sqrt{s_{NN}} = 17.3$ GeV.

different $\mathrm{d}E/\mathrm{d}x$ separation power could be compared. Eventually, only three ingredients proved to contribute to the systematic error of the present measurement:

1. The event cut on outliers in the multiplicity distribution as described in Section 5.1
2. Variations in the track quality cuts
3. A bias from the particle identification method ascertained in UrQMD simulations

The variations in σ_{dyn} resulting from 1 and 2 are shown in Figures 5.24 and 5.25, that resulting from 3 in Figure 5.23. The maximum deviation caused by 1 and 2 was carried over to all energies. Only the before-mentioned point $((\mathrm{K}^+ + \mathrm{K}^-)/(\mathrm{p} + \overline{\mathrm{p}})$ ratio at $\sqrt{s_{NN}} = 7.6$ GeV) was treated separately. The maximum error from 3 was added in quadrature as these error sources are uncorrelated. The result of this treatment is indicated as a grey band in Figures 5.24 and 5.25.

5.8 The Variable σ_{dyn}

Following the discussions in this chapter and in Section 2.2, the variable σ_{dyn} can not straightforwardly be interpreted. For comparisons to a statistical model or direct comparison to susceptibilities calculated in lattice QCD (cf. Section 1.4), it would be desirable to directly measure identified hadron variances (e.g. $\langle(\delta \mathrm{K}^+)^2\rangle$) or covariances between two hadron species (e.g. $\langle \delta \mathrm{K}^+ \delta \mathrm{p} \rangle$) to access the underlying correlations. In principle these values can be obtained from the event-by-event PID fits described in Section 5.4. The extracted quantities would however not be comparable to a model

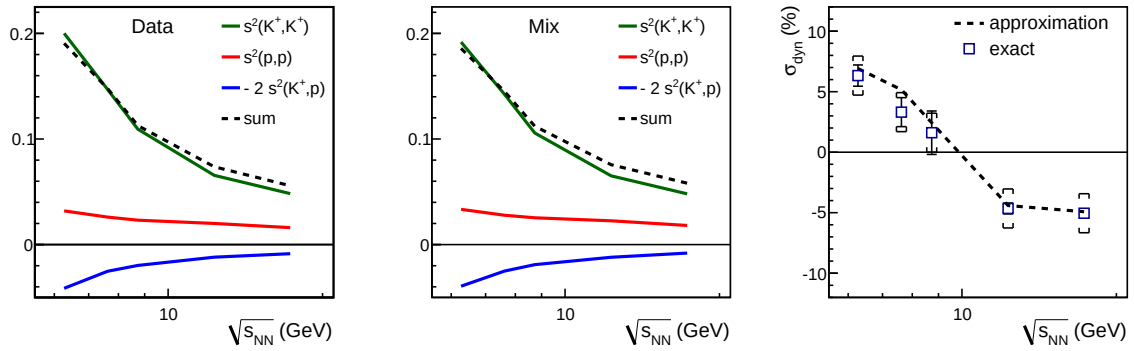

Figure 5.27: As a verification of the approximation for σ^2 made in equation (2.3), the individual terms defined in equation (5.9) have been evaluated. The approximation leads to the same result as the exact method using the definition of σ_{dyn} in equation (2.2).

because of two experimental biases, effects from centrality variation and PID effects. While in a statistical model, a fixed volume can be defined, even the centrality interval studied here represents a variation in impact parameter. The hadron ratio is an intensive quantity and σ_{dyn} has been studied not to be affected by the modest centrality variation here. The (co-)variances on the other hand will be directly affected. As an example, the multiplicity variation resulting from a large centrality variation will lead to a correlation between any two hadron species even in the absence of a physics correlation mechanism in the events.

Figure 5.26 demonstrates this for the kaon and proton multiplicities from Pb+Pb collisions at $\sqrt{s_{NN}} = 17.3$ GeV. The event-by-event multiplicities are shown in a correlation plot for real data events (left) and mixed events (center). A correlation (along the diagonal) could be deduced, but is only a consequence of high multiplicity events having a large number of kaons and protons at the same time. This feature is also present in mixed events. The right panel shows the ratio data/mix, similar to the bottom panels in Figure 5.18 to help compare the distribution shapes. Along the proton axis, the data distribution is narrower, while the kaon distribution in wider than the reference distribution. All variances and covariances that define the two-dimensional distribution can be calculated but remain intangible for models. A two-dimensional distribution like in Figure 5.26 for the particle species A and B could be fully described by five quantities: The variances $\langle(\delta A)^2\rangle$ and $\langle(\delta B)^2\rangle$, the means $\langle A\rangle$ and $\langle B\rangle$, as well as the covariance $\langle\delta A\delta B\rangle$.

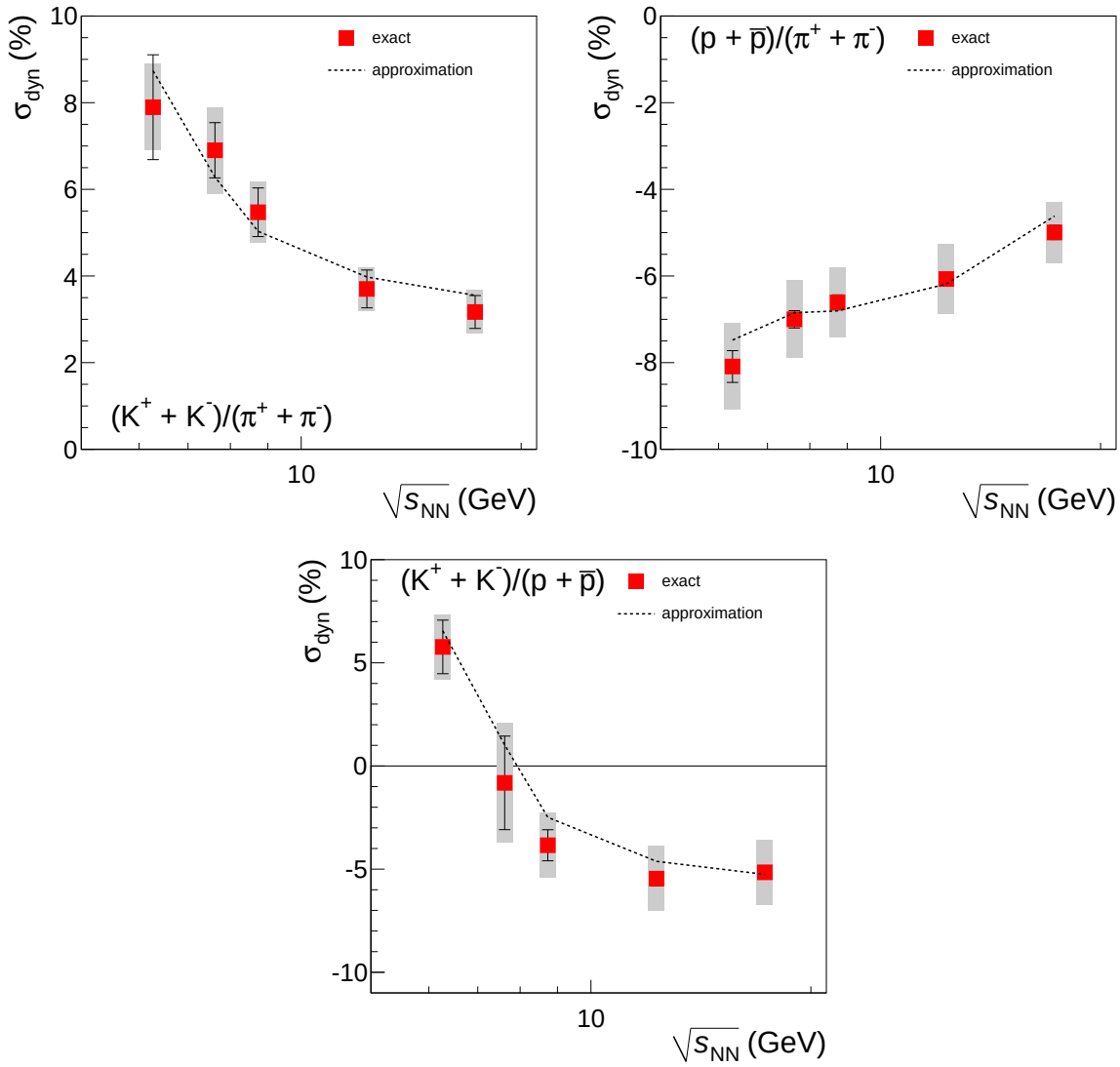

Figure 5.28: Comparison of an exact calculation of σ_{dyn} and the approximation from equation (2.3).

In this context, a test of equation (2.3) introduced on page 38 applies. With the definition of

$$s^2\left(A,B\right) := \frac{\langle AB\rangle}{\langle A\rangle\langle B\rangle}, \tag{5.8}$$

the leading order expansion of σ^2 can be rewritten as

$$\sigma^2\left(\frac{A}{B}\right) \approx s^2\left(A,A\right) + s^2\left(B,B\right) - 2s^2\left(A,B\right). \tag{5.9}$$

The s parameters have been evaluated in the data as well as in the reference events. The values of $s^2(\mathrm{K}^+,\mathrm{K}^+)$ and $s^2(\mathrm{p},\mathrm{p})$, as well as $-2s^2(\mathrm{K}^+,\mathrm{p})$ are displayed in Figure 5.27. The sum of these terms represents the approximation of σ^2_{data} and σ^2_{mix} according to equation (5.9). The right panel of Figure 5.28 demonstrates that σ_{dyn} calculated from this approximation agrees with the usual method. This also holds for combined charge ratios, shown in Figure 5.28. It has been noted in Section 2.2 that the approximation used here neglects higher order terms. The finding that approximation and exact treatment yield the same result for σ_{dyn} indicates that only the leading order plays a role in the studied ratio fluctuations.

It was argued in [124] that σ_{dyn} and ν_{dyn} measurements can be compared by the assumption $\nu_{\mathrm{dyn}} \approx \sigma^2_{\mathrm{dyn}}$. The above study supports this, as the approximation of σ^2 in equation (2.3) agrees to the definition of ν_{AB} (equation (2.5)). The remaining difference between σ_{dyn} and ν_{dyn} is that the latter can only be used when the reference background reduces to the expression found for ν_{stat} in equation (2.6). We have seen in Section 5.5 and Figure 5.19 that this is not the case for the present analysis but any additional correlations are present in data and reference events alike and are thus subtracted when calculating σ_{dyn}.

A further check on the validity of the above approximation is the reversibility of enumerator and denominator in the studied particle yield ratio. According to Equations 2.3 and 2.2, $\sigma_{\mathrm{dyn}}(A/B) \approx \sigma_{\mathrm{dyn}}(B/A)$. For the studies involving kaons here, this can not be studied at all energies: we have seen above (cf. Section 5.7) that toward lower energies, the case $\mathrm{K} = 0$ becomes populated. While for the K/p ratio, this represents no hindrance, the inverse ratio diverges toward infinity, making the determination of the moments mean and variance impossible. At higher energies, where the kaon number is always larger than zero, the validity is confirmed. Proton and pion numbers are always finite and the reversibility check is demonstrated for the $(\mathrm{p}+\overline{\mathrm{p}})/(\pi^+ + \pi^-)$ ratio in Figure 5.29.

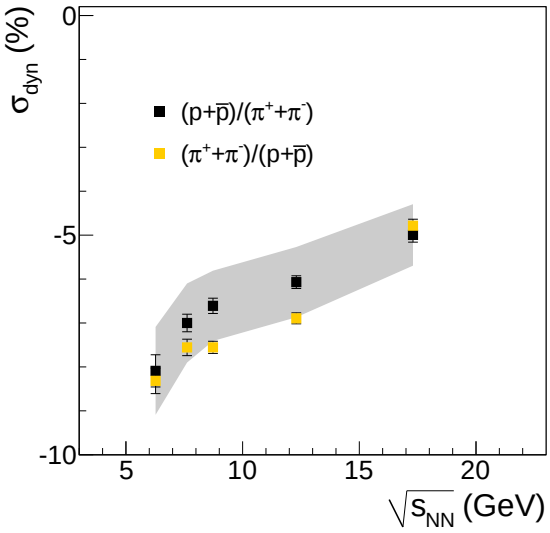

Figure 5.29: To test the reversibility of the variable, σ_{dyn} was evaluated for the $(\pi^+ + \pi^-)/(\mathrm{p} + \overline{\mathrm{p}})$ ratio. The result agrees with that for $(\mathrm{p} + \overline{\mathrm{p}})/(\pi^+ + \pi^-)$ fluctuations from [118] within the systematic errors.

Further above, the observation has been made that the statistical error on σ_{dyn} becomes large for small signals. Detailed studies found this to be caused purely by the definition of σ_{dyn}. This is confirmed by analytical derivations of the error propagations as well as by experimental tests, both leading to a proportionality of the error of

$$\Delta\sigma_{\mathrm{dyn}} \propto \frac{1}{\sqrt{\sigma_{\mathrm{dyn}}}}. \tag{5.10}$$

The corresponding calculations and simulations have been presented in [189] and are documented in Appendix B for clarity.

Chapter 6

Kaon-to-proton ratio fluctuations in central Pb+Pb collisions from $\sqrt{s_{NN}} = 6.3$ to 17.3 GeV

After the completion of all analysis steps and checks as described in the previous chapter, the final result of the present thesis will be discussed here. σ_{dyn} has been evaluated for the $(\mathrm{K}^+ + \mathrm{K}^-)/(\mathrm{p} + \overline{\mathrm{p}})$ and K^+/p ratios. The former probes correlations between all four involved hadron species, K^+, K^-, p and $\overline{\mathrm{p}}$. Studying charge separated ratios on the other hand may help to reveal the correlations in a more specific way. However, the low K^- and $\overline{\mathrm{p}}$ multiplicities at low energies, as indicated in Table 1.1 on page 21, make it impossible to study ratios involving those particles separately. Only the K^+/p ratio features large enough mean multiplicities to make a fluctuation study possible. A second consequence of the vanishing K^- and $\overline{\mathrm{p}}$ yields is that the two studied σ_{dyn} variants are expected to converge at low energies.

The excitation function of σ_{dyn} is shown in Figure 6.1 for $(\mathrm{K}^+ + \mathrm{K}^-)/(\mathrm{p} + \overline{\mathrm{p}})$ (left) and K^+/p (right). For both ratios, σ_{dyn} changes from a positive value at $\sqrt{s_{NN}} = 6.3$ GeV towards a plateau at negative values going to higher energies. This change of sign is a new feature that was not observed in previous ratio fluctuation analyses. It is reflected in the event-by-event ratio distributions shown in Figure 5.18 and discussed in Section 5.6. The systematic errors as evaluated in Section 5.7 are indicated by braces in Figure 6.1. As observed in Section 5.8 and explicated in Appendix B, the statistical error becomes large for small values of σ_{dyn}.

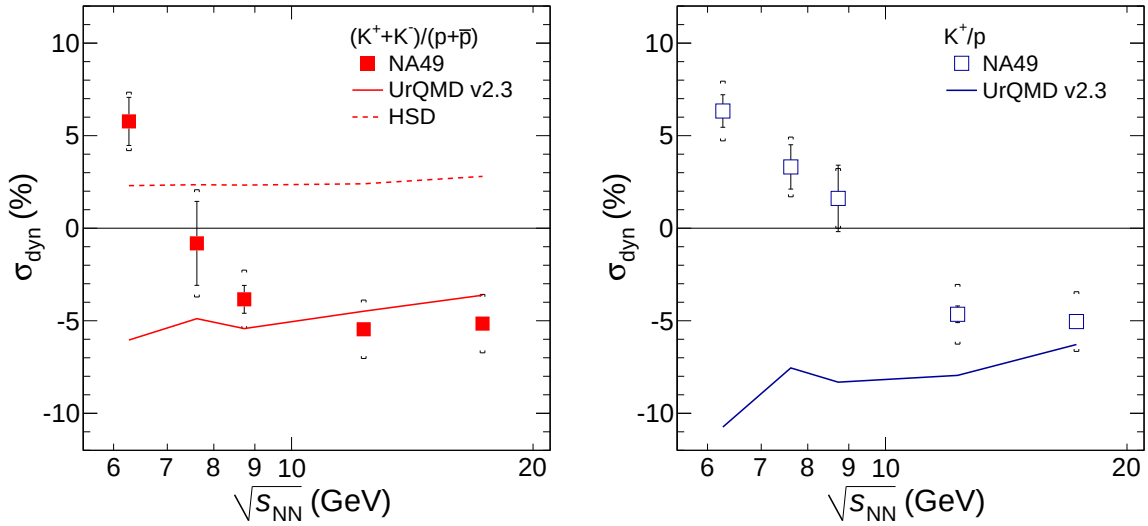

Figure 6.1: The energy dependence of σ_{dyn} for the $(\mathrm{K}^+ + \mathrm{K}^-)/(\mathrm{p} + \overline{\mathrm{p}})$ (left) and the K^+/p (right) ratios [64]. Symbols represent the measurements with statistical and systematic (braces) uncertainties. UrQMD and HSD transport model calculations, performed in the NA49 acceptance filter are represented by lines, the statistical error on the model results decreases from approximately 1.5% at 6.3 GeV to 0.5% at 17.3 GeV.

As expected, the two studied ratios converge at the lowest energy, where $\langle \mathrm{K}^- \rangle = 1$ and $\langle \overline{\mathrm{p}} \rangle = 0$. They also coincide at $\sqrt{s_{NN}} \geq 12.3$ GeV. Please recall from the discussion of equation (2.3) in Section 2.2 that $\sigma_{\mathrm{dyn}}(A/B)$ is sensitive to correlations among the enumerator $\langle (\delta A)^2 \rangle$, the denominator $\langle (\delta B)^2 \rangle$ and to cross-correlations $\langle \delta A \delta B \rangle$. The agreement at higher energies can thus either be attributed to the additional terms in $\sigma_{\mathrm{dyn}}((\mathrm{K}^+ + \mathrm{K}^-)/(\mathrm{p} + \overline{\mathrm{p}}))$ contributing only modestly, or canceling each-other. σ_{dyn} disagrees for the two studied ratios at $\sqrt{s_{NN}} = 7.6$ and 8.7 GeV.

6.1 Hadron Transport Model Comparison

In Section 2.2, the comparison of ratio fluctuation signals to hadronic transport calculations was already briefly introduced. They serve as a baseline to evaluate the influence of hadronic correlations to the experimental fluctuation signal. While a direct quantitative deduction of correlation coefficients from a measured σ_{dyn} is not possible (see Section 2.2), model results serve as a direct comparison. The experimental acceptance that is crucial to the observable correlations can also be implemented in these model studies.

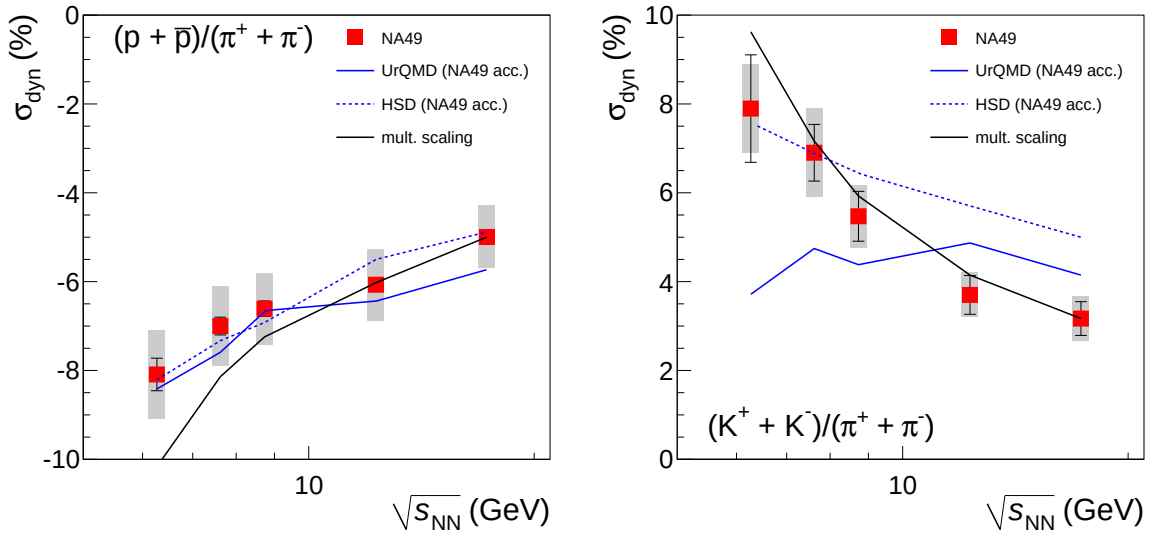

Figure 6.2: Energy dependence of σ_{dyn} for the $(\mathrm{p}+\overline{\mathrm{p}})/(\pi^+ + \pi^-)$ and $(\mathrm{K}^+ + \mathrm{K}^-)/(\pi^+ + \pi^-)$ ratios in central Pb+Pb collisions [118]. The NA49 results are compared to calculations in the transport models UrQMD [94] and HSD [123, 96], as well as to the multiplicity scaling [190, 121] described in Section 6.2.

Two hadron transport models are used here, Ultrarelativistic Quantum Molecular Dynamics (UrQMD) [92, 93, 94] and Hadron-String Dynamics (HSD) [95]. Both share the basic principle to describe the dynamical evolution of a heavy-ion collision in transport theory, through subsequent hadronic interactions. Input parameters are hadronic cross sections and decay parameters. These parameters are obtained from hadronic interaction measurements and complemented by estimates where necessary. Phase transition effects are clearly not expected here: Following from the non-equilibrium Boltzmann nature of the models, no phases are established. Further, the degrees of freedom remain hadronic, independent of the surrounding density. Both models have been used to evaluate inclusive hadron production, study stopping power and collective flow in nuclear collisions at a wide range of energies from the Coulomb barrier ($E_{\mathrm{Beam}} \approx 100A$ MeV) to RHIC energies ($\sqrt{s_{NN}} = 200$ GeV). UrQMD was even used beyond to make predictions for p+p and Pb+Pb collisions at LHC [191].

For the model comparisons presented in this thesis, 100k UrQMD events were generated at $\sqrt{s_{NN}} = 7.6$, 8.7, 12.3 and 17.3 GeV. At the lowest energy, to reduce the statistical error here, 200k events were produced. UrQMD version 2.3 [94] was run on the computing cluster at the Center for Scientific Computing Frankfurt. To reflect the centrality selection used in the experimental analysis, a random distribution of impact parameters with $b < 2.75$ fm was generated. This corresponds to the most central 3.5%. For HSD

comparisons, this thesis relies on results of the Frankfurt HSD group published in [123] (for the $(K^+ + K^-)/(\pi^+ + \pi^-)$ ratio) and [96] (for $(K^+ + K^-)/(p + \overline{p})$ and $(p + \overline{p})/(\pi^+ + \pi^-)$). In both model calculations, the NA49 acceptance for the present data analysis has been applied, by using the four-dimensional tables defined in [176].

The model comparison to $(K^+ + K^-)/(\pi^+ + \pi^-)$ and $(p + \overline{p})/(\pi^+ + \pi^-)$ fluctuations [118] was already discussed in Section 2.2. To summarize this discussion, the results are also shown in Figure 6.2. The proton to pion fluctuations were fully reproduced by the hadronic models, and UrQMD and HSD agree. Purely hadronic correlations such as resonance decays obviously govern the fluctuations of this ratio. In case of $(K^+ + K^-)/(\pi^+ + \pi^-)$ fluctuations, the situation is different: The two models UrQMD and HSD disagree on both the magnitude and on the shape of the energy dependence of σ_{dyn}. While HSD reproduces the $\propto 1/\sqrt{s_{NN}}$ dependence and meets the low energy points, it over-predicts the higher energies. UrQMD features a flat energy dependence at the level of the top energy measurements, thus missing the rise toward low energies.

For the new measurements of σ_{dyn} for $(K^+ + K^-)/(p + \overline{p})$ and K^+/p, the model comparison can be seen in Figure 6.1. HSD calculations are only available for the combined charges case. Both models see only a weak energy dependence of σ_{dyn}. The strong energy dependence seen in the data with the prominent change of sign is not reproduced. Although the two models disagree on the value and even the sign of σ_{dyn}, a common feature is the shape of the energy dependence, an almost constant value throughout the SPS energy range. The UrQMD prediction for both ratios is negative, meeting the high energy data points. With its weak energy dependence it fails to describe σ_{dyn} at the lower energies. In UrQMD, both charge combinations have a constant difference over the studied energy range, another feature in contrast to the data, where this difference develops a sudden maximum around $\sqrt{s_{NN}} = 8$ GeV.

The disagreement between the two hadronic models makes the interpretation difficult. When however just comparing the energy dependence of σ_{dyn} irrespective of its value, a strong change with energy is a feature of the data that cannot be reproduced in hadronic models. A possibility to explore the effect of equilibration as opposed to the out-of-equilibrium Boltzmann transport is given in the new version 3.3 of the UrQMD model [192]. It couples the transport and the hydrodynamic description of heavy-ion collisions. Non-equilibrium initial conditions are provided by UrQMD to account for initial state density fluctuations. The density distribution is fed into a (3+1)-dimensional hydro code that models the further evolution and expansion of the system until the energy density drops below a defined freeze-out criterion. Here, the hydrodynamic currents are

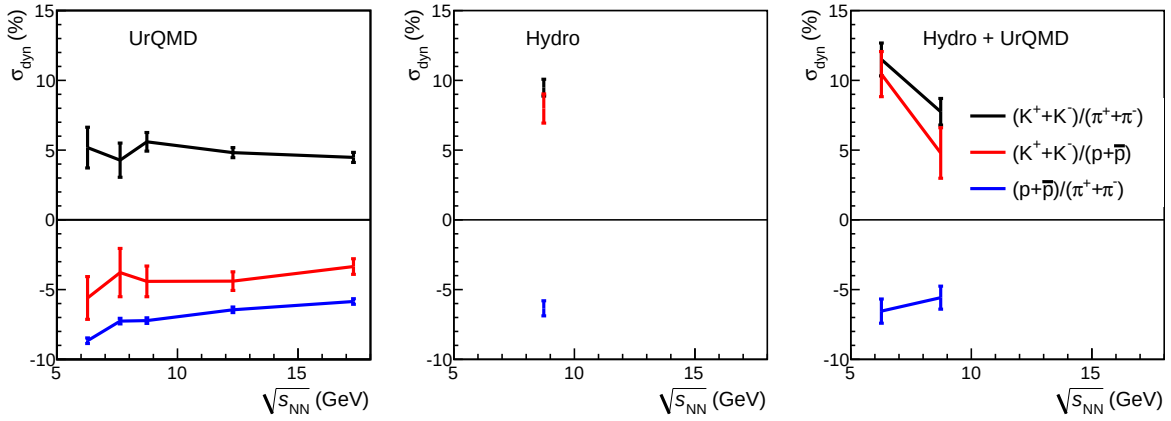

Figure 6.3: σ_{dyn} extracted from simulations in the combined transport/hydrodynamical model UrQMD 3.3 [192]. Different model options are compared: the conventional transport-only approach (left), hydrodynamics with free streaming after Cooper-Frye hadronization (center) and hydrodynamics coupled with the hadronic cascade (right).

converted via the Cooper-Frye formalism to individual hadrons. Their transport until thermal decoupling is again performed in UrQMD.

Particular phases can be skipped in the model, allowing to study the effect of the hadronic cascade after hadronization, or the impact of the intermediate hydro stage. A multitude of observables has been studied in the hybrid approach, e.g. the influence of the hydro stage on strangeness production [193] or elliptic flow and how the hydrodynamical stage conveys initial state fluctuations to final state flow observables [194]. Recently, the model was used to investigate how the grand-canonical hadro-chemical equilibrium provided by the Cooper-Frye hadronization is affected by the subsequent hadronic cascade [195]. In the present analysis, only a first attempt has been made with the new model. Figure 6.3 shows the comparison of σ_{dyn} for the $(\mathrm{K}^+ + \mathrm{K}^-)/(\pi^+ + \pi^-)$, $(\mathrm{K}^+ + \mathrm{K}^-)/(\mathrm{p} + \overline{\mathrm{p}})$ and $(\mathrm{p} + \overline{\mathrm{p}})/(\pi^+ + \pi^-)$ ratios from the usual UrQMD mode of hadronic transport from the early to the final state (left panel), at the end of the hydrodynamic evolution (center) and at the end of the hadronic cascade (right). While this study was only performed for few energies, it can be seen that the $(\mathrm{p} + \overline{\mathrm{p}})/(\pi^+ + \pi^-)$ fluctuations are not affected by the change of model parameters, while σ_{dyn} for $(\mathrm{K}^+ + \mathrm{K}^-)/(\pi^+ + \pi^-)$ is pushed to higher values. A spectacular effect is observed on the $(\mathrm{K}^+ + \mathrm{K}^-)/(\mathrm{p} + \overline{\mathrm{p}})$ fluctuations: The hydrodynamic stage induces a positive σ_{dyn} that is not obliterated by the hadronic cascade. A more detailed study is required to clarify the systematics of this effect and whether the hybrid model holds a potential explanation of the present data.

6.2 Multiplicity Scaling of Ratio Fluctuations

The following attempt to explain the rise of σ_{dyn} for $(\mathrm{K}^+ + \mathrm{K}^-)/(\pi^+ + \pi^-)$ towards low energies brings up the inherent multiplicity dependence of the variable itself. Such a dependence was already suggested in [77], and has been observed in the centrality dependence of $(\mathrm{K}^+ + \mathrm{K}^-)/(\pi^+ + \pi^-)$ fluctuations in the STAR experiment at RHIC [124]. While it was pointed out that uncorrected multiplicities in the acceptance of the particular fluctuation analysis are relevant [77, 190], the results from Au+Au collisions at $\sqrt{s_{NN}} =$ 62.4 and 200 GeV proved to scale with the midrapidity charged particle density $\mathrm{d}N/\mathrm{d}\eta$ in the same centrality bin, corrected for acceptance and efficiency losses [124]. The STAR results measured in the ν_{dyn} variable proved to follow $\nu_{\mathrm{dyn}} \propto 1/\mathrm{d}N/\mathrm{d}\eta + \nu_0$ with an offset ν_0. The NA49 results at lower energies [118] didn't seem to fit into the same picture until it was shown that uncorrected multiplicities should be used. For the STAR results, this change has no consequences as due to the acceptance, $\mathrm{d}N/\mathrm{d}\eta \propto \langle N \rangle$ here. For a fixed target experiment, this proportionality is no longer given as the acceptance changes as a function of energy. However taking into account this change through the use of the relevant multiplicities, a common scaling for STAR and NA49 data could be found. A further scaling approach was also pointed out in [196].

Following Chapter 2, the hadron ratios studied here are intensive quantities, and the ratio fluctuation observables are defined to be mostly independent of volume fluctuations. Nevertheless, σ_{dyn} holds an inherent remaining multiplicity dependence, simply by the normalization chosen in equation (2.1). As an example, in a hadron-resonance gas model, variances scaled by the mean $\omega = \mathrm{Var}(N)/\langle N \rangle$ are constant at a given temperature, while the $\sigma^2 = \mathrm{Var}(N)/\langle N \rangle^2 = \omega/\langle N \rangle$ hold a $1/\langle N \rangle$ dependence as a function of volume. A generic baseline for σ_{dyn} is derived in [77], suggesting that

$$\sigma^2_{\mathrm{dyn}} \propto \frac{1}{\langle A \rangle} + \frac{1}{\langle B \rangle}. \tag{6.1}$$

This multiplicity dependence only covers inherent properties of the variable itself. A deviation from this behavior would indicate a change in the underlying physics. In [190], a quantity similar to ω is defined, the scaled correlations

$$C_{AB} := \frac{\langle \delta A \delta B \rangle - \delta_{AB} \langle A \rangle}{\sqrt{\langle A \rangle \langle B \rangle}}. \tag{6.2}$$

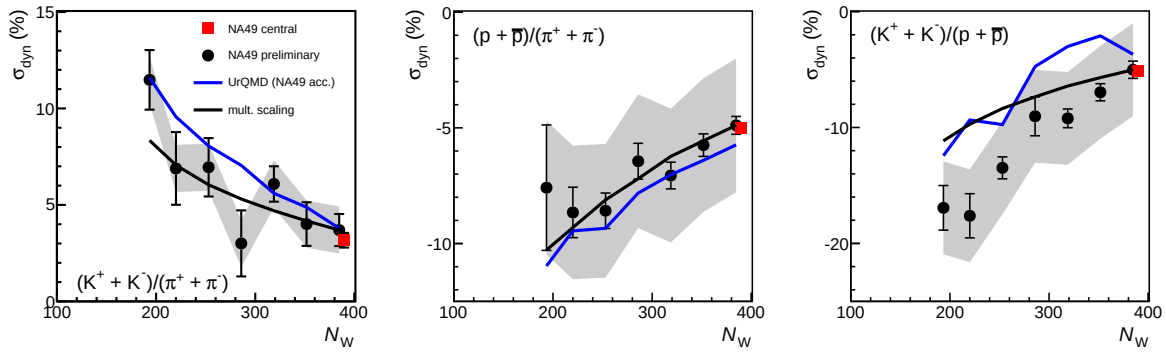

Figure 6.4: Centrality dependence of σ_{dyn} for $(\mathrm{K}^+ + \mathrm{K}^-)/(\pi^+ + \pi^-)$, $(\mathrm{p} + \overline{\mathrm{p}})/(\pi^+ + \pi^-)$ and $(\mathrm{K}^+ + \mathrm{K}^-)/(\mathrm{p} + \overline{\mathrm{p}})$ in Pb+Pb collisions at $\sqrt{s_{NN}} = 17.3$ GeV [106, 121]. The centrality is expressed in terms of N_{W}, the number of participating nucleons.

With them and the assumed equivalence of σ_{dyn} and ν_{dyn}, equation (2.7) can be rewritten as

$$\sigma^2_{\mathrm{dyn}} = \frac{1}{\langle A \rangle} C_{AA} + \frac{1}{\langle B \rangle} C_{BB} - \frac{2}{\sqrt{\langle A \rangle \langle B \rangle}} C_{AB}. \tag{6.3}$$

The C factors can be evaluated in a hadron-resonance gas model where they are constant at fixed temperature just like ω. A hadron-resonance gas has a limited number of correlation mechanisms: energy, momentum and charge conservation and resonance decays. As a consequence, the scaled correlations depend on the ratios of resonant to non-resonant states. A number of alternative scalings can be derived from equation (6.3) for special cases. As an example, for K/π fluctuations, the $1/\langle \mathrm{K} \rangle$ term dominates where $\langle \mathrm{K} \rangle \ll \langle \pi \rangle$, leading to

$$\sigma^2_{\mathrm{dyn}} \propto \frac{1}{\langle K \rangle}. \tag{6.4}$$

A detailed comparison of the different suggested proportionalities is given in [190] for the $(\mathrm{K}^+ + \mathrm{K}^-)/(\pi^+ + \pi^-)$ case. Here, the most general formula from equation (6.1) is used because it can be applied to all studied ratios. In Figure 6.2, the expectation from the multiplicity scaling is indicated by a black line and based on the top energy point:

$$\sigma_{\mathrm{dyn}}(\sqrt{s_{NN}}) = \sigma_{\mathrm{dyn}}(17.3\ \mathrm{GeV}) \frac{\sqrt{\frac{1}{\langle \mathrm{K}^+ + \mathrm{K}^- \rangle} + \frac{1}{\langle \pi^+ + \pi^- \rangle}}\Big|_{\sqrt{s_{NN}}}}{\sqrt{\frac{1}{\langle \mathrm{K}^+ + \mathrm{K}^- \rangle} + \frac{1}{\langle \pi^+ + \pi^- \rangle}}\Big|_{17.3\ \mathrm{GeV}}}. \tag{6.5}$$

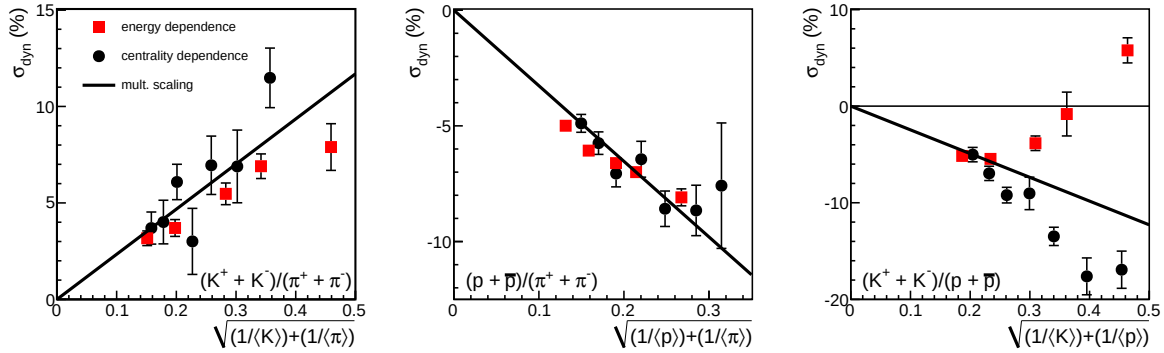

Figure 6.5: Energy and centrality dependence of σ_{dyn} for $(\mathrm{K}^{+}+\mathrm{K}^{-})/(\pi^{+}+\pi^{-})$, $(\mathrm{p}+\overline{\mathrm{p}})/(\pi^{+}+\pi^{-})$ and $(\mathrm{K}^{+}+\mathrm{K}^{-})/(\mathrm{p}+\overline{\mathrm{p}})$ [106, 121, 118, 64], as a function of the scaling variable suggested in the text.

It gives a good description of the energy dependence of $(\mathrm{K}^{+}+\mathrm{K}^{-})/(\pi^{+}+\pi^{-})$ and $(\mathrm{p}+\overline{\mathrm{p}})/(\pi^{+}+\pi^{-})$ fluctuations. The centrality dependence of ratio fluctuations is the ideal test for this approach. It is conceived as the setting to test an approximately unchanged system as a function of its size. The centrality dependence of $(\mathrm{K}^{+}+\mathrm{K}^{-})/(\pi^{+}+\pi^{-})$, $(\mathrm{p}+\overline{\mathrm{p}})/(\pi^{+}+\pi^{-})$ and $(\mathrm{K}^{+}+\mathrm{K}^{-})/(\mathrm{p}+\overline{\mathrm{p}})$ ratio fluctuations has been studied in NA49 [106, 186], and is presented in Figure 6.4 [121]. The analysis from [106] is in good agreement with the present study and [118] where overlapping. σ_{dyn} is positive for $(\mathrm{K}^{+}+\mathrm{K}^{-})/(\pi^{+}+\pi^{-})$ and negative for $(\mathrm{p}+\overline{\mathrm{p}})/(\pi^{+}+\pi^{-})$ and $(\mathrm{K}^{+}+\mathrm{K}^{-})/(\mathrm{p}+\overline{\mathrm{p}})$. Going to more peripheral collisions, the magnitude of σ_{dyn} shows an increase similar to the observation made in STAR [124] for the $(\mathrm{K}^{+}+\mathrm{K}^{-})/(\pi^{+}+\pi^{-})$ ratio fluctuations at two higher energies. The result of UrQMD calculations is also shown in Figure 6.4 (blue line), predicting the increase seen in the data. The scaling from equation (6.1) follows the same centrality dependence. This is compatible with the hypothesis that at constant energy the underlying correlations are not significantly changed by a variation of the system size [121].

The scaling properties observed in Figures 6.2 and 6.4 are brought together in Figure 6.5. Here, σ_{dyn} results from the centrality and the energy dependence are plotted as a function of the scaling variable from equation (6.1). For $(\mathrm{K}^{+}+\mathrm{K}^{-})/(\pi^{+}+\pi^{-})$ and $(\mathrm{p}+\overline{\mathrm{p}})/(\pi^{+}+\pi^{-})$, the individual energy and centrality scaling can be combined to a universal description. In contrast, when bringing the energy dependence of the $(\mathrm{K}^{+}+\mathrm{K}^{-})/(\mathrm{p}+\overline{\mathrm{p}})$ fluctuations on the same panel, it is obvious from the change of sign that no common energy-centrality scaling can be found. The right panel of Figure 6.5 is indicative of this behavior.

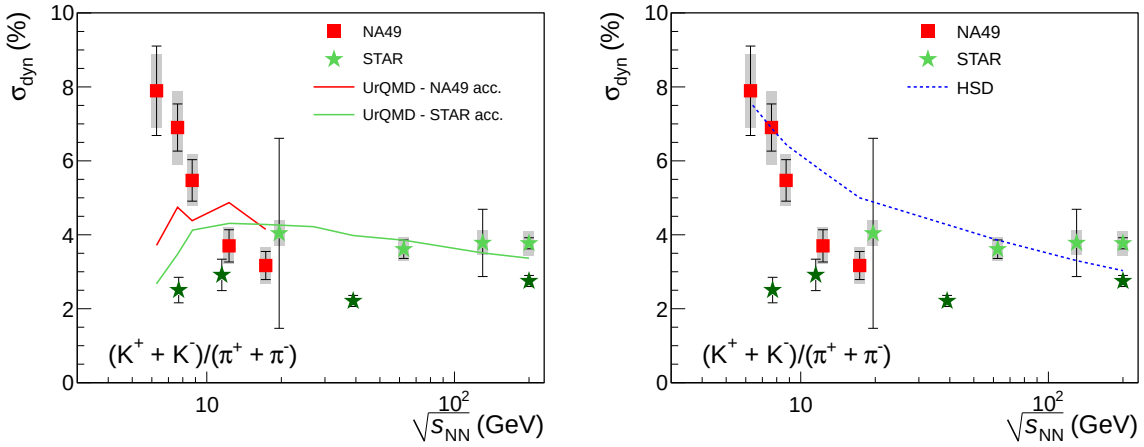

Figure 6.6: NA49 [118] and STAR data on $(K^+ + K^-)/(\pi^+ + \pi^-)$ fluctuations, compared to UrQMD (left) and HSD (right) calculations. Dark green stars represent new data from the RHIC beam energy scan [125], while light green symbols show the values published in [124].

6.3 Comparison to STAR Data

In Figures 6.6, 6.7 and 6.8, the NA49 data from [118, 64] is put into the context of existing data. STAR has measured ratio fluctuations in the energy range between $\sqrt{s_{NN}} = 7.7$ and 200 GeV. At this opportunity, also results from the transport models over the whole energy range are discussed. HSD calculations are taken from [104, 96], while UrQMD calculations at $\sqrt{s_{NN}} > 20$ GeV were kindly provided by [197].

The STAR measurements of $\sigma_{\mathrm{dyn}}((K^+ + K^-)/(\pi^+ + \pi^-))$ [124], indicated by light green markers in Figure 6.6 agree with the top SPS energy point from NA49 [118], and show a weak energy dependence toward higher energies. This behavior is is compatible with the UrQMD calculations and the scaling shown in [190]. The HSD predictions [104] meet the general trend but fail to describe the exact energy dependence at intermediate energies. New STAR measurements [125] in the recent RHIC beam energy scan [198] extend over the energy range $7.7 \leq \sqrt{s_{NN}} \leq 200$ GeV and are shown as dark green markers. The new STAR analysis is only performed using the ν_{dyn} variable and then converted to σ_{dyn}. It has been verified that this method agrees with the usual σ_{dyn} method on the same datasets. Nevertheless, a systematic offset is observed compared to the previous STAR measurements. The energy dependence remains weak. The lowest energy STAR point is in disagreement with the NA49 data. In common discussions between the two experimental collaborations, several potential reasons of this discrepancy were suggested. The most important differences are:

- The acceptance of the two experiments. STAR, in a collider environment has symmetric acceptance around midrapidity, fixed in the center-of-mass system, compared to the fixed-target geometry of NA49 described in Section 5.3. It also features full azimuthal acceptance. NA49 on the other hand has a wider acceptance toward forward rapidity, and in the low p_{T} region. In general, the correlations an experiment can probe are fully dependent on the acceptance (cf. Section 1.4). In the present case, the hadronic model UrQMD does not show an effect when going from NA49 to STAR acceptance (cf. Figure 6.6, left). In the experiment however, novel correlations that are not implemented in UrQMD may play a role that do depend on the acceptance.
- Different particle identification methods are used in the two experiments. In the collider, the $1/\beta^2$ region of the Bethe-Bloch $\mathrm{d}E/\mathrm{d}x$ description can be used and provides a better separation, so that a PID fit as in Section 5.4 is not necessary. Particles can rather be counted in suitable $\mathrm{d}E/\mathrm{d}x, p$ windows. This method is even extended using the new time of flight detector in STAR. In the future, the usage of a method that is applicable to both experiments [127] may resolve this difference.
- The equivalence between ν_{dyn} and σ_{dyn} is expected to break down for low multiplicities. Studies in NA49 and STAR don't confirm this (cf. e.g. Section 5.8), but it remains a suspect for the discrepancy at the lowest comparable multiplicity.
- While NA49 determines the centrality by measuring the projectile spectator energy in the veto calorimeter (see Section 3.4), STAR uses the midrapidity charged particle multiplicity that is correlated to the measured hadron multiplicities. Future model calculations are planned to evaluate the effect of the different centrality selection methods.

Following the first report on this discrepancy [199] both experiments have put a large effort into a verification of all experimental procedures. So far the reason for the disagreement could not be identified. A potential solution lies in the scaling discussed in Section 6.2, as the average multiplicities within the STAR acceptance are larger than in NA49. This however remains under discussion [200].

The same comparison for the $(\mathrm{p}+\overline{\mathrm{p}})/(\pi^+ + \pi^-)$ ratio shown in Figure 6.7 exhibits an agreement between NA49 [118] and STAR [201, 199, 125] at all overlapping energies. The transport models consistently describe the low energy part up to $\sqrt{s_{NN}} = 20 \ldots 40$ GeV very well, but then deviate from the data and change sign to positive values of σ_{dyn}. Positive values are associated to a correlation via pair production (see Section 1.4) that

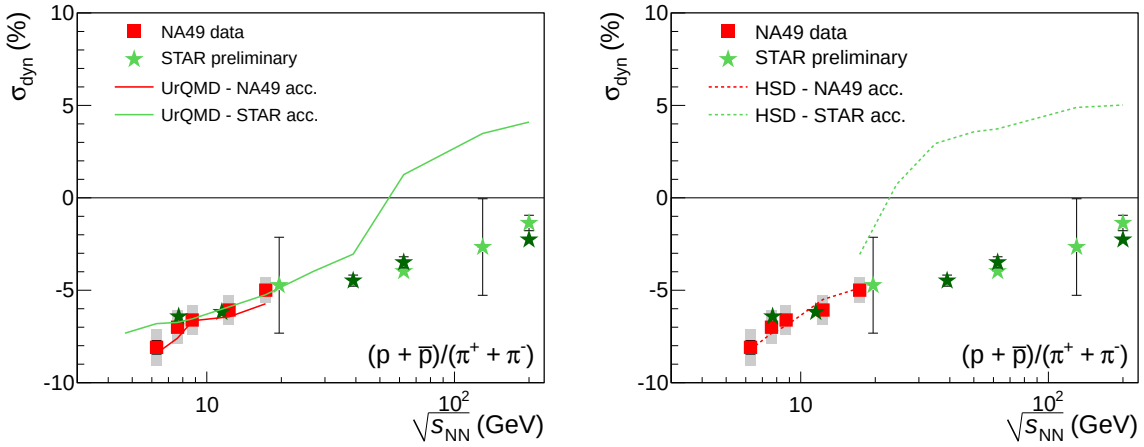

Figure 6.7: σ_{dyn} for the $(\mathrm{p}+\overline{\mathrm{p}})/(\pi^{+}+\pi^{-})$ ratio from NA49 and STAR. An agreement is observed in all overlapping regions between NA49 [118] (red markers), preliminary STAR results [201] (light green) and those from the beam energy scan [199, 125] (dark green). A comparison to the hadronic transport models UrQMD (left panel) and HSD (right) is also provided.

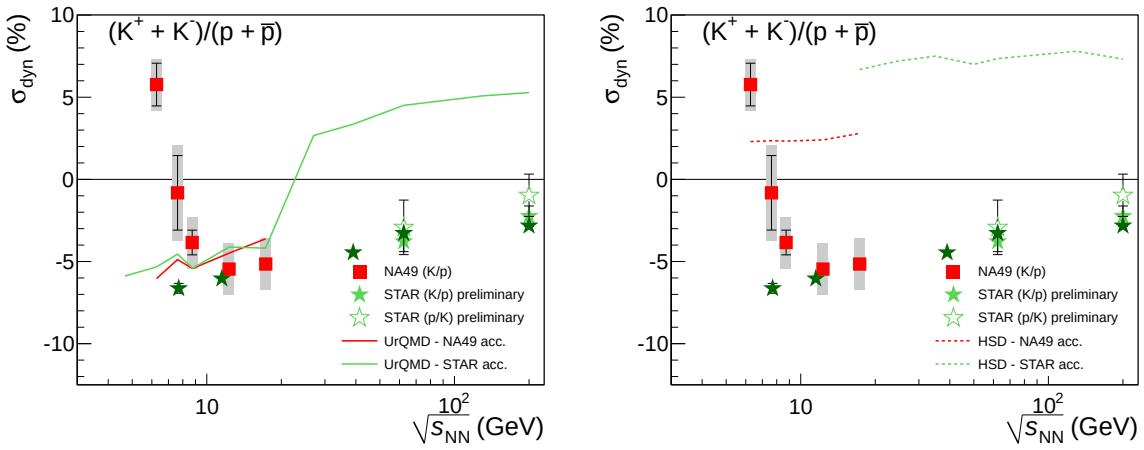

Figure 6.8: $(\mathrm{K}^{+}+\mathrm{K}^{-})/(\mathrm{p}+\overline{\mathrm{p}})$ fluctuations in the NA49 [64] and STAR [125] experiments as well as in the UrQMD and HSD transport models.

is expected to become more important at high energies. This mechanism seems to be overestimated in the models.

Finally in the comparison between the $(\mathrm{K}^{+}+\mathrm{K}^{-})/(\mathrm{p}+\overline{\mathrm{p}})$ fluctuation results between the two experiments (Figure 6.8), an agreement is observed except for the lowest energy STAR point ($\sqrt{s_{NN}} = 7.7$ GeV). Although the overall discrepancy is smaller, similar discussions as above for the $(\mathrm{K}^{+}+\mathrm{K}^{-})/(\pi^{+}+\pi^{-})$ case apply but did not lead to a conclusion as of yet. The hadronic models give a contradictory picture of potential acceptance effects. While in UrQMD (left panel of Figure 6.8), no acceptance effect

is seen, HSD (right) shows a step when changing from NA49 to STAR acceptance at $\sqrt{s_{NN}} \approx 20$ GeV.

The measurements within the STAR and NA49 collaborations provide the unique possibility to study the systematics of hadron ratio fluctuations over the wide energy range from $\sqrt{s_{NN}} = 6.3$ to 200 GeV. Future studies will clarify whether a disagreement at $\sqrt{s_{NN}} = 7.7$ GeV must be attributed to technical differences, the multiplicity scaling or the systematic error. The ratio fluctuation signal evolves smoothly with a weak energy dependence from the higher SPS energies on to $\sqrt{s_{NN}} = 200$ GeV.

6.4 Contribution to C_{BS} from Kaon-Proton Correlations

For a hadron-resonance gas, the definition of C_{BS} can be simplified. The derivation follows [66]. The total strangeness and baryon number in equation (2.9) can be calculated as $S = \sum_k n_k S_k$ and $B = \sum_k n_k B_k$, where the hadron species k has strangeness S_k, baryon number B_k and multiplicity n_k. Products in the full definition of C_{BS}, like e.g. $\langle BS \rangle$, in general contain diagonal terms $\propto \langle n_i^2 \rangle$ as well as cross terms $\propto \langle n_i n_j \rangle, i \neq j$. The latter vanish in the case of no correlation between hadron multiplicities, a general assumption in statistical models [37]. Using the multiplicity variances $\sigma_k^2 = \langle n_k^2 \rangle - \langle n_k \rangle^2$, C_{BS} of an uncorrelated hadron gas can be expressed as

$$C_{BS}^{(\mathrm{HG})} = -3 \frac{\sum_k \sigma_k^2 B_k S_k}{\sum_k \sigma_k^2 S_k^2}. \tag{6.6}$$

Under the further assumption $\sigma_k^2 = \langle n_k \rangle$, as realized e.g. in case of Poisson multiplicity distributions,

$$C_{BS}^{(\mathrm{HG,P})} = -3 \frac{\sum_k \langle n_k \rangle B_k S_k}{\sum_k \langle n_k \rangle S_k^2} = 3 \frac{\Lambda + \overline{\Lambda} + \Sigma + \overline{\Sigma} + 2\Xi + 2\overline{\Xi} + \ldots}{\mathrm{K} + \overline{\mathrm{K}} + \ldots + \Lambda + \overline{\Lambda} + \ldots} \tag{6.7}$$

When equation (6.7) is used to evaluate C_{BS}, all correlations are explicitly ignored. In a UrQMD model study, this approach has been compared to the full definition of C_{BS}. Figure 6.9 shows C_{BS} in the full definition as open symbols, compared to the approximation from equation (6.7). The difference between the two methods accounts for all correlations, and the model study can be used to evaluate the contribution of

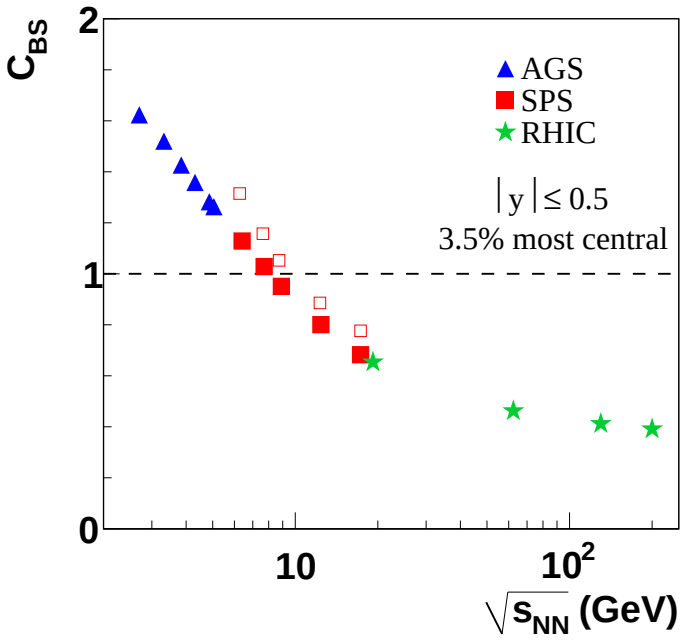

Figure 6.9: UrQMD evaluation of C_{BS} in the full definition (open symbols), compared to the result of the approximation from equation (6.7).

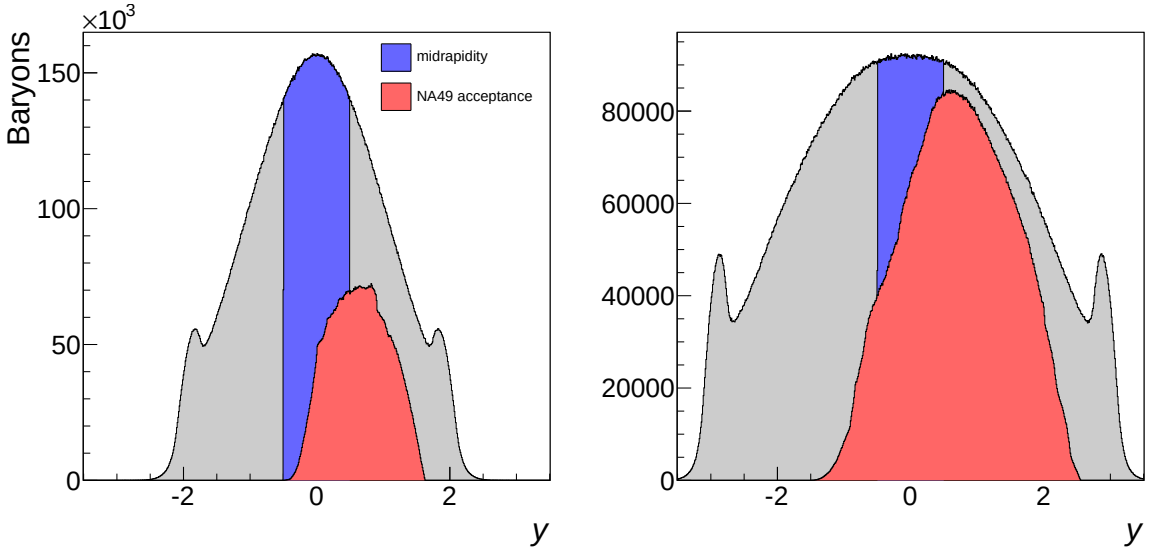

Figure 6.10: Effect of the acceptance cuts used in the UrQMD study on the distribution of all baryons for $\sqrt{s_{NN}} = 6.3$ (left) and 17.3 GeV (right). The midrapidity cut comprises $|y| < 0.5$. The NA49 cut tables were taken from [176].

hadronic correlations to C_{BS}. This comparison has been done in the SPS energy range, and Figure 6.9 indicates that the overall hadronic contribution is small and constantly positive here.

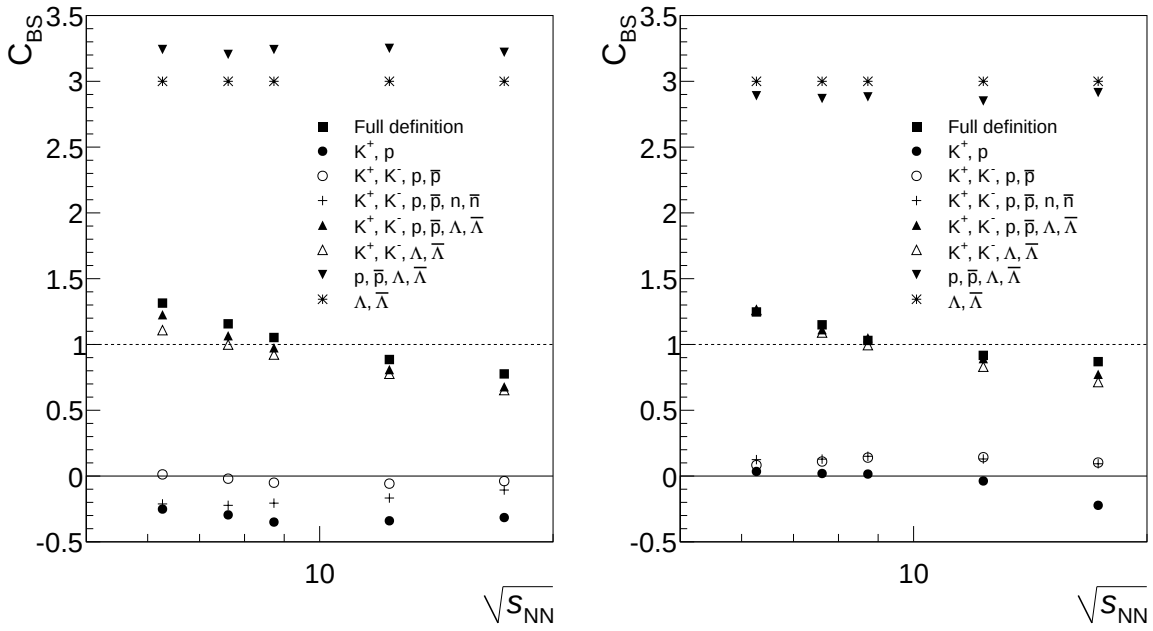

Figure 6.11: C_{BS} evaluated in the UrQMD model. The value based on the full definition from equation (2.9) is compared to selected individual contributions of particular hadron combinations. Small differences are visible comparing the midrapidity (left) to the NA49 acceptance (right).

Contributions from specific hadron combinations have been quantified using UrQMD. In the model, all strange hadrons and all baryons can be evaluated, while experimentally, event-by-event studies of e.g. neutrons or lambdas are not possible. By this means, a comparison of the observable quantities and the full baryon-strangeness correlation is achieved. In order to also explore the influence of acceptance changes, two acceptance filters were compared: the NA49 acceptance for the present analysis as tabulated in [176] and a simple midrapidity cut $|y| < 0.5$. The effect of these acceptances on the total baryon number distribution is sketched in Figure 6.10.

Figure 6.11 presents the C_{BS} values that are obtained when only evaluating certain hadron numbers in equation (2.9). Results in the midrapidity (left) and NA49 (right) acceptances show small differences. Note that the numbers presented in Figure 6.11 are not additive contributions, as the denominator is different for each. So for example, C_{BS} evaluated with K^+ and p only is here calculated as

$$C_{BS}(\mathrm{K}^+, \mathrm{p}) = -3\frac{\langle \mathrm{K}^+\mathrm{p}\rangle}{\langle \mathrm{K}^{+2}\rangle}. \tag{6.8}$$

When only considering lambdas, C_{BS} is constantly three, as expected from equation (2.9). A good approximation of the full definition is only achieved when at least kaons and lambdas are considered. The kaon only or kaon-proton cases are close to zero and show a strong acceptance effect in the model.

The influence of kaon-proton correlations is better considered as an additional contribution on top of the uncorrelated situation described by equation (6.7). In the presence of correlations, corrections to equation (6.7) apply, and the attempt to quantify them below follows [202]. In addition to the diagonal terms in the approximation, cross terms will play a role, and the contribution from a correlation between K^+ and p can be expressed as

$$\Delta C_{BS}(\mathrm{K}^+,\mathrm{p}) \approx -3\frac{\langle \delta \mathrm{K}^+ \delta \mathrm{p}\rangle}{\langle S^2\rangle} \approx -3\frac{\langle \delta \mathrm{K}^+ \delta \mathrm{p}\rangle}{\langle \mathrm{K}+\Lambda+\Sigma\rangle}. \tag{6.9}$$

The second approximate identity assumes small contributions from antiparticles to the strangeness. In contrast to equation (6.8), the full strangeness normalization makes it an additive correction to equation (6.7). Requiring strangeness conservation on the average

$$\begin{aligned} \langle \mathrm{K}\rangle &= \langle \Lambda+\Sigma\rangle \\ \langle \mathrm{K}\rangle &= \langle \mathrm{K}^+ + \mathrm{K}^0\rangle \approx 2\langle \mathrm{K}^+\rangle, \end{aligned}$$

approximations of the denominator can be made. When further using the correlation coefficient between K^+ and p,

$$\gamma_{\mathrm{K}^+\mathrm{p}} \equiv \frac{\langle \delta \mathrm{K}^+ \delta \mathrm{p}\rangle}{\langle \mathrm{K}^+\rangle\langle \mathrm{p}\rangle}, \tag{6.10}$$

$\Delta C_{BS}(\mathrm{K}^+,\mathrm{p})$ can be expressed as

$$\Delta C_{BS}(\mathrm{K}^+,\mathrm{p}) \approx -\frac{3}{4}\frac{\langle \delta \mathrm{K}^+ \delta \mathrm{p}\rangle}{\langle \mathrm{K}^+\rangle} = -\frac{3}{4}\langle \mathrm{p}\rangle \gamma_{\mathrm{K}^+\mathrm{p}}. \tag{6.11}$$

While the amplitude of this effect is not well traceable due to the assumptions in the approximations, we may learn something from the sign of the correlation coefficient. The correlation coefficient enters in the third term of the approximation of σ_{dyn}. Looking at Figure 2.5, the hadron gas and quark-gluon plasma predictions for C_{BS} cross in the SPS energy range. As a consequence the difference between the two changes sign and the same is expected from the additional correlations quantified in ΔC_{BS}. The approximation

made here is based on strong assumptions and preliminary. A qualitative connection to the change of sign observed in the data suggests itself but is as of yet inconclusive.

6.5 Conclusion

The dynamics of relativistic nucleus-nucleus collisions can transport the collision volume to energy densities well exceeding the QCD phase boundary between hadron-resonance and quark-gluon plasma matter. Upon expansion, the system traverses this line, hadronizing there. This occurs—according to present lattice QCD theory—under conditions that range from a mere cross-over from partons to hadrons, via a second order phase transition if the conjectured critical point of QCD is encountered, and finally to a first order phase transition line. The latter two constellations are expected to lead to substantial specific fluctuations of the emerging hadrons in momentum and number density space. Multiplicity ratios of created kaons and protons in particular can be defined for individual central collision events at SPS energies and above. Their fluctuations should also survive the final hadronic cascade expansion stage, serving as a diagnostic tool for the system properties during traversal of the phase boundary and, specifically, a search for a QCD critical point.

In the present study we have systematically investigated the second moments of the event-by-event fluctuations of the $(K^+ + K^-)/(p + \overline{p})$ and K^+/p ratios in Pb+Pb collisions over the energy domain provided by the CERN SPS, $6.3 \leq \sqrt{s_{NN}} \leq 17.3$ GeV. The lattice QCD estimates place the potential critical point into this interval. The data for central Pb+Pb collisions were gathered in the experiment NA49. Its large acceptance admits from 60 to 600 identified hadrons to be recorded per event, allowing the determination of meaningful moments from the event-by-event distribution. Hadron identification in individual events was accomplished in a maximum likelihood method based on hadron specific ionization measured to within 4% resolution in the large volume Time Projection Chambers of NA49.

For the fluctuation analysis, we employ the observable $\sigma_{\rm dyn}$ that was already used by NA49 in a preceding analysis of $(K^+ + K^-)/(\pi^+ + \pi^-)$ and $(p + \overline{p})/(\pi^+ + \pi^-)$ ratio fluctuations. It is based on the dispersion and the mean of the measured event-by-event hadron ratio distribution. An isolation of genuine dynamical fluctuations from finite number and experimentally (resolution) induced fluctuations is achieved in the observable $\sigma_{\rm dyn}$ by subtraction of a Monte Carlo generated mixed event background distribution.

Over the measured interval of SPS energies, both the $\sigma_{\rm dyn}$ for $({\rm K}^+ + {\rm K}^-)/({\rm p} + \overline{\rm p})$ and for ${\rm K}^+/{\rm p}$ exhibit a transition from values in the -5% domain at top SPS energy to positive values of 5–8% at the lowest energy. Transport models serving as a hadronic baseline do not exhibit this distinct change of sign. Also intuitively, the turn to positive values is difficult to trace: It indicates an anti-correlation between kaons and protons of unknown origin. An intrinsic multiplicity dependence of $\sigma_{\rm dyn}$ measurements leads to a scaling description of ratio fluctuations. The observed energy and centrality dependence of $({\rm K}^+ + {\rm K}^-)/(\pi^+ + \pi^-)$ and $({\rm p} + \overline{\rm p})/(\pi^+ + \pi^-)$ fluctuations can be reduced to this trivial background contribution in a consistent way. The $({\rm K}^+ + {\rm K}^-)/({\rm p} + \overline{\rm p})$ and ${\rm K}^+/{\rm p}$ fluctuations reported from the present analysis however require an additional physics input.

Fluctuation measurements can in general not directly be interpreted but require model comparisons to take into account superposed effects or the experimental acceptance. In addition to the failure of purely hadronic models in describing the present data it would be instructive to have a model that explicitly incorporates phase transition or critical point effects. Attempts of such a model, e.g. reproducing a critical refocussing of trajectories in the phase diagram exist so that a better understanding of the present data can be expected together with further model advancements.

Appendix A

Relativistic Kinematics

This appendix has been included from [138] for reference and completeness. In the heavy ion collisions studied here, both initial and final state are highly relativistic, hence the name *ultrarelativistic heavy ion collisions*. Suitable kinematic quantities have been defined. The most important variables and units used are summarized in the following.

When considering the relativistic effects of time dilation or length contraction, the *Lorentz factor* γ is used. It is defined as

$$\gamma \equiv \frac{E}{m} = \frac{1}{\sqrt{1-\beta^2}}, \tag{A.1}$$

where $\beta = v/c$ is the velocity expressed as fraction of the speed of light. Furthermore, the following relations between β, γ, particle mass m and energy E are useful:

$$\begin{aligned} \beta &= p/E \\ \beta\gamma &= p/m. \end{aligned} \tag{A.2}$$

Units

The standard units used are GeV for energies, GeV/c for momenta, GeV/c^2 for masses and cm for lengths. While in the units c still appears, the convention $\hbar = c = 1$ is used for calculations.

Phase Space Variables of Final State

The phase space of the particles produced in the collisions is spanned by the three components of the momentum $\boldsymbol{p}$: p_x, p_y and p_z. It may be necessary to do Lorentz transformations along the beam axis (which is, by convention, the z axis) in order to change e.g. from the laboratory frame into the centre of mass system of the collision. In addition, the momentum distribution in z is very broad (ranging from target to beam momentum) compared to the momenta perpendicular to the beam axis that only developed through scattering. This calls for different variables for *longitudinal* and *transverse* phase space.

p_x and p_y are replaced by the *transverse momentum* p_T and the azimuthal angle ϕ by the following conversions:

$$\begin{aligned} p_\mathrm{T} &= \sqrt{p_x^2 + p_y^2} \\ \phi &= \arctan \frac{p_y}{p_x} \end{aligned} \tag{A.3}$$

When only the statistical properties of many events are considered, azimuthal symmetry can be assumed and ϕ does not play a role. Another important quantity is the *transverse mass*, defined as

$$m_\mathrm{T} \equiv \sqrt{p_\mathrm{T}^2 + m^2}. \tag{A.4}$$

While the transverse momentum is Lorentz invariant under transformations along the beam axis, this is not the case for the longitudinal momentum p_z. It is therefore replaced by the *rapidity* denoted with y.

$$y = \frac{1}{2} \ln \left(\frac{E + p_z}{E - p_z} \right) \tag{A.5}$$

$E = \sqrt{|\boldsymbol{p}|^2 + m^2}$ is the particle's total Energy and m the mass. The shape of the rapidity distribution is invariant under Lorentz transformations. The effect of such a transformation (e.g. from laboratory to center-of-mass frame) is thus just a linear shift:

$$y' = y + y_0. \tag{A.6}$$

An alternative way to calculate the rapidity is

$$y = \text{arctanh}\beta_z,$$

where $\beta_z = v_x/c$ is the longitudinal velocity.

Invariant Mass Calculation

A particle's mass is invariant in any coordinate system. It can be expressed by

$$m = \sqrt{E^2 - |\boldsymbol{p}|^2} \tag{A.7}$$

In the V^0-decay, the mass m_V of the decayed particle can be reconstructed by using energy and momentum conservation in the decay. From equation A.7 then follows

$$\begin{aligned} m_\text{V} &= \sqrt{(E_1 + E_2)^2 - |\boldsymbol{p}_1 + \boldsymbol{p}_2|^2} \\ &= \sqrt{m_1^2 + m_2^2 + 2\left(E_1 E_2 - \boldsymbol{p}_1 \boldsymbol{p}_2\right)} \end{aligned}$$

where E_i, $\boldsymbol{p}_\text{i}$ and m_i are the energy, momentum and mass of the i-th daughter particle. The result depends on the assumption of the decaying particle, because the daughter particles' masses have to be put into the calculation. In the reconstruction, the invariant mass is calculated for any possible assumption.

Collision Energies

The collisions in fixed target experiments are characterized by the incident beam energy. In order to make them comparable to collider experiments, the energy disposable in the centre of mass frame is given per nucleon-nucleon pair:

$$\sqrt{s_{_{NN}}} = \sqrt{(E_\text{Beam} + E_\text{Target})^2 - |\boldsymbol{p}_\text{Beam} + \boldsymbol{p}_\text{Target}|^2}$$

At the highest SPS energy, where the beam energy per nucleon is $E_\text{Beam} = 158$ GeV and the target is at rest ($E_\text{Target} = 0$ GeV), the resulting centre of mass energy is $\sqrt{s_{_{NN}}} = 17.3$ GeV.

Appendix B

Statistical Error on σ_{dyn}

Gaussian Propagation of the Statistical Error on σ_{dyn}

Following the definition

$$\sigma_{\mathrm{dyn}} := \mathrm{sign}\left(\sigma^2_{\mathrm{data}} - \sigma^2_{\mathrm{mix}}\right)\sqrt{|\sigma^2_{\mathrm{data}} - \sigma^2_{\mathrm{mix}}|} \qquad \text{with} \qquad \sigma := \frac{\sqrt{\mathrm{Var(K/p)}}}{\langle \mathrm{K/p}\rangle}, \quad \text{(B.1)}$$

the statistical error in σ_{dyn} comes from the measured statistical errors in the following four quantities (for which we introduce a shorthand notation for readability in this appendix):

$$\begin{aligned} \mathrm{Var(K/p)_{data}} &=: v_{\mathrm{data}} \\ \mathrm{Var(K/p)_{mix}} &=: v_{\mathrm{mix}} \\ \langle K/p\rangle_{\mathrm{data}} &=: m_{\mathrm{data}} \\ \langle K/p\rangle_{\mathrm{mix}} &=: m_{\mathrm{mix}} \end{aligned}$$

Using this notation, σ_{dyn} reads

$$|\sigma_{\mathrm{dyn}}| = \sqrt{\left|\frac{v_{\mathrm{data}}}{m^2_{\mathrm{data}}} - \frac{v_{\mathrm{mix}}}{m^2_{\mathrm{mix}}}\right|}$$

The partial derivative needed for Gaussian propagation of uncertainties are:

$$\begin{aligned}
\frac{\partial \sigma_{\mathrm{dyn}}}{\partial v_{\mathrm{data}}} &= \frac{1}{2m_{\mathrm{data}}^2}\left(\left|\frac{v_{\mathrm{data}}}{m_{\mathrm{data}}^2} - \frac{v_{\mathrm{mix}}}{m_{\mathrm{mix}}^2}\right|\right)^{-\frac{1}{2}} \\
&= \frac{1}{2m_{\mathrm{data}}^2}\frac{1}{\sigma_{\mathrm{dyn}}} \\
\frac{\partial \sigma_{\mathrm{dyn}}}{\partial v_{\mathrm{mix}}} &= -\frac{1}{2m_{\mathrm{mix}}^2}\frac{1}{\sigma_{\mathrm{dyn}}} \\
\frac{\partial \sigma_{\mathrm{dyn}}}{\partial m_{\mathrm{data}}} &= -\frac{v_{\mathrm{data}}}{m_{\mathrm{data}}^3}\frac{1}{\sigma_{\mathrm{dyn}}} \\
\frac{\partial \sigma_{\mathrm{dyn}}}{\partial m_{\mathrm{mix}}} &= \frac{v_{\mathrm{mix}}}{m_{\mathrm{mix}}^3}\frac{1}{\sigma_{\mathrm{dyn}}}
\end{aligned}$$

Due to the outer derivation, each term contains an $1/\sigma_{\mathrm{dyn}}$ dependence. The complete expression for the statistical error in σ_{dyn} then reads

$$\begin{aligned}
\Delta\sigma_{\mathrm{dyn}} &= \sqrt{\left(\frac{\partial \sigma_{\mathrm{dyn}}}{\partial v_{\mathrm{data}}}\cdot\Delta v_{\mathrm{data}}\right)^2 + \left(\frac{\partial \sigma_{\mathrm{dyn}}}{\partial v_{\mathrm{mix}}}\cdot\Delta v_{\mathrm{mix}}\right)^2} \\
&\qquad \overline{+\left(\frac{\partial \sigma_{\mathrm{dyn}}}{\partial m_{\mathrm{data}}}\cdot\Delta m_{\mathrm{data}}\right)^2 + \left(\frac{\partial \sigma_{\mathrm{dyn}}}{\partial m_{\mathrm{mix}}}\cdot\Delta m_{\mathrm{mix}}\right)^2} \\
&= \frac{1}{2\sigma_{\mathrm{dyn}}}\sqrt{\left(\frac{1}{m_{\mathrm{data}}^2}\cdot\Delta v_{\mathrm{data}}\right)^2 + \left(\frac{1}{m_{\mathrm{mix}}^2}\cdot\Delta v_{\mathrm{mix}}\right)^2} \\
&\qquad \overline{+\left(2\frac{v_{\mathrm{data}}}{m_{\mathrm{data}}^3}\cdot\Delta m_{\mathrm{data}}\right)^2 + \left(2\frac{v_{\mathrm{mix}}}{m_{\mathrm{mix}}^3}\cdot\Delta m_{\mathrm{mix}}\right)^2}
\end{aligned} \tag{B.2}$$

From the last equation, we can see the observed dependence of $\Delta\sigma_{\mathrm{dyn}}$ on the values of v_{data}, v_{mix}, m_{data}, m_{mix} and especially on σ_{dyn} itself.

Exact treatment of the absolute value

When exactly treating the absolute value in equation B.1, we need to distinguish three cases:

$$\begin{aligned}\sigma_{\mathrm{dyn}} &:= \operatorname{sign}\left(\sigma_{\mathrm{data}}^2 - \sigma_{\mathrm{mix}}^2\right)\sqrt{\left|\sigma_{\mathrm{data}}^2 - \sigma_{\mathrm{mix}}^2\right|} \\ &= \begin{cases} \sqrt{\sigma_{\mathrm{data}}^2 - \sigma_{\mathrm{mix}}^2} & \sigma_{\mathrm{data}} > \sigma_{\mathrm{mix}} \\ 0 & \sigma_{\mathrm{data}} = \sigma_{\mathrm{mix}} \\ -\sqrt{\sigma_{\mathrm{mix}}^2 - \sigma_{\mathrm{data}}^2} & \sigma_{\mathrm{data}} < \sigma_{\mathrm{mix}} \end{cases}\end{aligned}$$

The partial derivatives and the resulting error for the different cases now read

- for $\sigma_{\mathrm{data}} > \sigma_{\mathrm{mix}}$

$$\begin{aligned}\frac{\partial\sigma_{\mathrm{dyn}}}{\partial v_{\mathrm{data}}} &= \frac{1}{m_{\mathrm{data}}^2}\cdot\frac{1}{2\sqrt{\sigma_{\mathrm{data}}^2 - \sigma_{\mathrm{mix}}^2}} \\ \frac{\partial\sigma_{\mathrm{dyn}}}{\partial v_{\mathrm{mix}}} &= -\frac{1}{m_{\mathrm{mix}}^2}\cdot\frac{1}{2\sqrt{\sigma_{\mathrm{data}}^2 - \sigma_{\mathrm{mix}}^2}} \\ \frac{\partial\sigma_{\mathrm{dyn}}}{\partial m_{\mathrm{data}}} &= -\frac{v_{\mathrm{data}}}{m_{\mathrm{data}}^3}\cdot\frac{1}{\sqrt{\sigma_{\mathrm{data}}^2 - \sigma_{\mathrm{mix}}^2}} \\ \frac{\partial\sigma_{\mathrm{dyn}}}{\partial m_{\mathrm{mix}}} &= \frac{v_{\mathrm{mix}}}{m_{\mathrm{mix}}^3}\cdot\frac{1}{\sqrt{\sigma_{\mathrm{data}}^2 - \sigma_{\mathrm{mix}}^2}}\end{aligned}$$

$$\begin{aligned}\Delta\sigma_{\mathrm{dyn}} = \sqrt{\left(\frac{\Delta v_{\mathrm{data}}}{2m_{\mathrm{data}}^2\sqrt{\sigma_{\mathrm{data}}^2 - \sigma_{\mathrm{mix}}^2}}\right)^2 + \left(\frac{\Delta v_{\mathrm{mix}}}{2m_{\mathrm{mix}}^2\sqrt{\sigma_{\mathrm{data}}^2 - \sigma_{\mathrm{mix}}^2}}\right)^2} \\ \overline{+\left(\frac{v_{\mathrm{data}}\cdot\Delta m_{\mathrm{data}}}{m_{\mathrm{data}}^3\sqrt{\sigma_{\mathrm{data}}^2 - \sigma_{\mathrm{mix}}^2}}\right)^2 + \left(\frac{v_{\mathrm{mix}}\cdot\Delta m_{\mathrm{mix}}}{m_{\mathrm{mix}}^3\sqrt{\sigma_{\mathrm{data}}^2 - \sigma_{\mathrm{mix}}^2}}\right)^2}\end{aligned}$$

- for $\sigma_{\mathrm{data}} = \sigma_{\mathrm{mix}}$

$$\frac{\partial\sigma_{\mathrm{dyn}}}{\partial v_{\mathrm{data}}} = \frac{\partial\sigma_{\mathrm{dyn}}}{\partial v_{\mathrm{mix}}} = \frac{\partial\sigma_{\mathrm{dyn}}}{\partial m_{\mathrm{data}}} = \frac{\partial\sigma_{\mathrm{dyn}}}{\partial m_{\mathrm{mix}}} = 0$$

$$\Delta\sigma_{\mathrm{dyn}} = 0$$

- for $\sigma_{\mathrm{data}} > \sigma_{\mathrm{mix}}$

$$\begin{aligned}
\frac{\partial \sigma_{\mathrm{dyn}}}{\partial v_{\mathrm{data}}} &= -\left(-\frac{1}{m_{\mathrm{data}}^2} \cdot \frac{1}{2\sqrt{\sigma_{\mathrm{mix}}^2 - \sigma_{\mathrm{data}}^2}}\right) \\
\frac{\partial \sigma_{\mathrm{dyn}}}{\partial v_{\mathrm{mix}}} &= -\left(\frac{1}{m_{\mathrm{mix}}^2} \cdot \frac{1}{2\sqrt{\sigma_{\mathrm{mix}}^2 - \sigma_{\mathrm{data}}^2}}\right) \\
\frac{\partial \sigma_{\mathrm{dyn}}}{\partial m_{\mathrm{data}}} &= -\left(\frac{v_{\mathrm{data}}}{m_{\mathrm{data}}^3} \cdot \frac{1}{\sqrt{\sigma_{\mathrm{mix}}^2 - \sigma_{\mathrm{data}}^2}}\right) \\
\frac{\partial \sigma_{\mathrm{dyn}}}{\partial m_{\mathrm{mix}}} &= -\left(-\frac{v_{\mathrm{mix}}}{m_{\mathrm{mix}}^3} \cdot \frac{1}{\sqrt{\sigma_{\mathrm{mix}}^2 - \sigma_{\mathrm{data}}^2}}\right)
\end{aligned}$$

$$\Delta\sigma_{\mathrm{dyn}} = \sqrt{\left(\frac{\Delta v_{\mathrm{data}}}{2m_{\mathrm{data}}^2\sqrt{\sigma_{\mathrm{mix}}^2 - \sigma_{\mathrm{data}}^2}}\right)^2 + \left(\frac{\Delta v_{\mathrm{mix}}}{2m_{\mathrm{mix}}^2\sqrt{\sigma_{\mathrm{mix}}^2 - \sigma_{\mathrm{data}}^2}}\right)^2 + \left(\frac{v_{\mathrm{data}} \cdot \Delta m_{\mathrm{data}}}{m_{\mathrm{data}}^3\sqrt{\sigma_{\mathrm{mix}}^2 - \sigma_{\mathrm{data}}^2}}\right)^2 + \left(\frac{v_{\mathrm{mix}} \cdot \Delta m_{\mathrm{mix}}}{m_{\mathrm{mix}}^3\sqrt{\sigma_{\mathrm{mix}}^2 - \sigma_{\mathrm{data}}^2}}\right)^2}$$

As

$$\left(\sqrt{\sigma_{\mathrm{data}}^2 - \sigma_{\mathrm{mix}}^2}\right)^2 = \left|\sigma_{\mathrm{data}}^2 - \sigma_{\mathrm{mix}}^2\right| = \left|\sigma_{\mathrm{mix}}^2 - \sigma_{\mathrm{data}}^2\right| = \left(\sqrt{\sigma_{\mathrm{mix}}^2 - \sigma_{\mathrm{data}}^2}\right)^2,$$

the expression found here is identical to equation B.2, besides the exception $\Delta\sigma_{\mathrm{dyn}} = 0$ for $\sigma_{\mathrm{data}} = \sigma_{\mathrm{mix}}$.

The role of the square root

The dependence $1/\sigma_{\mathrm{dyn}}$ found in $\Delta\sigma_{\mathrm{dyn}}$ is caused by the square root in the definition of σ_{dyn}. It is thus plausible to instead look at the quantity σ_{dyn}^2, and indeed its error

$$\Delta\sigma_{\mathrm{dyn}}^2 = \sqrt{\left(\frac{1}{m_{\mathrm{data}}^2} \cdot \Delta v_{\mathrm{data}}\right)^2 + \left(\frac{1}{m_{\mathrm{mix}}^2} \cdot \Delta v_{\mathrm{mix}}\right)^2 + \left(2\frac{v_{\mathrm{data}}}{m_{\mathrm{data}}^3} \cdot \Delta m_{\mathrm{data}}\right)^2 + \left(2\frac{v_{\mathrm{mix}}}{m_{\mathrm{mix}}^3} \cdot \Delta m_{\mathrm{mix}}\right)^2}$$

does not exhibit the divergence toward $\sigma^2_{\mathrm{dyn}} = 0$. However, when then calculating

$$\sigma_{\mathrm{dyn}} = \sqrt{\sigma^2_{\mathrm{dyn}}}$$

the error propagation again brings up an $1/\sigma_{\mathrm{dyn}}$ term:

$$\begin{aligned} \frac{\partial \sigma_{\mathrm{dyn}}}{\partial \sigma^2_{\mathrm{dyn}}} &= \frac{1}{2\sigma_{\mathrm{dyn}}} \\ \Delta\sigma_{\mathrm{dyn}} &= \frac{1}{2\sigma_{\mathrm{dyn}}} \Delta\sigma^2_{\mathrm{dyn}}, \end{aligned} \tag{B.3}$$

consistently leading to expression B.2 for $\Delta\sigma_{\mathrm{dyn}}$ eventually.

Separating all terms

Another analytic check on the error consisted of a further separation of the terms: If we first calculate the error on a single σ, i.e. σ_{data} or σ_{mix}, we obtain from

$$\sigma^2 = \frac{v}{m^2}$$

the partial derivatives

$$\begin{aligned} \frac{\partial \sigma^2}{\partial v} &= \frac{1}{m^2} \\ \frac{\partial \sigma^2}{\partial m} &= -2\frac{v}{m^3} \end{aligned}$$

and following, the error

$$\Delta\sigma^2 = \sqrt{\left(\frac{1}{m^2} \cdot \Delta v\right)^2 + \left(2\frac{v}{m^3} \cdot \Delta m\right)^2} \tag{B.4}$$

If we continue with this result and evaluate

$$\sigma^2_{\mathrm{dyn}} = \sigma^2_{\mathrm{data}} - \sigma^2_{\mathrm{mix}},$$

we obtain

$$\Delta\sigma^2_{\mathrm{dyn}} = \sqrt{\left(\Delta\sigma^2_{\mathrm{data}}\right)^2 + \left(\Delta\sigma^2_{\mathrm{mix}}\right)^2}. \tag{B.5}$$

Using the result from equation B.4, we end up with the same result as in equation B.3. When going from $\Delta\sigma^2_{\mathrm{dyn}}$ to $\Delta\sigma_{\mathrm{dyn}}$, again, the $1/\sigma_{\mathrm{dyn}}$ dependence appears according to equation B.3.

Disappearing error on σ_{mix}

We now consider the case of zero error on the mixed event terms v_{mix} and m_{mix}. Then, also the error on σ_{mix} disappears. This case could in principle be achieved by constructing a very large mixed event sample. Equation B.5 shows, that in the case $\Delta\sigma_{\mathrm{mix}} = 0$, we get

$$\Delta\sigma^2_{\mathrm{dyn}} = \Delta\sigma^2_{\mathrm{data}}.$$

This represents the lower limit on $\Delta\sigma^2_{\mathrm{dyn}}$. The error on σ_{dyn}, according to equation B.3, retains its $1/\sigma_{\mathrm{dyn}}$ dependence.

Toy Monte Carlo Model

In this section, the statistical error is studied in toy Monte Carlo simulations. Figure B.1 shows the effect of the applied rules of error propagation on a simple example: Here it is assumed that (on an arbitrary x-scale) the error on σ^2_{dyn} is constant, while its value goes linearly from 0.01 to -0.01. This corresponds to $10\% \geq \sigma_{\mathrm{dyn}} \geq -10\%$.

To test the method used for statistical error propagation used in the analysis and described above, the following Toy Monte Carlo Model study was conducted:

- A random event-by-event distribution of the K/p ratio is generated, assuming a Gaussian distribution with the parameters determined from the experimental data distribution.
- Generate several times such a Gaussian distribution by picking at random N times the K/p ratio, where N is the number of entries in the data distribution.
- Calculate σ_{dyn} from the difference of widths of pairs of these simulated distributions.
- Study the spread of resulting σ_{dyn} results as a measure for the statistical error.

The parameters derived from data are: $\langle \mathrm{K/p} \rangle = 0.74$, $\mathrm{RMS(K/p)} = 0.15$ for 158AGeV, $\langle \mathrm{K/p} \rangle = 0.22$, $\mathrm{RMS(K/p)} = 0.11$ for 20AGeV. According to the description above, Gaussian K/p distributions with the experimental parameters were generated. The

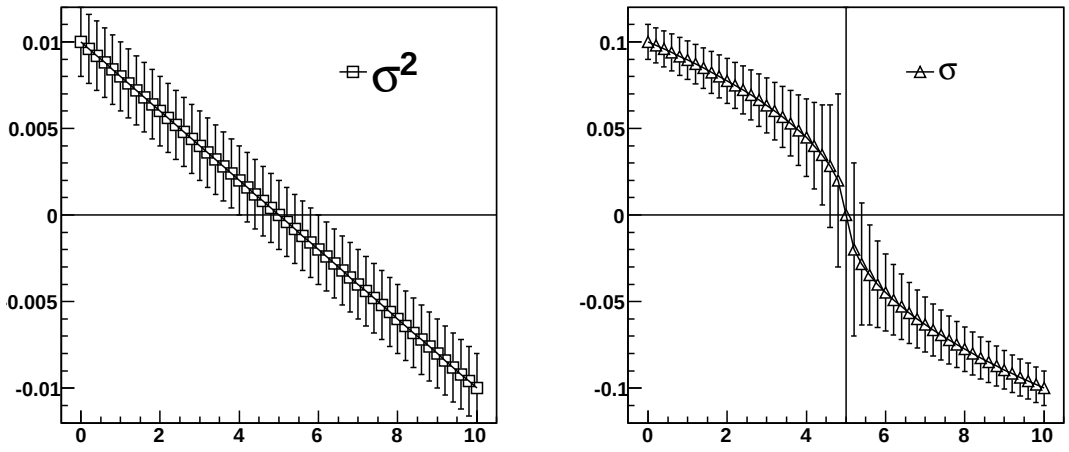

Figure B.1: The effect of the square root in the definition of σ_{dyn}: the assumption of equal sized errors in σ^2_{dyn} turns to diverging errors in σ_{dyn}.

part of the distribution extending to K/p < 0 was stacked at zero, comparable to what happens in the experiment. In the following examples, results for the 20AGeV number are shown. The numbers from 158AGeV were also used in the study and yielded the same behavior but a smaller statistical error $\Delta\sigma_{\mathrm{dyn}}$. This is consistent with equation B.2 which predicts an approximate 1/mean behavior.

Figure B.2 shows an example from the Monte Carlo toy model. In this example, $N_{\mathrm{run}} = 50$ runs with $N_{\mathrm{events}} = 100,000$ events each were generated. The resulting σ_{data} for each of the 50 runs is shown on the left panel, together with the statistical error, calculated as in the experimental analysis. This error behaves as expected: The spread in σ_{data} is on the same level as this error. When increasing the number of events per run, the error decreases and vice versa. From the $N_{\mathrm{run}} = 50$ runs, one can construct $N_{\mathrm{run}} * (N_{\mathrm{run}} - 1)$ disjoint combinations and calculate a $\sigma_{\mathrm{dyn}} = \sqrt{\sigma^2_{\mathrm{data},1} - \sigma^2_{\mathrm{data},2}}$. The 2450 resulting values are plotted on the right panel of figure B.2. They scatter around zero, their statistical error $\Delta\sigma_{\mathrm{dyn}}$ is calculated using the standard experimental method.

For better visibility, these values of σ_{dyn} are histogrammed and shown in the left panel of figure B.3. The distribution of $\Delta\sigma_{\mathrm{dyn}}$ is shown in the right panel of figure B.3. For this example ($N_{\mathrm{run}} = 50$, $N_{\mathrm{events}} = 100,000$), The RMS width of the σ_{dyn} distribution, and the average $\Delta\sigma_{\mathrm{dyn}}$ have the values 0.036 and 0.035, respectively (cf. RMS from the statistics box of the σ_{dyn} histogram and the mean of the $\Delta\sigma_{\mathrm{dyn}}$ histogram, respectively).

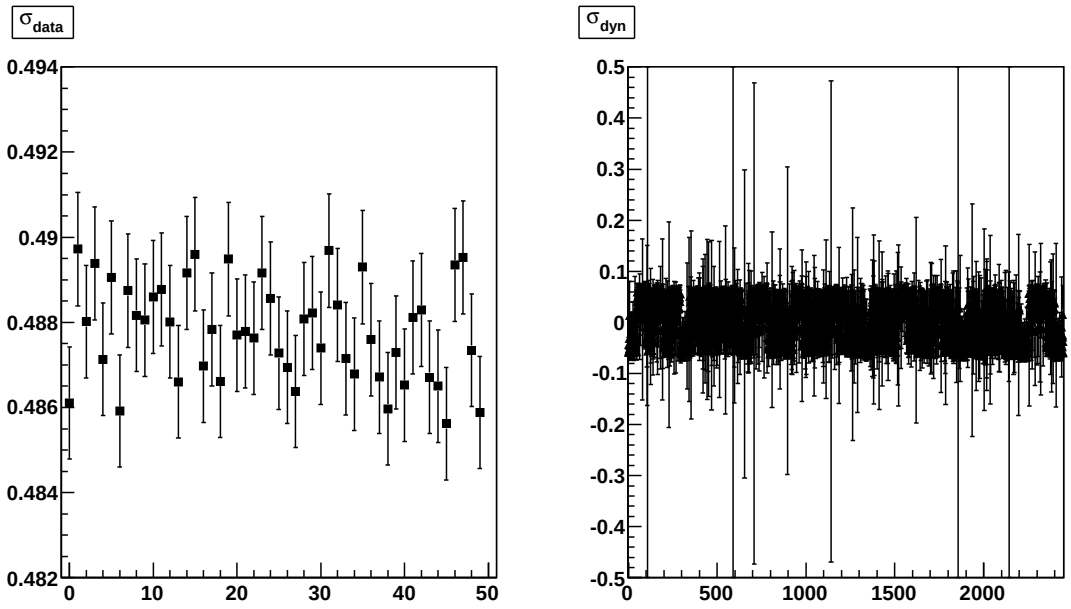

Figure B.2: σ_{data} as calculated from $N_{\mathrm{run}} = 50$ toy Monte Carlo model runs with $N_{\mathrm{events}} = 100,000$ events each (left). σ_{dyn} calculated from all disjoint combinations of two runs (right).

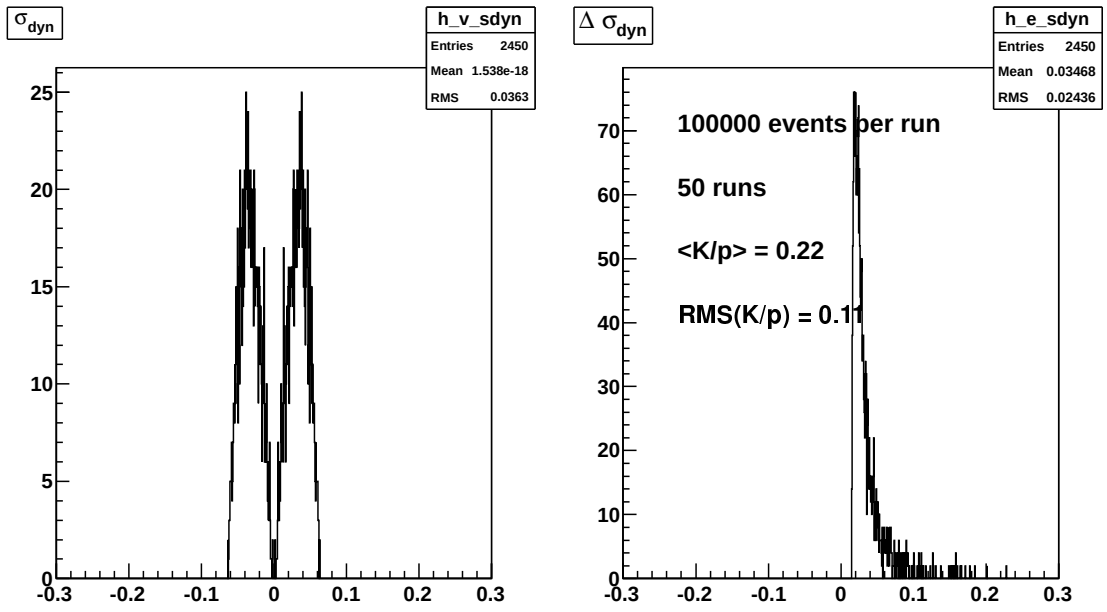

Figure B.3: Distribution of σ_{dyn} calculated in a toy Monte Carlo simulation (left). Distribution of $\Delta\sigma_{\mathrm{dyn}}$ calculated as in the experimental analysis (right). The spread of σ_{dyn} is in agreement with the mean $\Delta\sigma_{\mathrm{dyn}}$.

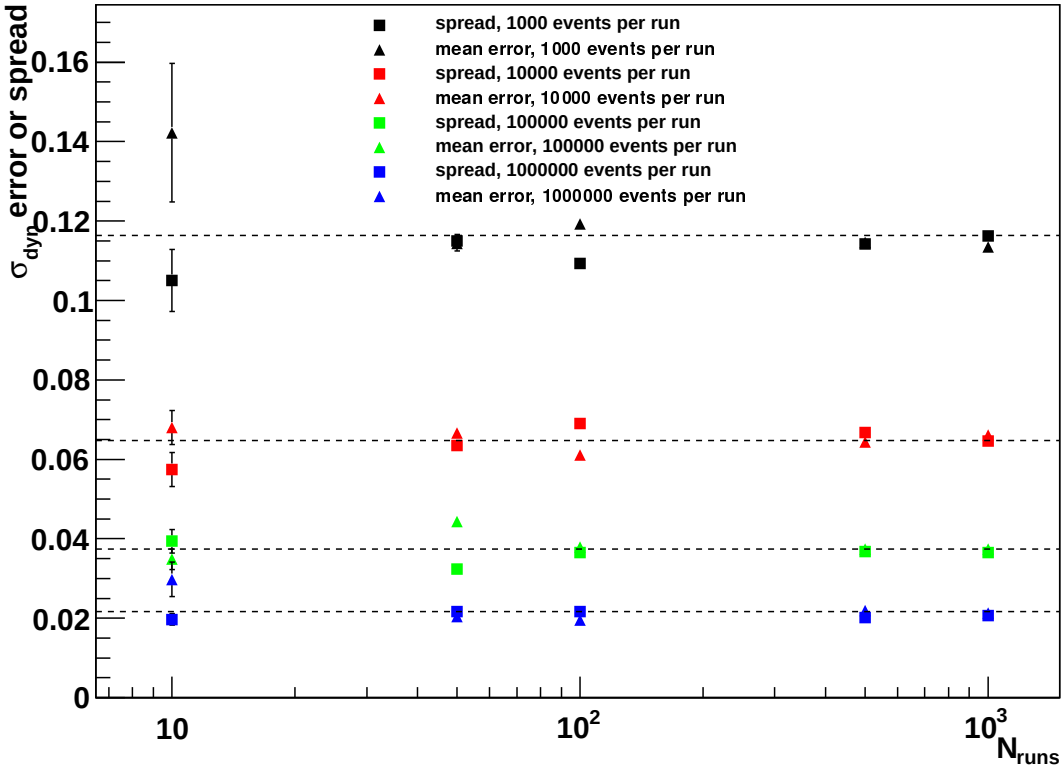

Figure B.4: Comparison of the spread in σ_{dyn} and $\langle \Delta\sigma_{\mathrm{dyn}} \rangle$ for different combinations of N_{run} and N_{events}. Both are in agreement and decrease with increasing event statistics.

A systematic comparison is displayed in figure B.4. In all cases, the two methods of estimating the error agree. The error gets smaller, when using larger event samples, but are constant as a function of N_{run}.

This study gives confidence in the method used for statistical error estimation. The observed divergence of statistical errors for $\sigma_{\mathrm{dyn}} \to 0$ is caused by the square root in the definition B.1.

Conclusion

No matter how we evaluate the statistical error on σ_{dyn}, we end up with equation B.2. The $1/\sigma_{\mathrm{dyn}}$ dependence is an intrinsic property of $\Delta\sigma_{\mathrm{dyn}}$, and is simply caused by the square root in the definition. The Monte Carlo Model confirms the error calculation method even in the region $\sigma_{\mathrm{dyn}} \to 0$. For equally sized errors in σ^2_{dyn}, one obtains an error growing like $1/\sigma_{\mathrm{dyn}}$ when evaluating the error on σ_{dyn}.

Bibliography

[1] E. Rutherford. The scattering of alpha and beta particles by matter and the structure of the atom. *Phil.Mag.*, 21:669–688, 1911.

[2] Steven Weinberg. The Making of the standard model. *Eur. Phys. J.*, C34:5–13, 2004.

[3] D.P. Roy. Basic constituents of matter and their interactions: A Progress report. *TIFR/TH/99-59*, 1999.

[4] K Nakamura et al. Review of particle physics. *J.Phys.G*, G37:075021, 2010.

[5] Richard E. Taylor. The Discovery of the point - like structure of matter. *Phil.Trans.Roy.Soc.Lond.*, A359:225–240, 2001.

[6] David J. Gross and Frank Wilczek. Ultraviolet behavior of non-abelian gauge theories. *Phys. Rev. Lett.*, 30(26):1343–1346, Jun 1973.

[7] H. David Politzer. Reliable perturbative results for strong interactions? *Phys. Rev. Lett.*, 30(26):1346–1349, Jun 1973.

[8] Ágnes Mócsy and Péter Petreczky. Can quarkonia survive deconfinement? *Phys. Rev. D*, 77(1):014501, Jan 2008.

[9] E. Eichten, K. Gottfried, T. Kinoshita, J. Kogut, K. D. Lane, and T. M. Yan. Spectrum of charmed quark-antiquark bound states. *Phys. Rev. Lett.*, 34(6):369–372, Feb 1975.

[10] F. Karsch and E. Laermann. Thermodynamics and in medium hadron properties from lattice QCD. 2003. Prepared for Quark-Gluon Plasma III, eds. R.C. Hwa and Xin-Nian Wang, World Scientific Publishing.

[11] O. Kaczmarek, F. Karsch, P. Petreczky, and F. Zantow. Heavy Quark Anti-Quark Free Energy and the Renormalized Polyakov Loop. *Phys. Lett.*, B543:41–47, 2002.

[12] O. Kaczmarek, F. Karsch, F. Zantow, and P. Petreczky. Static quark anti-quark free energy and the running coupling at finite temperature. *Phys. Rev.*, D70:074505, 2004.

[13] A. Bazavov et al. Equation of state and QCD transition at finite temperature. *Phys. Rev.*, D80:014504, 2009.

[14] Z. Fodor and S.D. Katz. Lattice determination of the critical point of QCD at finite T and mu. *JHEP*, 0203:014, 2002.

[15] Z. Fodor and S.D. Katz. Critical point of QCD at finite T and mu, lattice results for physical quark masses. *JHEP*, 0404:050, 2004.

[16] Frithjof Karsch. Recent lattice results on finite temperature and density QCD, part I. *PoS*, CPOD07:026, 2007.

[17] Frithjof Karsch. Recent lattice results on finite temerature and density QCD, part II. *PoS*, LAT2007:015, 2007.

[18] R. Rapp, Thomas Schafer, Edward V. Shuryak, and M. Velkovsky. High-density QCD and instantons. *Annals Phys.*, 280:35–99, 2000.

[19] Misha A. Stephanov, K. Rajagopal, and Edward V. Shuryak. Signatures of the tricritical point in QCD. *Phys. Rev. Lett.*, 81:4816–4819, 1998.

[20] Shinji Ejiri, Chris R. Allton, Simon J. Hands, Olaf Kaczmarek, Frithjof Karsch, et al. Study of QCD thermodynamics at finite density by Taylor expansion. *Prog.Theor.Phys.Suppl.*, 153:118–126, 2004.

[21] Werner Scheid, Hans Müller, and Walter Greiner. Nuclear shock waves in heavy-ion collisions. *Phys. Rev. Lett.*, 32(13):741–745, Apr 1974.

[22] J. Gosset, H.H. Gutbrod, W.G. Meyer, Arthur M. Poskanzer, A. Sandoval, et al. Central Collisions of Relativistic Heavy Ions. *Phys.Rev.*, C16:629–657, 1977.

[23] A.A. Kuznetsov. Experiments at the Dubna Synchrophasotron. *Nucl.Phys.*, A400:493C–524C, 1983.

[24] R. Stock. Particle Production in High-Energy Nucleus Nucleus Collisions. *Phys.Rept.*, 135:259–315, 1986.

[25] R. Stock. The Physics of Dense Nuclear Matter from Supernovae to Quark Gluon Plasma. *Nature*, 337:319–324, 1989.

[26] Cern presse release. `http://newstate-matter.web.cern.ch/newstate-matter/`, 2000.

[27] Ulrich W. Heinz and Maurice Jacob. Evidence for a new state of matter: An assessment of the results from the CERN lead beam programme. 2000. arXiv:nucl-th/0002042.

[28] C. Alt et al. Pion and kaon production in central Pb + Pb collisions at 20-A and 30-A-GeV: Evidence for the onset of deconfinement. *Phys.Rev.*, C77:024903, 2008.

[29] I. Arsene et al. Quark gluon plasma and color glass condensate at RHIC? The Perspective from the BRAHMS experiment. *Nucl.Phys.*, A757:1–27, 2005.

[30] B.B. Back, M.D. Baker, M. Ballintijn, D.S. Barton, B. Becker, et al. The PHOBOS perspective on discoveries at RHIC. *Nucl.Phys.*, A757:28–101, 2005. PHOBOS White Paper on discoveries at RHIC.

[31] John Adams et al. Experimental and theoretical challenges in the search for the quark gluon plasma: The STAR Collaboration's critical assessment of the evidence from RHIC collisions. *Nucl.Phys.*, A757:102–183, 2005.

[32] K. Adcox et al. Formation of dense partonic matter in relativistic nucleus-nucleus collisions at RHIC: Experimental evaluation by the PHENIX collaboration. *Nucl.Phys.*, A757:184–283, 2005.

[33] Edmond Iancu and Raju Venugopalan. The Color glass condensate and high-energy scattering in QCD. 2003.

[34] F. Becattini, J. Manninen, and M. Gazdzicki. Energy and system size dependence of chemical freeze-out in relativistic nuclear collisions. *Phys.Rev.*, C73:044905, 2006.

[35] A. Andronic, P. Braun-Munzinger, J. Stachel, and H. Stocker. Production of light nuclei, hypernuclei and their antiparticles in relativistic nuclear collisions. *Phys. Lett.*, B697:203–207, 2011.

[36] F. Becattini, M. Gazdzicki, A. Keranen, J. Manninen, and R. Stock. Chemical equilibrium in nucleus nucleus collisions at relativistic energies. *Phys.Rev.*, C69:024905, 2004.

[37] Peter Braun-Munzinger, Krzysztof Redlich, and Johanna Stachel. Particle production in heavy ion collisions. 2003. Prepared for Quark-Gluon Plasma III, eds. R.C. Hwa and Xin-Nian Wang, World Scientific Publishing.

[38] R. Hagedorn. Remarks on the thermodynamical model of strong interactions. *Nucl.Phys.*, B24:93–139, 1970.

[39] J. Cleymans and H. Satz. Thermal hadron production in high-energy heavy ion collisions. *Z.Phys.*, C57:135–148, 1993.

[40] Michael Kliemant, Raghunath Sahoo, Tim Schuster, and Reinhard Stock. Global Properties of Nucleus-Nucleus Collisions. *Lect.Notes Phys.*, 785:23–103, 2010.

[41] Steven Weinberg. The First Three Minutes. A Modern View of the Origin of the Universe. 1977.

[42] J. Cleymans and K. Redlich. Unified description of freezeout parameters in relativistic heavy ion collisions. *Phys.Rev.Lett.*, 81:5284–5286, 1998.

[43] C. Blume. Energy dependence of hadronic observables. *J.Phys.G*, G31:S57–S68, 2005.

[44] Ekkard Schnedermann, Josef Sollfrank, and Ulrich W. Heinz. Thermal phenomenology of hadrons from 200-A/GeV S+S collisions. *Phys.Rev.*, C48:2462–2475, 1993.

[45] Urs Achim Wiedemann and Ulrich W. Heinz. Resonance contributions to HBT correlation radii. *Phys.Rev.*, C56:3265–3286, 1997.

[46] Boris Tomasik. Blast-wave snapshots from RHIC. *CERN-TH/2003-093*, 2003.

[47] Michael Annan Lisa, Scott Pratt, Ron Soltz, and Urs Wiedemann. Femtoscopy in Relativistic Heavy Ion Collisions: Two Decades of Progress. *Ann. Rev. Nucl. Part. Sci.*, 55:357–402, 2005.

[48] C. Alt et al. Directed and elliptic flow of charged pions and protons in Pb + Pb collisions at 40-A-GeV and 158-A-GeV. *Phys. Rev.*, C68:034903, 2003.

[49] Sergei A. Voloshin, Arthur M. Poskanzer, and Raimond Snellings. Collective phenomena in non-central nuclear collisions. 2008. arXiv:0809.2949.

[50] John Adams et al. Evidence from d + Au measurements for final-state suppression of high p(T) hadrons in Au + Au collisions at RHIC. *Phys. Rev. Lett.*, 91:072304, 2003.

[51] S. S. Adler et al. Centrality dependence of direct photon production in s(NN)**(1/2) = 200-GeV Au + Au collisions. *Phys. Rev. Lett.*, 94:232301, 2005.

[52] S.S. Adler et al. Measurement of direct photon production in p + p collisions at s**(1/2) = 200-GeV. *Phys.Rev.Lett.*, 98:012002, 2007.

[53] Baldo Sahlmueller. Photons at PHENIX. *PoS*, High-pTphysics09:035, 2009.

[54] John Adams et al. Azimuthal anisotropy and correlations at large transverse momenta in p + p and Au + Au collisions at s(NN)**(1/2) = 200-GeV. *Phys. Rev. Lett.*, 93:252301, 2004.

[55] T. Matsui and H. Satz. J/psi Suppression by Quark-Gluon Plasma Formation. *Phys.Lett.*, B178:416, 1986.

[56] B. Alessandro et al. A New measurement of J/psi suppression in Pb-Pb collisions at 158-GeV per nucleon. *Eur.Phys.J.*, C39:335–345, 2005.

[57] S. Damjanovic et al. First measurement of the rho spectral function in nuclear collisions. *Nucl.Phys.*, A774:715–718, 2006.

[58] Marek Gazdzicki and Mark I. Gorenstein. On the early stage of nucleus nucleus collisions. *Acta Phys. Polon.*, B30:2705, 1999.

[59] S.V. Afanasiev et al. Energy dependence of pion and kaon production in central Pb + Pb collisions. *Phys.Rev.*, C66:054902, 2002.

[60] A. Wroblewski. On the Strange Quark Suppression Factor in High-Energy Collisions. *Acta Phys.Polon.*, B16:379–392, 1985.

[61] Anar Rustamov. The horn, kink and step from few GeV to few TeV. `https://indico.cern.ch/conferenceDisplay.py?confId=144745`.

[62] M. Gazdzicki, Mark I. Gorenstein, F. Grassi, Yogiro Hama, T. Kodama, et al. Incident energy dependence of the effective temperature in heavy ion collisions. *Braz.J.Phys.*, 34:322–325, 2004.

[63] M. Gazdzicki, for the NA49, and NA61/SHINE Collaborations. NA49/NA61: results and plans on beam energy and system size scan at the CERN SPS. 2011. Invited presentation at the Quark Matter 2011 conference, proceedings in print, arXiv:1107.2345.

[64] T. Anticic et al. Energy dependence of kaon-to-proton ratio fluctuations in central Pb+Pb collisions from $\sqrt{s_{NN}} = 6.3$ to 17.3 GeV. *Phys.Rev.*, C83:061902, 2011.

[65] Volker Koch. Hadronic Fluctuations and Correlations. 2008. arXiv:0810.2520.

[66] V. Koch, A. Majumder, and J. Randrup. Baryon-strangeness correlations: A diagnostic of strongly interacting matter. *Phys. Rev. Lett.*, 95:182301, 2005.

[67] R. Stock. Event by event analysis of ultrarelativistic nuclear collisions: A new method to search for critical fluctuations. *NATO Advanced Study Institute, Series B: Physics, v. 346*, 1995.

[68] H. Appelshauser et al. Event-by-event fluctuations of average transverse momentum in central Pb + Pb collisions at 158-GeV per nucleon. *Phys. Lett.*, B459:679–686, 1999.

[69] A D Panagiotou et al. Large acceptance hadron detector for an investigation of Pb-induced reactions at the CERN SPS. Technical Report CERN-SPSLC-91-31. SPSLC-P-264, CERN, Geneva, 1991.

[70] A D Panagiotou et al. Addendum to CERN-Proposal SPSLC/P264: Large Acceptance Hadron Detector for an Investigation of Pb-induced Reactions at the CERN SPS. Technical Report CERN-SPSLC-91-052. SPSLC-P-264-Add-1, CERN, Geneva, Aug 1991.

[71] G. Roland. First results of the NA49 event-by event analysis of Pb + Pb collisions at the SPS. *QCD Phase Transition, Proceedings GSI, Darmstadt, Germany*, pages 309–318, 1997.

[72] C. Alt et al. Electric charge fluctuations in central Pb+Pb collisions at 20-A-GeV, 30-A-GeV, 40-A-GeV, 80-A-GeV, and 158-A-GeV. *Phys.Rev.*, C70:064903, 2004.

[73] S. Jeon and V. Koch. Charged particle ratio fluctuation as a signal for QGP. *Phys.Rev.Lett.*, 85:2076–2079, 2000.

[74] Masayuki Asakawa, Ulrich W. Heinz, and Berndt Muller. Fluctuation probes of quark deconfinement. *Phys.Rev.Lett.*, 85:2072–2075, 2000.

[75] Jacek Zaranek. Measures of charge fluctuations in nuclear collisions. *Phys.Rev.*, C66:024905, 2002.

[76] Edward V. Shuryak and Misha A. Stephanov. When can long range charge fluctuations serve as a QGP signal? *Phys.Rev.*, C63:064903, 2001.

[77] S. Jeon and V. Koch. Fluctuations of particle ratios and the abundance of hadronic resonances. *Phys.Rev.Lett.*, 83:5435–5438, 1999.

[78] Yogiro Hama, T. Kodama, and Jr. Socolowski, O. Topics on hydrodynamic model of nucleus-nucleus collisions. *Braz.J.Phys.*, 35:24–51, 2005.

[79] B. Alver et al. Non-flow correlations and elliptic flow fluctuations in gold-gold collisions at $\sqrt{s_{NN}} = 200$ GeV. *Phys.Rev.*, C81:034915, 2010.

[80] B. Alver and G. Roland. Collision geometry fluctuations and triangular flow in heavy-ion collisions. *Phys.Rev.*, C81:054905, 2010.

[81] Misha A. Stephanov, K. Rajagopal, and Edward V. Shuryak. Event-by-event fluctuations in heavy ion collisions and the QCD critical point. *Phys.Rev.*, D60:114028, 1999.

[82] M. Gazdzicki, Mark I. Gorenstein, and S Mrowczynski. Fluctuations and deconfinement phase transition in nucleus nucleus collisions. *Phys.Lett.*, B585:115–121, 2004.

[83] C. Alt et al. Energy Dependence of Multiplicity Fluctuations in Heavy Ion Collisions at the CERN SPS. *Phys.Rev.*, C78:034914, 2008.

[84] T. Anticic et al. Energy dependence of transverse momentum fluctuations in Pb+Pb collisions at the CERN Super Proton Synchrotron (SPS) at 20A to 158A GeV. *Phys.Rev.*, C79:044904, 2009.

[85] Boris Berdnikov and Krishna Rajagopal. Slowing out-of-equilibrium near the QCD critical point. *Phys.Rev.*, D61:105017, 2000.

[86] M.A. Stephanov. Non-Gaussian fluctuations near the QCD critical point. *Phys.Rev.Lett.*, 102:032301, 2009.

[87] M.M. Aggarwal et al. Higher Moments of Net-proton Multiplicity Distributions at RHIC. *Phys.Rev.Lett.*, 105:022302, 2010.

[88] Volker Koch. Fluctuations of conserved quantities. *PoS*, CFRNC2006:008, 2006.

[89] M. Bleicher, S. Jeon, and V. Koch. Event-by-event fluctuations of the charged particle ratio from non-equilibrium transport theory. *Phys. Rev.*, C62:061902, 2000.

[90] Tim Schuster, Marlene Nahrgang, Michael Mitrovski, Reinhard Stock, and Marcus Bleicher. Analysis of the baryon-, proton-, and charged particle kurtosis in heavy ion collisions within a relativistic transport approach. 2009. arXiv:0903.2911.

[91] Michael Hauer. Multiplicity Fluctuations in Limited Segments of Momentum Space in Statistical Models. *Phys.Rev.*, C77:034909, 2008.

[92] M. Bleicher, E. Zabrodin, C. Spieles, S.A. Bass, C. Ernst, et al. Relativistic hadron hadron collisions in the ultrarelativistic quantum molecular dynamics model. *J.Phys.G*, G25:1859–1896, 1999.

[93] S.A. Bass, M. Belkacem, M. Bleicher, M. Brandstetter, L. Bravina, et al. Microscopic models for ultrarelativistic heavy ion collisions. *Prog.Part.Nucl.Phys.*, 41:255–369, 1998.

[94] Hannah Petersen, Marcus Bleicher, Steffen A. Bass, and Horst Stocker. UrQMD v2.3: Changes and Comparisons. 2008. arXiv:0805.0567.

[95] W. Ehehalt and W. Cassing. Relativistic transport approach for nucleus nucleus collisions from SIS to SPS energies. *Nucl.Phys.*, A602:449–486, 1996.

[96] V.P. Konchakovski, M. Hauer, M.I. Gorenstein, and E.L. Bratkovskaya. Particle Number Fluctuations and Correlations in Nucleus-Nucleus Collisions. *J.Phys.G*, G36:125106, 2009.

[97] M. Gazdzicki and S. Mrowczynski. A Method to study 'equilibration' in nucleus-nucleus collisions. *Z.Phys.*, C54:127–132, 1992.

[98] M. Bleicher, M. Belkacem, C. Ernst, H. Weber, L. Gerland, et al. Can momentum correlations proof kinetic equilibration in heavy ion collisions at 160/A-GeV? *Phys.Lett.*, B435:9–12, 1998.

[99] Benjamin Lungwitz and Marcus Bleicher. Searching for the Critical Point of QCD: Theoretical Benchmark Calculations. *Phys.Rev.*, C76:044904, 2007.

[100] Yoshitaka Hatta and Takashi Ikeda. Universality, the QCD critical / tricritical point and the quark number susceptibility. *Phys.Rev.*, D67:014028, 2003.

[101] M. Rybczynski et al. Energy dependence of fluctuations in central Pb+Pb collisions from NA49 at the CERN SPS. *J.Phys.G*, G35:104091, 2008.

[102] C. Alt et al. Centrality and system size dependence of multiplicity fluctuations in nuclear collisions at 158-A/GeV. *Phys.Rev.*, C75:064904, 2007.

[103] T. Anticic et al. Transverse momentum fluctuations in nuclear collisions at 158-A-GeV. *Phys.Rev.*, C70:034902, 2004.

[104] V. P. Konchakovski et al. Particle Number Fluctuations in High Energy Nucleus-Nucleus Collisions from Microscopic Transport Approaches. *Phys. Rev.*, C73:034902, 2006.

[105] Katarzyna Grebieszkow and for the NA49 Collaboration. Search for the critical point of strongly interacting matter in NA49. *Nucl.Phys.*, A830:547C–550C, 2009.

[106] Dmytro Kresan. *Event-by-event Fluctuations of the Particle Yield Ratios in Heavy-Ion Collisions at 20 - 158 AGeV*. PhD thesis, Johann Wolfgang Goethe-Universität Frankfurt am Main, 2010.

[107] Johann Rafelski and Berndt Muller. Strangeness Production in the Quark - Gluon Plasma. *Phys.Rev.Lett.*, 48:1066, 1982.

[108] Volker Koch, Abhijit Majumder, and Jorgen Randrup. Signals of spinodal hadronization: Strangeness trapping. *Phys.Rev.*, C72:064903, 2005.

[109] Joseph I. Kapusta and A. Mekjian. How Much Strangeness Production is there in Ultrarelativistic Nucleus Nucleus Collisions? *Phys.Rev.*, D33:1304–1313, 1986.

[110] L.P. Csernai and I.N. Mishustin. Fast hadronization of supercooled quark - gluon plasma. *Phys.Rev.Lett.*, 74:5005–5008, 1995.

[111] Mark I. Gorenstein, M. Gazdzicki, and O. S. Zozulya. Fluctuations of strangeness and deconfinement phase transition in nucleus nucleus collisions. *Phys. Lett.*, B585:237–242, 2004.

[112] Chiho Nonaka and Masayuki Asakawa. Hydrodynamical evolution near the QCD critical end point. *Phys.Rev.*, C71:044904, 2005.

[113] Reinhard Stock. Relativistic nucleus-nucleus collisions: From the BEVALAC to RHIC. *J.Phys.G*, G30:S633–S648, 2004.

[114] Mikhail A. Stephanov. QCD phase diagram and the critical point. *Prog.Theor.Phys.Suppl.*, 153:139–156, 2004.

[115] M. Gazdzicki. Statistical tool for particle 'identification' by 'mass' measurement. *Nucl.Instrum.Meth.*, A345:148–155, 1994.

[116] S.V. Afanasev et al. Event-by-event fluctuations of the kaon to pion ratio in central Pb + Pb collisions at 158-GeV per nucleon. *Phys.Rev.Lett.*, 86:1965–1969, 2001.

[117] Christof Roland. *Flavor Fluctuations in Central Pb+Pb Collisions at 158 GeV/Nucleon*. PhD thesis, Johann Wolfgang Goethe-Universität Frankfurt am Main, 1999.

[118] C. Alt et al. Energy dependence of particle ratio fluctuations in central Pb + Pb collisions from s(NN)**(1/2) = 6.3-GeV to 17.3-GeV. *Phys.Rev.*, C79:044910, 2009.

[119] Michael Hauer and Sascha Vogel. Some Considerations concerning the Fluctuation of the Ratios of two Observables. 2010. arXiv:1012.4703.

[120] Dmytro Kresan and Volker Friese. Hadronic sources of the event-by-event fluctuations of particle yield ratios. *PoS*, CFRNC2006:017, 2006.

[121] Tim Schuster for the NA49 collaboration. New results on event-by-event ratio fluctuations in Pb+Pb collisions at CERN SPS energies. 2011. Presentation at the Quark Matter 2011 conference, proceedings in print, arXiv:1107.1579.

[122] Michael Hauer. *Statistical Fluctuations and Correlations in Hadronic Equilibrium Systems*. PhD thesis, Johann Wolfgang Goethe-Universität Frankfurt am Main, 2010.

[123] M.I. Gorenstein, M. Hauer, V.P. Konchakovski, and E.L. Bratkovskaya. Fluctuations of the K/pi Ratio in Nucleus-Nucleus Collisions: Statistical and Transport Models. *Phys.Rev.*, C79:024907, 2009.

[124] B.I. Abelev et al. K/pi Fluctuations at Relativistic Energies. *Phys.Rev.Lett.*, 103:092301, 2009.

[125] Terence J Tarnowsky for the STAR Collaboration. Searching for the QCD Critical Point Using Particle Ratio Fluctuations and Higher Moments of Multiplicity Distributions. 2011. Presentation at the Quark Matter 2011 conference, proceedings in print, arXiv:1106.6110.

[126] C. Pruneau, S. Gavin, and S. Voloshin. Methods for the study of particle production fluctuations. *Phys.Rev.*, C66:044904, 2002.

[127] Marek Gazdzicki, Katarzyna Grebieszkow, Maja Mackowiak, and Stanislaw Mrowczynski. Identity method to study chemical fluctuations in relativistic heavy-ion collisions. *Phys.Rev.*, C83:054907, 2011.

[128] M. Mackowiak and for the NA49 Collaboration. Identity method - a new tool for studying chemical fluctuations. 2011. Presentation at the CPOD 2011 workshop, proceedings in print, arXiv:1102.4171.

[129] M.I. Gorenstein and M. Gazdzicki. Strongly Intensive Quantities. *Phys.Rev.*, C84:014904, 2011.

[130] T. Anticic et al. Event-by-Event Fluctuations and the Search for the Critical Point within the NA49 Experiment. *PoS*, CPOD2009:029, 2009.

[131] M. Cheng et al. Baryon Number, Strangeness and Electric Charge Fluctuations in QCD at High Temperature. *Phys. Rev.*, D79:074505, 2009.

[132] Christian Schmidt. Hadronic fluctuations and correlations at nonzero chemical potential. *PoS*, CPOD2009:024, 2009.

[133] C. Alt et al. Energy dependence of Lambda and Xi production in central Pb+Pb collisions at A-20, A-30, A-40, A-80, and A-158 GeV measured at the CERN Super Proton Synchrotron. *Phys.Rev.*, C78:034918, 2008.

[134] T. Anticic et al. System-size dependence of Lambda and Xi production in nucleus-nucleus collisions at 40A and 158A-GeV measured at the CERN Super Proton Synchrotron. *Phys.Rev.*, C80:034906, 2009.

[135] Stephane Haussler, Stefan Scherer, and Marcus Bleicher. Baryon-strangeness correlations from hadron/string- and quark-dynamics. *AIP Conf.Proc.*, 892:372–376, 2007.

[136] Stephane Haussler, Stefan Scherer, and Marcus Bleicher. The Effect of Dynamical Parton Recombination on Event-by-Event Observables. *Phys.Lett.*, B660:197–201, 2008.

[137] F. Jin, Y.G. Ma, G.L. Ma, J.H. Chen, S. Zhang, et al. Baryon-Strangeness correlations in Parton/Hadron transport model for Au + Au collisions at s(NN)**(1/2) = 200-GeV. *J.Phys.G*, G35:044070, 2008.

[138] Tim Schuster. Production of neutral strange hadrons with high transverse momentum in pb+pb collisions at 158A GeV. Diploma thesis, Johann Wolfgang Goethe-Universität Frankfurt am Main, 2006.

[139] S. Afanasev et al. [NA49 collaboration]. *The NA49 large acceptance hadron detector.* Nucl. Instrum. Meth. A430, 210-244, 1999.

[140] H. Haseroth. *The CERN heavy ion facility.* Invited Paper at the 4th EPAC - European Particle Accelerator Conference - Europhysics Conference, London, UK, 27 Jun - 1 Jul 1994.

[141] G. Brianti. *The CERN Synchrotrons.* CERN 97-04, 1997.

[142] The PS Staff, CERN. *40 years of CERN's Proton Synchrotron. CERN Courier*, 39(10), 1999.

[143] J. Dainton et al. [The CERN SPS and PS Committee]. *Fixed-Target Physiscs at CERN beyond 2005, Summary and Conclusions of an Evaluation by the SPSC.* CERN–SPSC–2005–010, SPSC–M–730, 2005.

[144] N. Antoniou et al. *Letter of intent: Study of Hadron Production in Collisions of Protons and Nuclei at the CERN SPS.* CERN-SPSC-2006-001 and SPSC-P-329, 2006.

[145] Marek Gazdzicki. *Onset of deconfinement and critical point: Future ion program at the CERN SPS.* nucl-ex/0512034, 2005.

[146] N. Antoniou et al. Study of hadron production in hadron nucleus and nucleus nucleus collisions at the CERN SPS. *CERN-SPSC-2006-034, CERN-SPSC-P-330*, 2006.

[147] N. Antoniou et al. Further information requested in the proposal review process. *CERN-SPSC-2007-019, CERN-SPSC-P-330*, 2007.

[148] H.H. Gutbrod, R. Bock, B.W. Kolb, H.R. Schmidt, A.L.S. Angelis, et al. Proposal for a large acceptance hadron and photon spectrometer. *CERN-SPSLC-91-17, CERN-SPSLC-P-260*, 1991.

[149] Itzhak Tserruya, P. Holl, H. Kraner, P. Rehak, J. Schukraft, et al. Study of electron pair and photon production in lead-lead collisions at the CERN SPS: Proposal. *CERN-SPSLC-94-1, CERN-SPSLC-P-280*, 1994.

[150] M.C. Abreu, C. Baglin, A. Baldit, C. Barriere, M. Bedjidian, et al. Study of muon pairs and vector mesons produced in high-energy Pb Pb interactions. *CERN-SPSLC-91-55, CERN-SPSLC-P-265*, 1991.

[151] R. Caliandro, F. Corsi, D. Di Bari, D. Elia, R. Fini, et al. Study of strange and multistrange particles in ultrarelativistic nucleus nucleus collisions. *CERN-SPSLC-96-40, CERN-SPSLC-P-300*, 1996.

[152] H. Appelshauser et al. Spectator nucleons in Pb + Pb collisions at 158-A-GeV. *Eur.Phys.J.*, A2:383–390, 1998.

[153] K. Werner. Strings, pomerons, and the venus model of hadronic interactions at ultrarelativistic energies. *Phys.Rept.*, 232:87–299, 1993.

[154] András László. Calculating mean values of collision parameters as a function of centrality. `https://edms.cern.ch/document/885329/1`, NA49 note, 2006.

[155] V.P. Konchakovski, M. Hauer, G. Torrieri, M.I. Gorenstein, and E.L. Bratkovskaya. Forward-backward correlations in nucleus-nucleus collisions: baseline contributions from geometrical fluctuations. *Phys.Rev.*, C79:034910, 2009.

[156] András László. Time-dependence calibration of the veto calorimeter. `https://edms.cern.ch/document/815907/1`, NA49 note, 2006.

[157] T. Alber, V. Eckardt, H. Fessler, S. Schoenfelder, and P. Seyboth. A Study of argon, neon and helium based gas mixtures for improving the spatial resolution in time projection chambers. *Nucl.Instrum.Meth.*, A349:56–61, 1994.

[158] Dmytro Kresan. NA49 weekly analysis meeting, Wednesday 31 August 2011.

[159] J.-P. Baud et al. *CASTOR status and Evolution*. Paper presented at the International Conference on Computing in High Energy and Nuclear Physics (CHEP), 2003.

[160] O. Bärring et al. *CASTOR: Operational Issues and New Developments*. Paper presented at the International Conference on Computing in High Energy and Nuclear Physics (CHEP), 2004.

[161] `http://consult.cern.ch/service/afs/`.

[162] R. Zybert and P. Bunčić. *DSPACK - Object Oriented Data Manager for HEP*. Paper presented at the International Conference on Computing in High Energy and Nuclear Physics (CHEP), 1995.

[163] Christina Markert. *Lambda (1520)-Produktion in Proton-Proton- und zentralen Blei-Blei-Reaktionen bei 158 GeV pro Nukleon*. PhD thesis, Johann Wolfgang Goethe-Universität Frankfurt am Main, 2001.

[164] Detlef Irmscher. *Philosophy and parts of the global tracking chain*. NA49 Note number 131, 1997.

[165] Marco van Leeuwen. *Kaon and open charm production in central lead-lead collisions at the CERN SPS*. PhD thesis, Universiteit Utrecht, 2003.

[166] Frank Eckhardt. *Entwicklung und Bau eines Flugzeitdetektors zur Untersuchung der Hadronenemission in Pb+Pb Reaktionen bei 158 GeV/u Strahlenergie*. PhD thesis, Philipps-Universität Marburg, 1996.

[167] P. Dinkelaker. *Kaon and Pion Production in Centrality Selected Minimum Bias Pb+Pb Collisions at 40 and 158A* GeV. PhD thesis, Johann Wolfgang Goethe-Universität Frankfurt am Main, 2009.

[168] Walter Blum. *The ALEPH handbook: 1989*. CERN, Geneva, 1989.

[169] L. Landau. On the energy loss of fast particles by ionization. *J.Phys.(USSR)*, 8:201–205, 1944.

[170] R. Brun and F. Rademakers. *ROOT: An object oriented data analysis framework. Nucl. Instrum. Meth.*, A389:81–86, 1997.

[171] `http://root.cern.ch/`.

[172] `http://na49info.cern.ch/na49/Software/minidst/`.

[173] K.J. Eskola, K. Kajantie, and J. Lindfors. Quark and Gluon Production in High-Energy Nucleus-Nucleus Collisions. *Nucl.Phys.*, B323:37, 1989.

[174] A. Bialas, M. Bleszynski, and W. Czyz. Multiplicity Distributions in Nucleus-Nucleus Collisions at High-Energies. *Nucl.Phys.*, B111:461, 1976.

[175] B. Lasiuk. Particle identification in the NA49 TPCs. *Nucl.Instrum.Meth.*, A409:402–406, 1998.

[176] Tim Schuster and Dmytro Kresan for the NA49 collaboration. Acceptance tables for hadron ratio fluctuation analysis. `https://edms.cern.ch/document/984431/1`, NA49 document, 2009.

[177] Frederick James. Statistical methods in experimental physics. 2006.

[178] F James. Determining the statistical significance of experimental results. oai:cds.cern.ch:1050342. (CERN-DD-81-02):182–219, Feb 1981. Lectures presented at the 1980 CERN School of Computing, Vraona, Attiki, Greece. 14-27 September 1980.

[179] Sourendu Gupta, Xiaofeng Luo, Bedangadas Mohanty, Hans Georg Ritter, and Nu Xu. Scale for the Phase Diagram of Quantum Chromodynamics. *Science*, 332:1525–1528, 2011.

[180] Masayuki Asakawa, Shinji Ejiri, and Masakiyo Kitazawa. Third moments of conserved charges as probes of QCD phase structure. *Phys. Rev. Lett.*, 103:262301, 2009.

[181] B. Friman, F. Karsch, K. Redlich, and V. Skokov. Fluctuations as probe of the QCD phase transition and freeze-out in heavy ion collisions at LHC and RHIC. *Eur.Phys.J.*, C71:1694, 2011.

[182] Frithjof Karsch and Krzysztof Redlich. Probing freeze-out conditions in heavy ion collisions with moments of charge fluctuations. *Phys.Lett.*, B695:136–142, 2011.

[183] R.V. Gavai and Sourendu Gupta. Lattice QCD predictions for shapes of event distributions along the freezeout curve in heavy-ion collisions. *Phys.Lett.*, B696:459–463, 2011.

[184] Frederick James. Private communication.

[185] Michiel Botje. Private communication.

[186] T. Anticic et al. System size dependence of particle ratio fluctuations in Pb+Pb collisions at 158A GeV. Article in preparation.

[187] T. Anticic et al. Inclusive production of charged kaons in p+p collisions at 158 GeV/c beam momentum and a new evaluation of the energy dependence of kaon production up to collider energies. *Eur.Phys.J.*, C68:1–73, 2010.

[188] C. Alt et al. Inclusive production of charged pions in p+p collisions at 158-GeV/c beam momentum. *Eur.Phys.J.*, C45:343–381, 2006.

[189] Tim Schuster and Thorsten Kollegger. Statistical error of σ_{dyn}. NA49 analysis meeting, Wednesday 5 January 2011, 2011.

[190] Volker Koch and Tim Schuster. On the energy dependence of K/pi fluctuations in relativistic heavy ion collisions. *Phys.Rev.*, C81:034910, 2010.

[191] Michael Mitrovski, Tim Schuster, Gunnar Graf, Hannah Petersen, and Marcus Bleicher. Charged particle (pseudo-) rapidity distributions in $p^+\bar{p}$ / p^+p and Pb+Pb/Au+Au collisions from SPS to LHC energies from UrQMD. *Phys.Rev.*, C79:044901, 2009.

[192] Hannah Petersen, Jan Steinheimer, Gerhard Burau, Marcus Bleicher, and Horst Stocker. A Fully Integrated Transport Approach to Heavy Ion Reactions with an Intermediate Hydrodynamic Stage. *Phys.Rev.*, C78:044901, 2008.

[193] Hannah Petersen, Michael Mitrovski, Tim Schuster, and Marcus Bleicher. Centrality and system size dependence of (multi-strange) hyperons at 40A and 158A-GeV: A Comparison between a binary collision and a Boltzmann+hydrodynamic hybrid model. *Phys.Rev.*, C80:054910, 2009.

[194] Hannah Petersen and Marcus Bleicher. Ideal hydrodynamics and elliptic flow at SPS energies: Importance of the initial conditions. *Phys.Rev.*, C79:054904, 2009.

[195] F. Becattini, M. Bleicher, T. Kollegger, M. Mitrovski, T. Schuster, and R. Stock. Validity of the Hadronic Freeze-Out Curve. 2011. arXiv:1107.1574.

[196] P. Christiansen, E. Haslum, and E. Stenlund. On number-ratio fluctuations in high-energy particle-production. 2009. arXiv:0902.4788.

[197] Hui Wang. Private communication.

[198] M.M. Aggarwal et al. An Experimental Exploration of the QCD Phase Diagram: The Search for the Critical Point and the Onset of De-confinement. 2010. arXiv:1007.2613.

[199] T. Tarnowsky for the STAR Collaboration. A study of the qcd critical point using particle ratio fluctuations. Presentation at the Winter Workshop on Nuclear Dynamics, 2011.

[200] T. Tarnowsky for the STAR Collaboration. Charge Dependence and Scaling Properties of Dynamical K/pi, K/p, and p/pi Fluctuations from the STAR Experiment. Presentation at the Strangeness in Quark Matter Conference, proceedings in preparation, 2011.

[201] G. Westfall for the STAR Collaboration. p/pi Fluctuations in Au-Au Collisions. Poster at the Quark Matter Conference, 2009.

[202] Volker Koch. Private communication.

Curriculum Vitae

Tim Schuster
Born July 27, 1981
in Bad Soden am Taunus.

Education

- *Since 06/2007* Member of the International Helmholtz Research School for Quark Matter Studies
- *Since 03/2007* PhD student at the Frankfurt Institute of Advanced Studies. Research topic: Fluctuations as signal for the critical point of strongly interacting matter, advisor: Prof. Dr. Dr. h.c. Reinhard Stock
- *11/2006* Diploma in Physics with Distinction ("Sehr Gut mit Auszeichnung"), Johann Wolfgang Goethe-Universität Frankfurt am Main Diploma thesis with the title: "Production of Neutral Strange Hadrons with High Transverse Momentum in Pb+Pb Collisions at 158A GeV", advisor: Prof. Dr. Christoph Blume
- *06/1999* University-entrance diploma (Abitur) at Altkönigschule Kronberg/Ts.

Professional Experience

- *Since 2008* Multiple research stays at the Brookhaven National Laboratory (BNL) Upton, NY (USA) with a total duration of 2 months
- *Since 2006* Student assistant at the Institute for Nuclear Physics at the Johann Wolfgang Goethe-Universität Frankfurt am Main for teaching in practical courses and for research
- *Since 2004* Multiple research stays at the European Organization for Nuclear Research (CERN) near Geneva (Switzerland) with a total duration of 7 months